Imperial College London

Hamlyn Centre

INSTITUTE OF GLOBAL HEALTH INNOVATION

# Robots and Fibres for MR-Guided Endovascular Interventions


**Author** Mohamed E. M. K. Abdelaziz

**Supervisors** Prof. Ferdinando Rodriguez y Baena [1]
Dr. Burak Temelkuran[2]
Prof. Eric Yeatman[3]
Prof. Guang-Zhong Yang[4]



**Submitted** May 25th 2021



[1]Hamlyn Centre for Robotic Surgery, Department of Mechanical Engineering, Imperial College London, UK.
[2] Hamlyn Centre for Robotic Surgery, Department of Electrical and Electronic Engineering, Imperial College London, UK.
[3] Department of Electrical and Electronic Engineering, Imperial College London, UK.
[4] Institute of Medical Robotics, Shanghai Jiao Tong University, China.


A thesis submitted in fulfilment of the requirements for the degree of *Philosophiae Doctor*


Hamlyn Centre for Robotic Surgery, Department of Mechanical Engineering,
Imperial College London

Hamlyn Centre for Robotic Surgery,
Department of Mechanical Engineering,
Bessemer Building,
Imperial College London,
South Kensington,
SW7 2AZ

Mohamed E. M. K. Abdelaziz © 2021

We Rise by Lifting Others

*Robert Ingersoll*

---

*To Hassna and my parents.*

# Declaration

The work hereby presented is based on research carried out by the author, with the following support:

- Chapters 2: Libaihe Tian provided support with the CAD designs of the instruments and overall review. Dennis Kundrat and Dr. Wenqiang Chi provided support with the Table 2.1.
- Chapters 3 and 4: Dr. Guilio Dagnino provided support with the navigation framework. Dennis Kundrat provided support with the master manipulator and slave robot, and the overall control of the system. Marco Pupillo provided support with the initial design of the slave robot. The entire team (Dr. Giulio Dagnino, Dennis Kundrat, Dr. Wenqiang Chi, Dr. Trevor M. K. Kwok, including myself) took part in the integration and testing of the system (pilot, user and animal studies under X-ray fluoroscopy guidance, and the preliminary compatibility testing in Magnetic Resonance Imaging (MRI)). Dr. Giulio Dagnino and Dennis Kundrat provided support with the data analysis for Figures 4.6, 4.7 and Tables 3.1, 4.3. In summary, my main contributions to this work is the design, fabrication, integration, and optimisation of the slave robot and the subsequent testing of the entire platform.
- Chapter 5: The optimisation of the manual handle design and mechanical characterisation was done in collaboration with Libaihe Tian. Dr. Stefano Del Rosso provided support with the overbraiding post-processing step. The testing of the catheter under MR guidance was done in collaboration with the University of Freiburg team (Thomas Lottner, Simon Reiss, PD Dr. med Timo Heidt, and Professor Dr. med. Constantin von zur Mühlen, Professor Michael Bock).

I herewith certify that all material in this dissertation which is not my own work has been properly acknowledged.

Mohamed E. M. K. Abdelaziz

"In reference to IEEE copyrighted material which is used with permission in this thesis, the IEEE does not endorse any of Imperial College London's products or services. Internal or personal use of this material is permitted. If interested in reprinting/republishing IEEE copyrighted material for advertising or promotional purposes or for creating new collective works for resale or redistribution, please go to this link to learn how to obtain a License from RightsLink. If applicable, University Microfilms and/or ProQuest Library, or the Archives of Canada may supply single copies of the dissertation."

The formatting for this thesis is taken from the Thesis Template by R. Robinson.

The copyright of this thesis rests with the author and is made available under a Creative Commons Attribution Non-Commercial No Derivatives license. Researchers are free to copy, distribute or transmit the thesis on the condition that they attribute it, that they do not use it for commercial purposes and that they do not alter, transform or build upon it. For any reuse or redistribution, researchers must make clear to others the license terms of this work.

# Acknowledgements

I would like to thank Professor Guang-Zhong Yang, who made this journey possible. His dedication, vision and passion have been inspirational. His insights opened my eyes to new and challenging frontiers of research; his support helped me gain confidence in my abilities and conviction in my work. This PhD period has definitely been a life-changing experience for me which I owe mostly to Professor Yang. Thank you for believing in me and giving me the opportunity to work in a unique and multi-disciplinary environment with so many talented, passionate and truly inspiring people.

My gratitude goes to Dr Burak Temelkuran for his daily guidance and availability. This work would not have been possible without his tireless help, continuous support, and insightful observations. He introduced me to the amazing world of fibre drawing, and in doing so, he shaped both my PhD and future carrier paths. His commitment to assist whenever needed, late-night or weekends, will always remind me of what it takes to become a great mentor "teşekkürler Burak".

I am very thankful to Professor Ferdinando Rodriguez Y Baena, who pushed me to bring my PhD to fruition. I am incredibly grateful for his dedication to providing me with feedback and suggestions to improve this dissertation. My gratitude and appreciation goes to Professor Eric Yeatman for his invaluable feedback and support over the last year.

I am honoured to have worked with the CathBot team; my utmost appreciation goes to Dr. Giulio Dagnino, Dennis Kundrat, Wenqiang Chi (Bobby), Dr. Jindong Liu, Dr. Trevor MY Kowk, Dr. Anh Nguyen, Marco Pupillo and Dr. Celia Riga. Without their support the work presented in this thesis would not have been possible. Working with the CathBot team taught me the true meaning of teamwork and how it can ameliorates one's work.

I would also like to thank our collaborators at the University of Twente (Dr. Vincent Groenhuis, Dr. Françoise Siepel, Professor Stefano Stramigioli) for their incredible support with MR safe actuation, the University of Freiburg (Thomas Lottner, Simon Reiss, PD Dr. med Timo Heidt, and Professor Dr. med. Constantin von zur Mühlen, Professor Michael Bock) for their immense ongoing support with MRI testing, and EPFL (Dr. Tung Nguyen-Dang, Andreas Leber, Professor Fabien Sorin) for their training and support with fibre drawing. I would also like to thank Dr. Klaus Düring and MaRVis Interventional GmbH for their support and confidence throughout the course of my PhD.

My recognition also goes to the MRes students (Libaihe Tian, Jinshi Zhao, Jianan Zhang) that I had the pleasure to mentor and work with. Their commitment and passion for research and learning were inspirational. Thank you all for your support, friendship and delicious treats over the course of last year. I would like to thank the many talented, dedicated, engaging and skilled colleagues (Dr.Pierre Berthet-Rayne, Shen Treratanakulchai, Daniel Bautista-Salinas, Rejin Varghese, Jiwoo Choi, Dr. Ning Liu, Dr. Anzhu Gao, Dr. Yang Hu, Dr. Jang Ah Kim, Dr. Antoine Barbot, Dr. Maura Power, Dr. Bruno M. G. Rosa, Dr. Bing Li, Dr. Piyamate Wisanuvej, Dr. Haijie Tian, Dr. Khushi Lavsi) that I had the honour and the pleasure to work with. I am also grateful to Professor Mohamad Hamady whose input greatly enriched my work. Special thanks to Mr. Paul Brown, Mr. David J. Williams, Mr. Steven Nelson, Mr. David

Bowler, and Mr. Graham Brooks for their support with machining. I would like to express my sincere gratitude to Mr. Jason Keane, Ms. Erh-Ya (Asa) Tsui, and Dr. Amani El-Kholy for their support, guidance and encouragement.

Furthermore, I would also like to acknowledge with much appreciation and gratitude, the role of the Institute of Global Health Innovation, who provided me with a scholarship to pursue my studies at Imperial College London, and the Engineering and Physical Sciences Research Council (EPSRC) whose grants have funded most of equipment and resources that were instrumental to my work.

I would like to sincerely thank my friends friends Maged, Mekki, Aboudonia, Hussein, and my family for their continuous support, understanding, encouragement and love that they have given me. Thank you to my mother Fatma, my father Essam, my sister May, my grandmother May, even though she is no longer here. Without their encouragement, I would not have been able to make it through this challenging, yet rewarding, journey.

Above all I would like to thank my wife Hassna for her love, care and constant support, and for keeping me sane over the past few years. Thank you for being my blessing, muse, inspiration and sounding board. But most importantly, thank you for being my best friend. I owe you everything and I dedicate this thesis to you.

# Abstract

*Interventional radiology and cardiology are rapidly growing areas of minimally invasive surgery, covering multiple diagnostic and interventional procedures. Treatment via endovascular techniques has become the go-to approach, thanks to its minimally invasive nature and its effectiveness in reducing hospitalisation and total time to recovery when compared to open surgery. Although X-ray fluoroscopy is currently the gold standard imaging technique for endovascular interventions, it presents occupational safety hazards to medical personnel and potential risks to patients, especially paediatric patients, because of its inherent ionising radiation. Magnetic resonance imaging (MRI), with its unique ability to provide radiation-free imaging, and acquiring morphologic and functional information, holds great promise in the advancement of image-guided navigation through the vasculature. Moreover, MRI has the potential to combine diagnosis, therapy and early evaluation of therapy in the same intervention. However, MR-guided interventions face major challenges due to the limited accessibility to patients (especially paediatric patients), excessive noise levels within the room which impede the communication between the medical personnel, and most prominently, the lack of MR safe and compatible instruments.*

*This thesis addresses these challenges in two main stages. The first centres on the development of a robotic platform that aims to improve the precision, safety, access, comfort and to minimise and possibly eliminate radiation exposure for the patient and medical personnel. The master-slave system allows clinicians to remotely manipulate commercially available instrumentation and in-house fabricated steerable catheters. The platform comprises a master manipulator that emulates conventional manipulation of instruments and offers haptic-feedback to the operator. In addition, the slave robot is pneumatically actuated using 3D printed linear and rotary stepper motors. The robotic system not only reduces the medical personnel's exposure to ionising radiation when used under X-ray fluoroscopy guidance, but also paves the way for endovascular interventions under MR as a result of the slave robot's polymeric nature. Assessment experiments under X-ray fluoroscopy guidance demonstrated the feasibility of the platform through clinically relevant endovascular tasks performed by clinical experts in an* in-vitro *phantom study. Subsequently, an animal study with an expert endovascular surgeon validated its efficacy and safety, by achieving lower occurrence and severity of injuries (as per post-mortem histopathological assessment).*

*The second complementing stage leverages the unconventional scalable fibre drawing technique to address the gap in MR safe instrumentation. By exploiting its unique advantages, a new low-cost rapid prototyping platform for the fabrication of arbitrary cross-sections and high aspect ratio materials, is presented, which aims to accelerate technology translation in the field of minimally invasive surgery. Using this technology, a novel 7Fr MR safe and passively visible steerable catheter was developed to navigate through the anatomy under MR-guidance. Thorough bench-top mechanical characterisation of the polymer-based catheter showed comparable mechanical performance, which did not differ significantly from the commercial metal-braided selective and steerable catheters on the market today. Real-time MR*

*image guidance of the in-house fabricated catheter was demonstrated in a vessel phantom under a clinical 3 Tesla MR scanner to evaluate the catheter's mechanical efficacy and MR visibility. Small vascular structures, such as the renal artery, could be probed efficiently with the polymer-only based catheter. With the integrated iron markers, it was visible in its entirety, and the limited artefact size allowed for the effective visualisation of surrounding tissue. Moreover, the catheter's steerability, visibility and safety were successfully demonstrated in a porcine model. Lastly, in an attempt to demonstrate the future potential of the work presented in this thesis, the robotic platform is extended to host the steerable catheter, paving the way for further testing under MR-guidance.*

# Contents


**1 Introduction** **30**

1.1 Motivation and Research Objectives . . . 31
1.2 Key Contributions . . . 33
1.3 Publications and Patents . . . 34
1.4 Overview . . . 36

**2 Endovascular Navigation under X-ray (Fluoroscopy) and MR-Guidance** **39**

2.1 Overview . . . 39
2.2 Navigation Under X-ray (Fluoroscopy) Guidance . . . 40
2.2.1 Guidewires . . . 40
2.2.2 Selective Catheters . . . 42
2.2.3 Challenges Associated with Navigation under X-ray (Fluoroscopy Guidance) . . . 46
2.2.4 Robot-Assisted Platforms for Endovascular Interventions . . . 46
2.2.4.1 Commercial Platforms for General Vasculature (PVI, PCI) . . . 47
2.2.4.2 Commercial Platforms for Electrophysiology (EP) . . . 48
2.2.4.3 Emerging Research Platforms for Endovascular Interventions . . . 49
2.3 Navigation Under MR Guidance . . . 51
2.3.1 MRI and MR-guided Endovascular Interventions . . . 51
2.3.2 MRI Safety Labelling . . . 52
2.3.3 Guidewires and Selective Catheters . . . 52
2.3.4 Steerable Catheters . . . 59
2.3.4.1 Pull-wire Driven . . . 59
2.3.4.2 Hydraulic . . . 61
2.3.4.3 Magnetic . . . 63
2.3.4.4 Shape Memory Alloys (SMAs) . . . 64
2.3.4.5 Comparison . . . 65
2.3.5 MR Visibility . . . 67
2.4 Future Directions . . . 72
2.4.1 Material and Fabrication Schemes . . . 72
2.4.2 Imaging Pulse Sequence Design . . . 73
2.4.3 Robotic Control . . . 73
2.4.4 Safety . . . 73
2.4.5 Coordinate Interdisciplinary Approach . . . 74
2.5 Conclusions . . . 74

**3 An MR-Safe Endovascular Robotic Platform: Pilot Study 76**
3.1 Introduction . . . 76
3.1.1 State of the Art . . . 77
3.1.2 Limitations & Contribution . . . 77
3.2 Clinical Requirements . . . 78
3.3 Robotic Design . . . 78
3.3.1 Haptic Master Device . . . 78
3.3.2 Slave Robot . . . 80
3.3.2.1 Robot Design . . . 80
3.3.2.2 Stepper Motors & Clamps . . . 81
3.3.2.3 Pneumatic Control . . . 81
3.3.2.4 Robot Kinematics . . . 81
3.3.2.5 Fabrication . . . 83
3.3.2.6 MRI-Compatibility . . . 83
3.4 Control Architecture . . . 83
3.4.1 Navigation System . . . 84
3.4.2 Robot Control . . . 85
3.5 Experimental Validation . . . 85
3.5.1 Clinical Workflow and Setup for Robotics Procedure . . . 85
3.5.2 X-Ray Fluoroscopy Pre-Clinical Trials . . . 85
3.5.3 MRI Preliminary Study . . . 86
3.6 Discussion . . . 87
3.6.1 Fluoroscopy Pre-clinical Trials Results . . . 87
3.6.2 MRI . . . 89
3.7 Conclusions . . . 89

**4 An MR-Safe Endovascular Robotic Platform: User Study 91**
4.1 Contribution . . . 91
4.2 Robotic Framework . . . 92
4.2.1 Master Manipulator . . . 93
4.2.2 Design Optimisation of Pneumatic Actuators . . . 95
4.2.3 MR-safe Slave Robot . . . 96
4.2.4 Control and Navigation . . . 97
4.3 UserStudy . . . 99
4.3.1 Experimental Setup . . . 99
4.3.2 Study Design . . . 101
4.3.3 Evaluation Methodology . . . 102
4.3.4 Statistical Considerations . . . 103
4.4 Results . . . 104
4.4.1 Study Metrics . . . 104
4.4.2 Questionnaire . . . 107

4.5 Discussion . . . 107
4.6 Extended Work: *in-vivo* Animal Trials . . . 110
4.7 Conclusions . . . 112

**5 Thermally Drawn Steerable Catheter for MR-guided Endovascular Interventions 113**
5.1 Contribution . . . 113
5.2 Limitations and Requirements . . . 114
5.2.1 Limitations Impeding Development of MR Safe Steerable Catheters . . . 114
5.2.2 Requirements for the Development of an MR Safe Steerable Catheter . . . 115
5.3 Steerable Catheter Fabrication . . . 116
5.3.1 Multi-Lumen Tubing . . . 116
5.3.2 Multi-lumen tubing with a Twist . . . 119
5.3.3 Post-Processing of Multi-Lumen Tubing . . . 124
5.4 Bench-top Mechanical Characterisation . . . 129
5.4.1 Flexural Rigidity . . . 129
5.4.1.1 Methodology . . . 129
5.4.1.2 Results and Discussion . . . 130
5.4.2 Pushability . . . 132
5.4.2.1 Methodology . . . 133
5.4.2.2 Results and Discussion . . . 134
5.4.3 Torquability . . . 134
5.4.3.1 Methodology . . . 134
5.4.3.2 Results and Discussion . . . 135
5.5 Manual Handle and Catheter Integration . . . 137
5.5.1 Manual Handle Design . . . 137
5.5.1.1 Design Requirements . . . 137
5.5.1.2 Handle Designs (State-of-Art) . . . 137
5.5.1.3 Proposed Handle Design . . . 138
5.5.2 Catheter Integration . . . 138
5.5.3 Discussion . . . 140
5.6 Steerability . . . 141
5.6.1 Methodology . . . 141
5.6.2 Results and Discussion . . . 141
5.7 Helical Compensation . . . 144
5.7.1 Methodology . . . 144
5.7.2 Results and Discussion . . . 145
5.8 *In-Vitro* and *In-Vivo* Studies . . . 146
5.8.1 *In-Vitro* MR Compatibility and Phantom Study . . . 146
5.8.2 *In-Vivo Animal Study* . . . 148
5.9 Catheter Robot Integration . . . 150
5.9.1 Robotic Catheterisation . . . 150

5.9.2 Actuation Unit . . . 150
5.9.2.1 Design Requirements . . . 150
5.9.2.2 Proposed Design . . . 150
5.9.3 Preliminary Test . . . 152
5.10 Conclusions . . . 153

**6 Conclusion and Future Work** **155**
6.1 Conclusions and Limitations . . . 156
6.2 Future Work . . . 158

**References** **161**

**Appendices** **178**

**A Fibre Draw Tower** **179**

**B Catheter Samples' Dimensions** **180**

**C Catheter Post-Processing** **182**

**D Steerability Results** **183**

**E Liner Feeding (Patent)** **199**

# List of Figures

1.1 Cardiovascular Diseases and their corresponding endovascular intervention(s): . . . . . 32

2.1 (a) Two different types of commonly used guidewire tips (distal ends): curved (angled) and straight. The distal ends tend to be heat treated to set the desired shape, e.g."J"-shape [22]. (b) The transition from an untapered to a tapered core wire using centreless grinding to achieve the desired taper profile across the distal end in (c). For (c-g), a sectioned view of the distal end of commercially available guidewires and their corresponding insets, illustrating the core design and its surrounding elements (coils, ribbons, etc). (c) Guidewire widely used in peripheral interventions (Radifocus® Guidewire (Terumo Europe NV, Leuven Beligum)). This type has a core-to-tip design and is fully covered with polymer. For radiopacity, the tip is plated with a radiopaque material (gold in this illustration). (d-g) Guidewires comprising a radiopaque coil instead of the aforementioned radiopaque plated core tip. Classification based on **polymer covering**: (d and e) guidewires covered fully with polymer, and (f and g) guidewires partially covered with polymer. Classification based on **core design**: (d and f) core-to-tip design, and (e and g) shaping/forming ribbon design. Guidewire **coating**: (b) has an additional layer of hydrophilic polymer that is added to improve lubricity, trackability and manoeuvrability. On the other hand, (e) employs a hybrid approach by coating the distal-most point with a hydrophobic polymer (e.g. silicone) to enhance tactile feedback and tip control. Note: The illustrated examples are merely a few examples of commercially available coating configurations. 41

2.2 (a-h) Guidewires comprising a radiopaque coil and an additional support coil to promote the tip's resilience and mechanical properties. A sectioned view of the distal end of commercially available guidewires and their corresponding insets, illustrating the core design and its surrounding elements (coils, shaping ribbon). Classification based on **support coil placement**: (a-d) coaxially placed support coil (commonly stainless steel) with respect to a radiopaque coil, and (e-h) support coil placed in series with respect to a radiopaque coil. Classification based on **polymer covering**: (a, b, e and f) guidewires fully covered with polymer, and (c, d, g and h) guidewires partially covered with polymer. Classification based on **core design**: (a, c, e and g) core-to-tip design, and (b, d, f and h) shaping/forming ribbon design. Guidewire **coating**: (b, c and f) have an additional layer of hydrophilic polymer to improve the guidewires' lubricity, trackability and manoeuvrability. Conversely (g) employs a hybrid approach by applying a hydrophobic polymer (e.g. silicone) at the distal-most point to enhance tactile feedback and tip control. Note: The illustrated examples are merely a few examples of commercially available coating configurations. . . . . 43

2.3 (a) A sectioned view of the distal end of a guidewire comprising a nitinol hypotube coaxially placed with respect to a radiopaque coil. The insets illustrate the core design and its surrounding elements (hypotube, core, coil). The design shown falls under the core-to-tip design category and consists of a partial polymer covering. Although not illustrated, the distal end can also be coated with hydrophilic/hydrophobic coatings to achieve the desired mechanical and physical properties. (b) Spring-coil covered guidewire with a fixed core design. (c-d) Spring-coil covered guidewire with a movable core design. (c) Initial state of the guide wire, i.e. angled distal end (tip). (d) The proximal end is pushed, thereby moving the core wire with respect to the spring coil, which in turn straightens the distal end (tip). The safety wire in (b-d), illustrated in red, minimises the possibility of tip detachment if the spring coil breaks. . . . . 44

2.4 Guiding Catheter Fabrication Steps: (a) A ram extruded PTFE mandrel is fed through a chemically etched ram extruded PTFE liner to prevent the liner from collapsing during the subsequent processes. (b) The liner/mandrel assembly is then braided with stainless-steel wires (e.g. $50\mu m$ 316L stainless-steel round wires) using a maypole braiding machine. (c) A small section of the liner is left non-braided to create a flexible atraumatic tip. (d) A multi-durometer PEBAX® outer layer is applied on top of the braided liner/mandrel assembly to encapsulate the braid. The stiffness of the outer catheter decreases progressively from the proximal end (Shore Hardness 72D) to the distal atraumatic radiopaque tip (Shore Hardness 35D). The transition segments (45D and 55D) are added to reduce the possibility of catheter kinking caused by abrupt changes in flexibility. This fabrication step can be achieved using various techniques, including thermal bonding of multi-durometer segments[28], intermittent extrusion[29]. (e) The PTFE mandrel is pulled out of the laminated tube. (f-g) The laminate is mounted onto a forming wire to form the desired distal end shape. (h) The distal end shape is modified using a template (e.g. Judkins right 4) and placed in a forming oven for a predetermined temperature and time. (i) After annealing, the assembly is cooled, followed by the removal of the forming wire. . . . . 45

2.5 2D X-ray fluoroscopy sequence illustrating the catheterisation of the Left Renal Artery (LRA) in an abdominal phantom (Elastrat, Geneva, Switzerland) using a selective catheter, IMPRESS®, Size = 5F (1.667mm outer diameter), Distal End Shape: Headhunter 1, Length = 100cm, Inner Diameter=0.046" (1.17mm), Reference: 510035HH1 (Merit Medical OEM, Utah, US) and a guidewire, Radifocus® Guidewire M Standard Type Guidewire, Length = 180cm, Outer Diameter = 0.035", Flexible Length = 10mm, Angled Distal Tip, Reference: RF-GA35181M, (Terumo Europe NV, Leuven Beligum). (1) Indicates the LRA target and the catheter. (2) Guidewire is advanced over the LRA whilst keeping the catheter in place. The catheter's distal end straightens due to the advancement of the guidewire. (3) Catheter is advanced over the guidewire. (4) Guidewire is partially retracted and the catheter restores the pre-shaped distal end. (5) The catheter is rotated to adjust its orientation. (6-8) The catheter and guidewire assembly is slowly retracted towards the LRA. (9) The catheter's distal end slides into the LRA, (10-11) The guidewire is advanced through the catheter to prevent the catheter from flipping back to the abdominal aorta. (12) The catheter is advanced over the guidewire. . . . . 47

2.6 **MR Physics (I):** (a) A human tissue voxel largely made of water and fat, which contain hydrogen atoms. (b) A simplified representation of the nucleus of a hydrogen atom. The nucleus is a positively charged proton with an intrinsic property, called spin or intrinsic angular momentum. The non-zero net spin generates a magnetic dipole moment ($\mu$ or MDM for short), which in turn generates a small magnetic field. MDMs and spins are used interchangeably in literature because they track each other. (c) A further simplified representation of the nucleus, which is used in the rest of the figure.(d) In the absence of an external magnetic field, the atoms' MDMs are pointing randomly, hence giving a uniform distribution of MDMs in the top and isometric views of an implicit coordinate system. The net magnetisation (denoted by $M$) is the sum of the individual MDMs. In the absence of an external magnetic field, $M$ is zero. (e) Upon the application of an external strong static magnetic field ($B_0$), i.e. the patient is placed in the MRI bore, two events take place: 1. The orientation of the MDMs is skewed slightly toward $B_0$'s direction (increased density of MDMs) resulting in an increase in $M$ (yellow arrow), 2. The ensemble of MDMs start precessing at the Larmor frequency (42 MHz at 1 Tesla) around $B_0$'s direction. Although the spins are precessing, $M$ remains in equilibrium. . . . . 52

2.7 **MR Physics (II):** (a) RF Pulse Excitation: When a rotating homogeneous RF field, denoted by $B_1$ , is applied perpendicular to $B_0$, the entire magnetisation distribution, is tipped away from its initial alignment with $B_0$ ($90°$ in this example). Simultaneously, the magnetisation distribution slowly rotates around the rotating $B_1$ axis (indicated by the blue circular arrow). Notes: The path followed by $M$ is observed from a stationary frame of reference, $B_1$ field does not change the relative orientation of individual MDMs, and the $B_1$ field rotates at the Larmor frequency. (b) After switching off the rotating RF field, $M$ returns to thermal equilibrium (relaxation), i.e. aligning back to $B_0$ direction. The inset (c) is zoomed-in in (d). (d) Plot illustrating the two magnetisation components of $M$, and their corresponding relaxation times. $T_2$ is the time required for the transverse magnetisation ($M_{xy}$) to decrease exponentially to approximately $37\%$ $(1/e)$ of its initial value. Conversely, $T_1$ is the time required for the longitudinal magnetisation ($M_z$) to return to $63\%$ $(1 - 1/e)$ of its maximum value ($M_0$), where $M$ is equal to $M_0$ at equilibrium (i.e. aligned with $B_0$'s direction). $M_{xy}$ is the component detected by the RF receiving coils which gives rise to the MR image. $M_z$ does not contribute to the acquired signals. An important mechanism for the decay in $M_{xy}$ , i.e. $T_2$ relaxation (spin-spin relaxation) is as follows. The MDMs (spins) experience local fields which are combinations of $B_0$ and the fields from their neighbouring protons' MDMs. The variations in local fields lead to different local precessional frequencies, and as a result, the protons' MDMs (spins) fan out in time, thereby reducing $M_{xy}$ . The fanning out of MDMs (spins) is referred to as dephasing. $T_1$ relaxation (spin-lattice relaxation), on the other hand, occurs when a proton exchanges magnetic energy with its external environment (lattice). $T_1$ relaxation also results in $T_2$ relaxation, ensuring that $T_2$ is longer than or equal to $T_1$. Note: The transition in (b) illustrates the overall effect of both relaxation mechanisms. . . . . 53

2.8 (Left) Hands-on MR-guided intervention: The operator manipulates the instruments manually with real-time MR images projected onto a screen inside the scanner room. Operators, staff, and patients wear noise reduction headsets to protect their hearing from the loud noises produced by the scanner's gradient coils [139]. (Right) Robotic-assisted MR-guided intervention: The operator uses a control console to remotely operate an MR safe/MR conditional robotic system which in turn manipulates the instruments. The operator can view the real-time MR images on the screen located in the scanner's control room [125]. . . . . 54

2.9 MR Guidewires (I): (a) Guidewire consisting of a glass-fibre reinforced PEEK core covered with a polyurethane jacket. The core is grounded at its distal end to create a flexible distal end. (b) Cross-sectional (inset) of the micropultruded glass-fibre reinforce PEEK core [138, 150, 153]. (c) Guidewire comprising a PEEK core with iron microparticles embedded in the polymeric coating [147]. (d) Steerable guidewire composed of a flexible PEEK shaft, a deflectable tip and a Dyneema® pull-wire travelling through the entire guidewire. The steerable tip is a re-purposed 2.4Fr microcatheter (flexible tube) embedded with a flattened nitinol rod to straighten the tip and to constrain its bending in one direction. At the very distal end of the guidewire is a PEEK cap. The entire body is covered with polyethylene heat shrink tubing to hold all the components together. (e) Pulling of the pull-wire results in the bending of the deflectable tip [2, 148]. (f) Guidewire constructed using short nitinol rod segments (guidewire shaft) and a tapered nitinol rod with a long coil mounted onto it (flexible distal end). The distal end is jacketed with a non-braided thermoplastic polymer and the entire body is covered with a soft polymer. (g-h) Zoom-in cross-sectional (inset) of the guidewire shaft which consists of nitinol rod segments (grey) joined by nitinol connectors (blue) with notched ends. For electrical insulation, the nitinol rod is coated with a thin film of parylene and jacketed with PEBAX® to achieve a consistent profile (between rods and connectors) [156]. *MRI markers are passive negative markers. . . . . 55

2.10 MR Guidewires (II): (a) Stiff MaRVis guidewire comprising of a shaft and an iron-doped PEBAX® flexible distal end. (b) Cross-sectional zoom-in (inset) of the shaft that consists of micropultruded glass and/or aramid fibres embedded in epoxy resin and in certain cases iron-doped epoxy resin for MR visibility (referred to as MaRVis rods). To construct the guidewire shaft, several MaRVis rods are arranged and embedded in a polymer matrix and are subsequently covered with a PTFE heat shrink tubing. (c) Further zoom-in (inset) of a MaRVis rod. (d) Further zoom-in (inset) of a iron-doped MaRVis rod [157, 158]. (e) Guidewire consisting of twisted high strength synthetic aramid fibres, surrounded by rings of passive negative markers for MR visibility (placed at discrete points) and a polymer composite to provide the desired mechanical performance. At the distal end, a flexible radiopaque tip is mounted at the tip for enhanced tip visibility. The entire body is covered with a PTFE heat shrink tubing. In [159, 160], instead of the coil and PTFE layer, the tip section was coated with PEBAX® and the guidewire was coated with a hydrophilic polymer. (f-g) Guidewire comprising a micropultruded glass-fibre reinforced core wrapped and consolidated with additional layers of high strength synthetic fibres. Passive negative markers are applied at discrete intervals for MR visibility and an outer layer is utilised to form the guidewire. (h) Flexible tip achieved by small winding pitch and (i) High bending and torsional stiffness of guidewire shaft achieved by large winding pitch [161]. . . . . 56

2.11 **(Manual) Pull-wire Driven Catheters for MR-guided interventions (I)** (a) A uni-directional catheter inspired by Bell et al.'s design: The deflectable distal end consists of a nitinol laser-cut hypotube, connected to a Kevlar® pull-wire. In the case of Bell et al., a nitinol spring was concentrically added to the laser profiled tube [173]. (b) Yao et al.'s uni-directional steerable catheter: A nitinol supported PTFE tube was used as the deflectable distal end. A control wire glued to a control rod was used for steering [174]. (c) Clogenson et al.'s multi-selective catheter: The design comprises a laser profiled PEEK tube with four pull-wires travelling through the entire catheter length. The first pair of pull-wires control segment#1 and the second pair of pull-wires control segment#2. In terms of joint design, a sliding curved joint was utilised to form the articulated deflectable segments [2, 175]. Note: The catheter is made from a single material, however, different segment colours (red and beige) are used only used for illustrative purposes. . . . . 61

2.12 **(Robotic) Pull-wire Driven Catheters for MR-guided interventions (II)** (a) Simplest form of concentric or telescopic catheters: The system consists of two uni-directional catheters (inner leader catheter and outer guide catheter) which are controlled independently and collaboratively to recreate the shapes of common selective catheters. (b) Ataollahi et al.'s additively manufactured deflectable catheter: The design consists of clockwise and counter-clockwise helical segments employed in an alternating fashion (illustrated in yellow and white). To control the distal end in 3D space, four polymeric pull-wires were utilised [177, 178]. . . . . 62

2.13 **Distal end of Hydraulic Driven Catheters (HDCs)** (a) Haga et al.'s uni-directional HDC: A laser profiled nitinol tube covered with a thin silicone rubber tube is controlled by changing the negative pressure of the fluid [179]. (b) De Boer et al.'s conceptual design of a multi-directional HDC: The distal end comprises a central lumen and four parallel pressurisable chambers. Changing the inner fluid pressure results in the bending of the deflectable tip of the catheter. Note: The figure illustrates deflection in only two directions [183]. (c) Skerven et al.'s conceptual design of a multi-directional (External Balloon) HDC: The deflectable tip consists of four external balloons attached to a flexible tubing. To steer the distal end towards a specific direction, the external balloons are inflated (pressurised) and deflated (unpressurised) accordingly. Similar to De Boer et al.'s design, the figure illustrates deflection in only two directions [185]. (d) Johansen et al.'s conceptual design of an (Internal Balloon) HDC: The distal end includes a corrugated section attached to the inner tube and an asymmetric internal balloon attached to the outer tube. The internal balloon is configured to deflect the distal end of the catheter [184]. (e) Ikuta et al.'s single-input, multi-output HDC: The steerable tip consists of serially placed, independently valve-controlled bellows. To bend a specific segment, the target valve is opened by increasing the pressure of the driving tube until it reaches the activation pressure band of the valve. The figure illustrates the case where both segments (bellows) are actuated [180–182]. . . . . 63

2.14 **Distal end of MR-actuated Magnetic Catheters** (a) (Simplified, Single Plane) microcoil-based: A microcoil is attached to a flexible tubing. Depending on the direction of flow of current, the distal bend is steered in a specific direction accordingly [188–194]. (b) Ferromagnetic sphere-based: The deflectable tip consists of ferromagnetic spheres [195–198]. (c) Ferrofluid-based: The distal end comprises a balloon filled with a ferrofluid [195]. All three distal ends (a-c) experience a turning force or torque to align its local magnetic field with the external field of the MRI scanner. The distal ends in the figure are placed within the bore of the MRI scanner, indicated by the three main components: Main Magnetic Coil, Gradient Coils and RF Coils. . . . . 65

2.15 **Distal end of Shape Memory Alloys (SMAs) actuated catheters** (a) SMA Microcoils/Springs (Fu et al.'s design): This design comprises three microcoil actuators, a bias spring and links (to fix and integrate the SMA actuators and bias spring). A silicone tube was utilised to cover the entire configuration [211–213]. (b) Electrochemically etched SMA sheets (Mineta et al.'s design): An SMA sheet was electrochemically etched into SMA (flat-spring-like) actuators, which were then attached to a helical bias spring. To form a unitary body, an outer tubing was employed, and inner tubing was added to facilitate the insertion/removal of guidewires and intravascular devices. Namazu et al. utilises similar fabrication and actuation techniques [214, 215]. (c) SMA wires: In this design, a plurality of parallel SMA wires (three or four) are embedded into a flexible multi-lumen tube [216–220, 225]. In all three embodiments of SMA actuated catheters (a)-(c), the actuators are embedded/added in an elongated (pre-loaded) condition and are distributed at an angle of $120°$. When the SMA actuator(s) is heated (illustrated in red), it contracts and results in the bending of the distal end towards a specific direction. (d) Conceptual design of a laser-profiled SMA tube (Langelaar et al.'s design): The distal end consists of laser-cut (or etched) a small diameter SMA tubing. The laser cut patterns facilitate the bending of the distal end in two orthogonal directions. When a specific segment of the tube is locally heated, it contracts, and the distal end bends accordingly [221–224]. In all the four cases illustrated (a)-(d), only two bending directions are shown (for better clarity). . . . . 66

2.16 Advantages and disadvantages of tracking methods (marking) for interventional devices . . . . . 71

3.1 Novel robotic platform with versatile, MR-safe slave robot (right) and intuitive master device (left) for endovascular interventions. . . . . 76

3.2 Conceptual design and prototype of the proposed haptic master with electro-mechanical set-up and sensing: (a) Top and (b) front view of the CAD model. . . . . 79

3.3 Conceptual design of the proposed slave robot: (a) Top and (b) side view of the CAD model, and (c) magnified details of quick release instrumentation mounting and mechanism for introduction of rotary motion to catheter and guidewire. . . . . 80

3.4 (a) Illustration of catheter buckling during feeding due to unsupported length in free space. (b) Example of the insertion sequence. (1) Starting from the initial static position, (2) P1 clamps the catheter. (3) P1 and P2 move at the same speed (to avoid buckling) and for the same predefined entire stroke. (4) P1 releases the catheter and returns to the initial position, (5) while P2 stays still. (6) P1 clamps the catheter again. (7) P1 and P2 advance simultaneously half of the defined stroke. (8) P1 releases the catheter. . . . . 82

3.5 Control architecture . . . 83
3.6 Experimental setup for fluoroscopy-based trials, where (1) Vascular phantom, (2) Pulsatile and continuous flow pump, (3) Slave robot, (4) C-arm, (5) Force/Torque sensor . . . 87
3.7 (a) Experimental MRI setup, where (1) SENSE-Torso coil with 16 elements, (2) Vascular Phantom, (3) Slave Robot . . . 88
3.8 (Projection of the abdominal aorta and illiac arteries with (a) manual, (b) robotic guidewire retraction. Magnified views show the passive MR markers of the guidewire (black spots, (c) Difference image . . . 89

4.1 (a) CAD rendering representing the system architecture of the proposed framework. (b) System architecture of the proposed versatile robotic framework. The surgeon, located in the control room, teleoperates the MR-safe slave robot deployed in the intervention room by manipulating the master manipulator. The navigation system provides real-time visual guidance and haptic feedback is rendered through the master manipulator to guide the surgeon during the procedure. . . . 92
4.2 Master Manipulator CAD renderings (a) Top view without the outer cover, (b) Front view without the outer cover, (c-d) Isometric views with the outer cover . . . 93
4.3 (a) Linear pneumatic stepper motor with floating silicone patch (previous design employed in the pilot study). (b) Linear pneumatic stepper motor with o-rings sealing (proposed new design). (c) Pressure-time plot for the proposed new piston design (red plot), previous piston design (blue plot), nominal pressure (dashed). Raw data is fitted with a polynomial. (d) Rotary pneumatic stepper motor with o-rings sealing (proposed new design). . . . 95
4.4 (a) Slave CAD model with kinematic annotations of the corresponding platforms. (b) Top view of the slave with the two quick release mechanisms (I) and (II) Labelled. (c-d) Inset of the quick release instrumentation mounting for the introduction of rotary motion to the catheter (c) and guidewire (d). (e) Back-sided view of the GR platform. (f-g) Inset of the optimised clamp. (h) Sequence of piston states during the translation of the rack to the left. After four steps the linear motor is back in the first state. The stepper motor has a step-size of 0.3mm. (i) Sequence of piston states during clockwise rotation of the geared axle. After four steps the rotary stepper motor is back in the first state. The rotary motor has a step size of 10°. Acronyms: Catheter (C), guidewire (G), catheter carrier (CC), guidewire carrier (GC), catheter rotation (CR), guidewire rotation (GR), and rotary actuator (RA) . . . 98
4.5 Experimental setup of user study: (a) Master manipualtor console with user interface in control room and (b) slave robot deployed to phantom installed in fluoroscopic monitoring (c) Phantom setup and task conditions: (c) Abdominal phantom with LCIA, LRA, and SMA tasks. (d) Thoracic phantom with RCCA task. Red markers denote start configurations and blue markers denote the nominal cannulation target of each trial. Acronyms describe: infrarenal aorta (IA), suprarenal aorta (SA), superior mesenteric artery (SMA), inferior mesenteric (IM), celiac artery (C), left subclavian artery (LSA), aortic arch (AA), right subclavian artery (RSA), left subclavian artery (LSA), aortic arch (AA), and left common carotid artery (LCCA). . . . 100
4.6 Boxplots: (a) Catheter path lengths, (b) guidewire path lengths, (c) task completion times, and (d) maximum forces. . . . 105

4.7 Forces and kinematics examples: (a) robotic LCIA cannulation, (b) robotic RCCA cannulation, (c) manual RCCA cannulation, (d) kinematics data to task in (a), and (e) kinematics data to task in (b). Colour overlays correlate tracked tip positions and corresponding force measurements. This enables identification of difficult anatomy or catheter handling issues. (f) Completion time and path lengths metrics for a robotic RCCA cannulation over number of study trials. (g) Survey results. Red plots annotate statements related to design and usability. Blue plots denote task specific statements. Marker * indicates negative statements. . . . . 106

4.8 (a) Operator remotely manipulating the robot using the master manipulator. (b) MR safe slave robot positioned next to the animal using a scope and holding arm (KARL STORZ SE & Co. KG, Tuttlingen, Germany). Acquired fluoroscopy scans of the deployed and inflated balloon catheter in the five different target arteries: (c) Left Common Iliac Artery (LCIA), (d) Left Renal Artery (LRA), (e) Right Renal Artery (RRA), (f) Right Common Carotid Artery (RCCA), (g) Superior Mesenteric Artery (SMA). . . . . 111

5.1 (a) Fibre to preform calculation. (b) Preform fabrication by peck drilling a polymeric rod from both ends. The preform was drilled from both ends to minimise the vibrations and drifting experienced while drilling across long lengths. (c) CAD rendering of the fibre draw tower. (d) Cross-sectional inset of the three-zone tube furnace with the corresponding preheating, heating and quenching temperatures.(e) A microscopic view of the thermally drawn fibre (multi-lumen tubing). . . . . 118

5.2 Three Phenomena experienced during the manipulation of flexible instruments through tortuous anatomies. (a-b) Uncontrollable lengthening (+$\delta$) and shortening (-$\delta$) of the pull-wires as a result of the passive deflection of a flexible shaft with parallelly routed pull-wires. (c) Consequent undesirable bending of the relatively flexible distal end of the catheter to which the pull-wires are anchored. (d-f) Pull-wires routed in helical lumina are exposed to counterbalanced extension and compression forces, which minimises the change in pull-wires length ($\delta \approx 0$). (h-k) muscling phenomenon. (h) Neutral axis of the catheter. (i) Ideal catheter steering, where pull-wire tensioning deflects only the flexible distal end by $\phi$. (j) Realistic catheter steering, where the tensioning of the pull-wire deflects the shaft by $\theta$, for a total catheter deflection of $\phi + \theta$. (k) Counterbalancing of opposing compressive and tensile forces minimises the muscling phenomenon. (l-o) curve alignment phenomenon. (l) Catheter in resting passive bent state with a radius angle of curvature $\tau$. (m) Tensioning of the pull-wire along the internal bend results in the cumulative bending of $\tau + \theta + \phi$. (n) Subsequent tensioning of the opposing pull-wire applies a compressive load which opposes the current extension loads applied for bending the catheter in its current resting state. (o) Undesirable rotation of the shaft as the tensioned pull-wires tries to rest in the internal bend. . . . . 121

5.3 CAD renderings of the thermal drawing of multi-lumen tubing (fibres) with parallel and helical lumina. (a) Parallel lumina of the distal end of the catheter are fabricated by switching off the spinning motor $\omega = 0$, where $\omega$ is the angular velocity of the spinning motor. (b) Helical lumina of the catheter shaft are fabricated by switching on the spinning motor $\omega > 0$. (b-i). (b-ii), (b-iii) are cross-sectional insets of the fibre across the helically routed catheter shaft. (c-d) $\mu$-CT scan of a multi-lumen tubing (fibre) with parallel channels embedded with four 0.4mm nitinol wires to visualise the lumina. (e-f) $\mu$-CT scan of a multi-lumen tubing (fibre) with helical channels and a pitch size of 50mm. . . . . 123

5.4 FEM static structural analysis (a-b) Steerable catheter with a flexible distal end and a parallelly routed pull-wire which is anchored at both ends of the catheter. The catheter shaft was subjected to a passive deflection (displacement) of 5mm midway to simulate passive deflection. (c) Total deformation contours of the flexible distal end for the parallel case. (d-e) Steerable catheter with a flexible distal end and a helically routed pull-wire which is also anchored at both ends. The catheter is subjected to the same boundary conditions and loads. (f) Total deformation analysis of the flexible distal end for the helical case. Note: The proximal end of the flexible distal end is fixed. Simulation settings and parameters: catheter material: Polycarbonate (PC), pull-wire material: stainless steel, coefficient of friction between the pull-wire and catheter: 0.2. . . . . 125

5.5 (a) CAD rendering of the Maypole braider used to overbraid the bare thermally drawn multi-lumen tubing (fibre). Note: The distal end of the tubing is left non-braided to facilitate subsequent laser profiling. (b) Inset of the yarns braiding point. (c) CAD rendering of the laser profiling setup. (d) Inset of the ultrashort laser pulses used to non-thermally ablate the polymeric substrate. (e-f) optical images of the laser cut samples with laser cut notches. (g-h) CAD renderings of covering the overbraided and laser cut multi-lumen tubing (fibre) with heat shrink tubing. (i) Plasma cleaning and surface activation of the catheter assembly. (j) Dip coating the assembly in primer (Note: A blocker (indicated in green) is added at the distal most point to prevent the coating material from infiltrating and blocking the lumina. (k) Withdrawal from the primer. (l) Primer-coated assembly is dried for 5 minutes at 80°C. (m) Dip coating the assembly in a hydrophilic coating. (n) Withdrawal from the hydrophilic coating. (o) Hydrophilic-coated assembly is dried for 8 hours at 80°C. (p) Adding the passive negative tip markers for visualisation under MR. (q) Inset of the tip marker. . . 127

5.6 Flexural Rigidity - Experimental Setup and Results. (a) *Experiment 1-1* and *1-2* results. (b) CAD renderings of the experimental setup. (c) Inset of the direction of translation of the push rod and force/torque assembly. (d) Inset illustrating the maximum deflection $\delta$ and the length of the sample $L$. (e) *Experiment 1-3* Stress relaxation results. . . . . 131

5.7 Experiment 2: Pushability - (a) Results, (b-c) CAD renderings of the experimental setup. (d) Force versus displacement . . . . . 133

5.8 *Experiment 3-1*: Torsional Rigidity - (b) CAD renderings of the experimental setup and (a) Results. (c) Kinked catheter sample. . . . . 135

5.9 *Experiment 3-2*: Torque Response - (a) CAD renderings of the experimental setup, (b) List of catheter samples used in this experiment, (c) Results of the angular response (input angle versus output angle). . . . . 136

5.10 Manual handle overview. CAD renderings of: (a) 4-way deflection using the dual dial knobs. The different colours indicate the different directions of bending. (b) Isometric view of the catheter handle assembly (top cover removed). (c) MR visible pull-wires. (d) Zoomed-in (inset) of the doped iron microparticles. (e) Dual rack and pinion mechanism. (f) Shape locking mechanism. Images of the (g) catheter-handle assembly (top view), (h) guidewire insertion (back view), (i) catheter tip steering (images of 8 configurations are superimposed) and (j) contrast (fluid) injection. . . . . 139

5.11 Experiment 4-1: **PC A** Catheter Steering in a Straight Configuration. (a-b) CAD renderings of the experimental setup. (c) Forward and backward steering definitions. (d) Markers added to the distal end for tracking purposes. Steerability results of the left and right steering of PC A catheter: (e) and (f) indicate the geometry of the catheter tip for each trial when the catheter is subjected to forward steering (Stroke I and Stroke III) and backward steering (Stroke II and Stroke IV) respectively. (g) Averaged catheter tip positions over five trials. The difference between the catheter tip positions corresponding to the same knob angle position during the forward and backward steering indicate backlash. For better visualisation, only the catheter tip shapes for knob rotation angles $\pm 22.5°$, $\pm 56.25°$ and $\pm 90°$, are represented. (h) Average $x$ and $y$ coordinates (with standard deviation) of the distal most point of the catheter over the course of the experiment. (e) Torque applied to the knob during the experiments. . . . . 142

5.12 Experiment 4-2: **PC A** Catheter Steering in a Bent Configuration. (a) CAD renderings of the experimental setup. (b) Forward and backward steering definitions. (c) Marker added to the distal end for tracking purposes. Steerability results of the up and down steering of PC A catheter: (d) and (e) indicate the geometry of the catheter for each trial when the catheter is subjected to forward steering (Stroke I and Stroke III) and backward steering (Stroke II and Stroke IV) respectively. (g) Averaged catheter tip positions over five trials. The difference between the catheter tip positions corresponding to the same knob angle position during the forward and backward steering indicate backlash. For better visualisation, only the catheter tip shapes for knob rotation angles $\pm 22.5°$, $\pm 56.25°$ and $\pm 90°$, are represented. (h) Average $x$ and $y$ coordinates (with standard deviation) of the distal most point of the catheter over the course of the experiment. (e) Torque applied to the knob during the experiments. . . . . 143

5.13 Experiment 5: (a-b) CAD renderings of the experimental setup. (c, d, f, h, i) Uncontrolled deflection of the catheter tip as a result of the 90° catheter shaft deflection. (e, g) Zoomed-in plots of the catheters with helically routed pull-wires. . . . . 145

5.14 (a) CAD rendering of the *in-vitro* experimental setup in an MR suite. (b) Inset of the operator's handling of the steerable catheter's manual handle. (c) Imaging artefacts of four steerable catheters acquired using a 3D Flash sequence in a 3T MRI scanner. (d) Labelling of the artefacts. (e) Inset of the catheter tip marker artefacts and its dimensions. (f) Inset of the catheter shaft artefacts and its dimensions. (g) Reconstructed 3D model of the steerable catheter from the acquired scan. (h) Acquisition settings of the MRI scanner. . . . . 147

5.15 (a) Abdominal phantom with left and right renal artery (LRA & RRA) targets. (b) 2D Flash sequence illustrating the probing of the LRA and RRA in an abdominal phantom (Elastrat, Geneva, Switzerland) using the steerable catheter under real-time MR-guidance. (c) Acquisition settings of the MRI scanner. . . . . 148

5.16 (a) Abdominal phantom with coeliac trunk artery target. (b) Zoomed-in inset of the coeliac trunk artery. (c) 2D Flash sequence illustrating the probing of the coeliac in an abdominal phantom (Elastrat, Geneva, Switzerland) using the steerable catheter under real-time MR-guidance. (d) Acquisition settings of the MRI scanner. (e-g) Four-way steering of the catheter. The images were simultaneously acquired in two different planes (transverse plane (TP) and frontal plane (FP)). (e) Catheter is steered to the left in the FP and the distal most tip marker moves up in the TP. (f) Labelled inset of the steerable catheter. (g) Catheter is steered to the right in the FP and the distal most tip marker moves down in the TP. (h) Catheter is steered out of the FP and the distal most tip marker moves to the left in the TP. (i) Catheter is steered into the FP the frontal plane and the distal most tip marker moves to the right in the TP. (j) Superimposed image of the steering in four different directions. (k) Acquisition settings of the MRI scanner. . . . . 149

5.17 (a) Laser profiled catheter tip with the positions of the additional tip markers labelled. (b) Optical image of the catheter tip marker. (c-d) Steerable catheter after the *in-vivo* animal trial. Acquired *in-vivo* MRI scans of the steerable catheter manipulation in a clinical 3T MR system (Magnetom Prisma, Siemens) using a GRE sequence (TE/TR: 1.3/2.1 ms, spokes: 105, FA: 10°, FoV: 289 × 289× 8 $mm^3$, matrix: 192 × 192, fat saturation) for real-time guidance. Dotted lines are added to mark the distal end of the catheter. (e) Catheter is advanced towards the aortic arch. (f) Catheter is steered towards the carotid artery. (g) Carotid artery is succeffuly intubated. (h-i) Catheter is retracted back and steered towards the aortic arch. (j) Catheter crosses the aortic arch towards the heart. . 151

5.18 (light and contrast enhanced) acquired *in-vivo* MRI scans of the steerable catheter manipulation. . 152

5.19 CAD renderings of the (a) Side view of the actuation unit, (b) Isometric view of the actuation unit (without the manual handle), (c) Isometric view of the actuation unit (with the manual handle docked), (d) Linear pneumatic stepper motor with o-rings sealing (Chapter 4). (e) Rotary pneumatic stepper motor with o-rings sealing (Chapter 4). Actuation unit performing its functions of (f) translational motion and (g) 4-way tip steering (where four images of where superimposed). . . . 153

A.1 The Hamlyn Centre's fibre draw tower. Note: The tower was assembled by yours truly in my second year of PhD. . . . . 179

C.1 (a-c) Examples of the three braiding patterns that can be produced using a Maypole braider: Diamond (1/1), Regular (2/2) and Hercules (3/3). (d-e) Optical images of overbraided thermally drawn polycarbonate fibres (multi-lumen tubing). The braiding pattern employed here is the diamond pattern. Liquid Crystal Polymer (LCP) 50$\mu$m monofilament yarns (Zeus Industrial Products Inc, Orangeburg, United States) is the braiding material. (f) Computational design tool (detasFLEX) developed by the Compliant Systems Group, TU Ilmenau [312]. . . . . 182

D.1 Steerability results of the left and right steering of PC A catheter in a straight configuration: Top left & middle plots indicate the geometry of the catheter tip for each trial when the catheter is subjected to forward steering (Stroke I and Stroke III) and backward steering (Stroke II and Stroke IV) respectively. Top right plot is the average catheter tip positions over five trials. The difference between the catheter tip positions corresponding to the same knob angle position during the forward and backward steering indicate backlash. For better visualisation, only the catheter tip shapes for knob rotation angles $\pm 22.5°$, $\pm 56.25°$ and $\pm 90°$, are represented. Bottom left plot is the average $x$ and $y$ coordinates (with standard deviation) of the distal most point of the catheter over the course of the experiment. Bottom right plot is the torque applied to the knob during the experiments. . . . . 183

D.2 Steerability results of the up and down steering of PC A catheter in a straight configuration: Top left & middle plots indicate the geometry of the catheter tip for each trial when the catheter is subjected to forward steering (Stroke I and Stroke III) and backward steering (Stroke II and Stroke IV) respectively. Top right plot is the average catheter tip positions over five trials. The difference between the catheter tip positions corresponding to the same knob angle position during the forward and backward steering indicate backlash. For better visualisation, only the catheter tip shapes for knob rotation angles $\pm 22.5°$, $\pm 56.25°$ and $\pm 90°$, are represented. Bottom left plot is the average $x$ and $y$ coordinates (with standard deviation) of the distal most point of the catheter over the course of the experiment. Bottom right plot is the torque applied to the knob during the experiments. 184

D.3 Steerability results of the left and right steering of PC A catheter in a bent configuration: Top left & middle plots indicate the geometry of the catheter tip for each trial when the catheter is subjected to forward steering (Stroke I and Stroke III) and backward steering (Stroke II and Stroke IV) respectively. Top right plot is the average catheter tip positions over five trials. The difference between the catheter tip positions corresponding to the same knob angle position during the forward and backward steering indicate backlash. For better visualisation, only the catheter tip shapes for knob rotation angles $\pm 22.5°$, $\pm 56.25°$ and $\pm 90°$, are represented. Bottom left plot is the average $x$ and $y$ coordinates (with standard deviation) of the distal most point of the catheter over the course of the experiment. Bottom right plot is the torque applied to the knob during the experiments. . . . . 185

D.4 Steerability results of the up and down steering of PC A catheter in a bent configuration: Top left & middle plots indicate the geometry of the catheter tip for each trial when the catheter is subjected to forward steering (Stroke I and Stroke III) and backward steering (Stroke II and Stroke IV) respectively. Top right plot is the average catheter tip positions over five trials. The difference between the catheter tip positions corresponding to the same knob angle position during the forward and backward steering indicate backlash. For better visualisation, only the catheter tip shapes for knob rotation angles $\pm 22.5°$, $\pm 56.25°$ and $\pm 90°$, are represented. Bottom left plot is the average $x$ and $y$ coordinates (with standard deviation) of the distal most point of the catheter over the course of the experiment. Bottom right plot is the torque applied to the knob during the experiments. . . . . 186

D.5 Steerability results of the left and right steering of PC C catheter in a straight configuration: Top left & middle plots indicate the geometry of the catheter tip for each trial when the catheter is subjected to forward steering (Stroke I and Stroke III) and backward steering (Stroke II and Stroke IV) respectively. Top right plot is the average catheter tip positions over five trials. The difference between the catheter tip positions corresponding to the same knob angle position during the forward and backward steering indicate backlash. For better visualisation, only the catheter tip shapes for knob rotation angles $\pm 22.5°$, $\pm 56.25°$ and $\pm 90°$, are represented. Bottom left plot is the average $x$ and $y$ coordinates (with standard deviation) of the distal most point of the catheter over the course of the experiment. Bottom right plot is the torque applied to the knob during the experiments. . . . . 187

D.6 Steerability results of the up and down steering of PC C catheter in a straight configuration: Top left & middle plots indicate the geometry of the catheter tip for each trial when the catheter is subjected to forward steering (Stroke I and Stroke III) and backward steering (Stroke II and Stroke IV) respectively. Top right plot is the average catheter tip positions over five trials. The difference between the catheter tip positions corresponding to the same knob angle position during the forward and backward steering indicate backlash. For better visualisation, only the catheter tip shapes for knob rotation angles $\pm 22.5°$, $\pm 56.25°$ and $\pm 90°$, are represented. Bottom left plot is the average $x$ and $y$ coordinates (with standard deviation) of the distal most point of the catheter over the course of the experiment. Bottom right plot is the torque applied to the knob during the experiments. 188

D.7 Steerability results of the left and right steering of PC c catheter in a bent configuration: Top left & middle plots indicate the geometry of the catheter tip for each trial when the catheter is subjected to forward steering (Stroke I and Stroke III) and backward steering (Stroke II and Stroke IV) respectively. Top right plot is the average catheter tip positions over five trials. The difference between the catheter tip positions corresponding to the same knob angle position during the forward and backward steering indicate backlash. For better visualisation, only the catheter tip shapes for knob rotation angles $\pm 22.5°$, $\pm 56.25°$ and $\pm 90°$, are represented. Bottom left plot is the average $x$ and $y$ coordinates (with standard deviation) of the distal most point of the catheter over the course of the experiment. Bottom right plot is the torque applied to the knob during the experiments. . . . . 189

D.8 Steerability results of the up and down steering of PC C catheter in a bent configuration: Top left & middle plots indicate the geometry of the catheter tip for each trial when the catheter is subjected to forward steering (Stroke I and Stroke III) and backward steering (Stroke II and Stroke IV) respectively. Top right plot is the average catheter tip positions over five trials. The difference between the catheter tip positions corresponding to the same knob angle position during the forward and backward steering indicate backlash. For better visualisation, only the catheter tip shapes for knob rotation angles $\pm 22.5°$, $\pm 56.25°$ and $\pm 90°$, are represented. Bottom left plot is the average $x$ and $y$ coordinates (with standard deviation) of the distal most point of the catheter over the course of the experiment. Bottom right plot is the torque applied to the knob during the experiments. . . . . 190

D.9 Steerability results of the left and right steering of PEI A catheter in a straight configuration: Top left & middle plots indicate the geometry of the catheter tip for each trial when the catheter is subjected to forward steering (Stroke I and Stroke III) and backward steering (Stroke II and Stroke IV) respectively. Top right plot is the average catheter tip positions over five trials. The difference between the catheter tip positions corresponding to the same knob angle position during the forward and backward steering indicate backlash. For better visualisation, only the catheter tip shapes for knob rotation angles $\pm 22.5°$, $\pm 56.25°$ and $\pm 90°$, are represented. Bottom left plot is the average $x$ and $y$ coordinates (with standard deviation) of the distal most point of the catheter over the course of the experiment. Bottom right plot is the torque applied to the knob during the experiments. 191

D.10 Steerability results of the up and down steering of PEI A catheter in a straight configuration: Top left & middle plots indicate the geometry of the catheter tip for each trial when the catheter is subjected to forward steering (Stroke I and Stroke III) and backward steering (Stroke II and Stroke IV) respectively. Top right plot is the average catheter tip positions over five trials. The difference between the catheter tip positions corresponding to the same knob angle position during the forward and backward steering indicate backlash. For better visualisation, only the catheter tip shapes for knob rotation angles $\pm 22.5°$, $\pm 56.25°$ and $\pm 90°$, are represented. Bottom left plot is the average $x$ and $y$ coordinates (with standard deviation) of the distal most point of the catheter over the course of the experiment. Bottom right plot is the torque applied to the knob during the experiments. 192

D.11 Steerability results of the left and right steering of PEI A catheter in a bent configuration: Top left & middle plots indicate the geometry of the catheter tip for each trial when the catheter is subjected to forward steering (Stroke I and Stroke III) and backward steering (Stroke II and Stroke IV) respectively. Top right plot is the average catheter tip positions over five trials. The difference between the catheter tip positions corresponding to the same knob angle position during the forward and backward steering indicate backlash. For better visualisation, only the catheter tip shapes for knob rotation angles $\pm 22.5°$, $\pm 56.25°$ and $\pm 90°$, are represented. Bottom left plot is the average $x$ and $y$ coordinates (with standard deviation) of the distal most point of the catheter over the course of the experiment. Bottom right plot is the torque applied to the knob during the experiments. . . . . 193

D.12 Steerability results of the up and down steering of PEI A catheter in a bent configuration: Top left & middle plots indicate the geometry of the catheter tip for each trial when the catheter is subjected to forward steering (Stroke I and Stroke III) and backward steering (Stroke II and Stroke IV) respectively. Top right plot is the average catheter tip positions over five trials. The difference between the catheter tip positions corresponding to the same knob angle position during the forward and backward steering indicate backlash. For better visualisation, only the catheter tip shapes for knob rotation angles $\pm 22.5°$, $\pm 56.25°$ and $\pm 90°$, are represented. Bottom left plot is the average $x$ and $y$ coordinates (with standard deviation) of the distal most point of the catheter over the course of the experiment. Bottom right plot is the torque applied to the knob during the experiments. . . . . 194

D.13 Steerability results of the left and right steering of PEI B catheter in a straight configuration: Top left & middle plots indicate the geometry of the catheter tip for each trial when the catheter is subjected to forward steering (Stroke I and Stroke III) and backward steering (Stroke II and Stroke IV) respectively. Top right plot is the average catheter tip positions over five trials. The difference between the catheter tip positions corresponding to the same knob angle position during the forward and backward steering indicate backlash. For better visualisation, only the catheter tip shapes for knob rotation angles $\pm 22.5°$, $\pm 56.25°$ and $\pm 90°$, are represented. Bottom left plot is the average $x$ and $y$ coordinates (with standard deviation) of the distal most point of the catheter over the course of the experiment. Bottom right plot is the torque applied to the knob during the experiments. 195

D.14 Steerability results of the up and down steering of PEI B catheter in a straight configuration: Top left & middle plots indicate the geometry of the catheter tip for each trial when the catheter is subjected to forward steering (Stroke I and Stroke III) and backward steering (Stroke II and Stroke IV) respectively. Top right plot is the average catheter tip positions over five trials. The difference between the catheter tip positions corresponding to the same knob angle position during the forward and backward steering indicate backlash. For better visualisation, only the catheter tip shapes for knob rotation angles $\pm 22.5°$, $\pm 56.25°$ and $\pm 90°$, are represented. Bottom left plot is the average $x$ and $y$ coordinates (with standard deviation) of the distal most point of the catheter over the course of the experiment. Bottom right plot is the torque applied to the knob during the experiments. 196

D.15 Steerability results of the left and right steering of PEI B catheter in a bent configuration: Top left & middle plots indicate the geometry of the catheter tip for each trial when the catheter is subjected to forward steering (Stroke I and Stroke III) and backward steering (Stroke II and Stroke IV) respectively. Top right plot is the average catheter tip positions over five trials. The difference between the catheter tip positions corresponding to the same knob angle position during the forward and backward steering indicate backlash. For better visualisation, only the catheter tip shapes for knob rotation angles $\pm 22.5°$, $\pm 56.25°$ and $\pm 90°$, are represented. Bottom left plot is the average $x$ and $y$ coordinates (with standard deviation) of the distal most point of the catheter over the course of the experiment. Bottom right plot is the torque applied to the knob during the experiments. . . . . 197

D.16 Steerability results of the up and down steering of PEI B catheter in a bent configuration: Top left & middle plots indicate the geometry of the catheter tip for each trial when the catheter is subjected to forward steering (Stroke I and Stroke III) and backward steering (Stroke II and Stroke IV) respectively. Top right plot is the average catheter tip positions over five trials. The difference between the catheter tip positions corresponding to the same knob angle position during the forward and backward steering indicate backlash. For better visualisation, only the catheter tip shapes for knob rotation angles $\pm 22.5°$, $\pm 56.25°$ and $\pm 90°$, are represented. Bottom left plot is the average $x$ and $y$ coordinates (with standard deviation) of the distal most point of the catheter over the course of the experiment. Bottom right plot is the torque applied to the knob during the experiments. . . . . 198

# List of Tables


2.1 **Abbreviations:** steerable catheter (SC), guidewire (G), catheter (C), customised catheter (CC), electrophysiology (EP), cardiac intervention (CI), general catherization (GC), rotation (R), feeding (F), bending (B), electromechanical (EME), friction wheels (FW), linear stepping mechanism (LSM), electromechanical clamping (EMC), hydraulics (HYD), laboratory test (LB), phantom study (PS), animal study (AS), cadaver study (CS), and human study (HS). . . . 50

2.2 Materials used for constructing guidewires for MR-Guided Interventions. Markers: Passive Negative Marker (PN), Passive Positive Marker (PP), Semi-Active Tracking (SA), Indirect Active Tracking (IA), Direct Active Tracking (DA) . . . 59

2.3 Materials used for constructing steerable catheters for MR-guided interventions,*patents are excluded, † Extends to the distal end, ‡ Only discussed in reference, Marker: Passive Negative Marker (PN), Passive Positive Marker (PP), Semi-Active Tracking (SA), Indirect Active Tracking (IA), Direct Active Tracking (DA) . . . 68

2.4 Actuation techniques summarised based on working principle, steerability and safety. . . . 69

3.1 Results of fluoroscopy pre-clinical trials (mean $\pm$ SD). Bold values indicate statistically significant results ($p<0.05$) according to Student's t-test . . . 87

4.1 Catheter and guidewire instruments of the user study. . . . 101

4.2 Questionnaire for subjective task evaluation. . . . 104

4.3 User study metrics for cannulation tasks (mean $\pm$ SD). . . . 107

4.4 Sheaths, catheters, guidewires, balloon catheters used in the animal study. [1] Cook Medical Europe, Limerick, Ireland [2] Merit Medical UK, Reading, UK [3] Terumo UK Ltd., Surrey, UK [4] Boston Scientific UK, Hemel Hempstead, UK . . . 110

5.1 Percentage drop in $EI$ of the 13 catheter shaft samples when immersed in warm water at 37.4°C . 132

B.1 Segmented Thermally Drawing Catheter Samples . . . 180

B.2 Segmented Commercial Catheter Samples . . . 181

Chapter 1

# Introduction

*This chapter provides a brief overview of the thesis, highlighting the aims, motivation and original contributions.*

## 1.1 Motivation and Research Objectives

Cardiovascular diseases (CVDs) are disorders and diseases affecting the heart or blood vessels, which lead to heart attacks, strokes, critical leg ischemia, and account for one-third of all deaths in the world (17.9 million each annually) [1]. Endovascular interventions have become the backbone of treatment for CVDs thanks to the combined efforts of interventional radiologists, cardiologists, physicists, and engineers. These minimally invasive and image-guided procedures are carried out by manipulating thin, long, and relatively flexible instruments (sheaths, catheters, and guidewires) within the vasculature to gain access to specific blood vessels, commonly referred to as catheterisation. Subsequent to catheterisation, various treatment options such as angioplasty, stenting, embolisation and ablation, as illustrated in Figure 1.1, are directed towards the diseased vessels. When compared to open surgery, these procedures not only lead to shorter convalescences, they also reduce operating time, hospitalisation, and total time to recovery.

A critical challenge clinicians face while preparing for an intervention is choosing the appropriate passive instrumentation (i.e. catheters and guidewires with pre-shaped distal ends mimicking the anatomy of blood vessels) from the myriad of shapes, sizes, and features (stiffness, braiding, coating) [2]. Furthermore, steering and manoeuvring of passive flexible instruments can become complicated due to their fixed shape at the distal end, long lengths, and unpredictable friction between the devices and vessel walls. In specific scenarios, where multiple catheterisations are performed, interventionalists exchange catheters to change the tip shape and guidewires to change its stiffness. Since the interventions are performed under X-ray fluoroscopy guidance, any difficulty in navigation increases the exposure of patient and staff to ionising X-ray radiation.

Commonly proposed techniques to mitigate radiation exposure and navigation difficulties include utilising steerable catheters with improved maneuverability and employing robotic systems to remotely and accurately manipulate off-the-shelf or bespoke instrumentation. Although the usage of steerable catheters and robotic systems improve stability and procedural efficacy [3–6], recent developments in cardiovascular science have highlighted the importance of including functional information (e.g. blood flow, tissue oxygenation, diffusion, perfusion) of the underlying pathology during endovascular interventions to guide treatment/therapy decisions [7]. As a result of its reliance on radiopaque contrast agents to indirectly visualise blood vessels, X-ray fluoroscopy cannot accommodate the aforementioned needs. In current practice, these needs are partly compensated for by using additional intravascular devices (e.g.optical coherence tomography). Although beneficial, their usage: (1) increases fluoroscopy time, which exposes medical personal and patients to higher doses of ionising radiation which is linked to a sizeable risk of cancer (1:137 to 1:370) [8], (2) leads to larger volumes of contrast agent being injected, which may impair kidney function. These concerns led to a strong consensus among researchers and clinical staff that X-ray, with its perennial safety concerns, should be replaced by a safer alternative.

Magnetic resonance imaging (MRI) has revolutionised diagnostic medicine, allowing unparalleled visualisation of soft tissue [9]. It offers 3D evaluations of pathology and function across the body. To benefit from the unique features of MRI, extensive research has been conducted in employing MRI as an alternative radiation-free imaging modality for image-guided endovascular procedures by combining diagnosis, therapy and early evaluation of the therapy in a single intervention [10–12]. Examples of explored MR-guided procedures include: right heart catheterisation [13], electrophysiology ablations [14, 15], and coronary interventions. Although MR-guided interventions have

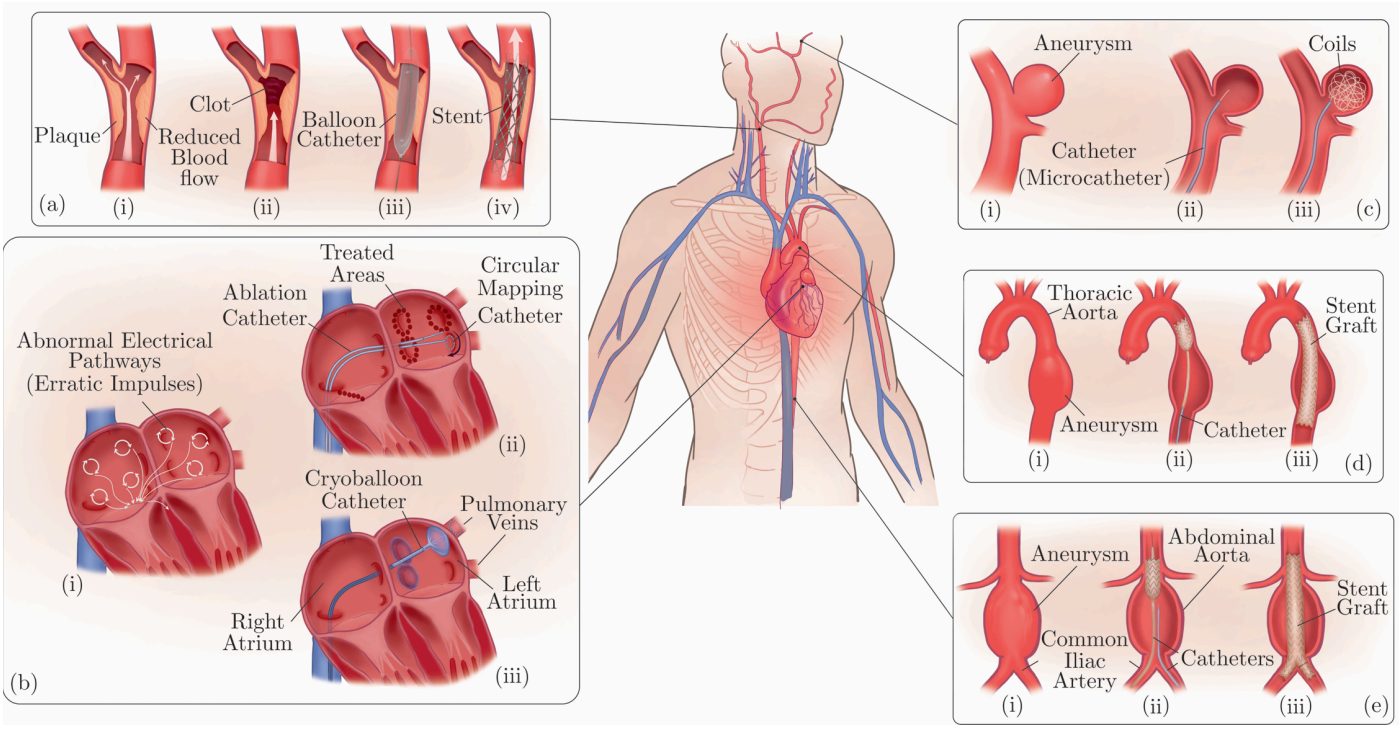



**Figure 1.1: Cardiovascular Diseases and their corresponding endovascular intervention(s):** (a) Carotid arteries stenosis: Narrowing of the arteries on either side of the neck which carry blood to the head, face and brain. This narrowing is usually the result of build-up of plaque within the arteries, a condition called atherosclerosis, Problems: (i) Reduced blood flow due to atherosclerosis plaque build-up, (ii) Possible formation of clots caused by the irregular surface of the artery wall, Possible interventions: (iii) Carotid angioplasty: A catheter with a deflated balloon is threaded up into the carotid artery, and once it reaches the narrowed portion, the balloon is inflated (iv) Carotid stenting: After angioplasty, the balloon catheter is removed, and a self-expanding stent is placed over the plaque to hold open the artery. (b) Atrial Fibrillation: Irregular and often rapid heart rate, Problem: (i) Abnormal electrical pathways in the heart disrupt the heart's normal rhythm, Possible interventions: (ii) Radiofrequency (heat) catheter ablation of the pulmonary veins (PVs) to disrupt faulty electrical signals. A circular mapping catheter is used in parallel to map the electrical signals between the left atrium and the PVs, (iii) Cryoablation uses extreme cold instead of heat to restore regular heart rhythm. (c) Cerebral Aneurysm: A bulged, weakened area of the cerebral artery wall, Problem: (i) Saccular aneurysm, Possible intervention: (ii) Endovascular Coiling: A catheter (microcatheter) is threaded up into the cerebral artery, (iii) A series of coils are pushed through the microcatheter. The coils fill the aneurysm which leads to clotting and protection from rupturing. (d) Thoracic Aortic Aneurysm: bulging of the aorta which extends from the chest to the abdomen, Problem: (i) Descending thoracic aortic aneurysm, Possible intervention: (ii) Thoracic Endovascular Aortic Repair (TEVAR): A stent graft deployment catheter is threaded into the aneurysm area, (iii) The stent graft is deployed and helps maintain the blood flow through its lumens. (e) Abdominal Aortic Aneurysm: bulging of the lower part of the aorta (abdominal region), Problem: (i) Fusiform aneurysm, Possible intervention: (ii) and (iii) Endovascular Aneurysm Repair (EVAR): Similar to the TEVAR procedure d (ii) and d (iii).

several advantages over X-ray guided interventions [7], there are still some challenges related to procedures conducted within an MR environment. One of these challenges include the lack of MR safe and compatible materials that could be employed in the construction of key instrumentation such as guidewires and catheters. Another challenge is the limited accessibility to the patient, especially paediatric patients. This can increase the surgeon's risk of developing musculoskeletal injury, which can, in turn, increase the possibility of medical errors and risk for the patient [16]. Various acoustic noise types are generated while operating MR systems, most prominently due to the gradient magnetic field. Problems associated with such noise for interventionalists may include simple annoyance,

verbal communication difficulties, heightened anxiety, and hearing impairment [17]. Therefore, it is recommended for both the patients and clinicians to wear ear protection during interventional MR procedures. Nevertheless, wearing ear protection can also be uncomfortable, if worn for a long period of time.

The goals of this thesis were: 1) to propose a robotic platform that not only reduces radiation exposure and improves the precision, comfort, stability of interventions, but also paves the way for endovascular interventions under MRI to benefit from its unique capacity, 2) to thoroughly evaluate the platform's feasibility in a number of simulated (*in-vitro*) clinical scenarios with several qualified vascular surgeons and *in-vivo* animal testing, 3) to address the gap in MR safe instrumentation (more specifically steerable catheters) by leveraging and re-purposing the scalable process of thermal fibre drawing, 4) to extensively evaluate the mechanical efficacy (flexibility, torquability, pushability, steerability) of the polymer-only based steerable catheter against its commercially available counterparts, 5) to demonstrate the steerability and visibility of the steerable catheter in a vessel phantom and a procine model under real-time MR guidance, 6) to alleviate the difficulties faced by clinicians in MR-guided interventions by demonstrating the robotic integration of the MR safe and visible steerable catheter. Overall, the work presented in this thesis represents a number of key steps towards the wider adoption of image-guided robotics and MR-guided interventions in interventional radiology and targeted therapy.

## 1.2 Key Contributions

They key contributions of this thesis include:

1. **Contribution 1:** Contributed towards the development of a versatile master-slave robotic platform with image-based haptic feedback to perform minimally invasive endovascular interventions through the remote manipulation of off-the-shelf catheters and guidewires in multi-modal imaging environments (fluoroscopy and MRI). The adoption of MR safe, metal-free, 3D printed, pneumatically driven stepper motors enabled the system to function in MR environments. The MR safe slave robot was also designed in accordance with the MHRA safety guidelines & ASTM F2503 standard for marking devices brought into the MR environment. The platform was preliminarily tested under fluoroscopy guidance against manual interventions using anatomical silicone phantoms *in-vitro* and was evaluated for MR compatibility in a 3T MR scanner. **Baseline:** The pneumatic stepper motors employed in Chapter 3 are adaptations of the motors designed, illustrated and discussed in [18, 19]. The slave robot presented in this chapter was designed from the ground up. The concept of the proposed haptic master for teleoperated intervention was initially reported in [20] and fundamentally revised in this chapter with regard to mechanical design, usability, and user interaction. **Declarations:** In this chapter, Dr. Guilio Dagnino provided support with the navigation framework. Dennis Kundrat provided support with the master manipulator and slave robot, and the overall control of the system. Marco Pupillo provided support with the design of the slave robot. The entire team (Dr. Giulio Dagnino, Dennis Kundrat, Dr. Wenqiang Chi, Dr. Trevor M. K. Kwok, including myself) took part in the integration and testing of the system under X-ray fluoroscopy guidance, and the preliminary compatibility testing in Magnetic Resonance Imaging (MRI). Dr. Giulio Dagnino and Dennis Kundrat provided support with the data analysis for Table 3.1. In summary, my main contributions to this chapter is the design, fabrication, integration of the slave robot and the subsequent integration and testing of the entire platform.

**2. Contribution 2:** Contributed towards the optimisation of the robotic platform based on the preliminary results of the pilot study (Chapter 3) to meet the requirements of frequent clinical use and performance characteristics. The previously adapted pneumatic stepper motors used in Chapter 3 were optimised to enable robust actuation of the second iteration of the slave robot. The optimised robotic platform was evaluated against manual interventions *in-vitro* with seven expert vascular surgeons using anatomical silicone phantoms. Compared to manual cannulations, slightly lower interaction forces between instrumentation and phantoms were measured for specific tasks. Subsequently, *in-vivo* (3 pigs) evaluation was performed with one expert vascular surgeon, all under fluoroscopy guidance. **Declarations:** Dr. Guilio Dagnino, Dennis Kundrat, Wenqiang Chi, and Dr. Trevor M. K. Kwok continued to provide technical/clinical support in terms of the robotic platform and its subsequent testing. Dr. Giulio Dagnino and Dennis Kundrat provided support with the data analysis for Figures 4.6, 4.7 and Table 4.3. My main contributions to Chapter 4, is the optimisation of the slave robot (iteration #2) and its subsequent integration and testing (user and animal studies) which were performed under X-ray fluoroscopy.

**3. Contribution 3:** Developed an MR safe, pull-wire driven steerable catheter using an unconventional, well-established scalable polymer processing technique, i.e. thermal fibre drawing process. Unlike previous work, the pull-wires used to steer the flexible distal end of the catheter were also passively MR visible, which makes the instrument also visible over its full length. Proposed a single step fabrication process (i.e. spinning of the polymeric preform while drawing) to fabricate catheter shafts with helically routed channels to compensate for undesirable effects experienced during the manipulation of flexible pull-wire driven instruments. The mechanical performance parameters of the in-house fabricated catheters were evaluated against commercial catheter shafts. An additively manufactured handle was designed, fabricated and integrated with the catheter to steer the distal end independently in all four directions. The catheter was subsequently evaluated under real-time MR guidance *in-vitro* using anatomical silicone phantoms and *in-vivo* in a procine model in a clinical 3T MRI scanner. Integrated the manual handle into a pneumatically actuated MR safe robotic system; to facilitate the seamless switching between remote (robot-assisted) and manual interventions. **Baseline:** The catheter presented in this chapter (5) was designed, fabricated, and tested from the ground up. **Declarations:** I am the main contributor to this chapter, however, the optimisation of the manual handle design and mechanical characterisation was done in collaboration with Libaihe Tian. Dr. Stefano Del Rosso provided support with the overbraiding post-processing step. The testing of the catheter under MR guidance was done in collaboration with the University of Freiburg team (Thomas Lottner, Simon Reiss, PD Dr. med Timo Heidt, and Professor Dr. med. Constantin von zur Mühlen, Professor Michael Bock).

## 1.3 Publications and Patents

The work presented in this thesis has been accepted to a number of peer-reviewed conferences and journals, or is in the process of submission/review. Below is a list of the publications directly related to the work in this thesis, followed by other publications less strongly related but also published within the same time frame. Lastly, a list of filed patents which are currently being exploited by Precision Robotics Ltd for further development and

commercialisation are presented thereafter.

Main publications:

- **M. E. M. K. Abdelaziz**, L. Tian, M. Hamady, G-Z. Yang, B. Temelkuran "X-ray to MR: The Progress of Flexible Instruments for Endovascular Navigation," under review in Progress in Biomedical Engineering.
- **M. E. M. K. Abdelaziz**, L. Tian, T. Lottner, S. Reiss, K. Düring, G-Z. Yang, M. Bock and B. Temelkuran, "An MR Safe Steerable Catheter for MR-guided Endovascular Interventions", Accepted to be published in proceedings of ISMRM & SMRT Annual Meeting & Exhibition 2021.
- D. Kundrat, G. Dagnino, T. M. Y. Kwok, **M. E. M. K. Abdelaziz**, W. Chi, A. Nguyen, C. Riga, S. Stramigioli, G-Z. Yang, "An MR-Safe Endovascular Robotic Platform: Design, Control, and Ex-Vivo Evaluation," in IEEE Transactions on Biomedical Engineering, doi.
- A. Nguyen, D. Kundrat, G. Dagnino, W. Chi, **M. E. M. K. Abdelaziz**, Y. Guo, Y. Ma, T. M. Y. Kwok, C. Riga, G-Z. Yang, End-to-End Real-time Catheter Segmentation with Optical Flow-Guided Warping during Endovascular Intervention, 2020 IEEE International Conference on Robotics and Automation (ICRA), Paris, France, 2020, pp. 9967-9973, doi.
- D. Kundrat, G. Dagnino, **M. E. M. K. Abdelaziz**, T. M. Y. Kwok, C. Riga, G-Z. Yang, Towards MR-Safe Endovascular Robotics, German Society of Computer and Robot-Assisted Surgery (CURAC) conference, Reutlingen 2019, Received Best Paper Award.
- M. B. Molinero, G. Dagnino, J. Liu, W. Chi, **M. E. M. K. Abdelaziz**, T. M. Y. Kwok, C. Riga, G-Z. Yang, "Toward a Versatile Robotic Platform for Fluoroscopy and MRI-Guided Endovascular Interventions: A Pre-Clinical Study," 2019 IEEE/RSJ International Conference on Intelligent Robots and Systems (IROS), Macau, China, 2019, pp. 5411-5418, doi.
- **M. E. M. K. Abdelaziz**, D. Kundrat, M. Pupillo, G. Dagnino, T. M. Y. Kwok, W. Chi, V. Groenhuis, F. J. Siepel, C. Riga, S. Stramigioli, G-Z. Yang, "Toward a Versatile Robotic Platform for Fluoroscopy and MRI-Guided Endovascular Interventions: A Pre-Clinical Study," 2019 IEEE/RSJ International Conference on Intelligent Robots and Systems (IROS), Macau, China, 2019, pp. 5411-5418, doi, **[Video]**. Selected by the Society for Cardiac Robotic Navigation (SCRN) as one of the top three experimental papers for the 2019-2020 period.
- W. Chi, J. Liu, **M. E. M. K. Abdelaziz**, G. Dagnino, C. Riga, C. Bicknell, G-Z. Yang, "Trajectory Optimization of Robot-Assisted Endovascular Catheterization with Reinforcement Learning," 2018 IEEE/RSJ International Conference on Intelligent Robots and Systems (IROS), Madrid, 2018, pp. 3875-3881, doi.
- G. Dagnino, J. Liu, **M. E. M. K. Abdelaziz**, W. Chi, C. Riga and G-Z. Yang, "Haptic Feedback and Dynamic Active Constraints for Robot-Assisted Endovascular Catheterization," 2018 IEEE/RSJ International Conference on Intelligent Robots and Systems (IROS), Madrid, 2018, pp. 1770-1775, doi.

Other publications:

- D. Bautista-Salinas, D. Kundrat, A. Kogkas, **M. E. M. K. Abdelaziz**, S. Giannarou and F. Rodriguez y Baena, "Integrated Augmented Reality Feedback for Cochlear Implant Surgery Instruments," in IEEE Transactions on Medical Robotics and Bionics, vol. 3, no. 1, pp. 261-264, Feb.2021, doi.

- M. Keshavarz, D. J. Wales, F. Seichepine, **M. E. M. K. Abdelaziz**, P. Kassanos, Q. LI, B. Temelkuran, H. Shen and G-Z. Yang, "Induced Neural Stem Cell Differentiation on a Drawn Fiber Scaffold - Toward Peripheral Nerve Regeneration," Biomedical Materials, vol. 15, no. 5, pp. 055011, July.2021, doi.
- A. Gao, N. Liu, M. Shen, **M. E. M. K. Abdelaziz**, B. Temelkuran, and G-Z. Yang, "Laser-Profiled Continuum Robot with Integrated Tension Sensing for Simultaneous Shape and Tip Force Estimation," in Soft Robotics, 2020, doi.
- A. Nguyen, D. Kundrat, G. Dagnino, W. Chi, **M. E. M. K. Abdelaziz**, Y. Guo, Y. Ma, T. M. Y. Kwok, C. Riga, G-Z. Yang, End-to-End Real-time Catheter Segmentation with Optical Flow-Guided Warping during Endovascular Intervention, 2020 IEEE International Conference on Robotics and Automation (ICRA), Paris, France, 2020, pp. 9967-9973, doi.
- Y. Hu, L. Zhang, C. A. Seneci, W. Li, **M. E. M. K. Abdelaziz** and G-Z. Yang, "Design, Fabrication, and Testing a Semiautomatic Sewing Device for Personalized Stent Graft Manufacturing," in IEEE/ASME Transactions on Mechatronics, vol. 24, no. 2, pp. 517-526, April 2019, doi:doi.
- N. Liu, **M. E. M. K. Abdelaziz**, M. Shen and G-Z. Yang, "Design and kinematics characterization of a laser-profiled continuum manipulator for the guidance of bronchoscopic instruments," 2018 IEEE International Conference on Robotics and Automation (ICRA), Brisbane, QLD, 2018, pp. 25-31, doi:doi.

Patents (Currently being licensed by a company):

- **M. E. M. K. Abdelaziz**, B. Temelkuran, H-T. Lee, J. Zhao. F. Seichepine, G-Z. Yang, A method, Application No: 2020346.9 (Filed 22.12.2020)
- **M. E. M. K. Abdelaziz**, B. Temelkuran, G-Z. Yang, A. Leber, F. Sorin, A method, Application No: 2020329.5 (Filed 22.12.2020)
- A. Barbot, S. Anastasova, D. Wales, J. A. Kim, **M. E. M. K. Abdelaziz**, B. Temelkuran, G-Z. Yang, A sensor, Publication No: WO2020234579A1 (Published 26.11.2020)
- S. Anastasova, B. Temelkuran, **M. E. M. K. Abdelaziz**, G-Z. Yang, F. Sorin, Fibre based sensor incorporating electrochemical sensing, Publication No: WO2020201741 (Published 08.10.2020)
- B. Temelkuran, **M. E. M. K. Abdelaziz**, G-Z. Yang, Longitudinally non-uniform preform and method of making the same, Publication No: WO2020174246A1 (Published 03.09.2020)
- **M. E. M. K. Abdelaziz**, A. Gao, B. Temelkuran, G-Z. Yang, A Method and Preform for Forming a Device Comprising a Shape Memory Polymer, Publication No: WO2020174248A1 (Published 03.09.2020)
- N. Liu, **M. E. M. K. Abdelaziz**, A. Gao, B. Temelkuran, G-Z. Yang, A Device, Publication No: WO2020016577A1 (Published 23.01.2020)

## 1.4 Overview

In order to guide the reader, an outline of the work presented in each chapter of this thesis is given below:

**Chapter 2** starts by giving a thorough overview covering the state-of-the-art passive instrumentation (i.e. guidewires

and selective catheters) used for navigation purposes in X-ray guided endovascular interventions. The overview focuses on the materials and manufacturing methods employed in constructing these devices to provide background for the subsequent sections. The challenges associated with choosing and using passive instrumentation and the side effects of using X-ray as an imaging modality are then outlined. This is followed by presenting the proposed solutions to resolve the aforementioned shortcomings by introducing the concepts of steerable catheters and robotic catheterisation. The chapter then sheds light on the importance of including functional information (e.g. blood flow, tissue oxygenation) of the underlying pathology during endovascular interventions to guide treatment/therapy decisions through the adoption of MRI as an alternative imaging modality. To familiarise the reader with the imaging modality, the fundamental physics of MRI is presented. This is complemented by the ongoing efforts made by academia and industry to develop instruments compatible for use in MR environments through the adoption of different materials and manufacturing methods. Finally, this chapter underlines the key challenges facing the field of MR-guided endovascular interventions and points out the aims that this thesis aims to tackle.

**Chapter 3** presents the development of a master-slave robotic platform and a navigation framework for the manipulation of standard endovascular instruments under the guidance of different imaging modalities (X-ray fluoroscopy and MRI). The chapter commences by outlining the clinical requirements and limitations of current and emerging robotic platforms. Followed by a thorough description of the design and fabrication methods of the proposed system, which consists of: (1) *a master manipulator that imitates human motion patterns of instrument manipulation during catheterisation and facilitates the adoption of haptic feedback to the user*, (2) *an additively manufactured, pneumatically-actuated, MR safe slave robot capable of manipulating passive catheters and guidewires under fluoroscopy and MR guidance*. Next, the integration of the master-slave hardware with the navigation system and control are presented. The resulting platform is evaluated through an *in-vitro* pilot study using a vascular silicone phantom by probing three target arteries under fluoroscopy guidance. To demonstrate the versatility and MRI compatibility of the slave robot, a preliminary study was conducted in an MR scanner to pave the way for subsequent work under MR-guidance.

**Chapter 4** builds upon the work presented in the previous chapter. Based on the end-user feedback received from the pilot study, the robotic system has been optimised. The chapter firstly demonstrates the modifications made to the master manipulator to improve and support its scalability prospects. Next, the slave robot's pneumatic stepper motors' redesigning to meet the requirements of frequent clinical use and performance characteristics are also presented. The revised platform performance is subsequently evaluated through an *in-vitro* user study with 7 qualified vascular surgeons and senior vascular surgery registrars. The study's experimental setting, workflow, evaluation methodologies and statistical considerations are presented and discussed.

**Chapter 5** addresses the lack of MR compatible instrumentation through the development of an MR safe and visible pull-wire driven steerable catheter using the thermal fibre drawing process. The chapter summarises Chapter 2's thorough review on the limitations of commercially available selective and steerable instrumentation and what impedes their deployment in MR environments. Followed by listing the structural and functional requirements for the development of an MR safe steerable catheter. The chapter focuses primarily on the fabrication, simulation and experimental characterisation of the in-house fabricated catheter against commercially available fluoroscopy-guided selective and steerable catheters. Next, the steerable catheter is integrated with an additively manufactured manual handle to facilitate its further evaluation in terms of steerability and compensation of undesirable effects experienced during its manipulation. Subsequent to integration and characterisation, an *in-vitro* pilot study is conducted

using a silicone vascular phantom by a novice under real-time MR guidance in a clinical 3T MRI scanner to evaluate the catheter's visibility, mechanical efficacy and steerability by probing several vascular structures such as the renal artery. The catheter is then further evaluated *in-vivo*, by testing it in a procine (pig) model. Lastly, to complement the work presented in Chapters 3 and 4, and to overcome the limitations of conventional MR-guided interventions, the catheter-handle assembly is integrated with a pneumatically actuated MR safe robotic system.

**Chapter 6** summarises the results and contributions of each chapter. The various limitations of the work are discussed and a description of the future directions of the research are also presented.

Chapter 2

# Endovascular Navigation under X-ray (Fluoroscopy) and MR-Guidance

"This chapter is currently under review in Progress in Biomedical Engineering".

## 2.1 Overview

In this review chapter, commercial guidewires (Section 2.2.1) and selective catheters (Section 2.2.2), the current state-of-the-art devices used for navigational purposes in endovascular interventions are presented. This introduction focuses on the materials and manufacturing methods employed in the construction of these devices to provide background for the following sections. Followed by their strengths and limitations in terms of navigation in the human vasculature and its accompanied side effects, mainly increased exposure to ionising radiation (Section 2.2.3). This is followed by presenting the commonly proposed solutions to resolve their navigational shortcomings by introducing the concepts of steerable catheters and robot-assisted endovascular interventions 2.2.4. Subsequently, a commonly proposed and investigated route, i.e. adopting MRI as an alternative imaging modality for its unique strength and capabilities when compared to X-ray fluoroscopy is introduced. To familiarise the reader with this imaging modality, the fundamental physics of MRI (2.3) is reviewed, followed by showcasing the ongoing efforts made by academia and industry to develop instruments compatible for use in MR environments through the adoption of different materials and manufacturing methods (Sections 2.3.3, 2.3.4, 2.3.5). Lastly, this review is used as a base for defining the future requirements and challenges of developing MR safe instrumentation and devices for endovascular interventions (Section 2.4). To generate this literature search, an up-to-date search was carried out in databases such as PubMed, Science Direct, and patent databases (e.g. Espacenet). The keywords used here, which was greatly inspired by Ali et al.'s review paper [21], covered three main categories: (1) instrument (mr/mri/magnetic resonance (imaging), guide*, guidewire, steer*, deflect*, selective, robot), (2) medical region (card*, heart*, atri*, vasc*), (3) instrument tracking (mr/mri/magnetic resonance (imaging), device tracking, catheter tracking, visualization).

# 2.2 Navigation Under X-ray (Fluoroscopy) Guidance

## 2.2.1 Guidewires

Guidewires are a key tool used by interventional radiologists and cardiologists to navigate through the vasculature, so larger, less manoeuvrable devices (such as catheters) can be pushed over the wire to reach the targeted vessel rapidly. Commercial guidewires are available in different sizes, lengths and constructions (Figure 2.1, Figure 2.2, and Figure 2.3). The rich repertoire of guidewires is an excellent demonstration of the efforts going into the choice of materials and their smart processing, each one of these having benefits helping interventionalists overcome different navigational challenges.

Guidewires, typically comprise of four major components: core wire, tip, body and coating [23, 24]. The central metallic core wire makes up most of the proximal section of the guidewire. The choice of core material(s) and its construction determines guidewire properties such as tip load, flexibility, steerability, trackability, torquability and support. Trackability is the ability of the guidewire's main body or shaft to follow its tip without buckling or kinking while navigating through the vasculature. Support, on the other hand, is the guidewire's ability to support the passage of other devices over it. Further, the thicker the core wire, the higher the support. Core wire materials are predominantly either stainless steel or nitinol. More recently, a combination of both materials is utilised to benefit from the columnar strength, pushability and torquability of stainless steel and the superelasticity and kink resistance of nitinol. In terms of construction, the core wire extends from the proximal end (shaft) of the guidewire and tapers towards the distal end to give the distal end more flexibility which facilitates guidewire navigation through tortuous anatomies. To achieve the desired taper profile across the distal end of the core wire (Figure 2.1b), guidewire manufacturers commonly employ the process of centreless grinding. The longer the tapered section of the core wire, the better the guidewire trackability and the lower its tendency to prolapse. On the other hand, the shorter the tapering, the better the support property, at the price of an increased tendency to prolapse [23].

The tip refers to the relatively flexible distal end of the guidewire. Guidewire tips are classified based on the degree to which the tapered core wire extends to the dome-shaped, distal-most point of the guidewire. If the core wire is fused, welded or bonded directly to the distal-most point of the guidewire tip, then this is considered a core-to-tip design (Figure 2.1c,d,f and Figure 2.2a,c,e,g). This design provides good tactile feedback and tip control with good torquability. Conversely, if the core wire is terminated several centimetres from the distal-most point and is replaced by a thin, flat stainless steel shaping or forming ribbon, then this is considered a shaping ribbon or forming ribbon design (Figure 2.1e,g and Figure 2.2b,d,f,h). This design provides good shape retention and a unique softness and flexibility of the tip, at the cost of less tip torque control. Moreover, the guidewire tip also comprises a radiopaque element which is achieved either by adding a flexible radiopaque coil (e.g. platinum coil (Figure 2.1d,e,f,g) coaxially to the core wire or by coating the tip of the core wire with radiopaque material (e.g. gold (Figure 2.1c)). In several other embodiments, a secondary stainless steel or nitinol coil is placed coaxially (Figure 2.2a,b,c,d) or in series (Figure 2.2e,f,g,h) with respect to the aforementioned radiopaque coil to promote tip resilience, mechanical properties and tactile feedback. Instead of using secondary coils, other guidewire manufactures use diamond-cut nitinol hypotubes (Figure 2.3a), by placing them coaxially to the radiopaque coil to enhance the guidewire's torquability and manoeuvrability (e.g. Fathom™ guidewire (Boston Scientific, Massachusetts, USA)).

The guidewire body refers to the additional encapsulation of material used to cover the core wire and distal coils(s).

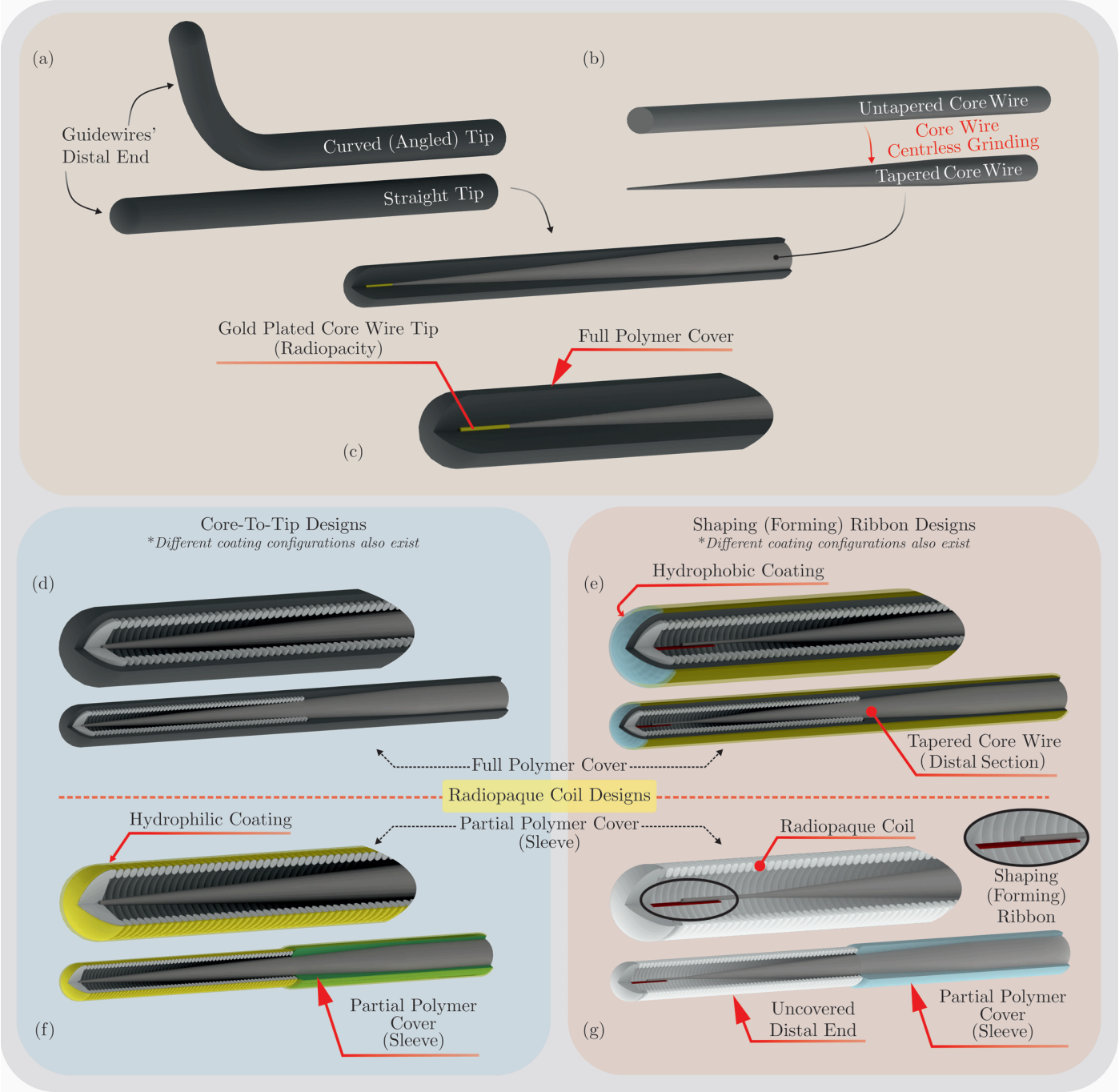



**Figure 2.1:** (a) Two different types of commonly used guidewire tips (distal ends): curved (angled) and straight. The distal ends tend to be heat treated to set the desired shape, e.g."J"-shape [22]. (b) The transition from an untapered to a tapered core wire using centreless grinding to achieve the desired taper profile across the distal end in (c). For (c-g), a sectioned view of the distal end of commercially available guidewires and their corresponding insets, illustrating the core design and its surrounding elements (coils, ribbons, etc). (c) Guidewire widely used in peripheral interventions (Radifocus® Guidewire (Terumo Europe NV, Leuven Beligum)). This type has a core-to-tip design and is fully covered with polymer. For radiopacity, the tip is plated with a radiopaque material (gold in this illustration). (d-g) Guidewires comprising a radiopaque coil instead of the aforementioned radiopaque plated core tip. Classification based on **polymer covering**: (d and e) guidewires covered fully with polymer, and (f and g) guidewires partially covered with polymer. Classification based on **core design**: (d and f) core-to-tip design, and (e and g) shaping/forming ribbon design. Guidewire **coating**: (b) has an additional layer of hydrophilic polymer that is added to improve lubricity, trackability and manoeuvrability. On the other hand, (e) employs a hybrid approach by coating the distal-most point with a hydrophobic polymer (e.g. silicone) to enhance tactile feedback and tip control. Note: The illustrated examples are merely a few examples of commercially available coating configurations.

The material can either be in the form of a polymeric cover or a metallic spring coil (commonly stainless steel). In the case of polymeric covering, if the layer of polymer covers both the core wire and distal coil(s), then this is commonly referred to as a full polymer cover (Figure 2.1c,d,e and Figure 2.2a,b,e,f). This type of covering improves deliverability at the cost of losing tactile feedback. On the other hand, if the polymer covers only the proximal (untapered) section of the core wire, whilst keeping the distal coils and distal (tapered) section of the core wire uncovered, then this is considered a partial polymer cover, also referred to as sleeve or hybrid design (Figure 2.1f,g and Figure 2.2c,d,g,h). This hybrid design not only improves tactile feedback, but it also ensures smooth deliverability. Other commercial guidewires (e.g. Amplatz Guidewire), adopt the second type of covering, where a metallic spring coil covers the core wire and the radiopaque distal coils (if placed coaxially) alongside an additional safety flat wire (Figure 2.3b,c,d). The safety wire in this design helps minimise the possibility of tip detachment if the spring coil breaks. Spring coil covered guidewires can be further classified into fixed core or movable core guidewires. As indicated by their names, for fixed core guidewires, the core wire cannot be moved with respect to the outer spring coil covering, conversely, the movable core guidewire allows the guidewire tip's softness and shape to be adjusted manually by moving the core wire back and forth with respect to the outer spring coil (Figure 2.3c,d).

In order to alleviate the surface friction and improve the guidewire's trackability and manoeuvrability, an additional layer of polymer coating (hydrophilic or hydrophobic) is added to the aforementioned elements. The hydrophilic coating's ability to attract water, makes the guidewire more lubricious and easier to navigate through tortuous anatomies. However in certain scenarios, the hydrophilically coated guidewire (Figure 2.1f, Figure 2.2b,c,f) can unintentionally end up in false subintimal spaces which increases the risk of perforation. Hydrophobic coating, on the other hand, enhances tactile feedback but decreases slipperiness and trackability. As shown in Figure 2.1e and Figure 2.2g, hybrid coatings also exist, for instance, the dome-shaped distal-most point is coated with hydrophobic material for enhanced tactile feedback and tip control, while the distal coils or the entire guidewire as a whole is coated with hydrophilic material for smoother device delivery.

### 2.2.2 Selective Catheters

A multitude of different catheters are developed for different tasks in image-guided endovascular interventions [2]. The catheters specifically designed for navigation in the vascular network, along with guidewires (Figure 2.5), are called selective catheters. Most commercial selective catheters are passive, single lumen tubing with pre-shaped distal ends mimicking the anatomy of blood vessels. They can be further classified into diagnostic angiographic catheters (DACs) and guiding catheters (GCs). DACs are used to inject a radiopaque contrast agent into cardiac, peripheral, and/or neurovascular blood vessels for angiography. Angiography is a medical imaging technique that uses real-time X-ray (fluoroscopy) to visualise blood vessels to help diagnose and evaluate diseases, such as aneurysms or atherosclerosis. Compared to DACs, GCs have larger inner lumens which facilitate the placement of other intravascular devices such as balloon and stent deployment catheters, into targeted blood vessels. Furthermore, GCs also permit contrast agent injection prior to angioplasty and/or stent deployment. In terms of construction, both types of catheters are typically comprised of a relatively stiff shaft and a soft pre-curved distal end with an atraumatic tip. The stiff shaft gives selective catheters enough pushability and torqueability to be inserted percutaneously into a peripheral blood vessel and to be navigated through the vasculature to a targeted site. Contrarily, the atraumatic tip minimises the risk of vessel perforation or dissection while manoeuvring the catheter through tortuous anatomies.

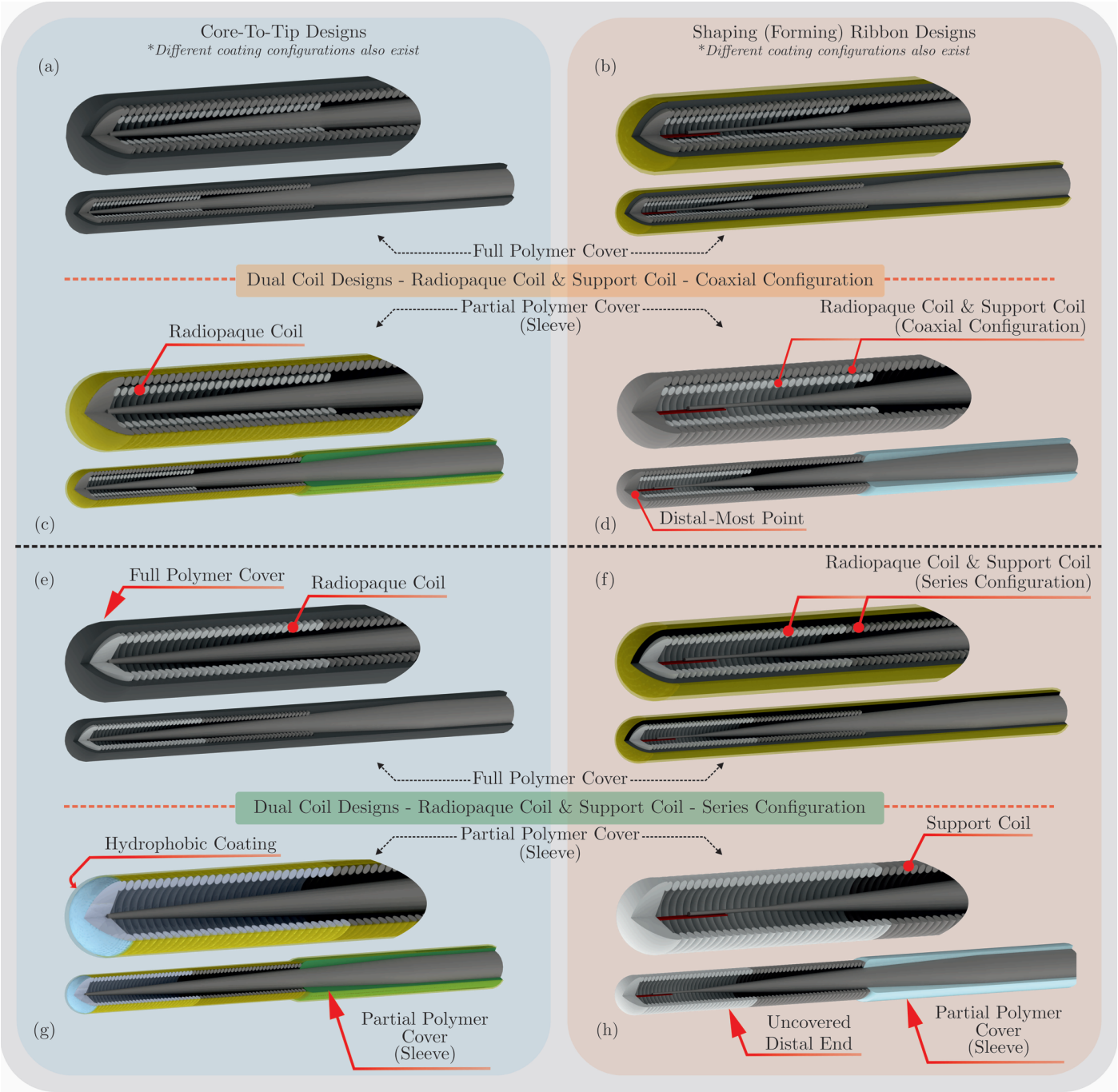



**Figure 2.2:** (a-h) Guidewires comprising a radiopaque coil and an additional support coil to promote the tip's resilience and mechanical properties. A sectioned view of the distal end of commercially available guidewires and their corresponding insets, illustrating the core design and its surrounding elements (coils, shaping ribbon). Classification based on **support coil placement**: (a-d) coaxially placed support coil (commonly stainless steel) with respect to a radiopaque coil, and (e-h) support coil placed in series with respect to a radiopaque coil. Classification based on **polymer covering**: (a, b, e and f) guidewires fully covered with polymer, and (c, d, g and h) guidewires partially covered with polymer. Classification based on **core design**: (a, c, e and g) core-to-tip design, and (b, d, f and h) shaping/forming ribbon design. Guidewire **coating**: (b, c and f) have an additional layer of hydrophilic polymer to improve the guidewires' lubricity, trackability and manoeuvrability. Conversely (g) employs a hybrid approach by applying a hydrophobic polymer (e.g. silicone) at the distal-most point to enhance tactile feedback and tip control. Note: The illustrated examples are merely a few examples of commercially available coating configurations.

To achieve the desired stiffness and mechanical properties, catheter shafts are usually composed of metal braids sandwiched between layers of polymer; commonly polyurethanes, nylon 12, polyamide elastomers (e.g.: PEBAX®)

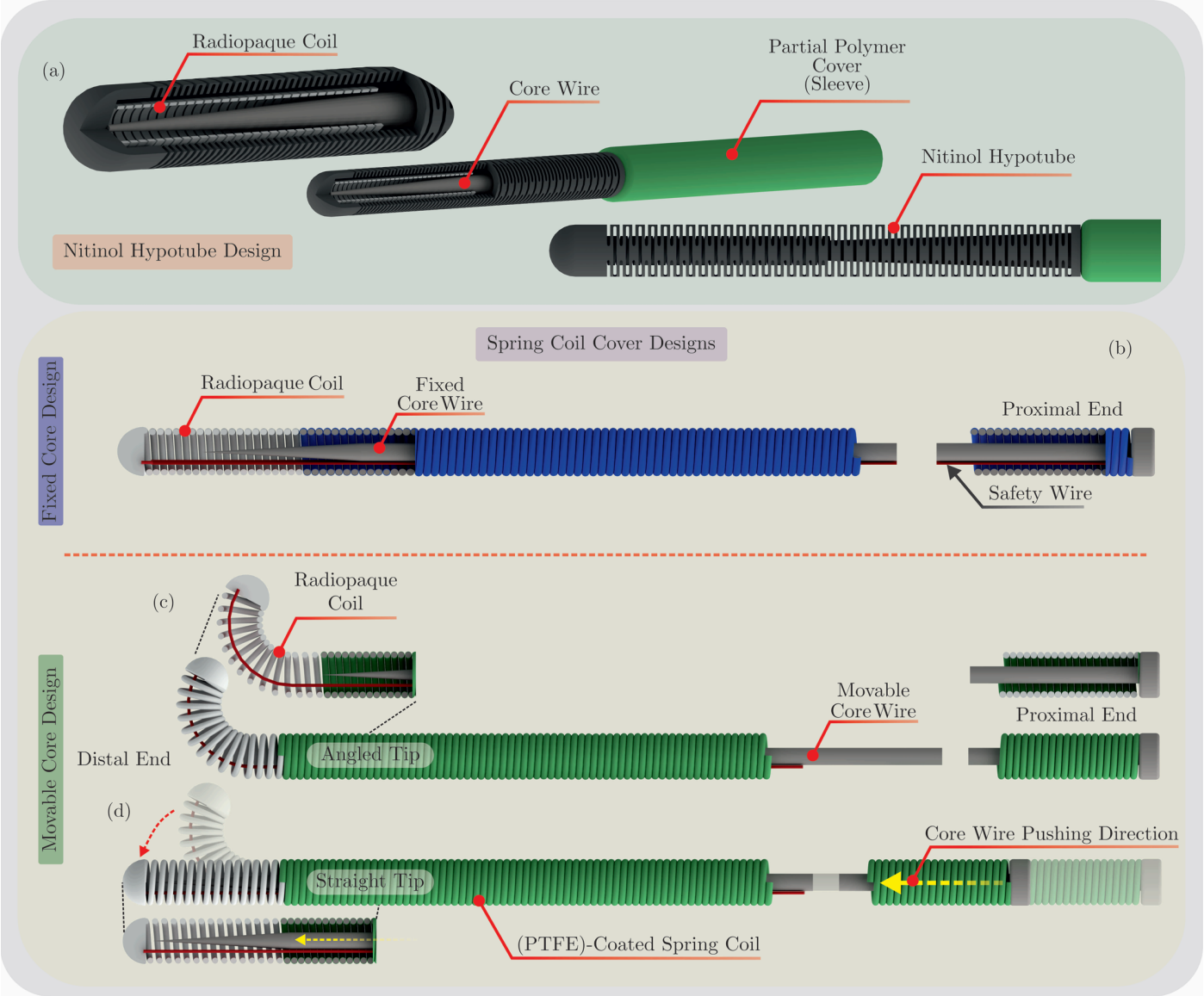



**Figure 2.3:** (a) A sectioned view of the distal end of a guidewire comprising a nitinol hypotube coaxially placed with respect to a radiopaque coil. The insets illustrate the core design and its surrounding elements (hypotube, core, coil). The design shown falls under the core-to-tip design category and consists of a partial polymer covering. Although not illustrated, the distal end can also be coated with hydrophilic/hydrophobic coatings to achieve the desired mechanical and physical properties. (b) Spring-coil covered guidewire with a fixed core design. (c-d) Spring-coil covered guidewire with a movable core design. (c) Initial state of the guide wire, i.e. angled distal end (tip). (d) The proximal end is pushed, thereby moving the core wire with respect to the spring coil, which in turn straightens the distal end (tip). The safety wire in (b-d), illustrated in red, minimises the possibility of tip detachment if the spring coil breaks.

and fluoropolymers (e.g.: Polytetrafluoroethylene (PTFE)). In some cases, the polymers are blended with radiopaque fillers (e.g.: Barium Sulphate – $BaSO_4$, Bismuth Subcarbonate – $(BiO)_2CO_3$) to increase the catheter's opacity to make them clearly visible under fluoroscopy. The metal braiding reduces the possibility of kinking or bending of the catheter during manipulation without a significant increase in the catheter's wall thickness. Thus, the same mechanical characteristics of thick-walled catheters can be achieved in thin-walled catheters [25]. Examples of metal braids include non-ferromagnetic metals such as 304V, 304L, and 316L stainless steels; nickel-titanium (Nitinol); and tungsten for radiopacity [26]. To create flexible distal ends, catheter manufacturers employ a plethora of techniques. One common approach is to thermally bond a relatively flexible tubing to the relatively stiff composite

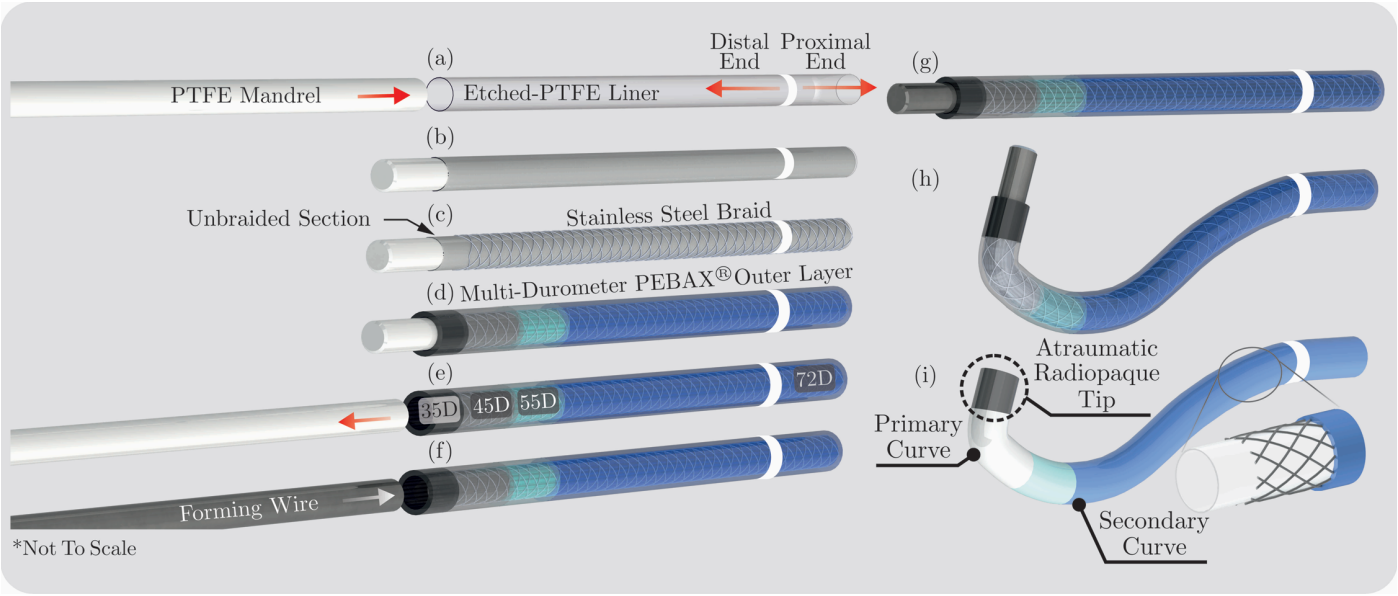



**Figure 2.4:** Guiding Catheter Fabrication Steps: (a) A ram extruded PTFE mandrel is fed through a chemically etched ram extruded PTFE liner to prevent the liner from collapsing during the subsequent processes. (b) The liner/mandrel assembly is then braided with stainless-steel wires (e.g. $50\mu$m 316L stainless-steel round wires) using a maypole braiding machine. (c) A small section of the liner is left non-braided to create a flexible atraumatic tip. (d) A multi-durometer PEBAX® outer layer is applied on top of the braided liner/mandrel assembly to encapsulate the braid. The stiffness of the outer catheter decreases progressively from the proximal end (Shore Hardness 72D) to the distal atraumatic radiopaque tip (Shore Hardness 35D). The transition segments (45D and 55D) are added to reduce the possibility of catheter kinking caused by abrupt changes in flexibility. This fabrication step can be achieved using various techniques, including thermal bonding of multi-durometer segments[28], intermittent extrusion[29]. (e) The PTFE mandrel is pulled out of the laminated tube. (f-g) The laminate is mounted onto a forming wire to form the desired distal end shape. (h) The distal end shape is modified using a template (e.g. Judkins right 4) and placed in a forming oven for a predetermined temperature and time. (i) After annealing, the assembly is cooled, followed by the removal of the forming wire.

laminated catheter shaft. Other techniques include varying the braid pitch of the reinforcement metal braid and/or varying the hardness of materials used in constructing the outer layer. Once fabricated, the resulting catheter may be coated with hydrophilic, lubricious polymers such as silicone and poly(vinylpyrrolidone) (PVP) to reduce frictional forces and risk of damage to blood vessel walls [27].

In terms of differences, DACs have smaller inner lumens and tapered distal tips. Tapered distal tips maximise flexibility and facilitate navigation through tight and tortuous anatomies [30]. GCs, on the other hand, have larger inner lumens and un-tapered distal tips. Most commercial GCs follow a two-layer catheter assembly with a chemically etched PTFE liner as an inner layer, braided stainless steel wires for reinforcement and multi-durometer PEBAX® as an outer layer. The PTFE liner's outer layer is etched to enhance its bondability with the PEBAX® outer layer. PTFE is frequently used as an inner layer because of its low coefficient of friction (0.05-0.8, static) which facilitates the insertion of other devices through GCs [31]. Similarly, PEBAX®, is widely used in the manufacturing of catheters because of its extensive range of hardness and flexibility, and superior bonding capability with other polymers [32]. Figure 2.4 illustrates the fabrication steps of commercial GCs [33].

### 2.2.3 Challenges Associated with Navigation under X-ray (Fluoroscopy Guidance)

One of the critical challenges clinicians face while preparing for an intervention is choosing the appropriate selective catheters and guidewires from the myriad of shapes, sizes, and features (stiffness, braiding, coating) [2]. Furthermore, steering and manoeuvring of selective catheters and guidewires can become complicated due to their fixed shape at the distal end, long lengths, and unpredictable friction between the devices and vessel walls. In specific scenarios, where multiple catheterisations are performed, e.g. Fenestrated Endovascular Aortic Aneurysm Repair (FEVAR), interventionalists exchange catheters to change the tip shape and guidewires to change its stiffness. The navigation difficulties and repeated instrument exchange consequently increase the risks of complications, such as infection, distal embolisation, dissection, perforation of vessels, and increase procedure time. Since endovascular interventions are performed under X-ray fluoroscopy guidance, any difficulty in navigation increases the exposure of patient and staff to ionising X-ray radiation. Besides, using X-ray fluoroscopy as an imaging modality per se introduces other drawbacks which make it sub-optimal for image-guided endovascular interventions. X-ray poorly depicts soft tissue contrast [34], may lead to significant career musculoskeletal injury to operators forced to wear protective lead aprons (designed to shield the body from harmful radiation) [35], increases cancer risks for paediatric patients who undergo cardiac catheterisation procedures [36], and may impair kidney function due to the use of large volumes of iodine-containing contrast media (used to visualise the blood vessels in fluoroscopy-based angiography) [37].

A commonly proposed technique to overcome the aforementioned navigational challenges is to use robotic platforms (summarised in the following section) to remotely and accurately manipulate off-the-shelf passive instrumentation (selective catheters, guidewires) and steerable catheters. Steerable catheters are catheters with improved manoeuvrability and stability, integrated with an actuation mechanism which enables the operator to change the distal end shape of the catheter manually or remotely (robotically). Commercial and under development steerable catheters make use of four actuation mechanisms: pull-wire-driven (also referred to as pull-wire driven or cable driven), magnetic, smart material-actuated and hydraulic [21]. Pull-wire-driven steerable catheters are the largest and most clinically used group of steerable catheters, especially in the field of cardiac electrophysiology. In addition to navigating through tortuous anatomies and guiding other intravascular devices, pull-wire-driven catheters embedded with conductive wires are used in the treatment of cardiac arrhythmia, i.e. abnormal heart rhythms (Figure 1.1b). Other applications include catheter-based intra-cardiac echocardiography (ICE), which is used in the visualisation of cardiac structures and blood flow. Apart from pull-wire-driven catheters, steering and orienting of catheters via controlled magnetic fields is one of the few robotic technologies that are commercially available, e.g. Niobe® and Genesis RMN® magnetic systems (Stereotaxis, Saint Louis, MO, USA). As in the case of pull-wire-driven catheters, the aforementioned magnetic systems are employed in cardiac electrophysiology [38]. To the best of our knowledge, the other two steering mechanisms (smart material-actuated and hydraulic) are yet to be used in an operating theatre. The different configurations of steerable catheters will be presented in Section 2.3.4.

### 2.2.4 Robot-Assisted Platforms for Endovascular Interventions

Recent advancements in robotic catheterisation systems aim to help surgeons manipulate instrumentation more effectively in order to improve surgical outcomes and to minimise radiation exposure for both the patients and clinicians alike. Robotic platforms can also eliminate hand tremors of the operator, and improve the stability and precision of procedures [39]. Furthermore, the adoption of remote manipulation allows the operator to perform

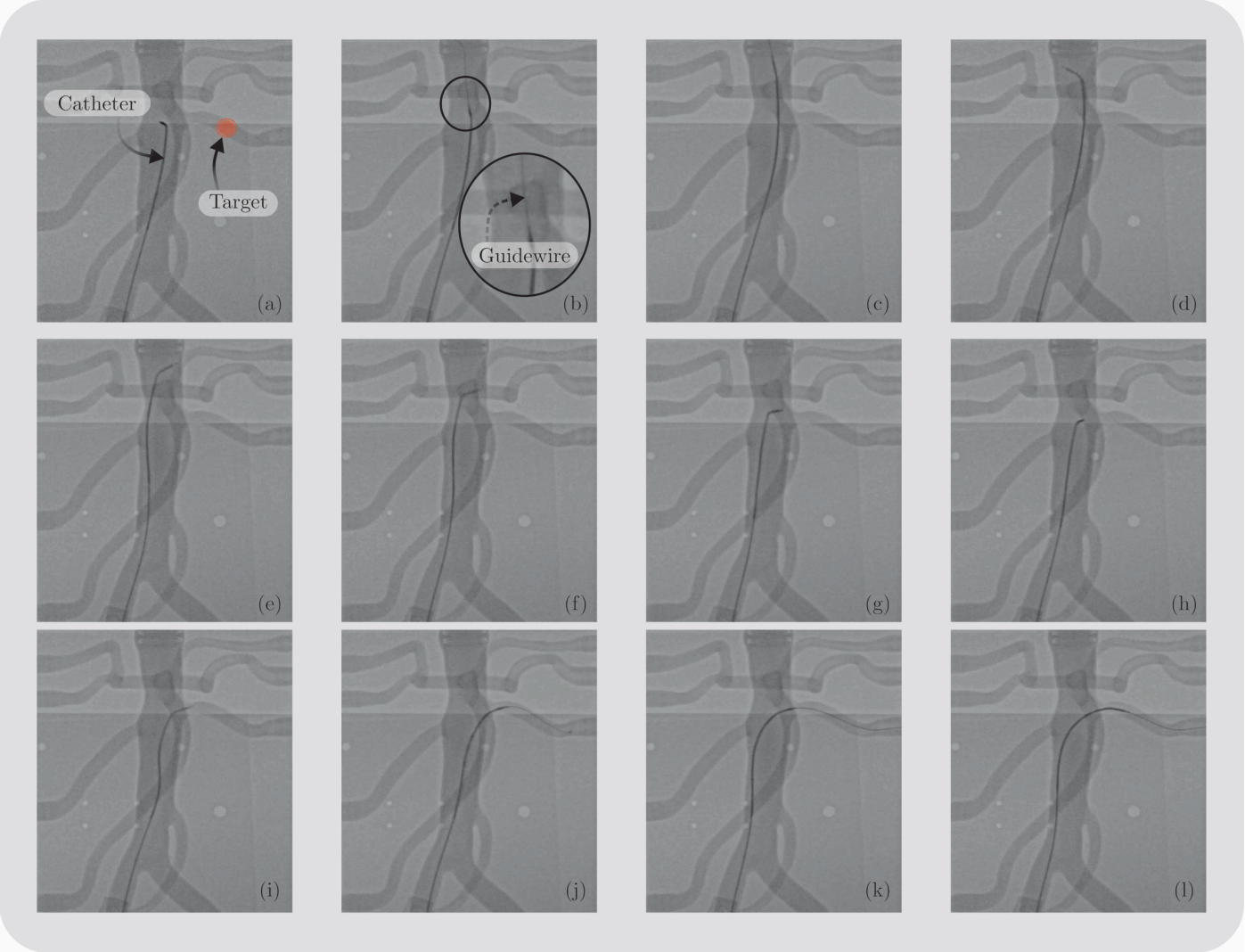



**Figure 2.5:** 2D X-ray fluoroscopy sequence illustrating the catheterisation of the Left Renal Artery (LRA) in an abdominal phantom (Elastrat, Geneva, Switzerland) using a selective catheter, IMPRESS®, Size = 5F (1.667mm outer diameter), Distal End Shape: Headhunter 1, Length = 100cm, Inner Diameter=0.046" (1.17mm), Reference: 510035HH1 (Merit Medical OEM, Utah, US) and a guidewire, Radifocus® Guidewire M Standard Type Guidewire, Length = 180cm, Outer Diameter = 0.035", Flexible Length = 10mm, Angled Distal Tip, Reference: RF-GA35181M, (Terumo Europe NV, Leuven Beligum). (1) Indicates the LRA target and the catheter. (2) Guidewire is advanced over the LRA whilst keeping the catheter in place. The catheter's distal end straightens due to the advancement of the guidewire. (3) Catheter is advanced over the guidewire. (4) Guidewire is partially retracted and the catheter restores the pre-shaped distal end. (5) The catheter is rotated to adjust its orientation. (6-8) The catheter and guidewire assembly is slowly retracted towards the LRA. (9) The catheter's distal end slides into the LRA, (10-11) The guidewire is advanced through the catheter to prevent the catheter from flipping back to the abdominal aorta. (12) The catheter is advanced over the guidewire.

the procedure with added comforts, without heavy protection suits [40]. Several commercial platforms have been developed for peripheral vascular interventions and electrophysiology.

#### 2.2.4.1 Commercial Platforms for General Vasculature (PVI, PCI)

Peripheral vascular interventions (PVI) are minimally invasive procedures used to treat diseases in the arteries leading to the intestines, head, arms and most commonly the legs. Percutaneous coronary interventions (PCI) on the other hand, treat diseased vessels in the heart. For fluoroscopy-guided peripheral vascular interventions,

the discontinued Magellan™ robotic platform (Johnson & Johnson, Redwood City, CA, USA) was designed to allow clinicians to remotely manipulate proprietary pull-wire driven steerable catheters/sheaths and standard off-the-shelf guidewires through a variety of anatomies and lesions from a remote workstation. Each bespoke steerable device comprised a base at its proximal end, which facilitated its coupling into a motorised actuation unit. The base of each instrument consisted of spring-loaded idler pulleys through which the pull-wires were routed and anchored. The rotation of the pulleys led to the tensioning and loosening of the pull-wires, which subsequently deflects the device's flexible distal end. Besides, the actuation unit enabled the precise advancement and retraction of the device. Similarly, it was also possible to translate and rotate guidewires by placing them between two conveyor belts which mimicked the surgeons' manipulation of guidewires using their thumb and forefinger. To manipulate the instruments, surgeons used a 3D joystick or navigation buttons which were located on the workstation. The Magellan™ robotic system was successfully used in several peripheral arterial interventions such as stent grafting and aneurysm repair [41, 42]. The limitations of the Magellan™ platform included its high installation costs and use of non-standard catheters and sheaths. Furthermore, the system did not allow the integration of therapeutic devices, which limited its use for navigation purposes only.

A recent trend in commercial robotic platforms, e.g. CorPath GRX® (Siemens Healthineers, Waltham, USA), facilitate the use of standard off-the-shelf devices. The CorPath GRX® system is the only commercially available FDA approved and CE-marked robotic platform dedicated for endovascular peripheral and coronary interventions. The GRX® platform builds upon its predecessor, the CorPath 200® [43], by enabling the control of a selective guiding catheter, along with a guidewire and a therapeutic catheter (e.g. balloon/stent). To dock the guiding catheter into the platform, the proximal luer lock of the guide catheter is connected to a drive gear add-on. The assembly is then mounted onto an actuation unit which enables the translation and rotation of the guiding catheter respectively. The guidewire and therapeutic catheters, on the other hand, are loaded into the robotic platform by placing them between a set of active and passive rollers (also referred to as friction wheels) which facilitate the insertion/retraction and rotation of the instruments. Similar to the Magellan™, the clinician remotely manipulates the instruments in a shielded cockpit using joystick and touchscreen controls. The GRX® platform includes other features such as partial automation (Rotate-on Retract feature) [44], and long distance teleoperation (20 miles away from the patients) [45]. Another emerging robotic platform dedicated for PCI procedures is the R-one™ system (Robocath, Rouen, France). The platform features a robotic manipulator for off-the-shelf guidewires and balloon catheters. The system recently obtained its CE certification.

#### 2.2.4.2 Commercial Platforms for Electrophysiology (EP)

Electrophysiology (EP) is the diagnosis and treatment of patients with electrical or rhythm disorders of the heart. Sensei® X2 by Hansen Medical (Johnson & Johnson, Redwood City, CA, USA) was a major commercial robotic platform dedicated for cardiac electrophysiology therapies [46, 47]. Similar to the Magellan™, the Sensei® platform comprised two pull-wire driven steerable catheters/sheaths, one inside the other. The inner guide catheter is flexible and accommodates standard ablation catheters while the outer guide sheath provides stability. The system also follows a master-slave architecture, where the operator remotely controls the instrumentation using a 3D joystick or navigation buttons. Unlike the Sensei® system, the Amigo™ Remote Catheter System (RCS) (Catheter Precision In, Mount Olive, NJ, USA) platform is a catheterisation system that navigates third party standard EP mapping and ablation steerable pull-wire driven catheters [48–52]. The system is equipped with an intuitive remote controller

that replicates the manual handle of a steerable catheter. Wutzler et al., reported that the use of the Amigo™ RCS for the treatment of atrial fibrillation led to a significant reduction in fluoroscopy exposure for the operator when compared to manual interventions (13.4±6.1 vs. 23.9±5.4 minutes, $p<0.001$) [53].

Another commercially available platform which employs magnetic steering is the Niobe® (Stereotaxis, Saint Louis, MO, USA) system. The robotic system consists of two large permanent magnets located on either side of the patient's bed. The rotation of the magnets using motors results in the subsequent steering of a steerable catheter embedded with a magnet at its distal end. As reported by Stereotaxis, the robotic platform has been already used in more than 100,000 procedures, and has been validated by several research groups through *in-vivo* and clinical trials in the treatment of cardiac arrhythmia [54–64]. The Genesis RMN® magnetic system is the more recent upgraded successor of the Niobe®. The platform is smaller in size, lighter, faster and more flexible when compared to the Niobe® platform. The aforementioned benefits result in improved responsiveness of the magnetic steering system and patient access for medical personnel (nursing team and anaesthetists). Stereotaxis has also commercialised a robotic navigation system (Vdrive) to remotely control third party diagnostic pull-wire driven steerable catheters. The Vdrive system consists of components such as the V-Sono™ manipulator. This manipulator controls ICE steerable catheters such as the SoundStar® (Johnson & Johnson, Redwood City, CA, USA) or Siemens AcuNav™ (Siemens Healthineers, Waltham, USA). Catheter Guidance Control and Imaging (CGCI) system (Magnetecs Corporation, CA, USA) is another master-slave, magnetic-based catheter navigation system which uses eight electromagnets, four of which are placed in a semi-spherical arrangement above the patient's bed, and the other four are placed symmetrically underneath the patient's torso [65–67].

The 8 electromagnets generate a "lobed" shaped dynamic magnetic field within the region of the patient's heart. Controlling the magnitude, direction and gradient of the generated magnetic fields results in the formation of a force or torque applied on a steerable catheter equipped with magnets at its distal tip. Another magnetic catheter steering system that employed seven electromagnets around the patient's torso for the treatment of cardiac arrhythmia is the Aeon Phocus system (Aeon Scientific AG, Zurich, Switzerland). As in the case of the Niobe® and CGCI systems, the operator can remotely control a steerable magnetic catheter with a joystick in a separate control room. Although the system was CE marked in 2014, Aeon Scientific is no longer in business. The main limitation of the aforementioned magnetic-based systems is the need for large magnets which usually require special considerations for operating theatres.

#### 2.2.4.3 Emerging Research Platforms for Endovascular Interventions

A variety of robotic systems for endovascular interventions were reported in literature. In general, such systems show low levels of robotic autonomy [115] and consider a master-slave set-up for teleoperated manipulation of instrumentation. Feeding (advancing & retracting) of catheters and guidewires are normally achieved by roller-based mechanisms [74, 86, 99, 116–119] or linear drives integrated with electromechanical clamps [93]. The corresponding master, with human machine interfaces (HMI), make use of conventional stationary joysticks, hand-held joysticks, or 3D input devices with force feedback capabilities. Novel master devices were proposed to improve the transparency of teleoperation. Exemplary, motion due to manipulation of standard catheters was sensed without user feedback and replicated to a slave robot [120]. More recently, magnetorheological fluid was used in combination with a catheter to mimic friction and generate user feedback [121]. Slave robots generally show alternative concepts with different electro-mechanical mechanisms for driving and clamping of instrumentation as reported in

**Table 2.1: Abbreviations:** steerable catheter (SC), guidewire (G), catheter (C), customised catheter (CC), electrophysiology (EP), cardiac intervention (CI), general catherization (GC), rotation (R), feeding (F), bending (B), electromechanical (EME), friction wheels (FW), linear stepping mechanism (LSM), electromechanical clamping (EMC), hydraulics (HYD), laboratory test (LB), phantom study (PS), animal study (AS), cadaver study (CS), and human study (HS).

| Device | FoA | Instrument | DoF | Actuation mechanism | MRI ($cm^3$) | Eval. ($mm, °$) | TRL |
|---|---|---|---|---|---|---|---|
| *Sensei*® X2 (Hansen Medical) [68] | EP | SC | 6 | RFB/RFB - EME | × | HS | 9 |
| *Amigo* (Catheter Precision) [69] | EP | SC | 3 | RFB - EME | × | HS | 9 |
| Cercenelli et al.[70–72] | EP | SC | 3 | RFB - EME | × | AS | 7 |
| Moon et al.[73] | EP | SC | 3 | RFB - EME | × | LB | 4 |
| Fu et al.[74, 75] | GC | SC | 3 | RFB - FW EME | × | PS | 4 |
| Park et al.[76] | EP | SC | 3 | RFB - EME | × | LB | 4 |
| Tavallaei et al. [77, 78] | GC | SC | 3 | RFB - EME | ✓ | AS | 6 |
| Ganji et al. [79] | EP | SC | 3 | RFB - EME | × | AS | 5 |
| Lee et al. [80] | EP | SC | 3 | RFB - HYD | ✓ | AS | 4 |
| *Magellan*™ (Hansen Medical) [81] | GC | G/SC | 5 | RF/RFB - FW EME | × | HS | 9 |
| *R-one*™ (Robotcath) [82] | GC | G/C | 3 | RF/F - FW/FW | × | HS | 8 |
| *CorPath GRX* (Corindus Robotics) [83] | GC | G/C | 4 | RF/RF - FW EME | × | HS | 9 |
| Bian et al. [84, 85] | CI | G/C | 2 | RF* - FW | × | LB | 5 |
| Srimathveeravalli et al. [86] | GC | G/C | 3 | RF/F - FW EME | × | PS | 4 |
| Mi et al.[87] | GC | G/C | 3 | RF/F - FW | × | LB | 3 |
| Cha et al.[88] | GC | G/C | 4 | RF/RF - FW/EME | × | PS | 4 |
| Wang et al.[89] | GC | G/C | 8 | 4 × RF - EME | × | AS | 4 |
| Bao et al.[90, 91] | GC | G/C | 4 | RF/RF - EME | × | HS | 6 |
| Zhang et al. [92] | GC | G/C | 3 | RF/F - EME FW | × | LB | 4 |
| Omisore et al. [93] | GC | C | 2 | RF - EMC | × | PS | 4 |
| Guo et al. [94–96] | GC | C | 2 | RF - FW | × | PS | 4 |
| Feng et al. [97] | GC | C | 2 | RF - FW | × | LB | 3 |
| Zakaria et al. [98] | GC | C | 2 | RF - FW | × | LB | 4 |
| Wang et al.[99] | GC | C | 2 | RF - EMC | × | LB | 4 |
| Zhao et al.[100–102] | GC | C | 2 | RF - FW | × | PS | 5 |
| Thakur et al.[103] | GC | C | 2 | RF/RF - FW | × | LB | 4 |
| Kesner et al.[104] | CI | G | 1 | F - EME | × | LB | 3 |
| Meng et al.[105, 106] | GC | C | 2 | RF - FW | × | LB | 4 |
| Arai et al. [107] | GC | C | 2 | RF - LSM | × | LB | 3 |
| Guo et al. [108–110] | GC | C | 2 | RF - EMC | × | PS | 4 |
| He et al. [111] | GC | C | 2 | RF - EMC | × | PS | 3 |
| Guo et al. [112] | GC | C | 2 | RF - EME | × | PS | 4 |
| Bao et al. [113] | GC | G | 2 | RF - EME | × | PS | 4 |
| Jayender et al. [114] | GC | CC | 7 | RF - IR | × | PS | 3 |

[122–124]. Device compliance with MR environments is restricted to [77, 125] and focuses on steerable catheters. For the sake of completeness, the reader is kindly referred to a comprehensive review of the emerging platforms [39, 126].

# 2.3 Navigation Under MR Guidance

## 2.3.1 MRI and MR-guided Endovascular Interventions

Although the usage of steerable sheaths/catheters and robotic systems contribute to improved stability and procedural efficacy [3–6], recent developments in cardiovascular science have highlighted the importance of including functional information (e.g. blood flow, tissue oxygenation, diffusion, perfusion) of the underlying pathology during endovascular interventions to guide treatment/therapy decisions [7]. Magnetic resonance imaging (MRI), more specifically, cardiovascular magnetic resonance (CMR) has seen significant advances in the last three decades, which paved the way for interventional applications using MRI [127–130]. MRI is a non-invasive and an ionisation free medical imaging technique that employs powerful magnets to produce a strong magnetic field (commonly denoted by $B_0$). $B_0$ aligns and precesses the hydrogen nuclei, which are abundant in the human body and have intrinsic magnetic properties, along its direction. When an additional radiofrequency (RF) field is applied perpendicularly to $B_0$, the precessing hydrogen nuclei are tipped out of their alignment with $B_0$. Once the RF pulse is switched off, the nuclei realign with $B_0$ and concurrently emit an electromagnetic signal, which is detected by the MRI's receiving coil. The detected signals are then processed to form an image of the scanned area. The time it takes for the nuclei to realign with the magnetic field, and the amount of signal emitted is dependent on the environment and the chemical composition of the molecules.2.1F 2.2g 2.3re 2.6 and Figure 2.7 illustrate the basic physics of MRI and its relevant terminology [131–134].

In addition to its non-invasive and ionisation-free nature, the previously described MR physics results in enhanced soft tissue visualisation [135, 136]. Furthermore, MRI can also provide functional information such as blood flow, tissue oxygenation, diffusion, perfusion, and mechanical properties of tissues (elastography). Magnetic resonance angiography (MRA) and MR-guided interventions (Figure 2.8) in general are performed with gadolinium-based contrast mediums instead of the iodine-based contrast agents. Similar to fluoroscopy-based angiography, MRA also provides a precise assessment of blood vessels. Even though MRA avoids the usage of iodine-based contrast agents, gadolinium-based mediums should be applied with care as they may increase the risk of a rare but serious disease called nephrogenic sclerosing fibrosis (NSF) in patients with severe kidney impairment [137, 138]. However, it has been shown that MRI has the ability to perform angiography and endovascular interventions with only small amounts or even without the use of any contrast medium [138]. The EPflex guidewire was also further evaluated in an MR setting vs X-ray fluoroscopy.

Despite its inherent potential, MR-guided interventions face a major challenge in the lack of MR safe and compatible instruments [135, 140]. Commercial catheters for navigation were designed for use under fluoroscopy guidance and cannot be used in an MR environment due to the frequent presence of long metal braids or coils along their shafts [9, 141]. Instead of directly guiding instruments under MRI, other research groups attempted combining X-ray fluoroscopy and MR-guided catheterisation (i.e. XMR procedures) by fusing a pre-operatively acquired MR image as an image overlay with real-time fluoroscopic images [142]. This provides a roadmap for guiding instruments in tortuous anatomies without the need for multiple contrast agent injections while lowering exposure time to ionising radiation. The drawback of this method, apart from still using ionising radiation, is the distortion of the anatomy caused by the interaction of stiff instruments with blood vessels; resulting in a significant incompatibility in the image overlay [135].

### 2.3.2 MRI Safety Labelling

As safety is a major concern in the development and application of medical devices for MR environments, it is important to understand the current classification of MR safety. To classify whether it is possible to use a device within an MR environment or not, the American Society for Testing and Materials (ASTM) devised a standard, namely ASTM F2503 [143]. This standard defines three possible classifications for medical devices used in MRI environments: MR safe, MR conditional and MR unsafe. The MR safe classification is assigned to devices composed of non-metallic, non-magnetic, and non-conductive materials by providing a scientifically based rationale rather than test data. Conversely, the MR conditional classification is assigned to an item with demonstrated safety in the MR environment within defined conditions (e.g. static magnetic field, the switched gradient magnetic field and the RF fields). The MR unsafe classification is designated to items which pose risks to the patient, medical personnel, or other persons within the MR environment.

### 2.3.3 Guidewires and Selective Catheters

*Guidewires:* For the adoption of existing guidewires (Figure 2.1, 2.2, 2.3) into MR environments, the long metal core wires commonly employed need re-evaluation. The non-ferromagnetic metal braids such as 304V, 304L, 316L stainless steels, and nitinol [144, 145] create acceptable susceptibility artefact, i.e. MRI artefacts such as distortions and local signal change due to local magnetic field inhomogeneities. However, these are conductive metals

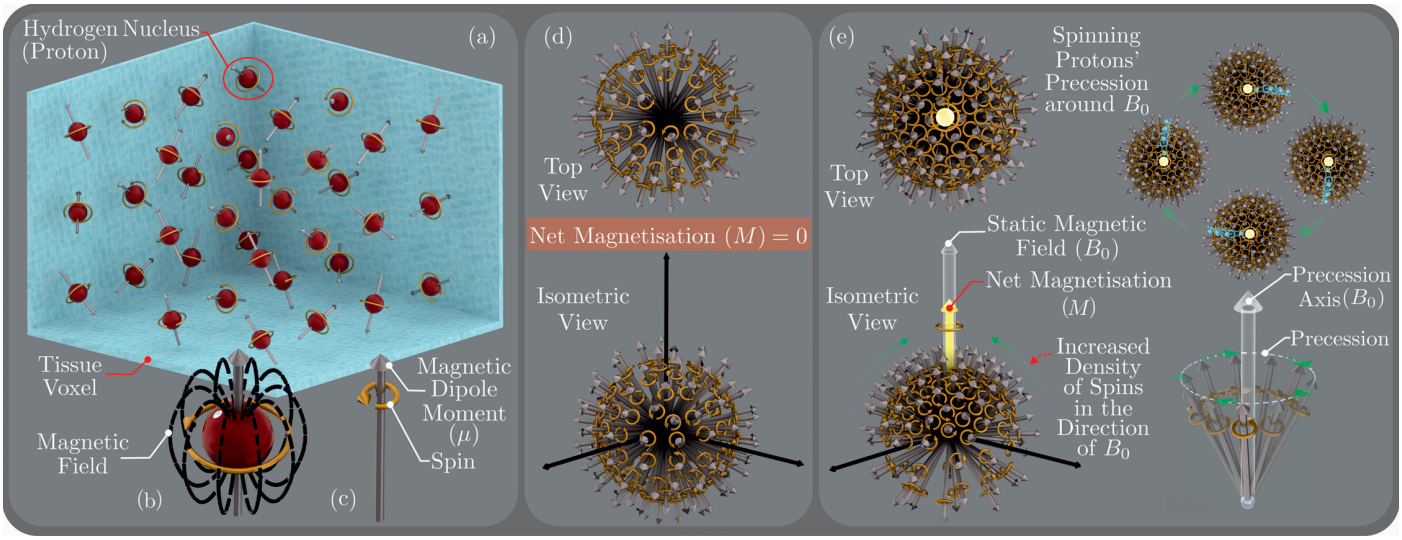



**Figure 2.6: MR Physics (I):** (a) A human tissue voxel largely made of water and fat, which contain hydrogen atoms. (b) A simplified representation of the nucleus of a hydrogen atom. The nucleus is a positively charged proton with an intrinsic property, called spin or intrinsic angular momentum. The non-zero net spin generates a magnetic dipole moment ($\mu$ or MDM for short), which in turn generates a small magnetic field. MDMs and spins are used interchangeably in literature because they track each other. (c) A further simplified representation of the nucleus, which is used in the rest of the figure.(d) In the absence of an external magnetic field, the atoms' MDMs are pointing randomly, hence giving a uniform distribution of MDMs in the top and isometric views of an implicit coordinate system. The net magnetisation (denoted by $M$) is the sum of the individual MDMs. In the absence of an external magnetic field, $M$ is zero. (e) Upon the application of an external strong static magnetic field ($B_0$), i.e. the patient is placed in the MRI bore, two events take place: 1. The orientation of the MDMs is skewed slightly toward $B_0$'s direction (increased density of MDMs) resulting in an increase in $M$ (yellow arrow), 2. The ensemble of MDMs start precessing at the Larmor frequency (42 MHz at 1 Tesla) around $B_0$'s direction. Although the spins are precessing, $M$ remains in equilibrium.

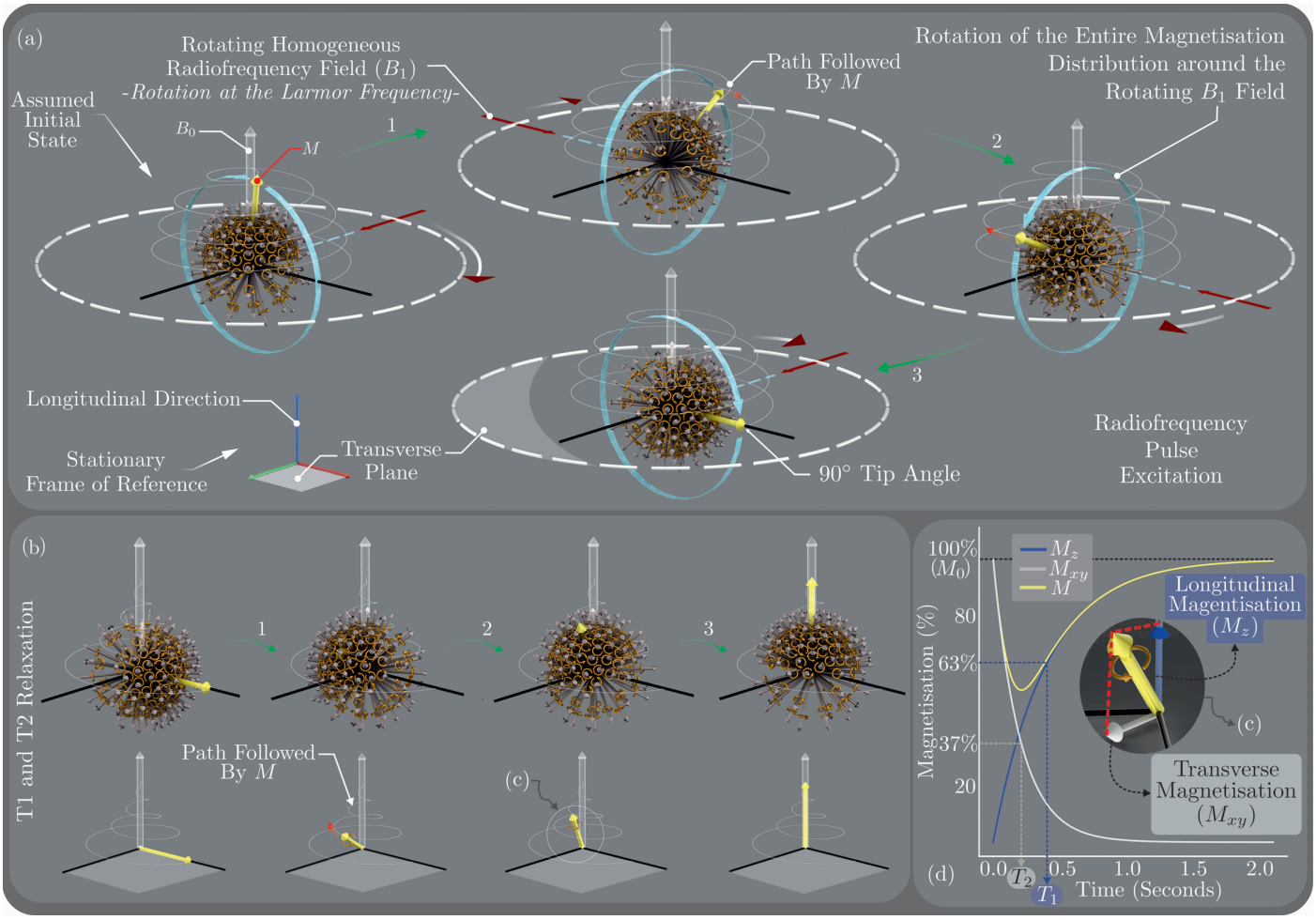



**Figure 2.7: MR Physics (II):** (a) RF Pulse Excitation: When a rotating homogeneous RF field, denoted by $B_1$ , is applied perpendicular to $B_0$, the entire magnetisation distribution, is tipped away from its initial alignment with $B_0$ ($90°$ in this example). Simultaneously, the magnetisation distribution slowly rotates around the rotating $B_1$ axis (indicated by the blue circular arrow). Notes: The path followed by $M$ is observed from a stationary frame of reference, $B_1$ field does not change the relative orientation of individual MDMs, and the $B_1$ field rotates at the Larmor frequency. (b) After switching off the rotating RF field, $M$ returns to thermal equilibrium (relaxation), i.e. aligning back to $B_0$ direction. The inset (c) is zoomed-in in (d). (d) Plot illustrating the two magnetisation components of $M$, and their corresponding relaxation times. $T_2$ is the time required for the transverse magnetisation ($M_{xy}$) to decrease exponentially to approximately $37\%$ $(1/e)$ of its initial value. Conversely, $T_1$ is the time required for the longitudinal magnetisation ($M_z$) to return to $63\%$ $(1 - 1/e)$ of its maximum value ($M_0$), where $M$ is equal to $M_0$ at equilibrium (i.e. aligned with $B_0$'s direction). $M_{xy}$ is the component detected by the RF receiving coils which gives rise to the MR image. $M_z$ does not contribute to the acquired signals. An important mechanism for the decay in $M_{xy}$ , i.e. $T_2$ relaxation (spin-spin relaxation) is as follows. The MDMs (spins) experience local fields which are combinations of $B_0$ and the fields from their neighbouring protons' MDMs. The variations in local fields lead to different local precessional frequencies, and as a result, the protons' MDMs (spins) fan out in time, thereby reducing $M_{xy}$ . The fanning out of MDMs (spins) is referred to as dephasing. $T_1$ relaxation (spin-lattice relaxation), on the other hand, occurs when a proton exchanges magnetic energy with its external environment (lattice). $T_1$ relaxation also results in $T_2$ relaxation, ensuring that $T_2$ is longer than or equal to $T_1$. Note: The transition in (b) illustrates the overall effect of both relaxation mechanisms.

which makes them intrinsically susceptible to RF-induced heating under MRI, risking thermal injury [141, 146]. The induced heating is a result of standing wave formation along the conductive parts longer than a quarter wavelength, which corresponds to approximately $12\text{cm}$ in humans at 1.5 Tesla. To prevent RF induced heating, researchers explored using (extruded) PEEK-based passive [147] (Figure 2.9c) and deflectable guidewires (Figure 2.9d,e) [148]. In

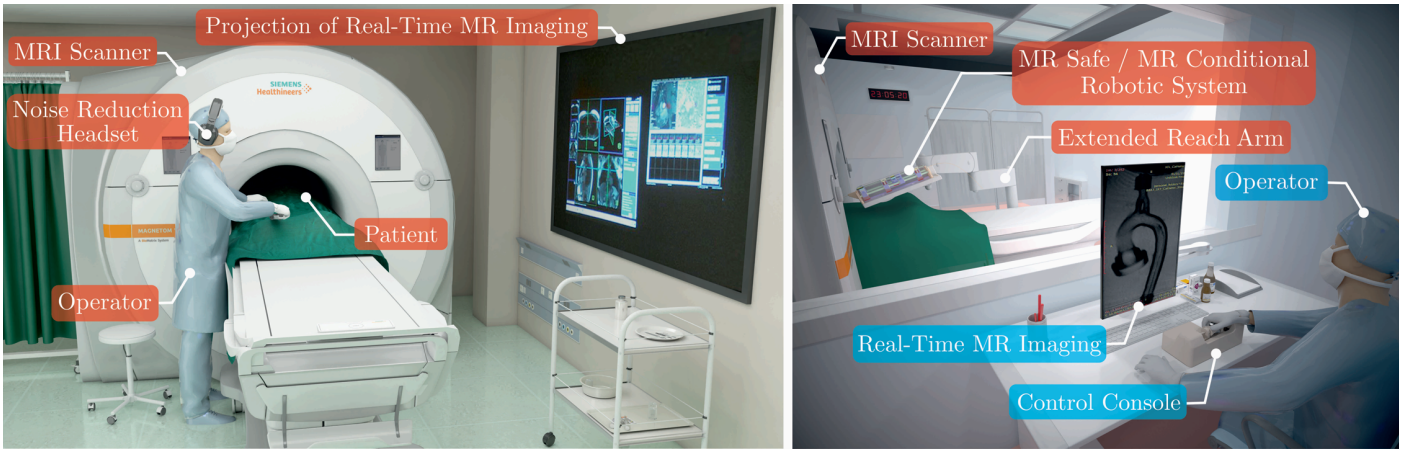



**Figure 2.8:** (Left) Hands-on MR-guided intervention: The operator manipulates the instruments manually with real-time MR images projected onto a screen inside the scanner room. Operators, staff, and patients wear noise reduction headsets to protect their hearing from the loud noises produced by the scanner's gradient coils [139]. (Right) Robotic-assisted MR-guided intervention: The operator uses a control console to remotely operate an MR safe/MR conditional robotic system which in turn manipulates the instruments. The operator can view the real-time MR images on the screen located in the scanner's control room [125].

other instances, researchers repurposed a microcatheter by filling it's lumen with a low-viscosity resin microparticle compound to form a polymer-based guidewire [146]. Although simple in terms of construction, polymer only-based guidewires have lower bending stiffness when compared to their metallic counterparts [147]. This drawback led to the development of glass fibre-reinforced polymer-based guidewires which were found to have improved mechanical properties (i.e. improved kink resistance, flexural and torsional stiffness) [149–152]. In [138, 150, 153], Kos et al. fabricated a glass fibre-reinforced PEEK core, a soft tip, polyurethane jacket and a hydrophilic coating. They utilised the (thermoplastic) micropultrusion process to fabricate the core material of the guidewire (Figure 2.9a,b). To achieve the desired distal end flexibility (soft tip), they grounded the core to a desired profile. The guidewire was evaluated *in-vitro* and *in-vivo* under MR-guidance to demonstrate feasibility for stenting of iliac and supraaortic arteries [138], renal artery angioplasty [150], and percutaneous transluminal aortic stenting and cava filter placement [153]. In [151], Krueger et al. fabricated a similar guidewire with a glass fibre-reinforced core wire. Instead of PEEK as the base material for the micropultrusion process, they used epoxy (thermoset micropultrusion). For distal end flexibility, the core wire was later attached to a nitinol soft tip ($10\text{cm}$ in length) and covered with a polyurethane jacket. This cover served as a base for coating the guidewire with a hydrophilic, biocompatible polymer [151]. The guidewire was evaluated in 5 pigs under MR-guidance by catheterising the carotid and renal arteries, segmental arteries of the kidneys, the contralateral inguinal artery, and the left ventricle. Several other interventional applications were also investigated such as balloon dilation, stent deployment and embolisation of small blood vessels [154]. To further evaluate its efficacy and safety, the guidewire was utilised to perform 20 cardiac interventions in 5 female domestic pigs, and 2 MR-guided balloon dilation of the pulmonary valves of two patients (a child and an adult) with congenital heart diseases (pulmonary valve stenosis). The preclinical and first-in-man trials results were encouraging, with no procedural complications for both patients [152]. It was subsequently realised whilst performing additional clinical trials that glass fibre-reinforced guidewires were prone to fracture during intervention as experienced by Pushparajah et al. [155].

The risk of guidewire fracture led to the development of not only new fibre composites, utilising both glass and aramid fibres (Kevlar®), but also new manufacturing technologies based on micropultrusion, i.e. micro-pullwinding




**Figure 2.9:** MR Guidewires (I): (a) Guidewire consisting of a glass-fibre reinforced PEEK core covered with a polyurethane jacket. The core is grounded at its distal end to create a flexible distal end. (b) Cross-sectional (inset) of the micropultruded glass-fibre reinforce PEEK core [138, 150, 153]. (c) Guidewire comprising a PEEK core with iron microparticles embedded in the polymeric coating [147]. (d) Steerable guidewire composed of a flexible PEEK shaft, a deflectable tip and a Dyneema® pull-wire travelling through the entire guidewire. The steerable tip is a re-purposed 2.4Fr microcatheter (flexible tube) embedded with a flattened nitinol rod to straighten the tip and to constrain its bending in one direction. At the very distal end of the guidewire is a PEEK cap. The entire body is covered with polyethylene heat shrink tubing to hold all the components together. (e) Pulling of the pull-wire results in the bending of the deflectable tip [2, 148]. (f) Guidewire constructed using short nitinol rod segments (guidewire shaft) and a tapered nitinol rod with a long coil mounted onto it (flexible distal end). The distal end is jacketed with a non-braided thermoplastic polymer and the entire body is covered with a soft polymer. (g-h) Zoom-in cross-sectional (inset) of the guidewire shaft which consists of nitinol rod segments (grey) joined by nitinol connectors (blue) with notched ends. For electrical insulation, the nitinol rod is coated with a thin film of parylene and jacketed with PEBAX ® to achieve a consistent profile (between rods and connectors) [156]. *MRI markers are passive negative markers.

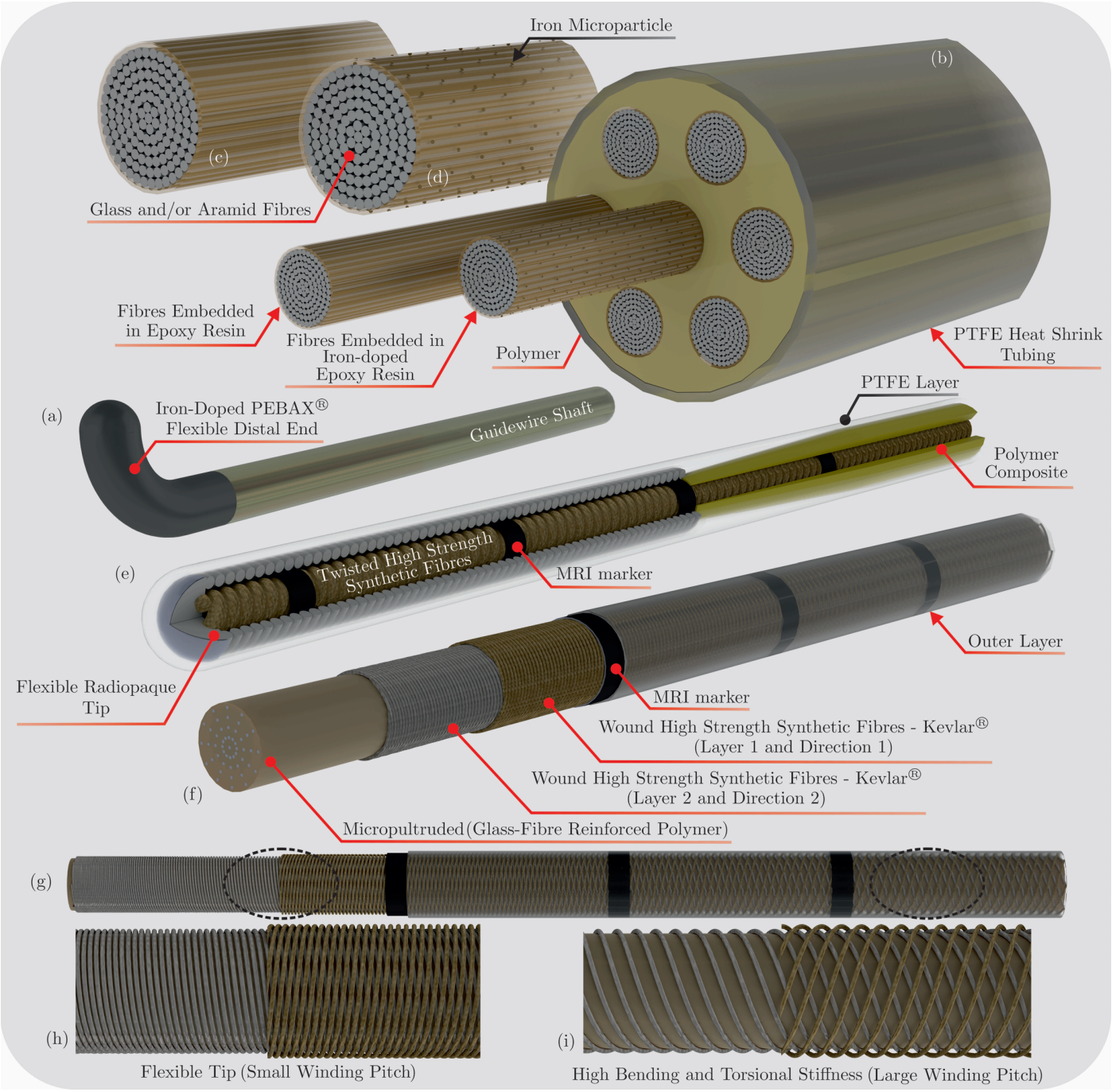



**Figure 2.10:** MR Guidewires (II): (a) Stiff MaRVis guidewire comprising of a shaft and an iron-doped PEBAX® flexible distal end. (b) Cross-sectional zoom-in (inset) of the shaft that consists of micropultruded glass and/or aramid fibres embedded in epoxy resin and in certain cases iron-doped epoxy resin for MR visibility (referred to as MaRVis rods). To construct the guidewire shaft, several MaRVis rods are arranged and embedded in a polymer matrix and are subsequently covered with a PTFE heat shrink tubing. (c) Further zoom-in (inset) of a MaRVis rod. (d) Further zoom-in (inset) of a iron-doped MaRVis rod [157, 158]. (e) Guidewire consisting of twisted high strength synthetic aramid fibres, surrounded by rings of passive negative markers for MR visibility (placed at discrete points) and a polymer composite to provide the desired mechanical performance. At the distal end, a flexible radiopaque tip is mounted at the tip for enhanced tip visibility. The entire body is covered with a PTFE heat shrink tubing. In [159, 160], instead of the coil and PTFE layer, the tip section was coated with PEBAX® and the guidewire was coated with a hydrophilic polymer. (f-g) Guidewire comprising a micropultruded glass-fibre reinforced core wrapped and consolidated with additional layers of high strength synthetic fibres. Passive negative markers are applied at discrete intervals for MR visibility and an outer layer is utilised to form the guidewire. (h) Flexible tip achieved by small winding pitch and (i) High bending and torsional stiffness of guidewire shaft achieved by large winding pitch [161].

[161]. (Micro)pultrusion is a scalable process which allows for the production of fibre-reinforced composite material [151]. Depending on the base material to be reinforced, pultrusion can be further classified into the conventional thermoset pultrusion and thermoplastic pultrusion [162]. The process of thermoset pultrusion commonly starts by unwinding the fibres from spools, followed by pulling the fibres into a resin bath (e.g. epoxy) that saturates or wets out the reinforcement. The wet out reinforcements are then pulled into a heated pultrusion die to cure the finished part. Thermoplastic pultrusion on the other hand, involves the pulling the fibres into a pre-heated unit comprising the melt thermoplastic resin, followed by a die to consolidate the fibre/resin mass. The consolidated fibre/resin is then passed through a cooling device to ensure a dimensionally stable end product [162]. In attempt to manufacture guidewires with different mechanical properties along its length, the Fraunhofer IPT team developed the micro-pullwinding process [161], a process combining both pultrusion and filament winding. In this process, the pultruded profile (using glass fibres) is wrapped and consolidated with additional layers of high-strength synthetic fibres (e.g. Kevlar®) in several winding units to significantly enhance its torsional and radial stiffness (Figure 2.10f,g,h,i) [161]. Moreover, since glass fibres are susceptible to buckling, the wound layers provide protection in the case of accidental fracture. This process led to the development of a commercially available MR conditional guidewire EmeryGlide™ (Nano4imaging, Düsseldorf, Germany). The EmeryGlide™ comprises a high strength core composite of glass fibres and polymers, protected by a double winding of aramid fibres embedded in polymer. The full body is covered by a PTFE sleeve to minimise intravascular friction to protect the tip and shaft from breakage. To proof feasibility, Reddy et al. used the guidewire in a pilot study performing real-time interventional cardiac magnetic resonance (iCMR) in a 1.5 Tesla system on 34 patients, with a success rate of 91% (31/34) [163]. In an attempt to mitigate the lack of MR compatible instrumentation, Nano4imaging recently signed a US distribution agreement with B. Braun Interventional Systems Inc. to sell their MR conditional guidewire to the US market.

Simultaneously, Wolska-Krawczyk et al. used an MR conditional guidewire (EPflex, Dettingen an der Erms, Germany) to examine its heating and safety when compared to a standard nitinol guidewire (Figure 2.10e). The MR conditional guidewire used consisted of (twisted) high-strength aramid synthetic fibres along its longitudinal axis, surrounded by a bending-resistant high performance polymer composite and a PTFE layer. The tip section is conically tapered to create an atraumtic, and a radiopaque flexible tip [159, 160]. Their investigation showed insignificant temperature elevation during near-real-time MR sequences. A preclinical in-vitro (phantom) study was performed using the same guidewires to test the feasibility of a developed framework for guiding endovascular interventions in MR environments [164]. Further, a recent iteration of the EPflex MRLine guidewire was employed in the evaluation of an MR conditional cardiac phantom [165]. The phantom was developed as a training platform for interventional CMR procedures. The EPflex guidewire was also used in a comparative in-vitro study with X-ray fluoroscopy to evaluate its efficacy [166]. Five EPflex guidewires were used alongside one EmeryGlide™ guidewire in the right heart catheterisation of 6 patients (out of 50 patients in total) to investigate the association between catheterisation time and hemodynamic parameters in an MR setting [167].

The drawback of using polymeric materials is the poor visualisation and localisation in MRI environments due to their low magnetic susceptibility [135]. In order to visualise the previously described guidewires, passive negative markers are commonly employed. In the negative contrast approach, the incorporated materials or added markers make guidewires visible by introducing localised magnetic field inhomogeneities which lead to the dephasing of adjacent proton spins and a local signal void (susceptibility artefact) on an MR image [168, 169]. The common method adopted by research groups and guidewire manufacturers involves the gluing or adhering (super)paramagnetic iron

oxide microparticles embedded in curable resin at different (discrete) points along the length of the guidewire to provide better MR visibility. However, as indicated in [167], one of the limitations of using such discrete markers, is the inability to visualise the whole length of the guidewire as clinicians would normally do in a fluoroscopy setting. Moreover, this limitation is overcomed by the continuous visualisation of the MR Safe MaRVis guidewire (MaRVis Interventional GmbH, Krün, Germany), as a result of the centrally localised passive negative iron microparticles along the guidewire's length (Figure 2.10a,b,c,d). The MaRVis guidewire comprises several thin rod-shaped composite material (MaRVis rods) embedded in a polymer matrix and covered by a PTFE sleeve. These micropultruded rods are composed of non-metallic filaments (e.g. glass and/or aramid fibres) impregnated by a high temperature resistant epoxy resin. For continuous MR visibility, some of the fibres are impregranted with epoxy doped with iron microparticles. The iron-doped rods tend to be placed at the centre of the guidewire to limit the size of the artefacts [157]. The MaRVis guidewires were thoroughly evaluated in-vitro (phantom models) and in-vivo [7, 158, 170]. The preliminary results reported by the three studies showed that the usage of the MaRVis guidewires in MR-guided interventions is technically feasible and safe in swine models and potentially, in humans.

Alongside these promising MR guidewires developments, Basar et al. proposed using a segmented-core nitinol device construction, where they maintained less than one-quarter wavelength at 1.5 Tesla, which eliminates standing wave formation, and the possibility of RF heating along the shaft [156]. The guidewire's core consists of a $10\text{cm}$ PEBAX®-coated nitinol rod segments joined by $5\text{mm}$ connectors for stiffness matching. The shaft of the segmented-core assembly was covered by a liquid crystal polymer (Vectran™) fibre-braided polyimide tubing to enhance the guidewire's pushability, torque response, kink resistance, and dielectric properties. For the distal end, a tapered nitinol rod was employed, with a coaxially placed $3\text{cm}$ support Nickel-Cobalt-Chromium-Molybdenum Alloy coil ((MP35N alloy), Heraeus, Minnesota, USA) to enhance the tip's flexion and recoil [156]. The distal end was covered by a non-braided thermoplastic polymer to ensure softness and flexibility. The guidewire was visualised under MR by placing passive negative iron oxide markers at $10\text{cm}$ intervals. The entire guidewire assembly was then covered by a thermoplastic jacket to avoid blood contact and to achieve a standard outer diameter of 0.035" (Figure 2.9f,g,h). To compare the MR segmented guidewire with a commercial nitinol guidewire, the MR guidewire was mechanically characterised and test in-vitro and in-vivo in an MR setting. The passive guidewire exhibited similar mechanical behavior to its commercial counterpart, with a significant drop in guidewire heating from $13°$ to $1.2°$ [156]. Table 2.2 provides an overview of the materials employed in the construction of the previously described MR safe and MR conditional guidewires.

*Selective Catheters:* To prevent RF induced heating in selective catheters, researchers explored substituting metal braids with non-metallic, non-conductive polymeric braids, such as aramid fibres (e.g. Kevlar® [7]) in selective catheters. As in the case of guidewires, replacing metallic braids (Figure 2.4c) may also result in the reduction of the overall mechanical performance (flexibility, torquability, pushability) of catheters [171], and limit their appropriateness for interventions. Similar to the previously described nitinol rod segmentation approach [156], Yildirim et al. proposed a promising alternative technique to modify braided selective catheters by creating discontinuities within the insulated metal wires to limit RF induced heating while preserving their mechanical properties and kink resistance [141].

**Table 2.2:** Materials used for constructing guidewires for MR-Guided Interventions. Markers: Passive Negative Marker (PN), Passive Positive Marker (PP), Semi-Active Tracking (SA), Indirect Active Tracking (IA), Direct Active Tracking (DA)

| | Ref | Materials Used (Function) | Marker |
|---|---|---|---|
| MR Guidewires | [160] | Distally tapered PEEK rod (core), Synthetic material embedded with iron microparticles (coating) | PN |
| | [148] | **(Proximal Shaft)**: PEEK Tube (core), Polyehtylene (PE) heat-shrink (outer layer), **(Distal End)**: Repurposed 2.4 Fr micro-catheter (steerable tip), Flattened nitinol rod (Straighten the tip & Constrain bending to one plane), **(Entire Guidewire)**: Dyneema (pull-wire)† | PN |
| | [149] | Glass fibre-reinforced guidewire | PN |
| | [138, 150, 153] | Distally tapered, micropultruded glass fibre-reinforced PEEK rod (core), Polyurethane (jacket), Hydrophilic polymer (coating) | PN |
| | [151, 152] | **(Proximal Shaft)**: Micropultruded glass fibre-reinforced epoxy rod (core), **(Distal End)**: Cone shaped nitinol wire (flexible distal end), **(Entire Guidewire)**: Polyurethane (jacket)†, Hydrophilic biocompatible polymer (coating) | PN |
| | [161] | Micropultruded glass fibre-reinforced polymer (core), Wrapped and consolidated Kevlar fibres using the filament winding process (protection from accidental fracture and enhancing torsional/radial stiffness) → Nano4imaging employs a similar construction in their EmeryGlide™ guidewire | PN |
| | [159, 160] | Twisted high-strength aramid synthetic fibres (core), Distally tapered bending-resistant high performance polymer composite (core support), PTFE heat-shrink tubing (outer layer), Radiopaque flexible tip (tip visibility) → EPflex employs a similar construction in their MRLine guidewire | PN |
| | [157, 158, 170] | Micropultruded rod-shaped composite material (aramid/glass fibre), polymer matrix, PTFE heat-shrink sleeve (outer layer), **(Distal End)**: PEBAX® embedded with iron microparticles → MaRVis Interventional GMBH employs this construction in their MaRVis guidewires | PN |
| | [156] | **(Proximal Shaft)**: $10\text{cm}$ PEBAX®-coated nitinol rod segments joined by $5\text{mm}$ nitinol rod segments for stiffness matching (core), Liquid crystal polymer (Vectran™) braided polyimide tubing (jacket), **(Distal End)**: Tapered nitinol rod (flexible tip), Nickel-Cobalt-Chromium-Molybdenum Alloy coil (enhance tip's flexion and reocil), Non-braided thermoplastic polymer (jacket) | PN |
| | [172] | **(Proximal Shaft)**: Laser cut nitinol hypotube (outer tube), **(Distal End)**: Copper solenoid coil (tip tracking) **(Entire Guidewire)**: Nitinol rod (core and loopless antenna), Polyimide tube (accommodate temperature probe), PEBAX® tube (first insulation cover), PEBAX® tube (Outer insulation layer) | IA |

## 2.3.4 Steerable Catheters

In parallel to the advancements in MR guidewires and MR selective catheters, a plethora of work has been conducted in the field of "MR safe" and "MR conditional" steerable catheters for MR-guided interventions. The following summary of findings is classified based on the actuation mechanism. The summary will cover the steerable catheters developed both for guiding intravascular devices and for the treatment of atrial fibrillation (electrophysiology). In addition, Table 2.3 provides an overview of the materials employed in the construction of the following steerable catheters.

### 2.3.4.1 Pull-wire Driven

Pull-wire Driven steerable catheters are generally constructed from a stiff shaft and a compliant distal end. To steer the distal end, high strength, polymeric pull-wires are incorporated in the catheters, travelling from the proximal end through the stiff shaft to the flexible distal end. The push/pull movement of the pull-wires causes the tip to deflect. The simplest form of pull-wire driven catheters is demonstrated by Bell et al., where they developed a uni-directional pull-wire driven steerable guiding catheter. Their catheter is composed of a proximal shaft with Kevlar® braiding encapsulated between an inner PTFE liner and an outer thermoplastic polyurethane (Pellethane®) layer. For the distal end, they used a 5cm nitinol laser-cut hypotube supported by a nitinol spring to provide kink resistance and to help restore the distal end shape upon release of the 0.38mm Kevlar® pull-wire (Figure 2.11a). To form a unitary catheter, the entire assembly was covered by PEBAX® tubing. The catheter was controlled using a

custom-made 3D printed manual handle, which incorporated a distal end shape locking mechanism. In addition to mechanically assessing their catheter, they investigated three MR visualisation strategies (in-vitro and in-vivo); with active tracking providing the best visibility [173]. Yao et al. followed a similar catheter construction to [173], where they utilised a nylon braided shaft glued to a nitinol-supported PTFE deflectable distal end. To steer the distal end, a 0.5mm carbon fibre rod travelling from the manual handle through the shaft is glued to a thinner (0.25mm) carbon fibre wire travelling from the shaft's distal end to the tip of the deflectable section (Figure 2.11b). They benchmarked their catheter's mechanical performance alongside three commercial MR unsafe ablation catheters by performing in-vitro flexibility, torquability and pushability tests. Furthermore, they attempted a preliminary MR compatibility test by placing the catheter in a contrast-enhanced medium [174].

A drawback of steerable catheters with single deflectable segments is their inability of mimicking the shapes of commonly used pre-curved selective catheters, such as Headhunter1 (H1), Sos Omni, Simmons2 (SIM2), Judkins Right 4 (JR4) and Renal Double Curve (RDC). Such selective catheters have primary, secondary and in some instances tertiary curves formed onto their distal ends to facilitate navigation through the aortic arch and subsequent blood vessels. Figure 2.4i illustrates the two curves of a Judkins right catheter. To tackle this challenge, Clogenson et al. proposed a steerable catheter with two independent deflectable sections which can be manually controlled using four ultra-high molecular weight polyethylene Dyneema® pull-wires [2, 175]. The catheter was constructed using a monolithic approach, where a subtractive manufacturing method was employed to laser profile the distal end of an inherently stiff extruded polymeric tube (polyether ether ketone (PEEK)). Thereby, creating an articulated structure where the links or hinges of the structure are interlocked and move with respect to each other when the pull-wire is pulled (Figure 2.11c). In order to better visualise the catheter under MRI, paramagnetic iron oxide microparticles (1-6$\mu$ m) were glued at three different points along the distal end of the catheter. The handle/catheter assembly was evaluated in-vitro in a 1.5 Tesla MRI scanner, and in-vivo in a 3 Tesla MRI scanner. As reported in [2, 175], the main limitation of their design is the difficulty in controlling the two segments independently, i.e. steer one segment without involuntarily moving the other. This is caused by the change in length of a segment's pull-wire when the other segment is being steered. One way to avoid such undesired motion would be to compensate for this change with the manual control handle.

In line with robotic endovascular interventions, an alternative design was proposed where two catheters, each with its own single deflectable segment are placed over one another, referred to as "concentric or telescoping catheters." This method not only improves controllability, it also increases the number of degrees of freedom (DOF) [176]. Due to the unavailability of an MR compatible embodiment, the only example of this type is the fluoroscopy-guided Magellan 9Fr and 10Fr robotic catheter systems (AurisHealth, Redwood city, CA, USA). The 9Fr version released 2012, consisted of an inner leader catheter and an outer guide catheter. The leader catheter consists of four pull-wires articulating the single distal segment in two directions (bi-directional) and accommodates a standard 0.035" guidewire. Similarly, the guide catheter is bi-directional and fits around the leader catheter. With this configuration, both catheters are independently and collaboratively controlled to recreate the shapes of common selective catheters (Figure 2.12a).

For MR-guided robotic endovascular interventions, Ataollahi et al. explored the benefits of additive manufacturing by 3D printing steerable catheter distal ends (Figure 2.12b). Their design comprised clockwise and counterclockwise helical segments employed in an alternating fashion [177, 178]. A distinctive feature of helical structures is the possibility of adjusting the stiffness of the deflectable distal end by tensioning all pull-wires simultaneously. To

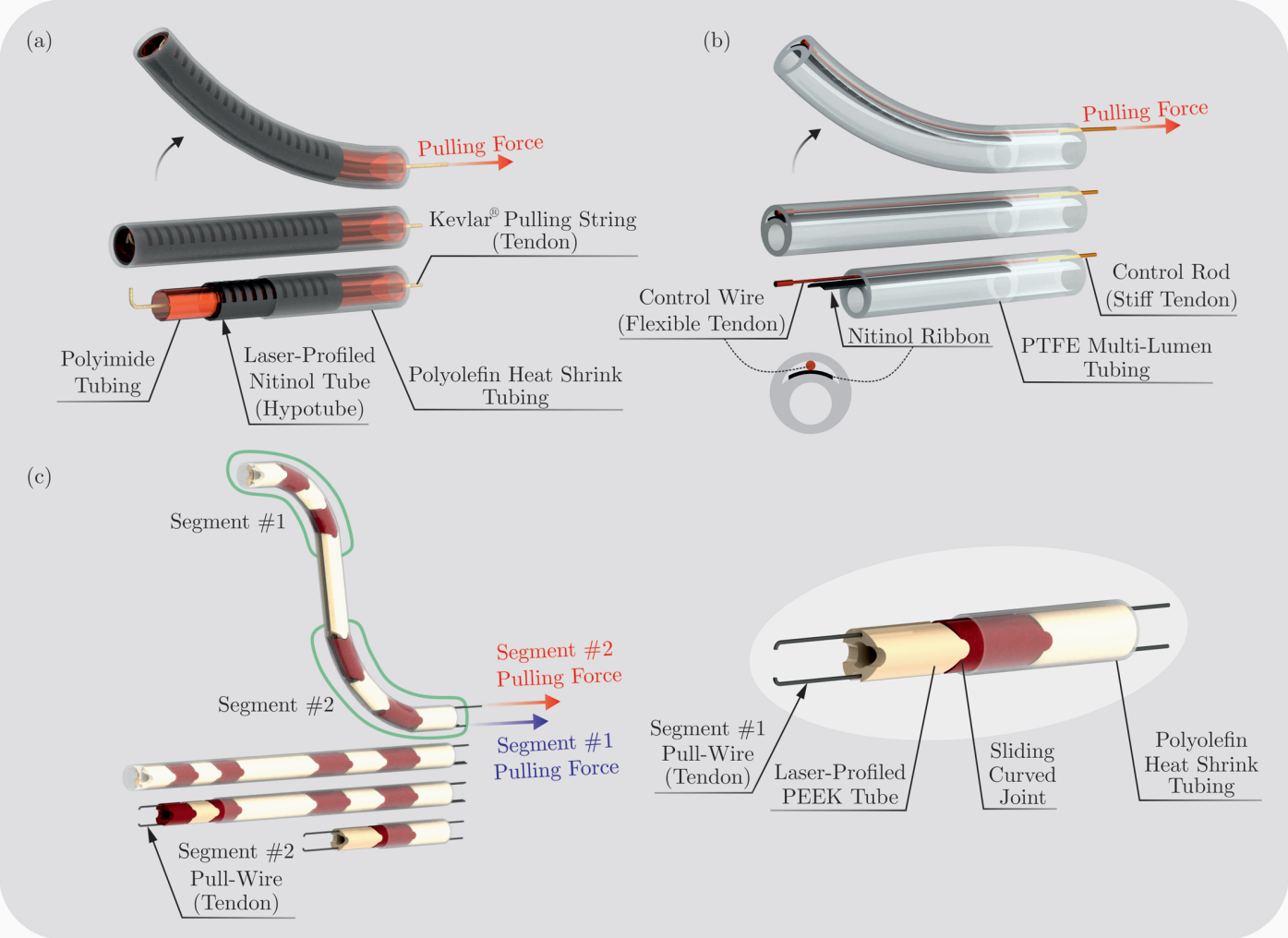



**Figure 2.11: (Manual) Pull-wire Driven Catheters for MR-guided interventions (I)** (a) A uni-directional catheter inspired by Bell et al.'s design: The deflectable distal end consists of a nitinol laser-cut hypotube, connected to a Kevlar® pull-wire. In the case of Bell et al., a nitinol spring was concentrically added to the laser profiled tube [173]. (b) Yao et al.'s uni-directional steerable catheter: A nitinol supported PTFE tube was used as the deflectable distal end. A control wire glued to a control rod was used for steering [174]. (c) Clogenson et al.'s multi-selective catheter: The design comprises a laser profiled PEEK tube with four pull-wires travelling through the entire catheter length. The first pair of pull-wires control segment#1 and the second pair of pull-wires control segment#2. In terms of joint design, a sliding curved joint was utilised to form the articulated deflectable segments [2, 175]. Note: The catheter is made from a single material, however, different segment colours (red and beige) are used only used for illustrative purposes.

evaluate the deflectable segment's workspace and positioning accuracy in 3D space, the prototype was connected via four UHMWPE Spectra® pull-wires to an "MR unsafe" robotic system. Further, in-vitro tests were performed to evaluate the segment's MR-compatibility and visibility.

### 2.3.4.2 Hydraulic

Hydraulically driven catheters (HDCs) are controlled by single or multiple pressurised tubes that run to chamber(s) of a soft and flexible distal end. Once a chamber is pressurised with fluid (e.g. saline), the catheter's distal end bends accordingly. Although not clearly stated by some of the authors who developed HDCs [179, 180], these catheters are good candidates for MR-guided interventions, due to the absence of "MR unsafe" components in most of their constructions. Haga et al. developed a $0.94\text{mm}$ diameter uni-directional HDC by using a laser profiled nitinol tube

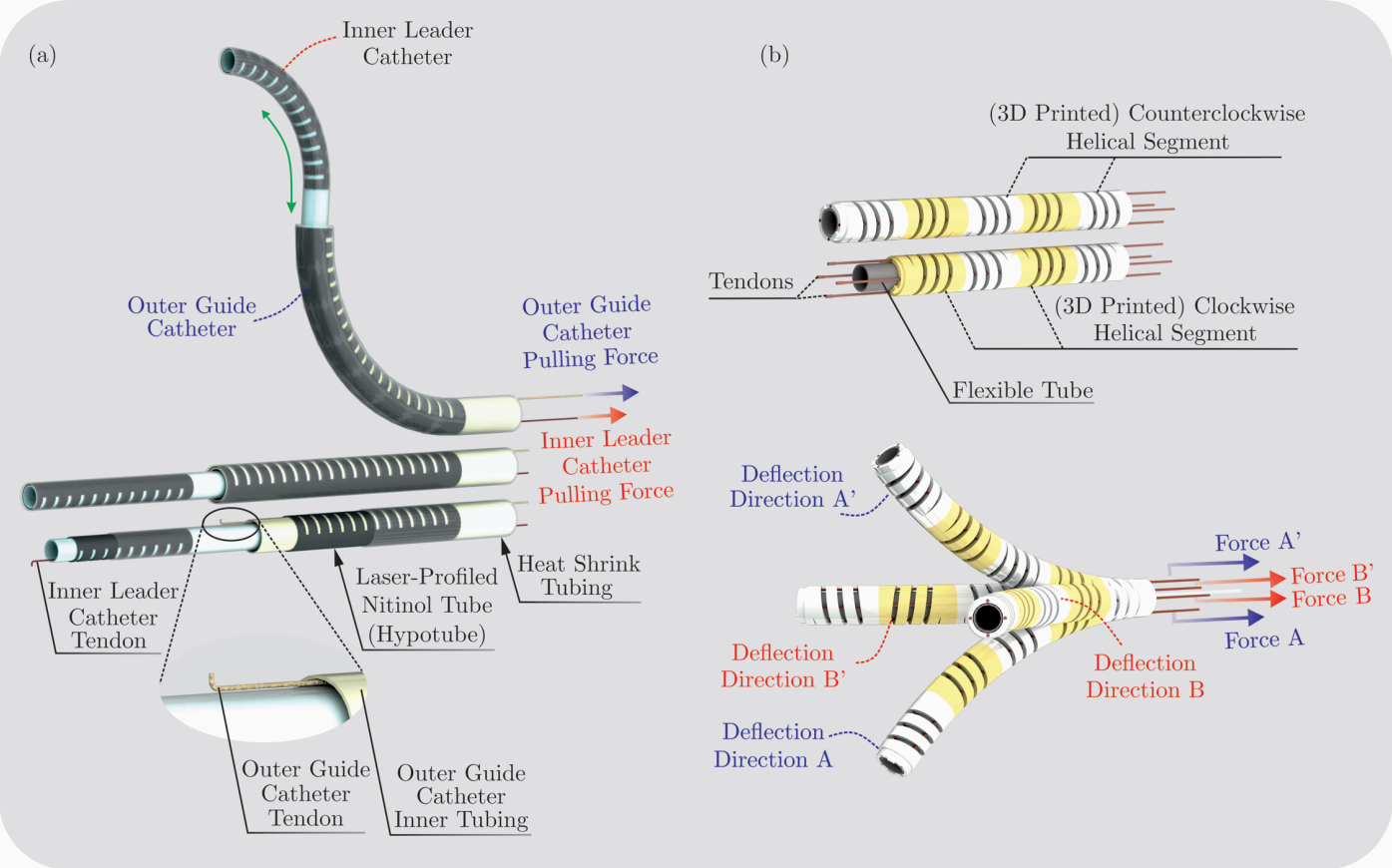



**Figure 2.12: (Robotic) Pull-wire Driven Catheters for MR-guided interventions (II)** (a) Simplest form of concentric or telescopic catheters: The system consists of two uni-directional catheters (inner leader catheter and outer guide catheter) which are controlled independently and collaboratively to recreate the shapes of common selective catheters. (b) Ataollahi et al.'s additively manufactured deflectable catheter: The design consists of clockwise and counter-clockwise helical segments employed in an alternating fashion (illustrated in yellow and white). To control the distal end in 3D space, four polymeric pull-wires were utilised [177, 178].

covered with a thin silicone rubber tube and connected to a $2\mathrm{m}$ long PTFE tube [179] (Figure 2.13a). They controlled the bending angle of the distal end by changing the negative pressure of the water in the catheter. Ikuta et al. developed a "single-input, multi-output" control mechanism to bend a multi-segment distal end [180–182] (Figure 2.13e). Their catheter's distal end consisted of serially placed, independently valve-controlled bellows. Stereolithographed band pass valves (BVPs) were fabricated to control the fluid flow between the single pressurised-tube and the bellow it is attached to. Each BVP's inner pressure range is set at a unique value to enable independent control of each segment. To bend a specific segment, the target valve is opened by increasing the pressure of the tube until it reaches the activation pressure band of the walls of the deflectable segment, each filled with a pressurisable fluid (Figure 2.13b). Changing the inner fluid pressure creates bending in a specific direction [183]. Actuation using inflatable balloons attached to the internal [184] (Figure 2.13d) and external [185] (Figure 2.13c) surfaces of the catheter's deflectable segment have also been proposed. Caenazzo et al. proposed multi-functionalising the fluid used within the chamber of a 3D printed deflectable segment (inspired by Haga et al.'s design) [186]. In their preliminary study, they employed conductive fluids (hypertonic saline solution) to replace the low-impedance wires used in steerable diagnostic and ablation catheters (Figure 1.1b). This stemmed from the fact that wires tend to heat and cause significant artefacts in MR-environments.

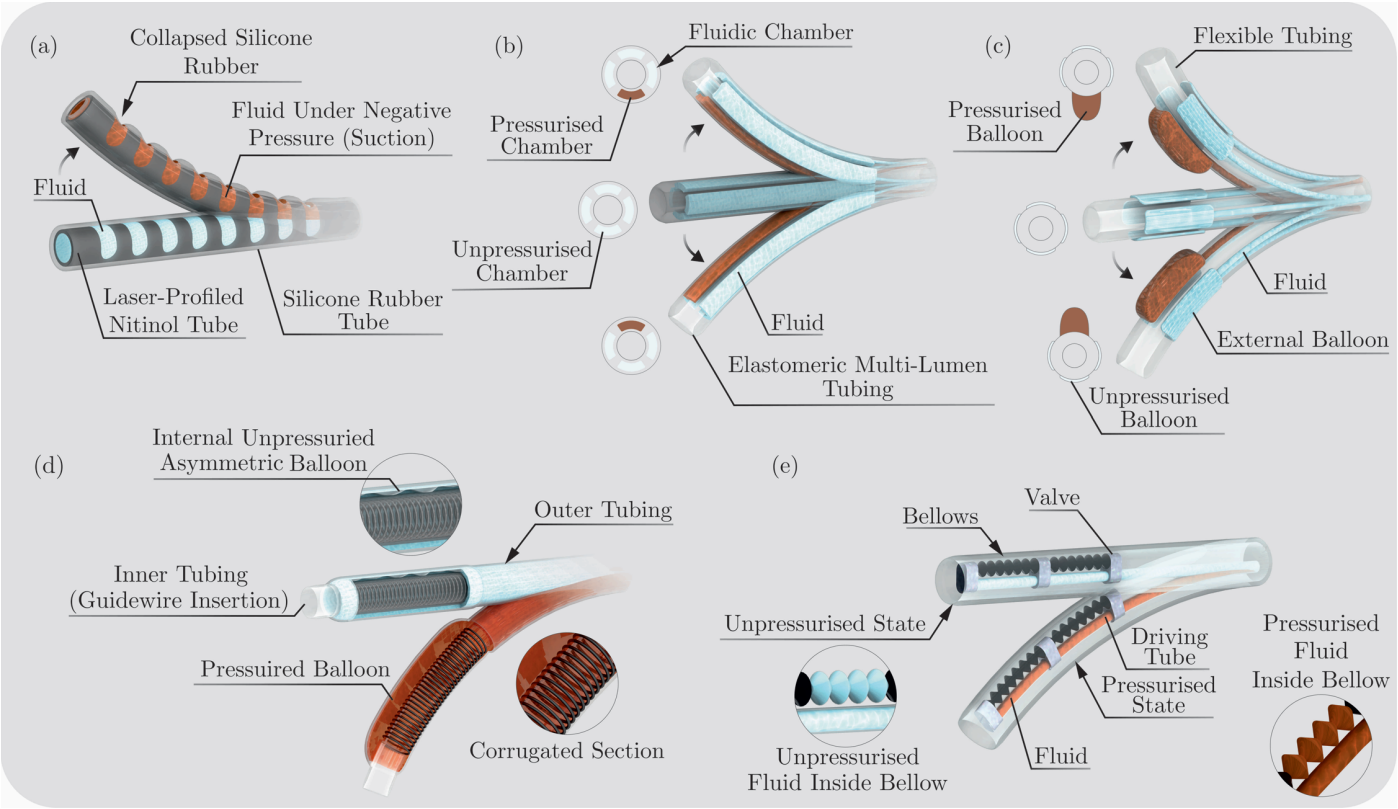



**Figure 2.13: Distal end of Hydraulic Driven Catheters (HDCs)** (a) Haga et al.'s uni-directional HDC: A laser profiled nitinol tube covered with a thin silicone rubber tube is controlled by changing the negative pressure of the fluid [179]. (b) De Boer et al.'s conceptual design of a multi-directional HDC: The distal end comprises a central lumen and four parallel pressurisable chambers. Changing the inner fluid pressure results in the bending of the deflectable tip of the catheter. Note: The figure illustrates deflection in only two directions [183]. (c) Skerven et al.'s conceptual design of a multi-directional (External Balloon) HDC: The deflectable tip consists of four external balloons attached to a flexible tubing. To steer the distal end towards a specific direction, the external balloons are inflated (pressurised) and deflated (unpressurised) accordingly. Similar to De Boer et al.'s design, the figure illustrates deflection in only two directions [185]. (d) Johansen et al.'s conceptual design of an (Internal Balloon) HDC: The distal end includes a corrugated section attached to the inner tube and an asymmetric internal balloon attached to the outer tube. The internal balloon is configured to deflect the distal end of the catheter [184]. (e) Ikuta et al.'s single-input, multi-output HDC: The steerable tip consists of serially placed, independently valve-controlled bellows. To bend a specific segment, the target valve is opened by increasing the pressure of the driving tube until it reaches the activation pressure band of the valve. The figure illustrates the case where both segments (bellows) are actuated [180–182].

### 2.3.4.3 Magnetic

Magnetic actuation is based on the changes in the magnetic field applied to the distal end of catheters having magnetic or electromagnetic elements. However, the previously mentioned remote magnetic navigation systems are inherently incompatible for use in MR-environments [187]. Roberts et al. explored the use of the MRI scanner per se, to steer the distal end of catheters with copper coils wound around its tip [188] (Figure 2.14a). In their design, the coils at the catheter's distal end generate a magnetic field when electric current is passed through it. As a result, when placed in the MRI's strong magnetic field (1.5 Tesla or 3 Tesla), the coiled distal end experiences a turning force or torque to align its magnetic field with the external field of the MRI scanner [188]. To achieve remote control in 3D space and reduce resistive heating, the authors improved their design by fabricating solenoidal microcoils by laser lathe lithography on polyimide and alumina substrates [189, 190]. In [189], in-vitro and preliminary in-vivo tests were performed to evaluate the resistive heating of the microcoils. To further assess their catheter's

feasibility under real-time MR-guidance, in-vitro [191] and in-vivo (renal artery embolisation) [192] studies were performed. In both studies, the tests were compared with standard X-ray fluoroscopy guidance to determine the value of MR-guidance. The results of both studies show that MR-guided navigation is comparable to its fluoroscopy-guided counterpart. Liu et al. proposed a design optimisation process for MRI-actuated catheters based on task and anatomical constraints [193]. In efforts to (semi-)automate catheter ablation procedures, Greigarn et al. developed a mathematical model for MR-actuated catheters and designed a motion planning algorithm to generate desired catheter distal end trajectories [194]. Concurrently, several other groups demonstrated feasibility by using a catheter tip equipped with ferromagnetic spheres (Figure 2.14b, e.g. neodymium NeFeB [195], chrome steel [196, 197], bearing steel SUJ2 [198]) and, in other instances, ferrofluids [195] (Figure 2.14c) instead of the aforementioned microcoils. One of the main challenges behind magnetic actuation is the size of the artefact caused by the presence of a ferromagnetic body within the MRI bore. Moreover, this artefact makes it difficult to visualise the surrounding soft tissue structures [197].

A unique feature of the magnetic actuation, which differentiates it from other actuation mechanisms investigated in this review, is that it does not need physical connection. Thanks to this feature, in addition to the tethered applications, the magnetic actuation also allows remote powering facilitating navigation of untethered objects. While actuation mechanisms of tethered systems can utilise large Lorenz forces, the untethered particles in the absence of current need to rely on gradient pulling forces. This untethered powering of ferrous (ferromagnetic) particles, as stated in the review paper [199], is a great advantage as it allows miniaturisation of the ferromagnetic particles, enhancing the navigation potential under MRI to reach challenging targets or increase efficacy of the procedures. Millimetre size robots encapsulating ferro beads are proposed to introduce orientation-dependent tasks [200, 201] and therapeutics [202, 203]. This gradient pulling actuation method for untethered particles usually targets interventions involving embolisation procedures with the help of the materials loaded to these particles [204–206]. More sophisticated structures involving magnet to magnet interactions for particles that could still be navigated under MRI have been investigated for purposes like drug delivery [207, 208] and tissue penetration [209].

#### 2.3.4.4 Shape Memory Alloys (SMAs)

Shape memory alloys are a unique class of material which exhibit the shape memory effect, an effect which occurs when a material deformed at low temperature reverts to its prior shape upon heating above a temperature characteristic of the alloy at hand [210]. The most prevalent SMAs are the nickel-titanium (nitinol) alloys, which are commonly employed as actuating elements in steerable catheters. SMA actuators can be in the form of microcoils [211–213] (Figure 2.15a), electrochemically etched sheets [214, 215] (Figure 2.15b), wires [216–220] (Figure 2.15c), and laser cut tubes [221–224] (Figure 2.15d). To bend the catheter's distal end, SMA actuators are often placed at an offset from the catheter's central axis in their deformed martensite phase. When the SMA actuators are heated, either by joule, optical or conductive heating, the actuators return (contract) to their high temperature austenite phase. Upon passive cooling, the SMA actuators extend back to their deformed martensite phase. As in the case of hydraulic actuation, most of the previously proposed works do not discuss the potential of MR-guided interventions, although nitinol based SMAs have an acceptable susceptibility artefact. Recently, Sheng et al. developed an SMA actuated steerable catheter to treat atrial fibrillation under MR-guidance [225]. In their design, the distal end of their catheter consisted of multiple bending modules, with each module being actuated by a pair of antag-

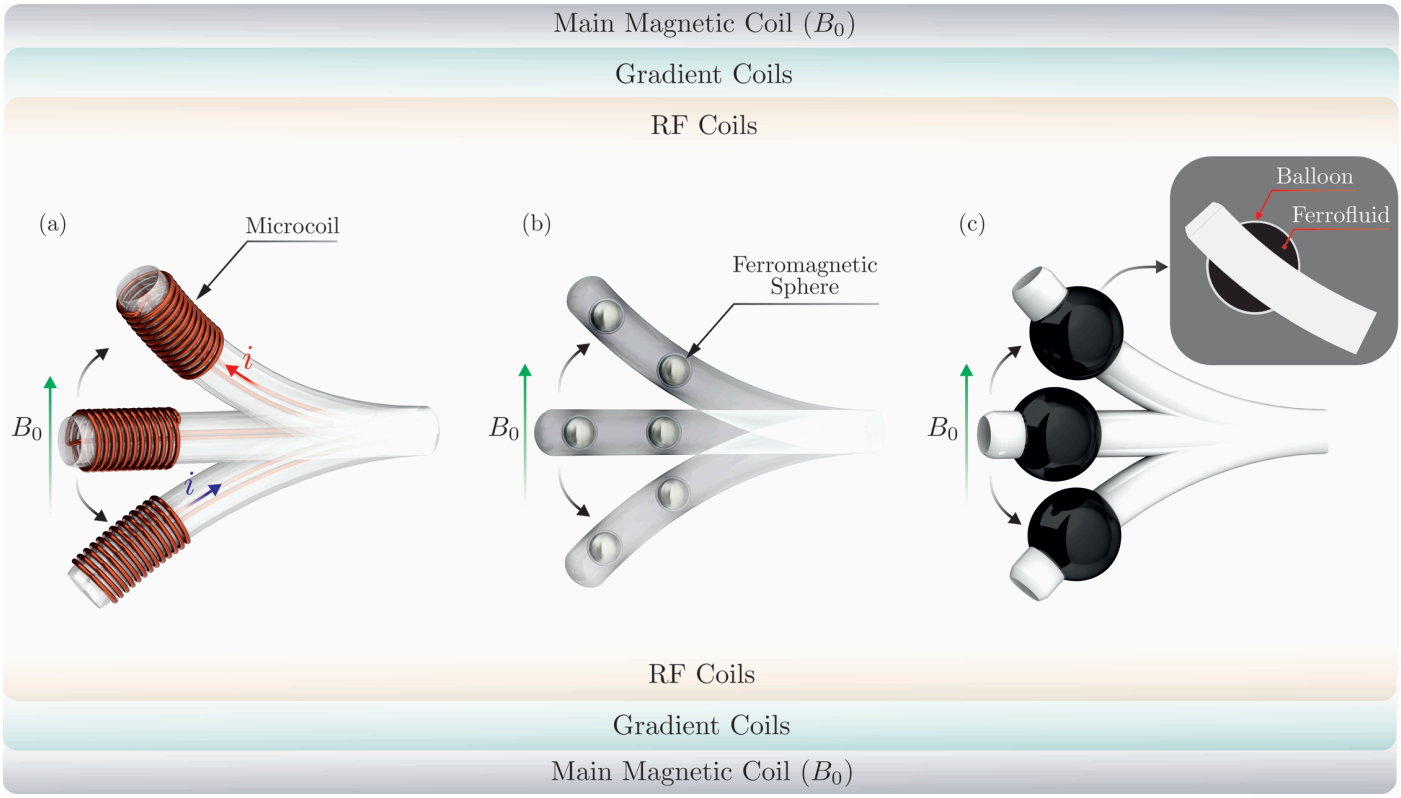



**Figure 2.14: Distal end of MR-actuated Magnetic Catheters** (a) (Simplified, Single Plane) microcoil-based: A microcoil is attached to a flexible tubing. Depending on the direction of flow of current, the distal bend is steered in a specific direction accordingly [188–194]. (b) Ferromagnetic sphere-based: The deflectable tip consists of ferromagnetic spheres [195–198]. (c) Ferrofluid-based: The distal end comprises a balloon filled with a ferrofluid [195]. All three distal ends (a-c) experience a turning force or torque to align its local magnetic field with the external field of the MRI scanner. The distal ends in the figure are placed within the bore of the MRI scanner, indicated by the three main components: Main Magnetic Coil, Gradient Coils and RF Coils.

onistic SMA wires. To actuate the SMA wires, conductive heating was implemented by routing nickel-chromium (nichrome) coils around the SMA wires. The steerable catheter was evaluated by performing in-vitro phantom tests and preliminary MR-compatibility experiments.

### 2.3.4.5 Comparison

Each actuation method has its own set of strengths and limitations. To comparatively assess the aforementioned steering mechanisms, the following categories are considered: steerability and safety. Table 2.4 summarises the comparison.

**Steerability**: Pull-wire driven catheters are generally lightweight, manually controllable and can be swiftly manoeuvred when compared to other methods. Their main challenge lies in the mechanical nonlinearities experienced with an increase in the number of moving components and DOF [21]. Examples of such nonlinearities include friction between pull-wires and their corresponding catheter lumens; and the backlash caused by pull-wire slack and moving components of the pull-wire driving mechanism (e.g. gears). Other challenges include the uncontrolled change in length of pull-wires caused by the passive bending of catheter shafts while manoeuvring through tortuous anatomies. In the case of HDCs, the use of incompressible fluids facilitates the smooth motion and precise control of deflectable segments [226]. Nevertheless, fluidic actuation presents several drawbacks such as slower

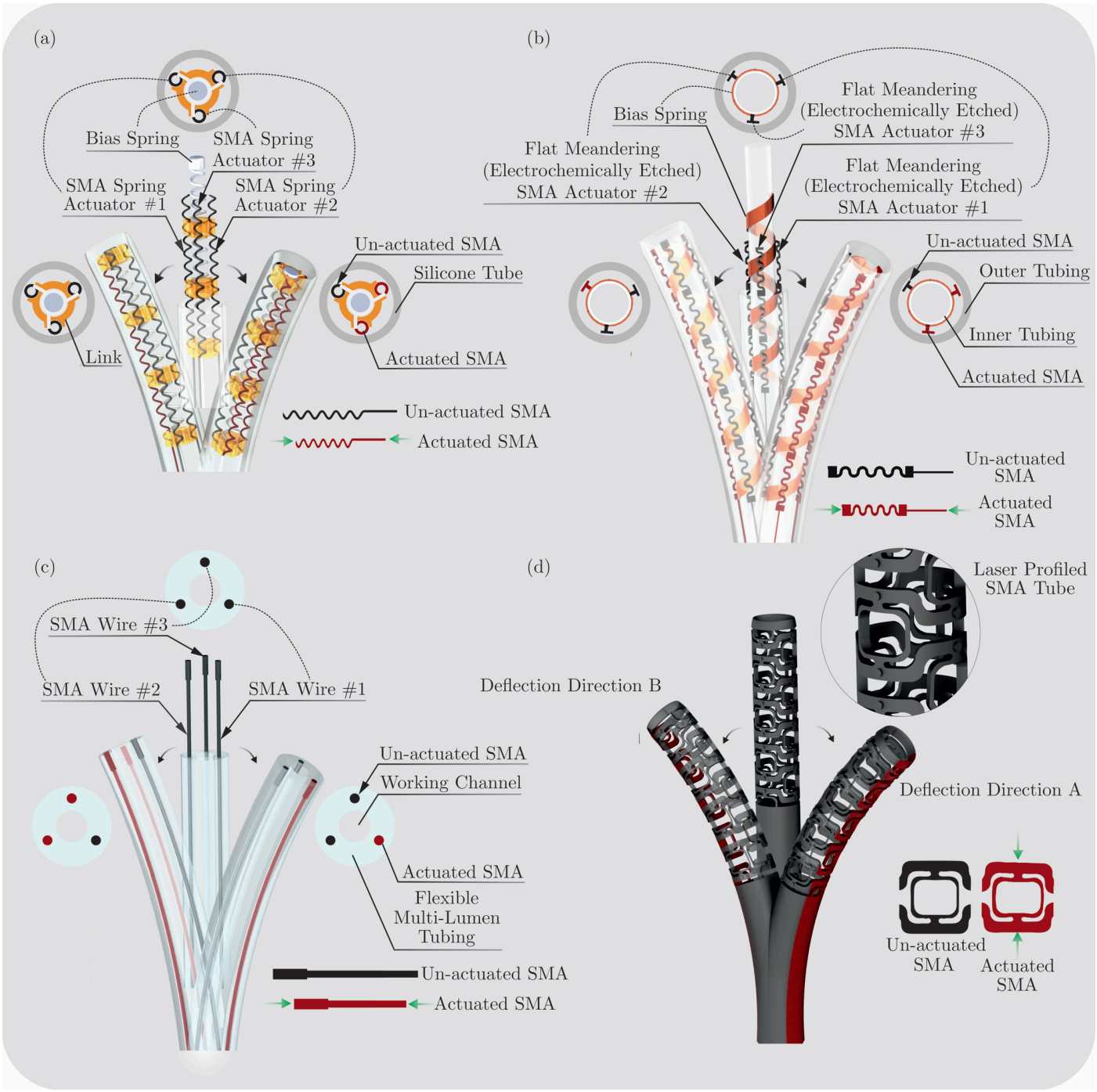



**Figure 2.15: Distal end of Shape Memory Alloys (SMAs) actuated catheters** (a) SMA Microcoils/Springs (Fu et al.'s design): This design comprises three microcoil actuators, a bias spring and links (to fix and integrate the SMA actuators and bias spring). A silicone tube was utilised to cover the entire configuration [211–213]. (b) Electrochemically etched SMA sheets (Mineta et al.'s design): An SMA sheet was electrochemically etched into SMA (flat-spring-like) actuators, which were then attached to a helical bias spring. To form a unitary body, an outer tubing was employed, and inner tubing was added to facilitate the insertion/removal of guidewires and intravascular devices. Namazu et al. utilises similar fabrication and actuation techniques [214, 215]. (c) SMA wires: In this design, a plurality of parallel SMA wires (three or four) are embedded into a flexible multi-lumen tube [216–220, 225]. In all three embodiments of SMA actuated catheters (a)-(c), the actuators are embedded/added in an elongated (pre-loaded) condition and are distributed at an angle of $120°$. When the SMA actuator(s) is heated (illustrated in red), it contracts and results in the bending of the distal end towards a specific direction. (d) Conceptual design of a laser-profiled SMA tube (Langelaar et al.'s design): The distal end consists of laser-cut (or etched) a small diameter SMA tubing. The laser cut patterns facilitate the bending of the distal end in two orthogonal directions. When a specific segment of the tube is locally heated, it contracts, and the distal end bends accordingly [221–224]. In all the four cases illustrated (a)-(d), only two bending directions are shown (for better clarity).

response times when compared to pull-wire driven catheters; the need for equipment like pumps, valves and pipes; the possibility of leakage which can limit the catheter's efficiency [227]; the need for sophisticated control methods [226, 228]; and difficulty in miniaturisation because of the space occupied by the driving fluid. The main strength of magnetic actuation is its ability to "wirelessly" manipulate catheters without the need for mechanical and fluidic components. On the other hand, the difficulty of achieving precise motions, and the need for customised "interleaved" MRI sequences to simultaneously visualise and steer catheters continue to remain as challenges for MR-actuated catheters. SMA actuated catheters show great potential for miniaturization as a result of their large power (work) density, i.e. ability to lift more than 100 times its weight. They are, however, inherently nonlinear materials exhibiting significant hysteresis, which makes it difficult to control them in a repeatable manner [229, 230].

**Safety**: Steering without posing any risk to the physiological processes and causing any complications to anatomical structures is crucial for the adoption and commercialisation of deflectable catheters [21]. The two main sources of safety hazards are the steering mechanism and/or the catheter tracking method. Pull-wire driven catheters, HDCs, and magnetic driven (ferromagnetic spheres) catheters all have the added advantage of not having any long conductive wires, unlike SMA driven catheters, magnetic driven (microcoiled) catheters, and actively tracked catheters. The drawback of having long conductive wires is the risk of resistive heating and RF induced heating. Heating leads to heat stress (inability to control the body's internal temperature), induced current burns and contact burns of body tissues. As summarised by the international commission on Non-Ionising Radiation Protection (ICNIRP): with regards to localised heating, adverse effects can be avoided, if temperatures in localised regions of the head are less than $38°\mathrm{C}$, the trunk less than $39°\mathrm{C}$, and the limbs less than $40°\mathrm{C}$ [231]. Typically, the temperature rise is dependent on the balance between the energy absorbed by, and the energy transferred from the region of interest. The factors which play a role in the rate of heat dissipation include the ambient temperature, blood flow, airflow, patient clothing, and humidity [232]. To ameliorate the resistive heating effect, Bernhardt et al. employed an alumina catheter tip over the initially used polyimide material and by running saline fluid at room temperature through the lumen of the catheter. This approach is similar to current clinical practice in which saline drips are used to reduce the risk of catheter thrombosis, i.e. formation of blood clots [187, 189]. As previously mentioned, Caenazzo et al. on the other hand, proposed the concept of using conductive fluids to alleviate the effects of heating and artefacts in MR environments [186]. The safety hazard associated with HDCs is the need for high fluidic pressures which, if not controlled properly, may result in jets of pressurized liquid that could damage soft tissue [226, 233]. The safety concern linked to catheters driven by ferromagnetic spheres is the insertion of ferromagnetic components at the entry region of the MRI bore, where a very strong static gradient of 20 T/m exists. In this region, magnetic forces would be high enough to damage the blood vessel wall [198]. Pull-wire driven catheters are generally considered safe; however, catheters with multiple segments should not have any sharp or irregular edges which can damage blood vessel walls and increase the risk of embolisation [21].

### 2.3.5 MR Visibility

Real-time tracking and visualisation of instruments (guidewires, selective and steerable catheters) in MRI environments are crucial to the success of, and transition to MR-guided endovascular interventions [135]. The restriction on the usage of ferromagnetic materials due to the presence of a strong magnetic field and the difficulty of visualising and localising the relatively safe polymeric materials due to their low magnetic susceptibility [135], has impeded

**Table 2.3:** Materials used for constructing steerable catheters for MR-guided interventions,*patents are excluded, † Extends to the distal end, ‡ Only discussed in reference, Marker: Passive Negative Marker (PN), Passive Positive Marker (PP), Semi-Active Tracking (SA), Indirect Active Tracking (IA), Direct Active Tracking (DA)

| | | Ref | Proximal End Material (Function) | Distal End (Function) | Marker |
|---|---|---|---|---|---|
| Steerable Catheters | Pull-wire driven | [173] | PTFE (inner liner), Kevlar® (braiding), Pellethane® (outer layer), PEBAX® jacket (outer cover)†, Kevlar®† | Laser-cut nitinol slotted tube (steerable tip), Nitinol Spring (kink resistance, shape restoration), Polyolefin heat-shrink tubing (outer layer), | PN, SA, IA |
| | | [174] | Nylon braided tubing, Carbon fibre (pull-rod, pull-wire)† | PTFE multi-lumen tubing (steerable tip), Nitinol ribbon (kink resistance) | - |
| | | [2, 175] | PEEK multi-lumen tubing (base), Nitinol rod (additional stiffness), Polyethylene (PE) heat-shrink tubing (outer layer), Dyneema® (pull-wire)† | Laser-cut distal end of PEEK multi-lumen tubing (steerable tip), Relatively thicker and more flexible polyolefin heat-shrink (outer layer) | PN |
| | | [177, 178] | Monofilament braided tubing (catheter shaft), Polyethylene Fibre (steerable tip pull-wire)†, Glass fibre (carbon-fibre control wire)† | 3D Printed Acrylonitrile Butadiene Styrene (ABS) segments (steerable tip), Flexible guide tube (inner layer), Sliding carbon fibre tube (inner tube, deflectable segment control), Central carbon fibre rod (stiffness enhancement) | - |
| | Hydraulic | [179] | Teflon tubing | Laser-cut nitinol tube (steerable tip), Silicone rubber tube (cover) | - |
| | | [180–182] | Polymeric tubing†, Saline (drive fluid)† | Moulded silicone bellow (steerable tip), Hybrid micro stereolithography of UV curable epoxy resin (valve) | - |
| | | [186] | - | 3D Printed Polyethylene terephthalate glycol (PETG) (steerable tip), Silicone tubing (cover) | - |
| | Magnetic | [188] | - | Copper wire (coil) | DA |
| | | [189] | 2.7 Fr microcatheter† | Copper microcoils laser lithographed onto a polyimide tube and an alumina tube (coil), Heat-shrink tubing (outer layer) | - |
| | | [191, 192] | 2.9 Fr microcatheter (PEEK braided)† | Microcoils laser lithographed onto an alumina tube (coil), Heat-shrink tubing (outer layer) | DA |
| | | [193, 194] | - | Silicone tubing (steerable tip), Copper wire (coil) | - |
| | | [195] | Experiment 1: 5 Fr Catheter†, Experiment 2: Balloon Catheter† | Experiment 1: Cubic neodymium (NeFeB) magnets , Experiment 2: $Fe_3O_4$ ferrofluid (balloon catheter fluid) | NP |
| | | [196, 197] | 2.5 Fr microcatheter & Guidewire† | Ferromagnetic chrome steel bead (magnet) | NP |
| | | [198] | 8 Fr catheter† | Silicone tubing (steerable tip), Ferromagnetic high carbon bearing steel (SUJ2 - magnet) | NP |
| | Shape Memory Alloy | [211] | - | Glass-silicone stacked three-dimensional structure (links), Nickel thin film deposited on a Parylene coated SMA coil (actuator) | - |
| | | [212] | - | SMA coils (actuator), Silicone tubing (cover) | - |
| | | [213] | - | Biomedical engineering plastic and brass (links), Parylene and polyurethane coated SMA Spring (inner tube), Parylene thin film (outer layer), Silicone rubber tube | - |
| | | [214] | - | Electrochemically etched nitinol SMA sheet (actuator) and Nitinol tube (bias spring), Silicone rubber tube (cover). | - |
| | | [215] | Polyethylene double lumen tube (inner tube)† | Electrochemically etched nitinol SMA sheet (actuator), Polyurethane tube (outer cover) | - |
| | | [216] | - | SMA wires (actuator) | - |
| | | [217] | PTFE tubing (inner)†, PTFE multi-lumen tubing (outer)† | SMA wires (actuator) | - |
| | | [218, 220] | - | Nitinol wire (central beam), SMA wires (actuator), 3D Printed Acrylic plastic (collets) | - |
| | | [225] | 3D printed plastic tube | SMA wires (actuator), Nichrome wires (SMA wire heating) | - |
| | | [196] | - | Radifocus® Guidewires (core structure), SMA wires (actuator), Isolated copper wires (SMA wires fixation) | - |

**Table 2.4:** Actuation techniques summarised based on working principle, steerability and safety.

| Actuation [Ref] | Working Principle | Steerability | Safety |
|---|---|---|---|
| Pull-wire driven [2, 173–175, 177, 178] | Pull-wires run from the proximal end through the catheter shaft to the distal end. When the pull-wire is pushed/pulled, the distal end of the catheter tip is deflected. | + Swift manipulation<br>– Mechanical nonlinearities which increase with the number of moving parts and DOF<br>– Uncontrollable changes in pull-wire length due to the passive bending of the catheter shaft while manoeuvring through tortuous anatomies | + No risk of resistive heating and RF induced heating<br>– (Multi-segment) Sharp or irregular edges may cause damage to the vessel wall |
| Hydraulic [179–186] | Catheters are controlled by a single or multiple pressurized tube that run to the soft and flexible distal chamber(s). The drive of the hydraulic chamber relies on the pressure of the fluid to cause a bending force in a specific direction. | + Smooth movement<br>+ Precise control of deflectable segments<br>– Slower response time (when compared to pull-wire driven catheters)<br>– Need for additional equipment such as pumps, valves, and pipes<br>– Possible leakage may limit the catheter's efficiency<br>– Requirements of sophisticated control methods | + No risk of resistive heating and RF induced heating<br>– If not properly controlled, the pressurised fluid ejected can damage soft tissue |
| Magnetic [188–198] | Magnetic actuation is based on the changes in magnetic field applied to the distal end of catheters having magnetic or electromagnetic elements. | + "Wireless" manipulation without mechanical and fluid components<br>– Difficult to achieve precise motion<br>– Requires customised "interleaved" MR sequences for simultaneous visualisation and control | **Microcoiled catheter**<br>– Possibility of resistive heating and RF induced heating<br>**Ferromagnetic Spheres**<br>+ No risk of resistive heating and RF induced heating<br>– Strong static gradient at the entrance of the MRI bore creates a magnetic force acting on the ferromagnetic element, which can damage the vessel wall |
| SMAs [211–225] | SMA driven method takes advantage of the shape memory effect of SMA. | + Great potential for miniaturization<br>– Difficult to be controlled in a repeatable manner due to hysteresis | – Possibility of resistive heating and RF induced heating |

the advancement of MR-guided interventions. In 2001, Duerk et al. broadly classified catheter tracking methods into passive tracking, semi-active tracking and active tracking (Figure 2.16) [234].

Passive tracking is visualising instruments within MR images either by the materials incorporated in the instrument's construction or by the added markers that enhance, reduce, or distort the $T_1$- and/or $T_2$- weighted MR signals (Figure 2.7 illustrates the definitions of $T_1$ and $T_2$). An image is considered $T_1$-weighted when the signal acquisition parameters are chosen to reflect the variations in $T_1$ (same applies to $T_2$-weighted images). Passive markers can be further classified into negative contrast, positive contrast, and non-proton multispectral contrast [168].

In the negative contrast approach, the incorporated materials or added markers make instruments visible by intro-

ducing localised magnetic field inhomogeneities which lead to the dephasing of adjacent proton spins and a local signal void (susceptibility artefact) on an MR image [168, 169]. From the previously described steerable catheters, the ones which make use of the negative contrast effect are constructed from the following materials: nitinol hypotubes [173, 174], ferromagnetic spheres [195–198], and SMA wires [225]. In addition to their primary function of providing kink resistance (nitinol hypotubes) and catheter steering (ferromagnetic spheres and SMA wires), these materials produce susceptibility artefacts which make catheters visible on an MR image. Negative contrast passive tracking can also be realised by adding markers to catheters which are not constructed from components that generate susceptibility artefacts. A majority of the previously described guidewires developed for MR-guidance adopt this type of marking for MR visibility; by employing discretely attached and/or adhered (super) paramagnetic iron oxide (SPIO) nanoparticles [148, 150, 156, 159, 161], iron microparticles embedded in the guidewire's coating [147] and iron microparticles doped in the epoxy resin used in the micropultrusion process of glass and/or aramid fibres [157]. Simiarly, for steerable catheters, paramagnetic iron oxide (FeO) microparticles were also adhered to the catheter's shaft and distal end in order to create signal voids [175]. Other marker materials include ferromagnetic (e.g. AISI 410 stainless-steel, nickel), ferrimagnetic (e.g. copper zinc ferrite), and strongly paramagnetic (e.g. dysprosium oxide) [168]. Maes et al. and Miquel et al. adopted the negative contrast approach by injecting carbon dioxide ($\mathrm{CO}_2$) through a catheter lumen [235] and using balloon catheters inflated with $\mathrm{CO}_2$ [236] respectively. Although the negative contrast approach is relatively simple, safe and low cost, the tracking cannot be controlled (i.e. switched off), leads to loss of anatomical information around the artefact and is susceptible to motion and flow artefacts [168].

Passive tracking with positive contrast, on the other hand, is achieved by using paramagnetic materials (e.g. gadolinium) that cause shortening of the spin-lattice relaxation ($T_1$ relaxation time). The shortening of $T_1$, results in a signal enhancement/bright spot, which enables the visualisation and tracking of the catheter. Omary et al. and Unal et al. tested the feasibility of positive contrast tracking by filling the catheter lumen with gadolinium-based contrast [237, 238]. Other research groups employed multi-step processes to coat off-the-shelf catheters with gadolinium-based coatings [239]. Furthermore, when it comes to steerable catheters, Muller et al. proposed the possibility of adding contrast agents to the driving fluid of HDCs for better catheter visualisation [187]. The positive contrast effect is best visualised on a standard $T_1$-weighted pulse sequence. Contrary to negative contrast, positive contrast preserves the anatomical information around the marker. However, positive contrast coating materials are unstable, and filling the catheter lumen with contrast agents prevents it from being used for the insertion of guidewires and intravascular catheters.

Instead of solely depending on the presence of hydrogen protons ($^1\mathrm{H}$), researchers investigated the simultaneous detection of signals from other nuclei such as fluorine ($^{19}\mathrm{F}$), hyperpolarised carbon ($^{13}\mathrm{C}$), sodium ($^{23}\mathrm{Na}$), and phosphorus ($^{31}\mathrm{P}$). In this case, device visualisation and localisation are achieved by overlaying a second coloured layer of the independent information detected from the additional nuclei to the anatomical details provided by the standard grey-scale ($^1\mathrm{H}$) image [240]. Kozerke et al. filled a balloon catheter with perfluorooctylbromide (PFOB), and extended the imaging capabilities of a standard system to allow for ($^{19}\mathrm{F}$) excitation and signal detection [241]. Similarly, Magnusson et al. modified an MRI scanner to enable the tracking and visualisation of a catheter filled with hyperpolarised ($^{13}\mathrm{C}$) [242]. The main benefit of using non-proton passive tracking is its ability to provide high contrast-to-noise ratio (CNR) and signal-to-noise ratio (SNR). In terms of limitations, this method requires additional hardware and software to excite and detect signals from non-($^1\mathrm{H}$) nuclei [168].

While passive tracking relies on intrinsic material properties, semi-active tracking uses wireless self-resonant RF circuits as markers to visualise MR invisible catheters [243]. The resonant circuit is triggered/detuned by the MRI scanner using specially designed MRI sequences [125]. The triggering of the circuit induces a magnetic field which dephases the MR-signal and leads to a susceptibility artefact [244]. To adjust the resonance frequency, Weiss et al. proposed connecting optical fibres to the circuit to illuminate a photodiode placed in parallel to the coil [245]. The challenges of semi-active tracking include the need for bespoke tracking sequences, and difficulties in assembly and miniaturisation due to the optical interface [125]. In terms of strengths, there are no direct electrical connections with the MRI scanner. This, in turn, eliminates the possibility of standing wave formation and subsequent physiologically relevant heating. Note: Some research groups classify semi-active tracking as inductively coupled coils.

Active tracking of catheters can be implemented in two different ways, i.e. indirect active tracking, and direct active tracking. Generally speaking, actively tracked catheters are equipped with receiver resonant RF coils that are electrically connected via coaxial cables to the receiver channel of the MRI scanner in the case of indirect active tracking and to a controllable power source in the case of direct active tracking. In indirect active tracking, the connection to the MRI receiver channel facilitates the determination of the three-dimensional coordinates of the resonant RF coils, which are then superimposed to previously acquired MR images [246]. Although restricted by the number of MR receiver channels, the main advantage of this method is the ability to get accurate and fast position updates, i.e. high temporal resolution [247, 248]. Several research works used indirect active tracking to track their guidewires under MR guidance where by combining a loopless antenna (e.g. coaxial cable, nitinol rod) for shaft visibility with a coil at the distal end for better tip visibility [172, 249, 250]. In [172], Sonmez et al. added a fibre optic temperature probe to the guidewire's construction to monitor the temperature in real-time and ensure safe operation. Recently, Alipour et al., who adopted indirect active tracking, proposed attenuating induced currents along long metallic components of guidewires and catheters by employing miniaturised resonant floating RF traps [251].

**1. Passive Tracking**

**(a) Negative contrast**
- \+ Simple, safe and low cost
- − Cannot be switched off
- − Loss of anatomical information around the artefact
- − Susceptible to motion and flow artefacts

**(b) Positive contrast**
- \+ Preservation of information around the contrast agent (compared to negative contrast)
- − Unstable positive contrast coating material
- − Filling the catheter lumen with contrast results in the inability to insert the guidewire or intravascular devices
- − Cannot be switched off

**(c) Non-proton multispectral contrast**
- \+ High contrast-to-noise ratio (CNR) and signal-to-noise ratio (SNR)
- − Additional hardware and software to excite and detect signals from non-$^{1}$H nuclei

**2. Semi-active Tracking (Inductively Coupled Coils)**
- \+ No direct electrical connections with the MRI scanner
- \+ No standing wave formation or physiologically relevant heating
- − Needs bespoke tracking sequences
- − Difficult to assemble and miniaturize

**3. Active Tracking**

**(a) Indirect**
- \+ Can obtain the 3D coordinates of resonant RF coil
- \+ High temporal resolution
- − Long conducting cables are susceptible to RF heating

**(b) Direct (Direct Currents)**
- \+ Easy control of artefacts by adjusting current
- \+ No need for bespoke tracking sequences
- − Unwanted magnetic steering
- − Long conducting cables are susceptible to RF heating

**Figure 2.16:** Advantages and disadvantages of tracking methods (marking) for interventional devices

In direct active tracking, the flow of current through the RF coils is adjusted using the controllable power source, resulting in an adjustable, locally induced magnetic field inhomogeneity (similar to passive and semi-active tracking methods) [246]. The main difference between this active tracking method and passive tracking is the ability to control the generated artefacts interactively during the procedure by simply adjusting the current. When compared to semi-active tracking, which triggers similar coils using the MR scanner, this active tracking method does not require custom MRI sequences to operate. A common problem faced by this type of active tracking is the movement of the catheter due to the magnetically induced forces and torques experienced by the coiled distal end. Nevertheless, Muller et al. identified this issue as an opportunity to magnetically actuate and visualise catheters simultaneously [187]. The main limitation of active tracking, for both indirect and direct active tracking, is the potential safety hazards imposed by the long conducting coaxial cables that connect the coil and the MRI receiver/power supply [247]. Note: Some research groups classify direct active tracking as a passive tracking method (referred to as Direct Current(s)) instead of active tracking because of its close correspondence to passive tracking [10, 168].

## 2.4 Future Directions

Navigation under MRI promotes endovascular intervention with improved safety and efficacy compared to traditional X-ray guided intervention. One of the most significant obstacles to shifting from X-rays to MRI is the lack of MR-compatible instruments [135, 140]. Although much effort has been made in the development of MR-compatible medical instruments, there are still various challenges that limit the commercialisation of these devices, and thus popularity of MR-guided interventions. The future development and adaptation of MR-compatible devices necessitates a focused collaborative research effort, which is summarized within the following categories: materials and fabrication schemes, imaging pulse sequence design, robotic control, safety and coordinated interdisciplinary approach.

### 2.4.1 Material and Fabrication Schemes

Metals with their excellent mechanical properties and mature fabrication methods are widely used in various medical devices. However, the use of metals in the MR environment is restricted due to safety concerns. Polymers are currently the most commonly used alternative to metals in the MR environment. Despite their wide range of applications, the polymer family of materials does not offer the same diverse mechanical properties as metals . The development of new materials with enhanced mechanical properties, such as high flexibility, elasticity and resistance to kinking, would speed up the commercialisation of MR-compatible devices. MR-adapted materials with appropriate MR sensitivity hold great promise for solving visualisation-related problems such as artefacts caused by passive negative markers and overheating associated with active tracking.

The challenges faced in materials reflect directly to manufacturing as well. The development of MR safe devices with similar mechanical performances to those built with metals is introducing manufacturing challenges, increasing the cost of development as well as production. Fabrication approaches that allow rapid and low-cost prototyping are crucial for accelerating the research around these devices. Many of the proposed navigation solutions in literature require tedious manual assembly, which makes it difficult to adapt to scalable manufacturing. Manufacturing solutions that offer scalable productivity with high reproducibility are also important factors to consider during the design and development of new medical devices. In parallel, cost control of the device should be considered

as MR-safe devices at a competitive selling price with those used for conventional X-ray guided interventions are required.

### 2.4.2 Imaging Pulse Sequence Design

During image-guided endovascular interventions, radiologists rely on imaging modalities - fluoroscopy or MR - for visualisation of tissues and guiding of instruments for diagnosis or therapy. In the case of MRI, it can provide information based on 3D, 2D or line projections. As the amount of information detailed in the image increases, the refresh rate decreases. This is a big challenge not only for clinicians looking for speed and detail, but also for devices utilising magnetic fields for simultaneous actuation and visualisation. An important future direction is to find the balance between high feedback rates and information detail by identifying the truly critical feedback information based on the application [199]. For semi-active tracking method, which requires bespoke tracking sequences to visualise the device as well as the tissue, similar problems are faced. Regarding the other tracking techniques, depending on the characteristics of the marker or antenna material, suitable sequences need to be selected or adapted accordingly to control the artefact size and achieve the optimum visualisation.

### 2.4.3 Robotic Control

Robotic surgery is one of the most popular topics in the field of biomedical engineering, and it has become a growing trend by virtue of its great potential. With adequate control, robotic manipulator could enhance precision of the surgery and allow flexible complex movements in tight spaces, making it possible to provide safer and minimally invasive surgical procedures . Of the several actuation modes examined in the article, except for pull-wire driven catheters that can be directly controlled manually, all other types of actuation modes (hydraulic, magnetic and SMA) require varying degrees of remote or automated control. To achieve reliable, stable, and precise catheter movement, appropriate control methods, such as closed-loop control as well as machine-learning based control, should be implemented to overcome non-linearities during the surgery. In fluoroscopy-guided endovascular interventions, robotic surgery enabling surgeons to perform procedures outside the operating theatre has been explored and accepted as a solution to minimise radiation exposure to medical personnel. In MR-guided interventions, robotic surgery can also address issues such as limited access to the patient and noise generated by the MR scanner. Choosing the suitable level of automation for the medical application and the drive mechanism is of great importance in the development and design of the new instruments [199].

### 2.4.4 Safety

Safety is the primary consideration in medical interventions at all times. The radiation problems caused by conventional fluoroscopy imaging can be solved by replacing X-rays with MR. For procedures under MR environment, the main safety concern is related to the RF heating caused by long conductive wires in the catheter. Some actuation methods, i.e., Lorentz force based magnetically driving method and SMA driving method, as well as active tracking method have an inbuilt requirement for the presence of long conductive wires, which will affect the MR compatibility of catheters employing these methods. Future directions could focus on solutions to the overheating problem, including approaches for cooling and the design of actuation or tracking modes. Most MR-compatible designs are still at the stage of prototyping, and only a few commercial products are available for MR-guided endovascular interventions, but none of these are labelled as 'MR safe' according to ASTM standard [143] due to the presence of

metal components. The development of products that comply with higher safety standards is also a proposition of potential concern, which could be addressed from both regulatory and manufacturer sides.

### 2.4.5 Coordinate Interdisciplinary Approach

A system level approach is highly needed. All these approaches for future directions involve a diverse set of skills from a variety of fields. It is therefore difficult to make breakthroughs in this field with isolated efforts. To advance the progress of endovascular interventions, and in particular to fully exploit the potential of MR in endovascular interventions, there is an urgent need for a systematic communication and collaboration among researchers from different backgrounds – engineers, physicists, radiologists, physicians etc. With the synergy of research efforts from various fields, safer medical treatments will become widespread for the benefit of healthcare professionals and patients.

## 2.5 Conclusions

MRI has greatly improved the sensitivity and accuracy of diagnostic imaging. However, for the wider adoption of MRI in interventional radiology and targeted therapy, it is crucial for all the stakeholders involved (MRI and medical device manufacturers, interventional radiologists, cardiologists, engineers, and researchers) to collaborate more effectively on overcoming the barriers for safer endovascular treatments. For MR-guided interventions to become part of the clinical routine, the following challenges need to be addressed: high setup and running costs of MRI scanners, lack of MR safe interventional instruments, increased complexity of workflow, and access to clinical training in MR environments. Despite these challenges, in recent years, researchers have proven that MRI is safe and practical in a clinical setting [9, 13, 252, 253], permits better soft tissue visualisation, provides more pertinent physiological information (e.g. perfusion MR imaging), and results in no radiation exposure when compared to fluoroscopy-guided procedures. Such clinical endeavours can be further accelerated by supporting on-going research in the fields of MR compatible and visible materials, novel fabrication schemes, dedicated pulse sequence designs, and robotic-assisted surgery. Moreover, companies such as Imricor (electrophysiology mapping and ablation catheters), MaRVis Medical (guidewires), nano4imaging (guidewires), EPFlex (guidewires), and Innovative Tomography Products GmbH (biopsy catheters) are paving the way towards the translation and commercialisation of MR safe and MR conditional devices [254].

In this chapter, the ongoing research and development on navigational instruments and devices for MR-guided interventions was presented. While a number of challenges remain, this chapter has sought to highlight the importance of structural and functional materials for the advancement of multi-functional, easy to use, safe and cost-effective MR safe medical devices. With the pursuit of adopting endovascular interventions under MR-guidance still underway, the following take-home messages outline the requirements to be fulfilled by researchers and companies targeting the development of navigational devices for MRI: (1) MR visible navigational instruments, i.e. clinicians should be able to visualise the instrument's shaft in its entirety, along with the exact tip location as experienced under fluoroscopy. This would significantly speed up the learning curve of clinicians trained on fluoroscopy-guided endovascular interventions. (2) Instruments should have the same mechanical integrity and features as their MR unsafe equivalents. (3) For steerable catheters: Development of an intuitive method of controlling the catheter without the need for cumbersome hardware and software [21]. Reducing the complexity of the steerable catheter

construction not only simplifies the regulatory process of the medical device, but it also speeds up the clinician's learning curve, reduces the device's cost, and increases the overall reliability and safety of the system. (4) MR safe instrumentation should be made available at a competitive price point when compared to fluoroscopy-guided catheters. This is based on the fact that public healthcare systems would greatly adopt new technologies if they are cost-effective and provide added value in the clinical care of patients. (5) Closely collaborating with clinicians who can identify diseases where MR-guidance can provide a competitive advantage over fluoroscopy-guidance (e.g. ventricular tachycardia [255]). (6) Adoption of robotics and teleoperation to overcome the challenges of manual MR-guided endovascular interventions previously described in Chapter 1.

Bearing these thoughts in mind, this thesis aims to address a subset of the challenges described above by devising a robotic platform that not only targets to improve the outcomes and safety of X-ray guided endovascular interventions, but also pave the way for MR-guided interventions through the adoption of MR safe actuation techniques (i.e. pneumatic-based). Over the course of the next two chapters (Chapters 3 and 4), the robotic system is designed, fabricated, integrated, optimised and thoroughly evaluated under X-ray fluoroscopy guidance in vascular phantoms and porcine models. In addition, the system is preliminary tested under MR-guidance (Chapter 3) to prove its compatibility in MR environments. To complement this work and to address the lack of MR compatible instrumentation, the fibre production technology is employed to accelerate the development of an MR safe and visible steerable catheter (Chapter 5). In an attempt to combine both sides of the spectrum, the robotic platform is extended and integrated with the steerable catheter to facilitate further testing under MR-guidance.

Chapter 3

# An MR-Safe Endovascular Robotic Platform: Pilot Study

"This chapter was published in 2019 IEEE/RSJ International Conference on Intelligent Robots and Systems (IROS), Macau, China. ©2021 IEEE. Reprinted, with permission, from (Abdelaziz, M. E. M. K., Kundrat, D., Pupillo, M., et al. "Toward a Versatile Robotic Platform for Fluoroscopy and MRI-Guided Endovascular Interventions: A Pre-Clinical Study". In: Proceedings of 2019 IEEE/RSJ International Conference on Intelligent Robots and Systems (IROS). Macau, China, 2019, pp. 5411–5418. doi: 10.1109/IROS40897.2019.8968237. " [256]).

## 3.1 Introduction

This chapter introduces a versatile master-slave robotic platform that aims to: (1) improve the efficacy and overall safety of interventions under X-ray fluoroscopy guidance, and (2) facilitate the adoption of a safer alternative imaging modality which provides unique functional imaging capacities (i.e. MRI).

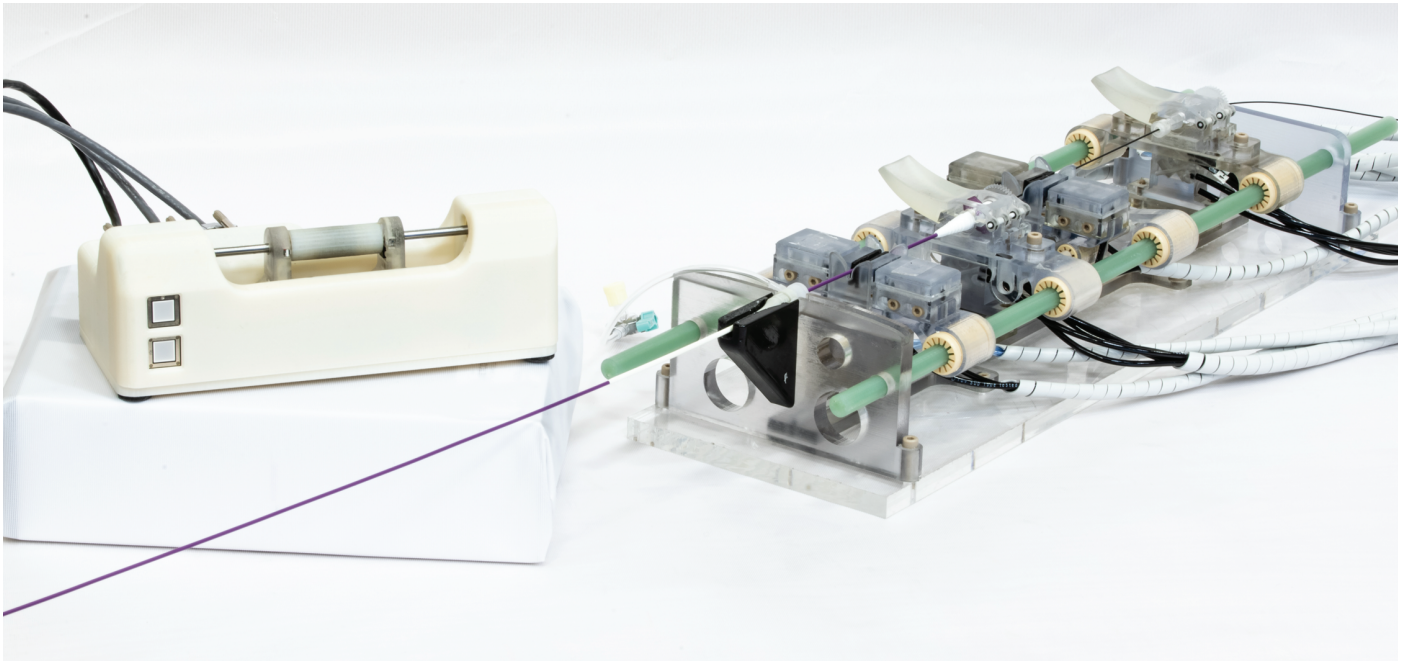


**Figure 3.1:** Novel robotic platform with versatile, MR-safe slave robot (right) and intuitive master device (left) for endovascular interventions.

### 3.1.1 State of the Art

A variety of robotic systems for endovascular or cardiac catheterisation were reported in research or translated to commercialisation. In general, such systems show low levels of robotic autonomy [115] and consider a master-slave set-up for teleoperated manipulation of instrumentation. Commercial systems targeting different fields of application in endovascular and cardiac cases comprise the *Magellan* and *Sensei*® X2 platforms (AurisHealth, Redwood city, CA, USA), the *Amigo* platform (Catheter Precision, Mt. Olive, NJ, USA), the *R-one*™ robot (Robocath, Rouen, France), or the *CorPath® GRX* platform (Corindus, Waltham, MA, USA). The corresponding master, with human machine interfaces (HMI), makes use of conventional stationary joysticks, hand-held joysticks, or 3D input devices with force feedback capabilities. Commercial platforms enable electro-mechanical manipulation of customised (steerable) catheters and guidewires in up to 6 degrees of freedom (DOF) and were successfully used in clinical scenarios [257–260]. Novel master devices were proposed to improve the transparency of teleoperation. Exemplary, motion due to manipulation of standard catheters was sensed without user feedback and replicated to a slave robot [120]. More recently, magnetorheological fluid was used in combination with a catheter to mimic friction and generate user feedback [121]. Slave robots generally show alternative concepts with different electro-mechanical mechanisms for driving and clamping of instrumentation as reported in [122–124]. Device compliance with MR environments is restricted to [77, 125] and focuses on steerable catheters. For the sake of completeness, the reader is kindly referred to a comprehensive review of devices [39].

### 3.1.2 Limitations & Contribution

Related work has highlighted a range of emerging catheterisation platforms for endovascular or cardiac applications. However, devices show a number of limitations regarding clinical translation: (1) Use of different standard catheters and guidewires with reported devices is limited and generally requires manufacturer-specific instruments. This impedes a cost-effective and versatile application. (2) Usability of the teleoperation set-up neglects established manual procedures. HMIs rarely imitate the human motion patterns of the procedure, e.g. joysticks. Also, many systems lack force feedback, or, when present, it is provided through commercial interfaces or joysticks, not properly capturing surgeons' skills. (3) Collaborative instrument handling, i.e. quick and easy transition between manual and robotic manipulation is currently disregarded. Robotic assistance is predominantly required for challenging cannulation tasks or instrument deployment. (4) Fluoroscopy is still considered the gold standard for robotic assistance. X-ray exposure is only reduced for the user. This limits use to pediatric patients. (5) Future directions are towards MRI-based interventions to reduce ionizing radiation exposure [261, 262]. MR-compatible devices are exclusively reported for cardiac cases with steerable catheters.

In order to overcome the aforementioned limitations, this chapter proposes the design and preliminary evaluation of a versatile robotic master-slave platform and navigation framework for manipulation of standard endovascular instruments in multi-modal imaging environments, e.g. fluoroscopy and MRI. Inspired by previous work [20, 263], a novel master manipulator is introduced as HMI. The device imitates the human motion pattern of translating and rotating instruments during catherisation. Furthermore, the user can perceive haptic and visual feedback related to the device or procedural states. The design of the slave robot, in particular addresses the aspect of versatility from two directions: 1.) The robotic instrument interface enables intuitive use and fast exchange of standard endovascular instruments (catheters, guidewires) to extend the range of potential clinical applications. 2.) Take advantage of additive manufacturing and pneumatic actuation to establish full compliance of the slave robot with MR safety

guidelines facilitating robotic assistance in different imaging environments. This in particular targets clinical cases of pediatric MRI-guided catheterization, as exposure to x-rays is not recommended or possible. The proposed platform is evaluated in combination with a navigation framework in a study on manual and robotic vessel cannulation under fluoroscopy and an MRI-compatibility test. Results strongly motivate versatile robotic platforms that take emerging trends in medical imaging into account and improve outcomes for patients and clinical users.

## 3.2 Clinical Requirements

Clinical requirements were established by reviewing prior art (e.g. [120, 264]), analysing various endovascular procedures and interviewing vascular surgeons. Such specifications can be summarised as follows. The system should be versatile and capable to perform different vascular interventions (i.e. lower limb peripheral, aortic, iliac, carotid, visceral, upper limb peripheral, cardiac and coronary interventions). This requires the system to accommodate a wide selection of instruments (i.e. catheters and guidewires) available on the market [265] and precisely manipulate them. The system should include a navigation system to visualize the surgical site and provide image and haptic guidance to minimise contacts between the manipulated instrument and the endothelial wall. The system should be compatible with different imaging modalities, including x-ray fluoroscopy and MRI. The system should be teleoperated to remove or minimize the exposure of surgeons to x-rays. The surgeon should be always in control of the procedure and his/her motion skills should be captured by the system and properly translated to the surgical site. The system should be hands-on, easy-to-use and have a small footprint to be well integrated within the clinical workflow. In terms of safety, the procedure should be quickly revertible to manual, and the surgeon should be able to take over in a few seconds. Thus, the system should have a quick and simple method to dock and release catheters and guidewires. Finally, the system should not be harmful for both patient and operators.

## 3.3 Robotic Design

The design of the robotic platform addresses the clinical requirements reported above. This section describes the master and slave, while the next section reports their integration with the navigation system and the control architecture.

### 3.3.1 Haptic Master Device

The concept of the proposed haptic master for teleoperated intervention was initially reported in [20] and fundamentally revised in this contribution with regard to mechanical design, usability, and user interaction. Design objectives of the device, presented in Figure 3.2, target to mimic and map the established manual intra-procedural handling of standard catheters and guidewires to the master device for improved teleoperation transparency and intuitive user assistance. Hence, a cylindrical user handle attached to a robotic stage represents the core component of the HMI and imitates the clinically established interaction and executable DOF of standard catheters and guidewires. More precisely, the handle mounts a torque-resistant linear bushing that slides on a slotted shaft (custom-made component, Bosch Rexroth GmbH, Lohr am Main, Germany). This enables the user to grip the handle and introduce displacement $x_{\mathrm{M}}$ along the shaft axis. Simultaneously, the mechanical design of the bushing allows for angular

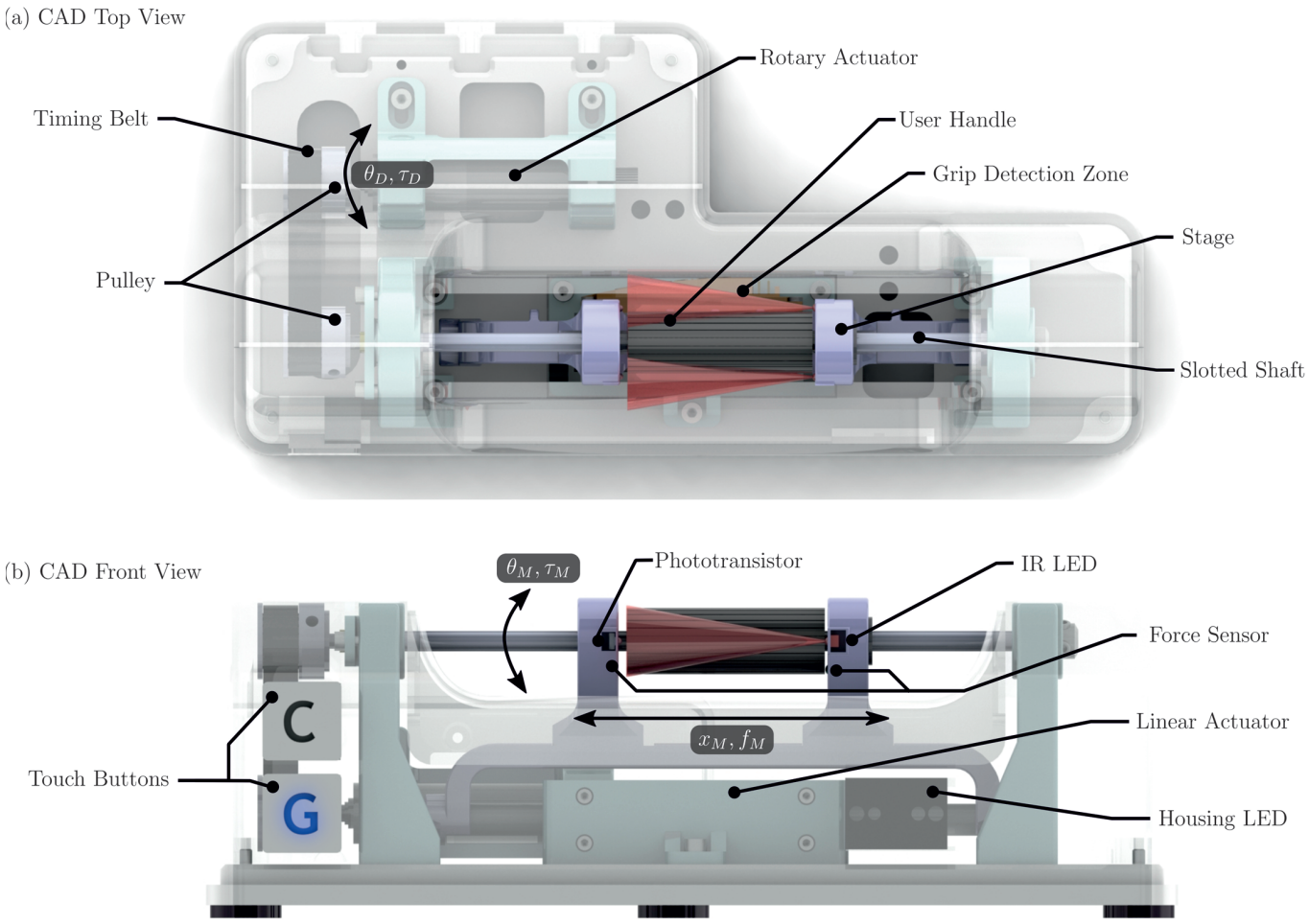



**Figure 3.2:** Conceptual design and prototype of the proposed haptic master with electro-mechanical set-up and sensing: (a) Top and (b) front view of the CAD model.

displacement $\theta_\mathrm{M}$ of the shaft. Thus, two DOF can be executed, i.e. feeding/retraction and rotation. Haptic feedback is generated in corresponding DOF with a linear and a rotary BLDC motor (1247 and 1226 B012, Faulhaber GmbH, Schönaich, Germany) that use appurtenant motion controllers with CAN interface (MCLM/MCBL 3006, Faulhaber GmbH, Schönaich, Germany). The customised shaft enables stationary mounting of both motors and improved dynamics due to reduced moving mass and less space incorporation. In detail, torques perceived by the user yield to $\tau_\mathrm{M} = i_\mathrm{G} i_\mathrm{P} \tau_\mathrm{D}$ with gear transmission $i_\mathrm{G} = 16$, pulley transmission $i_\mathrm{P} = 1$, and drive-sided torque $\tau_\mathrm{D}$. Forces of the linear actuator along the shaft axis are described by $f_\mathrm{M}$ with maximum stroke lengths of $\pm$20mm. Disturbances due to mechanical friction are neglected. After user displacement, the linear motor homes the stage back to the initial (central) position, providing the user with sufficient stroke to carry on with the linear manipulation. The master joint state is described by

$$\vec{q}_\mathrm{M} = \left(x_\mathrm{M}, \theta_\mathrm{M}, \dot{x}_\mathrm{M}, \dot{\theta}_\mathrm{M}, f_\mathrm{M}, \tau_\mathrm{M}\right)^\mathrm{T} \in \mathbb{R}^6. \tag{3.1}$$

Complementary to the electro-mechanical design of the HMI, the contribution proposes an integration of safe, reliable, and robust user interaction. Thus, user actions are continuously monitored during manipulation. The user intention related to the direction of linear motion $x_\mathrm{M}$ is detected with uniaxial force sensors (FSS1500NSB, Honeywell International Inc., Charlotte, NC, USA). The latter measure interaction forces in between handle and stage.

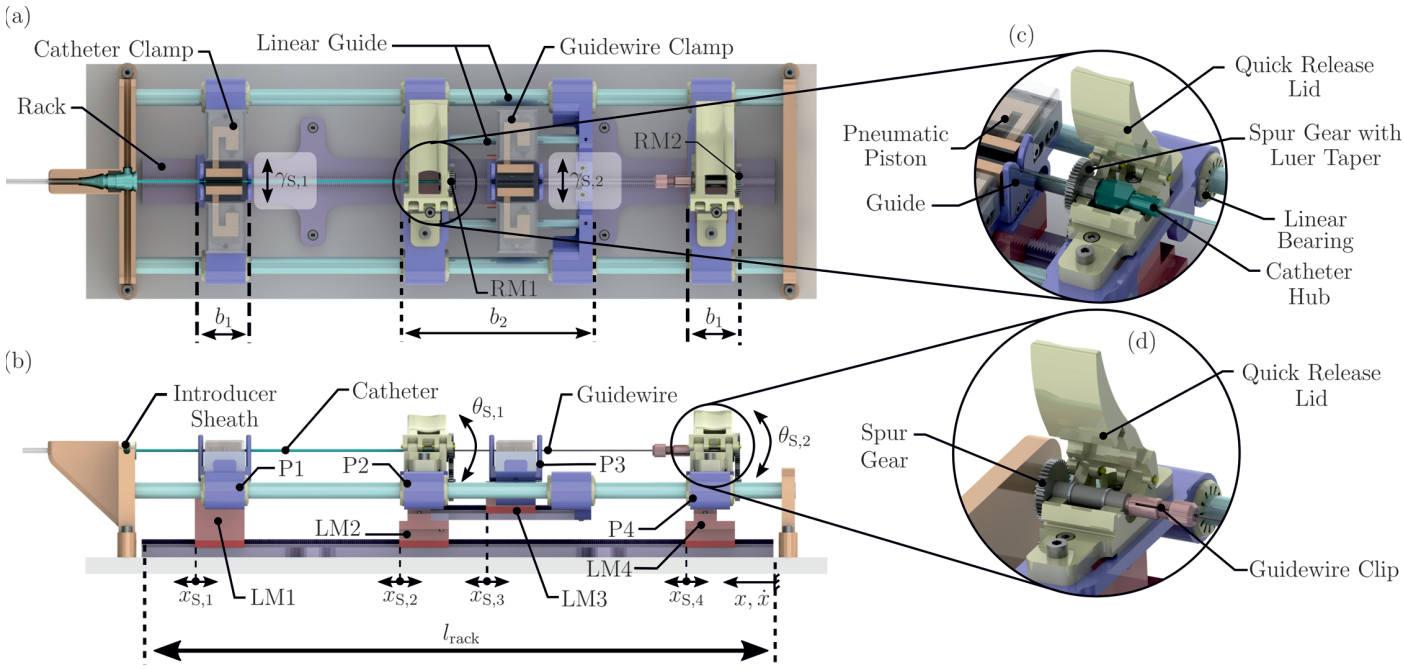



**Figure 3.3:** Conceptual design of the proposed slave robot: (a) Top and (b) side view of the CAD model, and (c) magnified details of quick release instrumentation mounting and mechanism for introduction of rotary motion to catheter and guidewire.

Acquired voltages are processed with a moving average filter of window size of $N$ = 10. If threshold $\sigma_{\mathrm{F}}$ is exceeded on one of the sensors, the intended direction is set in accordance with the sensor location. Additionally, contactless detection of handle interaction is implemented with two pairs of subminiature IR LEDs (VSMY2850G, Vishay, Malvern, PA, USA) and phototransistors (SFH 3015, Osram AG, Munich, Germany). Sensor pairs are mounted in parallel to the cylindrical handle to detect user contacts in the area covered by red cones shown in Figure 3.2. Lastly, visual feedback is provided for indication of system conditions (idle, ready, error) and generated by modulation (sweeping, continuous, or flashing) of housing illumination. Likewise, capacitive illuminated touch buttons at the front of the device enable an intuitive selection of the desired slave mode, i.e. manipulation of catheter or guidewire. The overall dimensions of the current prototype are (190 $\times$ 90 $\times$ 64)mm$^3$.

## 3.3.2 Slave Robot

### 3.3.2.1 Robot Design

To address the clinical and technical requirements presented in Section 3.2, a versatile pneumatically actuated robot with 4-DOF was developed to manipulate off-the-shelf angiographic catheters and guidewires by emulating the haptic master device. Each instrument is driven by two pneumatic linear stepper motors to translate the instrument, one pneumatic rotational stepper motor to rotate the instrument, and two pneumatic J-clamps to clamp while translating the instrument. The robot base measures (500 $\times$ 140 $\times$ 100)mm$^3$. The conceptual design of the slave robot is shown in Figure 3.3 and comprises the following platforms:

- Catheter Feeding Platform (P1): Linear stepper motor (LM1) carrying two J-clamps,
- Catheter Following/Rotation Platform (P2): Linear stepper motor (LM2) carrying a rotary stepper motor (RM1), a catheter hub docking station, and a guidewire feeding platform (P3),

- Guidewire Feeding Platform (P3): Linear stepper motor (LM3) carrying two J-clamps,
- Guidewire Following/Rotation Platform (P4): Linear stepper motor (LM4) carrying a rotary stepper motor (RM2) and a guidewire torque device docking station.

For each instrument, the feeding platforms (P1 and P3) serve as an axial drive clamp, positioned at a defined distance from the instrument's corresponding entry point. This prevents buckling of instruments during remote (robot-assisted) manipulation as depicted in Figure 3.4a. An example of the catheter insertion motion sequence is illustrated in Figure 3.4b.

To address the requirement of seamless switching between remote (robot-assisted) and manual operations, quick release add-ons for the catheter (spur gear with Luer taper) and guidewire (guidewire clip) were developed to introduce rotary motion and to facilitate quick and safe dock/release. The magnified views of Figure 3.3 illustrate both add-ons.

### 3.3.2.2 Stepper Motors & Clamps

The pneumatic stepper motors used herein are adaptations of the motors designed, illustrated and discussed in [18, 19]. The linear motor (miniaturized variant of T-63) consists of two sealed, dual-acting pistons acting on a rack. The pistons and rack have a teeth pitch of 1.2mm and a teeth depth of 2mm resulting in a step size of $s_{\mathrm{t}}$ = 1.2/4 = 0.3mm. The motor measures (32 $\times$ 30 $\times$ 16)mm$^3$ excluding the rack. The rotary motor (miniaturized version of R-80) consists of two sealed, dual-acting pistons placed in a cross configuration acting on a geared axle. The geared axle has 9 teeth with a circular pitch of 40° resulting in a step angle of $s_{\mathrm{a}}$ = 360°/(9 $\times$ 4) = 10°. The motor measures (25 $\times$ 25 $\times$ 20)mm$^3$. The pneumatic J-clamp is a miniaturised, 3D printed double-acting cylinder. The clamp comprises two sealed chambers acting on a J-shaped piston with a protruding rod. Depending on which chamber is pressurised, the piston outstrokes or instrokes, with a stroke of 3.8mm. The clamp measures (31 $\times$ 25 $\times$ 19)mm$^3$ excluding the piston. The theoretical force exerted by the piston is $F = P \cdot A = 79 \times 10^{-6} P$ (equivalent to 7.9N at 1 bar).

### 3.3.2.3 Pneumatic Control

The robot is controlled by a pneumatic valve manifold, where each stepper motor (linear and rotary) is independently operated by a pair of 5/2-way directional control valves MHA2-MS1H-5/2-2 (FESTO AG and Co. KG, Esslingen, Germany). In the case of clamps, one valve controls a pair of clamps. In total, 14 valves are composed and driven by customised driver boards that interface digital outputs of employed real-time hardware (see Section 3.4). An oil free air compressor, Bambi PT15 (Air supplies, Nottingham, United Kingdom) is used to deliver pressurised air to the valves.

### 3.3.2.4 Robot Kinematics

For control purposes, the slave robot can be decomposed to two coupled robotic manipulators described by joint state $\vec{q}_{\mathrm{S},j}$ with $j = \{1, 2\}$. More explicitly, the state of the catheter driver is given by $\vec{q}_{\mathrm{S},1} = (x_{\mathrm{S},1}, x_{\mathrm{S},2}, \theta_{\mathrm{S},1})^{\mathrm{T}} \in \mathbb{R}^3$ and of the guidewire driver by $\vec{q}_{\mathrm{S},2} = (x_{\mathrm{S},3}, x_{\mathrm{S},4}, \theta_{\mathrm{S},2})^{\mathrm{T}} \in \mathbb{R}^3$. Clamping is described with binary vector $\vec{q}_{\mathrm{CL}} = (\gamma_{\mathrm{S},1}, \gamma_{\mathrm{S},2})^{\mathrm{T}}$. Kinematic parameters are described in detail in Figure 3.3 and the composed joint state of the slave

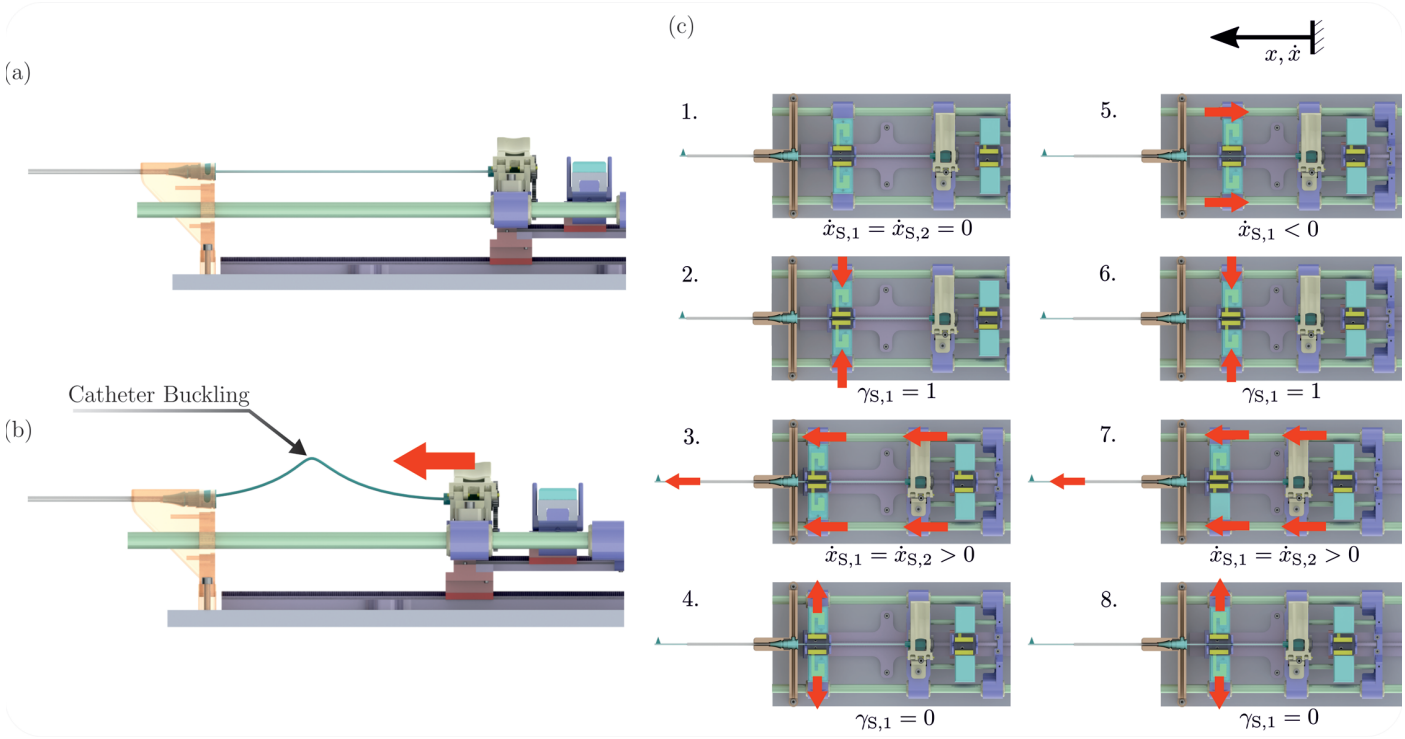



**Figure 3.4:** (a) Illustration of catheter buckling during feeding due to unsupported length in free space. (b) Example of the insertion sequence. (1) Starting from the initial static position, (2) P1 clamps the catheter. (3) P1 and P2 move at the same speed (to avoid buckling) and for the same predefined entire stroke. (4) P1 releases the catheter and returns to the initial position, (5) while P2 stays still. (6) P1 clamps the catheter again. (7) P1 and P2 advance simultaneously half of the defined stroke. (8) P1 releases the catheter.

robot yields to

$$\vec{q}_S = (\vec{q}_{S,1}, \vec{q}_{S,2})^T \in \mathbb{R}^6. \tag{3.2}$$

The proposed robotic system is capable of rotating both instruments infinitely in both directions, but this does not apply to translation. The executable insertion and retraction strokes are dependent on the states of each instrument. During insertion, the achievable strokes are:

$$s_{cat,ins} = l_{rack} - (x_{s,2} + b_1). \tag{3.3}$$

$$s_{gw,ins} = x_{s,2} - (x_{s,4} + b_2); \tag{3.4}$$

where $s_{cat,ins}$ and $s_{gw,ins}$ are the executable insertion strokes of the catheter and guidewire respectively. $b_1$ is the width of platforms P1 and P4, $b_2$ is the width of platform P2, $l_{rack}$ is the total length of the rack as shown in Figure 3.3. For retraction:

$$s_{cat,ret} = x_{s,2} - (b_2 + x_{s,4}). \tag{3.5}$$

$$s_{gw,ret} = x_{s,4} - b_1; \tag{3.6}$$

where $s_{cat,ret}$ and $s_{gw,ret}$ are the achievable retraction strokes of the catheter and guidewire respectively. Boundary

conditions of positions $x_{s,2}$ and $x_{s,4}$ are:

$$(b_1 + b_2) < x_{\mathrm{s},2} < l_{\mathrm{rack}} - b_1; \tag{3.7}$$

$$b_1 < x_{\mathrm{s},4} < (b_1 + b_2). \tag{3.8}$$

#### 3.3.2.5 Fabrication

The parts of the slave robot were printed with Objet 500 Connex3 (Stratasys Ltd., Eden Prairie, MN, USA) in materials VeroClear and VeroBlack (standard quality, glossy finish). The seals were laser-cut from 0.5 mm silicone rubber (Silex Ltd, Bordon, UK). The moving parts were lubricated and the motor/clamp housings and covers were glued together. Polyetheretherketone (PEEK) fasteners were used to assemble components and pairs of epoxy glass rods (⌀ 10mm) and PEEK rods (⌀ 6mm) were used to guide the platforms (Misumi Europa GmbH, Frankfurt, Germany).

#### 3.3.2.6 MRI-Compatibility

Since the robot is composed of materials that are electrically non-conductive, non-metallic, and non-magnetic, it complies with the MR-Safe classification of the American Society for Testing and Materials (ASTM) standard F2503. A preliminary MR study was conducted as presented in Section 3.5.3.

## 3.4 Control Architecture

The system control architecture is based on the integration of the robotic system in Section 3.3 with subsequently described navigation system, which includes real-time image-guidance and haptic feedback. This configuration provides the following benefits: (1) the surgeon is always in control of the procedure, by teleoperating the slave robot through the master manipulator; (2) real-time navigation and haptic feedback guides the surgeon throughout

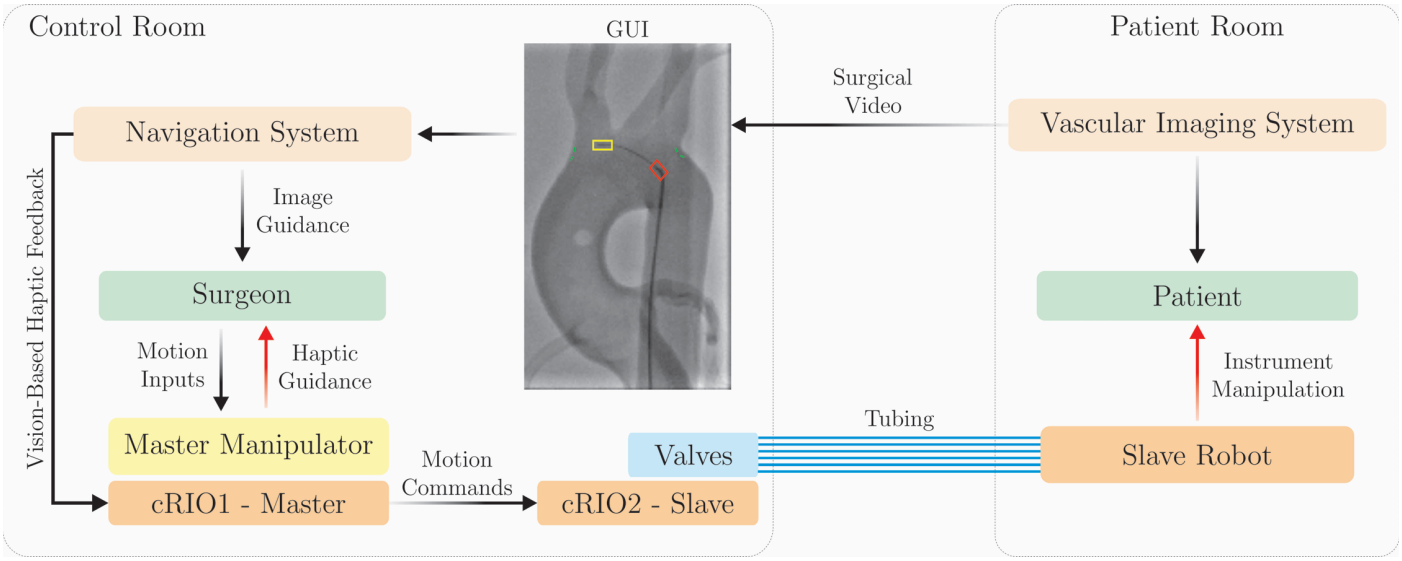



**Figure 3.5:** Control architecture

the procedure increasing the instrument manipulation accuracy and minimising endothelial damages to the vessel wall, thus potentially improving the overall safety of the procedure.

The control architecture employs a host-target structure based on a PC (host), and two real-time controllers with FPGA (targets). The PC (Windows 7, Intel i7-6700, 3.4 GHz, 16 GB RAM) runs the navigation system GUI (30 Hz), while the two real-time controllers (compactRIO 9022, National Instruments, Austin, TX, USA) run the control algorithms (1kHz) for the haptic master device (1st target) and the slave robot (2nd target). The host PC and the targets communicate via Ethernet. User inputs are captured by the master manipulator and processed by the control algorithms to generate corresponding motion commands on the slave robot which replicates the input into the surgical field. The overall system architecture is summarised in Figure 3.5 and further described below.

### 3.4.1 Navigation System

The navigation system, introduced in [266], has two main functions: (1) receive and display in real-time the intra-operative video of the surgical scene on a GUI; and (2) generate dynamic active constraints with safety margins (adaptively enforced in real-time to constrain the catheter motion) for vision-based haptic feedback. A real-time video stream of the surgical scene is acquired using an image grabber (DVI2USB3, Epiphan Video, Ottawa, Canada) from a vascular imaging system - in this study we used a fluoroscopic system for interventional radiology procedure (Innova 4100 IQ, GE Healthcare, Chicago, Il, USA). The video stream is displayed on the navigation system GUI and processed to generate vision-based haptic feedback. The matching pattern algorithm (NI Vision 2018, National Instruments, Austin, TX, USA) introduced in [266] was improved to track both catheter and guidewire in a fluoroscopy video stream providing tip position (in pixels) and orientation (in degrees). The vessel wall is dynamically tracked using the vessel tracker algorithm described in [266]. Data from instrument and vessel trackers are used to generate and render vision-based haptic feedback to the master device. The clinical user perceives a viscous friction which increases proportionally to the instrument-vessel distance (i.e. the closer the instrument is to the vessel, the higher is the generated force feedback). The viscous friction is modelled for both DOF as:

$$\dot{x}_{\mathrm{M}} = \frac{1}{\kappa_{\mathrm{d}}\kappa_{\nu}} I_{\mathrm{M,t}} \tag{3.9}$$

$$\dot{\theta}_{\mathrm{M}} = \frac{1}{\kappa_{\mathrm{d}}\kappa_{\nu}} I_{\mathrm{M,a}}, \tag{3.10}$$

where $I_{\mathrm{M,t}}$ and $I_{\mathrm{M,a}}$ are surgeon inputs, i.e., currents of the linear and rotary motor when a force is applied on the user handle, $\dot{x}_{\mathrm{M}}$ and $\dot{\theta}_{\mathrm{M}}$ are control outputs (i.e. nominal master motor velocity), and $\kappa_{\mathrm{d}}\kappa_{\nu} > 0$ is the damping of the virtual contacts, i.e. $\kappa_{\mathrm{d}}$ is generated by the proximity of the catheter tip to the vessel wall, and $\kappa_{\nu}$ by the direction and orientation of motion of the catheter with respect to the vessel wall. A comprehensive description is provided in [266] and summarised as follows: (1) The viscous friction is minimum if the instrument is located in the centre of the vessel and not pointing toward the vessel wall, (2) The viscous friction increases if the instrument-wall distance is closer and moving toward the vessel wall.

### 3.4.2 Robot Control

Master velocities related to user input and navigation in Equation (3.9) and Equation (3.10) are mapped to the slave robot with

$$\dot{\vec{q}}_{\mathrm{S},j} = \begin{pmatrix} \dot{x}_{\mathrm{S},2j-1} \\ \dot{x}_{\mathrm{S},2j} \\ \dot{\theta}_{\mathrm{R},j} \end{pmatrix} = \underbrace{\begin{pmatrix} 1 & 0 \\ 1 & 0 \\ 0 & 1 \end{pmatrix}}_{\vec{B}} \underbrace{\begin{pmatrix} S_{\mathrm{t}} & 0 \\ 0 & S_{\mathrm{r}} \end{pmatrix}}_{\vec{S}} \begin{pmatrix} \dot{x}_{\mathrm{M}} \\ \dot{\theta}_{\mathrm{M}} \end{pmatrix}, \tag{3.11}$$

where matrix $\vec{S} \in \mathbb{R}^{2\times2}$ applies input scaling for translation and rotation with user-adaptive scalars $S_{\mathrm{t}} \in \mathbb{R}_{>0}$ and $S_{\mathrm{r}} \in \mathbb{R}_{>0}$, $\vec{B} \in \mathbb{R}^{3\times2}$ describes a selection matrix to sync both linear motors during feeding and retraction, and $j = \{1, 2\}$. According to the user selection, velocities are computed for actuators driving the catheter $(j = 1)$ or guidewire manipulator $(j = 2)$. Hence, nominal frequencies of pulse-width modulated (PWM) signal pairs for dual-valve control (see Section 3.3.2) of each linear motor $i$ yield to $f_{\mathrm{S},i} = \dot{x}_{\mathrm{S},i}/s_{\mathrm{t}}$ with $i = \{1, \ldots, 4\}$ and for each rotary motor to $f_{\mathrm{S},k} = \dot{\theta}_{\mathrm{S},k}/s_{\mathrm{a}}$ with $k = \{1, 2\}$. Phase shift $\phi$ = 0.25 within signal pairs and duty cycle $\eta$ = 0.5 are constant parameters of the corresponding period [18]. The maximum frequency for safe operating conditions of actuators is set to $f_{\max} = 35$Hz which allows linear actuator velocities of $\dot{x}_{\max} \approx 10\mathrm{mms}^{-1}$ and angular velocities of $\dot{\theta}_{\max} \approx 300°\mathrm{s}^{-1}$. The 12-channel PWM output is implemented on FPGA level for reliable timing.

## 3.5 Experimental Validation

### 3.5.1 Clinical Workflow and Setup for Robotics Procedure

The main system architecture is shown in Figure 3.5. The master device is placed in the control room of the CathLab together with the host PC running the navigation system. The latter is connected to the vascular imaging system to grab the surgical video, display it on the navigation GUI, and perform image processing as described in Section 3.4. Pneumatic valves, real-time controllers and air compressor are placed in the control room as well. Plastic tubes to connect valves and slave robot are passed through the wall between the control and patient rooms. The robotic slave is located on the surgical table in the patient room as depicted in Figure 3.5 close to the patient. This configuration presents two major benefits: (1) it allows the surgeon to perform the procedure from the control room, thus not being exposed to radiation when x-ray guidance is used; (2) it allows to perform an MRI-guided procedure by locating the entire hardware in the control room except of the MR-safe slave robot. When the robotic setup is completed, the surgeon enters the patient room and manually accesses the arterial system as in a conventional procedure (e.g. through the femoral artery). Once, vascular access is gained, the instruments (catheter and guidewire) are connected to the slave robot, and the surgeon performs the surgical procedure using the master device from the control room. If needed, the procedure can be reverted to manual in a few seconds, by quickly releasing the instruments from the slave, as shown in the supplemental video.

### 3.5.2 X-Ray Fluoroscopy Pre-Clinical Trials

This section discusses the experimental setup and methods undertaken to validate the robot in a number of simulated clinical scenarios, which involved a series of arterial cannulation maneuvers performed by a qualified vas-

cular surgeon, both with the robot (i.e. using the clinical workflow above) and manually (i.e. using conventional techniques without the robot) under fluoroscopy guidance. Experiments were conducted in a research angiography theatre (Northwick Park Hospital, London, UK). The experimental setup was as shown in Figure 3.6. A vascular phantom, a semi-radiolucent soft silicone full-scale model of a normal adult human aortic arch (Elastrat, Geneva, Switzerland), was rigidly coupled to 6-DOF force-torque sensor (Mini40, ATI Industrial Automation, Apex, NC, USA) to measure forces 25Hz applied to the vascular model during the procedure. This apparatus was placed underneath an x-ray imaging system (Innova 4100 IQ, GE Healthcare, Barrington, IL, USA) to simulate a patient lying on the angiography table to undergo an endovascular procedure. The robot was then positioned and oriented relative to the phantom to simulate access into the arterial system via the femoral artery. The phantom was connected to a pulsatile pump to simulate normal human blood flow. To reduce the effect of a learning curve, the operator was given a familiarization period of 6min to manipulate the guidewire and catheter within the setup both manually and with the robot. A single guidewire (Radifocus Guide Wire M .035" 180cm angled, Terumo, Tokyo, Japan) and catheter (Beacon Tip 5 Fr VanSchie2, Cook Medical, Bloomington, IN, USA) were used throughout the experiment. The operator was then asked to perform, in turn, by manipulation of wire and catheter, cannulation of 3 arteries with increasing difficulty in the following order: the left subclavian (LSA), left common carotid (LCCA) and right common carotid (RCCA) arteries. Each task consisted of traversing the descending aorta, navigating the aortic arch, and finally cannulating the artery. At the start of the experiment a coin toss was used to determine whether the first maneuver would be robotic or manual.

The operator performed cannulation of the nominated artery four times with the determined modality (i.e. robot or manual); each time, guidewire and catheter were returned to a standard starting position in the descending aorta. The task is repeated with the second modality. Attention was then turned to the next artery, and the above sequence was repeated. Modality was not changed upon moving to a new artery, so that at least one artery would be cannulated with the robot first, and at least one would be cannulated manually first. During each manoeuvre, fluoroscopy was activated by the operator using a pedal. The feed from the video display of the imaging system, the time taken for the manoeuvre, and fluoroscopy time were recorded. Within each sequence of four arterial cannulations, the first manoeuvre was excluded from the analysis, to minimise the effect of a learning curve. For each artery-modality pair, means and standard deviations were compared for: time taken for cannulation, fluoroscopy time, mean overall force and mean maximum force. Results are summarised in Table 3.1 and discussed in Section 4.5.

### 3.5.3 MRI Preliminary Study

To demonstrate the versatility and MRI compatibility of the slave robot, a preliminary study was conducted in an MRI scanner. The robot was placed in an Achieva 3T MR imaging system (Philips Healthcare, Best, the Netherlands) equipped with a SENSE-Torso coil with 16 elements and placed adjacent to a plastic phantom of abdominal aorta filled with water (Elastrat Sàrl, Geneva, Switzerland). The phantom was placed inside the coil at the isocenter of the scanner as shown in Figure 3.7. With this setup, an MR-conditional guidewire (EPflex GmbH, Dettingen, Germany) was initially manipulated manually and then robotically. The guidewire consists of passive negative paramagnetic MR markers at discrete steps of 5cm, which provide MRI visibility. The images were acquired using a 2D imaging sequence with a large slice thickness to project the guidewire and anatomy onto a plane, emulating a fluoroscopic projection. The 2D imaging sequence used was a real time 2D Turbo Spin Echo (TSE) with the shortest




**Figure 3.6:** Experimental setup for fluoroscopy-based trials, where (1) Vascular phantom, (2) Pulsatile and continuous flow pump, (3) Slave robot, (4) C-arm, (5) Force/Torque sensor

possible echo spacing. The MRI acquisition settings were: TE/TR = 35/536.6ms, TA/image = 537ms, $\alpha$ = 45°, FoV = 300*142mm$^2$.

## 3.6 Discussion

### 3.6.1 Fluoroscopy Pre-clinical Trials Results

Results reported in Table 3.1 show a reduction of forces applied to the phantom when the robotic system is used, compared with a conventional manual technique. Using the robot, the mean overall force exerted on the phantom is significantly (Student's t-test) reduced by about 20% when cannulating LSA, and by more than 30% for LCCA and RRCA. This is corroborated by the analysis of maximum forces, which resulted in a reduction of up to 77% when

| | **LSA** | | **LCCA** | | **RCCA** | |
|---|---|---|---|---|---|---|
| | Manual | Robotic | Manual | Robotic | Manual | Robotic |
| Mean force (N) | **0.37 ± 0.21** | **0.18 ± 0.09** | **0.59 ± 0.22** | **0.28 ± 0.12** | **0.68 ± 0.33** | **0.35 ± 0.18** |
| Maximum force (N) | 1.01 ± 0.41 | 0.37 ± 0.04 | **1.45 ± 0.09** | **0.68 ± 0.22** | 1.85 ± 0.89 | 1.10 ± 0.29 |
| Cannulation time (s) | **6.7 ± 4.5** | **50.0 ± 28.3** | **32.0 ± 2.8** | **65.0 ± 10.8** | 58.3 ± 24.9 | 43.7 ± 15.0 |
| Fluoroscopy time (s) | **9.7 ± 7.3** | **134.0 ± 48.6** | **69.3 ± 31.6** | **302.0 ± 56.0** | **86.7 ± 31.4** | **189.3 ± 9.0** |

**Table 3.1:** Results of fluoroscopy pre-clinical trials (mean ± SD). Bold values indicate statistically significant results ($p<0.05$) according to Student's t-test

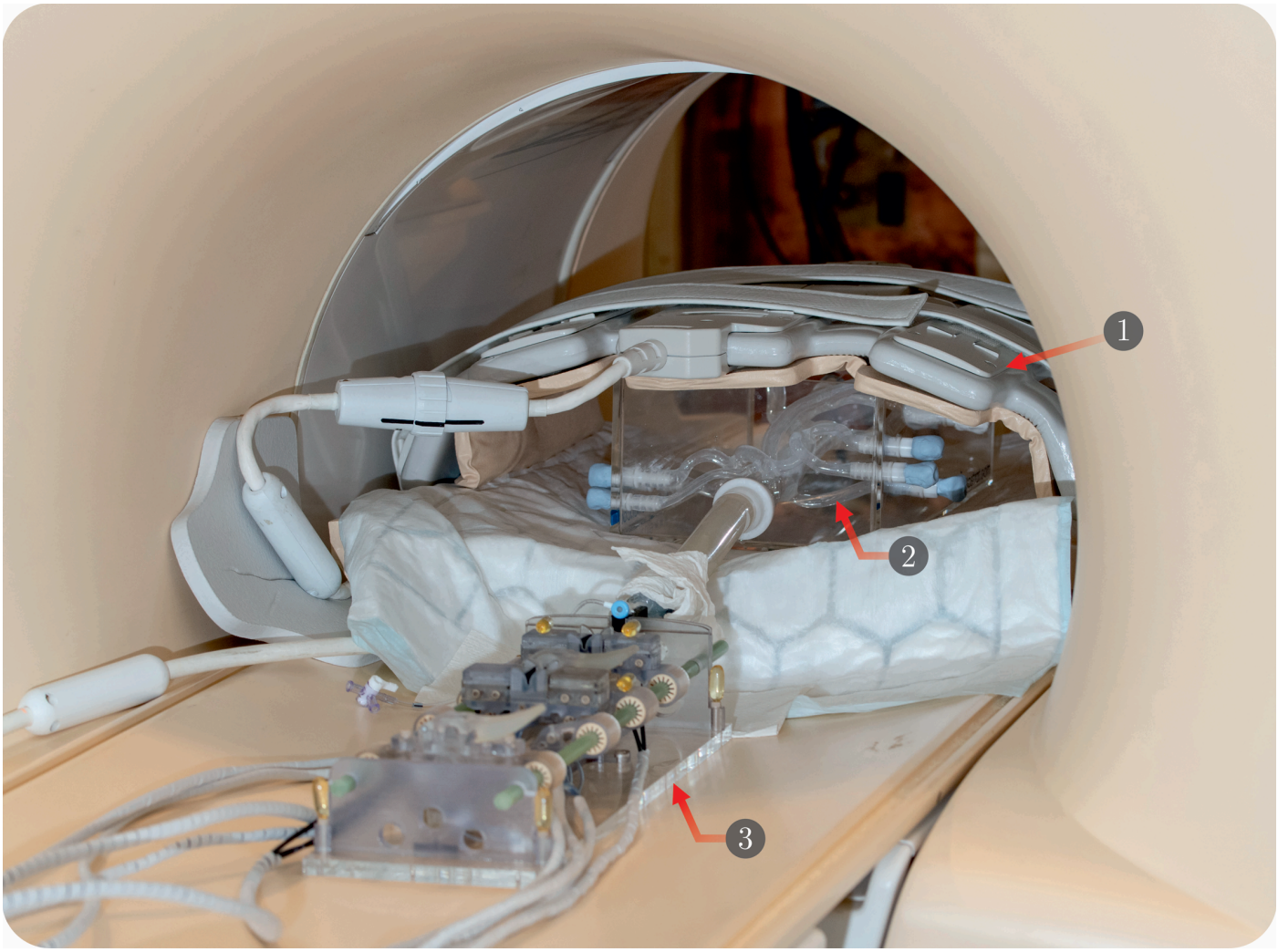



**Figure 3.7:** (a) Experimental MRI setup, where (1) SENSE-Torso coil with 16 elements, (2) Vascular Phantom, (3) Slave Robot

LCCA is cannulated robotically. This may be related to the vision-based control architecture that automatically slows down the velocity of the robot when the instrument approaches the vessel wall (see Section IV).

From the clinical point of view, this is an important consideration, as dangerous collisions between instruments and vessel wall are minimised, thus increasing the overall safety of the procedure. On the other hand, this has the effect of increasing the procedure time when compared to manually performing the procedure, as reflected by the measured fluoroscopy times. This was expected, as the trials were conducted by a trained surgeon with relevant experience in manual catheterisation but no formal training with the robotic platform. Therefore, a direct comparison of manual vs robotic procedures on this metric may not be fair at this stage. However, the results show that the robotic procedure mean fluoroscopy times were between 2 and 5 minutes. We believe that these times are acceptable and that this is a promising result, especially considering that the surgeon can operate the robot from outside the angiography room and therefore not exposed to radiation. Also, it is worth noting that the fluoroscopy time refers to the entire procedure, including the traversal of the descending thoracic aorta, the navigation of the aortic arch, and finally the cannulation of the target artery (LSA, LCCA, RCCA).

When comparing fluoroscopy with cannulation time (i.e. the time spent to cannulate only the target artery), it appears that when the robot is used, a high proportion of the time is spent navigating the descending aorta and

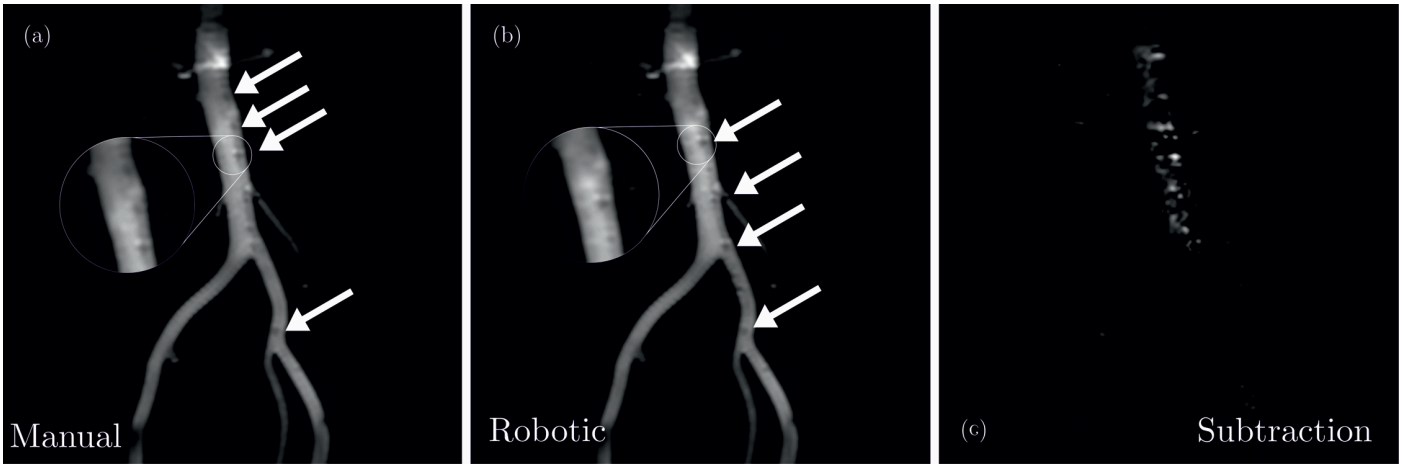



**Figure 3.8:** (Projection of the abdominal aorta and illiac arteries with (a) manual, (b) robotic guidewire retraction. Magnified views show the passive MR markers of the guidewire (black spots, (c) Difference image

the aortic arch. These relatively simpler tasks can be done more quickly manually. However, when a more complex task such as cannulation of the RCCA was performed, the robotic procedure time was comparable with (slightly shorter than) the manual. This suggests that the robot can be potentially employed in complex phases of the procedure (when manipulation accuracy and safety are more relevant than time), while manual manipulation can continue to be used for less critical phases that can be accomplished equally well and more quickly in this way. The proposed system lends itself to this approach, given its capability of quickly switching between robotic and manual manipulation. Overall, these trials demonstrated that robotic cannulation of the LSA, LCCA, and RCCA is feasible using the proposed platform. Surgeon's skills are successfully captured by the master device and mapped to the slave robot to accomplish the cannulation.

### 3.6.2 MRI

Figure 3.8a, b shows the projected MRI image of the manual and robotic retractions of the guidewire, with no geometric distortions detected during the robot manipulation. Figure 3.8c shows the image difference between Figure 3.8a, b. The bright spots in the subtraction image might be caused by collisions of the guidewire with the anatomy and susceptibility artefacts of the passive negative MR markers. The average signal intensity of the brightest patch and the standard deviation of the background (noise) were evaluated for each image. The computed signal-to-noise ratio (SNR) show no significant change for both interventions ($\approx$ 26dB).

## 3.7 Conclusions

A master-slave system platform and a navigation framework for manipulation of standard endovascular instruments in different imaging environments has been developed. The proposed system was evaluated pre-clinically by cannulating three target arteries (LSA, LCCA and RCCA) under fluoroscopy guidance. Results show a reduction of forces applied when the robotic system is used compared to manual interventions. This was followed by a preliminary MRI compatibility experiment. The system shows its capability of manipulating instruments under MRI which not only potentially eliminates x-ray exposure, but also highlight its potential to improve manual MRI-guided treatment. In fact, based on [16], performing manual interventions under MRI creates additional challenges such as

risk of musculoskeletal injury, which can, in turn, increase the possibility of medical errors and risk for the patient. In the following chapter, the platform is further optimised and evaluated to determine its safety and efficacy within a standard clinical workflow.

Chapter 4

# An MR-Safe Endovascular Robotic Platform: User Study

"The work presented in this chapter (excluding the animal study) was published in the Transactions on Biomedical Engineering. © 2021 IEEE. Reprinted, with permission, from (Kundrat, D., Dagnino, G., Kwok, T. M. Y., Abdelaziz, M. E. M. K., et al. "An MR-Safe Endovascular Robotic Platform: Design,Control, and Ex-Vivo Evaluation". In:IEEE Transactions on Biomedical Engineering(2021), pp. 1–1, doi: 10.1109/TBME.2021.3065146 [267])."

## 4.1 Contribution

This chapter focuses on the optimisation of the robotic platform based on the preliminary results of Chapter 3 to meet the requirements of frequent clinical use and performance characteristics. The previously adapted pneumatic stepper motors used in Chapter 3 were optimised to enable robust actuation of the second iteration of the slave robot. The next generation of the master-slave robotic platform has been equipped with real-time low-level controllers to handle data processing and bus communication. The bus-based device interfacing to a decentralised high-level controller has enabled full system integration and further supports prospective scalability. A user study with seven clinical experts demonstrates the performance characteristics of the proposed platform and an animal study with an expert endovascular surgeon validates its efficacy and safety and motivates prospective deployment to interventions with MR-guidance.

The work is structured as follows. Design, control, and navigation of the robotic framework are presented in Section 4.2. Further on, the experimental setup and design of the user study are introduced in Section 4.3. This is complemented by evaluation methodologies and statistical considerations. Study results in Section 4.4 and a discussion in Section 4.5 underline performance characteristics. To further evaluate the safety and efficacy of the robotic platform, an in-vivo study is presented and discussed in 4.6. Lastly, Section 5.10 concludes the work and provides an outlook on future work.

## 4.2 Robotic Framework

The general architecture of the robotic framework is summarised in Figure 4.1. The robotic platform presents a master-slave configuration and includes the following components: 1) MR-safe slave robot, 2) master manipulator, 3) control workstation, and 4) navigation system. Only the MR-safe slave robot is located in the interventional room and facilitates instrument manipulation. In contrast, the master manipulator and valve controller are located outside the controlled MR environment to implement remote input and valve-based generation of pneumatic pressure patterns for motor control. Real-time imaging data from fluoroscopy or MR are provided to the operator located in the control room. This enables closed-loop visualisation of operator inputs. Features of master, slave, and control hierarchy are detailed in subsequent sections.

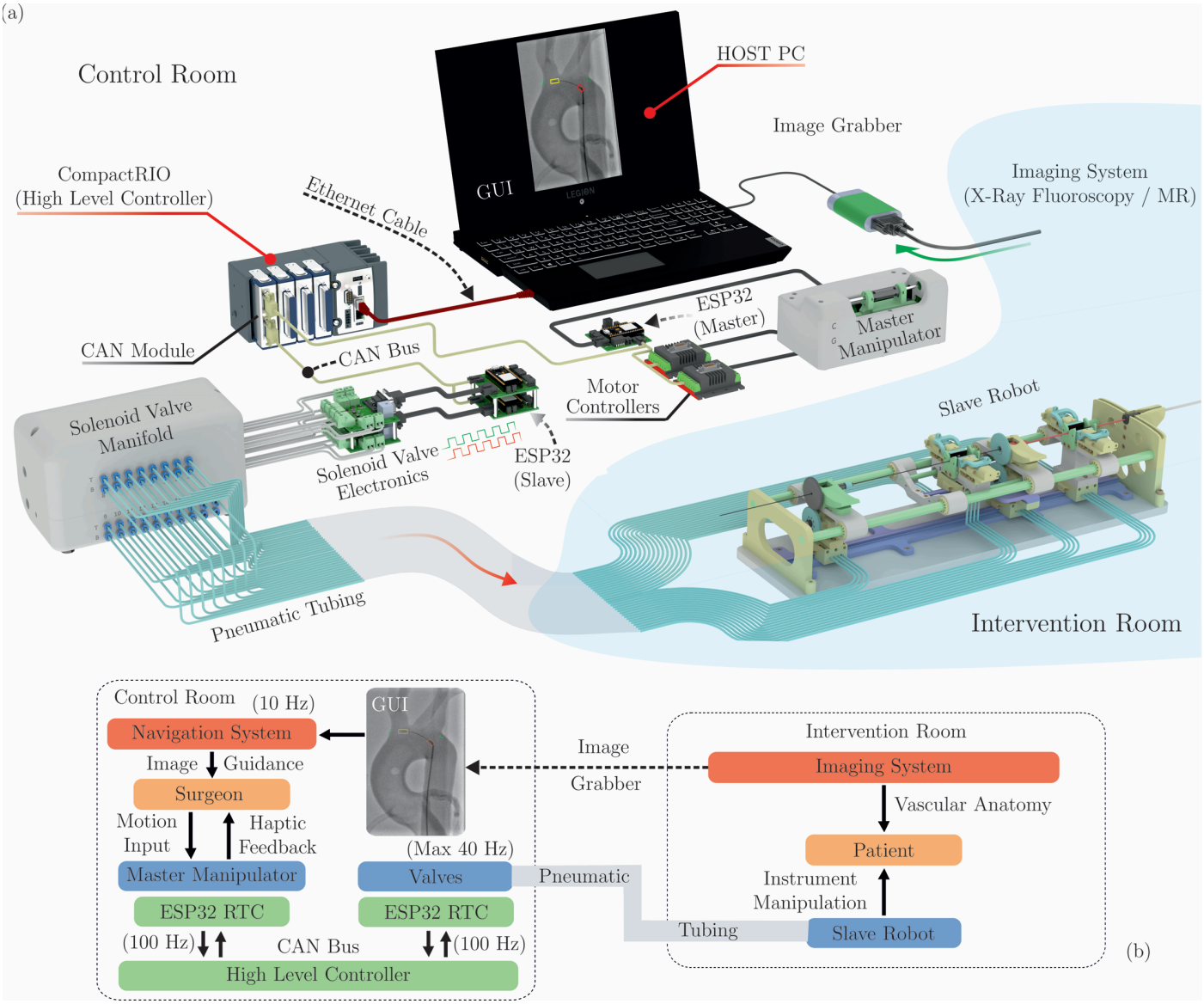



**Figure 4.1:** (a) CAD rendering representing the system architecture of the proposed framework. (b) System architecture of the proposed versatile robotic framework. The surgeon, located in the control room, teleoperates the MR-safe slave robot deployed in the intervention room by manipulating the master manipulator. The navigation system provides real-time visual guidance and haptic feedback is rendered through the master manipulator to guide the surgeon during the procedure.

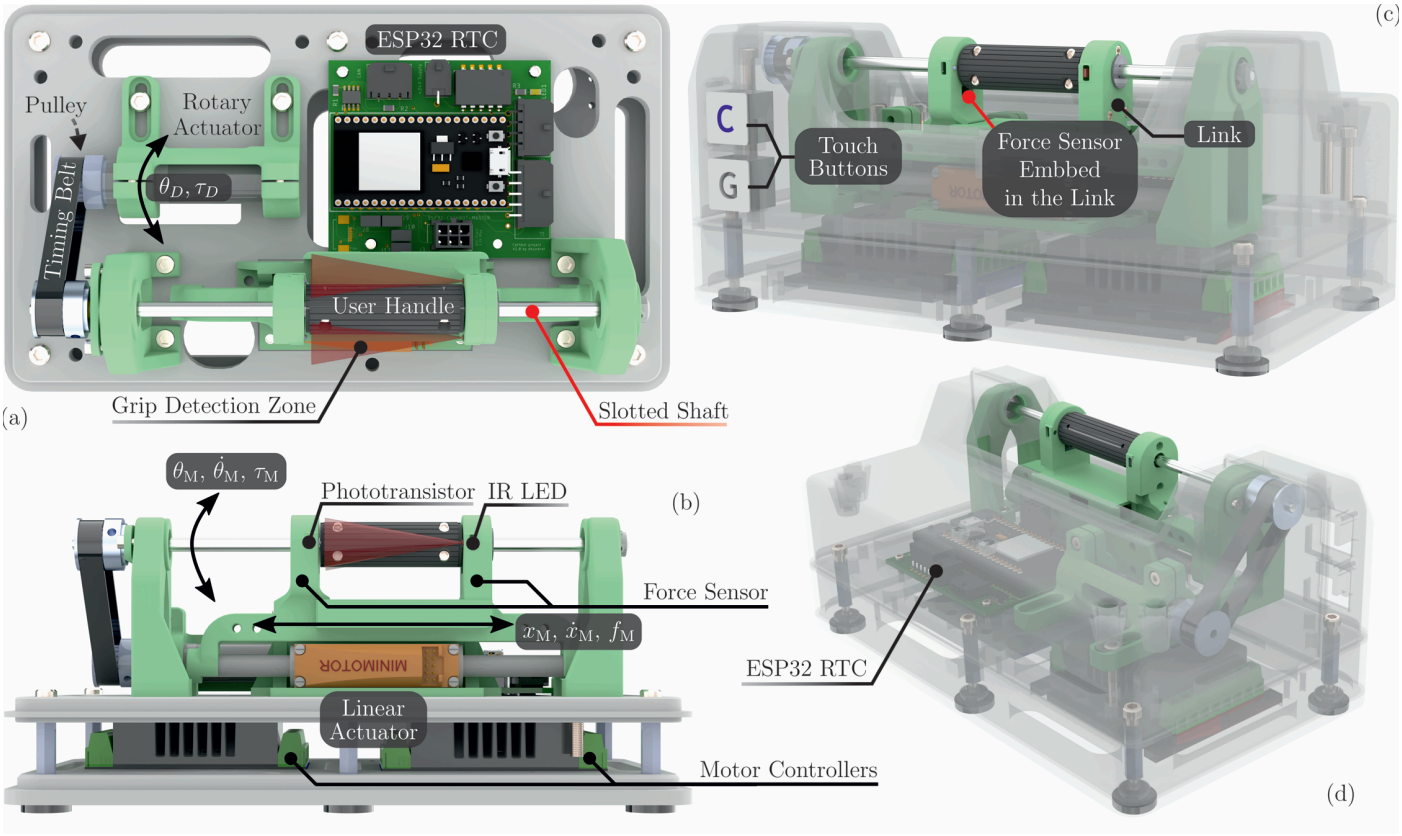



**Figure 4.2:** Master Manipulator CAD renderings (a) Top view without the outer cover, (b) Front view without the outer cover, (c-d) Isometric views with the outer cover

### 4.2.1 Master Manipulator

The main design objective of the master manipulator targets intuitive and remote manipulation of endovascular off-the-shelve instrumentation for optimal teleoperation transparency and procedural assistance. Master kinematics that mimic conventional manual instrument manipulation and feasibility of haptic feedback were targeted, enabling clinicians to control the instruments in a manner already familiar and intuitive to them. This workflow commonly comprises a two DoF motion of catheters and guidewires, i.e. manual linear push/pull displacement and rotation of the extracorporeal section. Inspired by the master prototype presented in the previous chapter, the proposed device in Section 4.2 has been revised according to expert feedback to match clinical requirements. The core component of the HMI considers a cylindrical handle that substitutes the direct contact between the clinician and the instrument. As in the case of manipulating catheters/guidewires, the handle can be rotated and displaced linearly. The electro-mechanical design applied to both DoF enables the rendering of torque and force feedback. Finite stroke lengths of the linear input are compensated by an automated homing feature. This adapts human motion patterns of concurrent object gripping and manipulation. After linear displacement and sensor-based detection of a terminated action, the handle is homed to the centre of the executable stroke range.

Contrary to what has been proposed in the previous control architecture (Section 3.4), the real-time controller (compactRio 9022, National Instruments, Austin, TX, USA) employed to run the control algorithm for the haptic master manipulator, is substituted with a dual-core ESP32 system-on-the-chip (SoC) controller (Espressif Systems, Shanghai, China) with FreeRTOS real-time operating system. The EPS32 microcontroller implements signal acquisition, signal processing, control, and management of the CAN bus communication with the high level controller. The first

core handles signal acquisition, processing, and control tasks. The second core is exclusively dedicated to low latency bus communication.

As in the case of the previous design, the user handle contains a torque-resistant linear bushing that is guided on a bespoke slotted shaft (Bosch Rexroth GmbH, Lohr am Main, Germany). This configuration facilitates linear handle displacement $x_{\mathrm{M}}$ from operator input. Mechanical characteristics of the bushing concurrently enable angular handle input $\theta_{\mathrm{M}}$. This configuration realises operator input in two DoF, i.e. feeding/retraction and angular displacement. This concept enables haptic feedback for both DoF. The latter is generated by linear and rotary brushless DC motors (1247 and 1226 B012, Faulhaber GmbH, Schönaich, Germany). Motor control is provided by motion controllers with CAN interface (MCLM/MCBL 3006, Faulhaber GmbH, Schönaich, Germany). The transmission principle of the slotted shaft motivates stationary drive integration and enhanced manipulation dynamics. The torque feedback rendered to the gripped handle yields with reduction ratios to $\tau_{\mathrm{M}} = i_{\mathrm{G}} i_{\mathrm{P}} \tau_{\mathrm{R}}$, where ($i_{\mathrm{G}}$ =16) is the gearhead ratio, ($i_{\mathrm{G}} = 1$) is the pulley ratio, and $\tau_{\mathrm{R}}$ is the motor-sided torque input. Force feedback $f_{\mathrm{M}}$ along the handle axis is directly generated under disregard of external disturbances by the linear drive within a maximum stroke of $\pm$ 20mm.

The interaction between operator and master is detected with two sensor concepts for safety and control. Primarily, operator proximity and contact with the handle are sensed wirelessly by two opposing pairs of infrared LEDs (VSMY2850G, Vishay, Malvern, PA, USA) and phototransistors (SFH 3015, Osram AG, Munich, Germany). Each pair forms an optical switch that is mounted to the support structure in parallel to the handle. Operator interaction modulates intensity levels detected by phototransistors. Corresponding voltages are processed by the ESP32 ADC module. A valid grip $\rho_{\mathrm{M}}$ is detected if sensor values exceed threshold $\sigma_{\mathrm{G}}$. Secondly, after device-operator contact is acknowledged, user intentions $\kappa_{\mathrm{M}}$ (feeding, retraction) are extracted from two miniature uniaxial force sensors (FSS1500NSB, Honeywell International Inc., Charlotte, NC, USA) which are located adjacent to both side of the user handle. The latter are integrated to the support link (see Figure 4.2c) to measure interaction forces between displaced handle and link. Sensor voltages are processed with a customised differential amplifier and output voltages are sampled using the ADC of the ESP32 board. A valid operator intention is indicated if sensor values exceed threshold $\sigma_{\mathrm{I}}$. Based on a preliminary study with novice and expert users, the trigger threshold was determined to 3N, enabling a robust decoupled manipulation of rotary and linear axis without cross-talk. This is further supported by velocity modulation of the handle from haptic feedback (Section 4.2.4). Two capacitive touch sensors located at the front of the housing enable the operator to switch the driver mode $\lambda_{\mathrm{M}}$ between catheter or guidewire instrumentation. Lastly, the master state yields to

$$\boldsymbol{q}_{\mathrm{M}} = \left( x_{\mathrm{M}}, \theta_{\mathrm{M}}, \dot{x}_{\mathrm{M}}, \dot{\theta}_{\mathrm{M}}, f_{\mathrm{M}}, \tau_{\mathrm{M}}, \rho_{\mathrm{M}}, \kappa_{\mathrm{M}}, \lambda_{\mathrm{M}} \right)^{\mathrm{T}} \in \mathbb{R}^9. \tag{4.1}$$

Intuitive visual rendering of device states is provided by LED embedded to the housing, e.g. flashing or fading illumination. Generally, ADC acquisition and processing is executed at 200Hz and 12-bit resolution. The module updates the master state in Equation 4.1 and error messages on the common CAN bus at 100Hz and reads CAN data from the high-level controller for settings and diagnostics. It is externally supplied by 24V. The device footprint is (191 $\times$ 111 $\times$ 85)mm$^3$.

### 4.2.2 Design Optimisation of Pneumatic Actuators

MR-safe actuation implemented in the previous chapter with linear and rotary pneumatic stepper motors adapted from [268]. These mechanisms contain dual pistons that are acting on a rack or gear. Actuators were fabricated as a whole with additive manufacturing based on the polyjet technology (Objet 500 Connex3, Stratasys Ltd., Eden Prairie, MN, USA) using VeroClear materials in standard quality and glossy surfaces.

Although principles of employed motors enable robust actuation in combination with valve units, the need for design optimisation was identified in our pilot user study [269]. This substantiated to:

1. Use of adhesives for actuator assembly disturbed piston motion and prevented corrective actions.
2. Deficient piston sealing with silicone patches lowered force generation and randomly caused excessive leakage.
3. Reduction of parts desirable to enable advanced fabrication technologies (e.g. injection moulding).

Pressure leaks are mainly due to clearances between additively fabricated pistons and housings to ensure component motion [268, 270]. Sealing was implemented with floating silicone patches in the piston chamber. Although this approach minimises friction, the sealing performance is inferior and may affect generation of piston forces. This also limits multi-actuator networks due to leak accumulation and generates acoustic emissions. The latter lowers the device acceptance in clinical environments. Prior actuators based on rectangular pistons [268, 269] were converted to cylindrical pistons (see Figure 4.3). The sealing uses industrial O-rings (1.6/9.3 VITON™Rubber

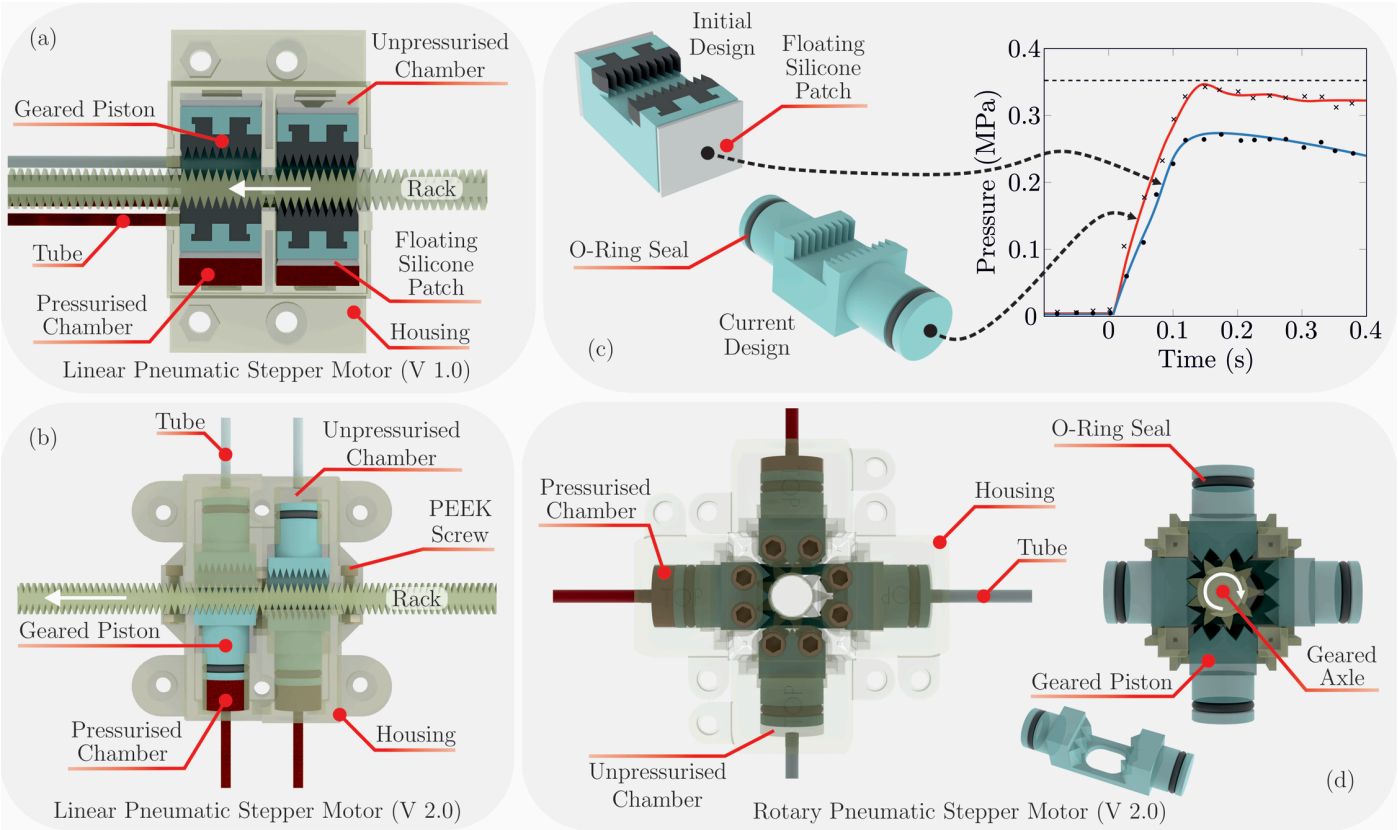



**Figure 4.3:** (a) Linear pneumatic stepper motor with floating silicone patch (previous design employed in the pilot study). (b) Linear pneumatic stepper motor with o-rings sealing (proposed new design). (c) Pressure-time plot for the proposed new piston design (red plot), previous piston design (blue plot), nominal pressure (dashed). Raw data is fitted with a polynomial. (d) Rotary pneumatic stepper motor with o-rings sealing (proposed new design).

O-Rings, Simply Bearings, Leigh, UK) that are installed to grooves in the piston.

In order to evaluate the design optimisation, pressure responses of actuators (miniaturised T-63) from related work and proposed approach were compared experimentally. Piston chambers of both designs were equipped with pressure gauges (ABPMANN004BGAA5, Honeywell Inc, Charlotte, NJ, USA) and sampled at 1kHz. A secondary pressure gauge is attached to the reservoir outlet to reference the nominal pressure of 0.35MPa. The pneumatic stepper motors and the valves were connected with tubes of 3m length in total and composed of a 2m section with 3mm outer diameter (PUN-3X0,5-SW, Festo AG, Esslingen, Germany) and 1m section with 2mm outer diameter (TU0212C-20, Active Air Automation, Surrey, UK).

Following assumptions in [268], both observations have response latencies of 10 ms to 15 ms with a valve contribution of 1.8 ms and tube propagation (length 3m $\approx$ 9ms latency). Beyond that, the design optimisation demonstrated lower chamber pressure losses from only 10% to 23% with respect to the nominal pressure of 0.35MPa (see Figure 4.3c).

Beyond pneumatic optimisation, the part number for the linear actuator was reduced by 30 $\%$. Reversible actuator assembly was achieved with five PEEK screws (Misumi Europa GmbH, Frankfurt, Germany) after piston mounting. The optimised MR-safe linear actuator is shown in Figure 4.3b. Dimensions are slightly increased to (47 $\times$ 30 $\times$ 18)mm$^3$ to accommodate piston strokes. With a chamber pressure of 0.35MPa, a piston area $A_{\mathrm{P}}$ =63mm$^2$, and ideal sealing conditions, the piston force results to 18.5N. The corresponding nominal output force report to 30.6N for the linear actuator according to [18]. This design was also transferred to rotary actuators and yielded for the given geometry a nominal output torque of 1.15Nm/MPa. The maximal axial force of each penumatic clamp (see Figure 4.4f, g), without presence of slipping is determined by the estimated friction coefficient ($\approx$0.55) of the material pairing between the high performance textured rubbery inlay (BFG1, Thorlabs GmbH, Bergkirchen, Germany) of the clamp and the instrument (catheter, guidewire) with plastic coating to 10.2N. Optimisation of pressure responses for rotary mechanisms was achieved at the expense of a slightly increased part number and dimensions. Hence, the robotic platform described in the previous chapter is equipped with optimised pneumatic actuators. A comprehensive accuracy evaluation of this actuation principle is described in [18].

### 4.2.3 MR-safe Slave Robot

Kinematics of the slave robot mimic manual patterns of instrument handling (catheter/guidewire) in 6 DoF and enable mapping of master input according to Section 4.2.4. The device consists of four modular platforms that are attached to a common linear rail as depicted in Figure 4.4. More specifically, catheter (CC) and guidewire (GC) carriers are dedicated to instrument clamping and linear force transmission for the realisation of insertion and retraction. Both platforms are equipped with pneumatic clamps and linear actuators described in Section 4.2.2. Rotary catheter (CR) and guidewire (GR) platforms implement transmission of angular motion to corresponding instruments. Both rotary actuators are further linked to linear actuators that share the common rail. This approach accommodates for instrument displacement and is complemented by the stacked layout of platforms CR and GC.

Usability and efficient transition from robotic to manual instrument manipulation was facilitated by customised instrument add-ons (see Figure 4.4c, d). A bespoke spur gear with Luer lock interface enables direct docking of catheters to platform CR and meshing with the rotary actuator. Similarly, a guidewire clip was implemented for plat-

form GR. Dimensions of add-ons were adapted from off-the-shelf instruments to address versatility. Equivalently to Section 4.2.2, structural components were additively fabricated or customised from PEEK material to comply with MR-Safe classification of the American Society for Testing and Materials (ASTM) standard F2503. The footprint of the robot yields $(520 \times 140 \times 120)\text{mm}^3$. With respect to the clinical workflow, the design concept of the slave robot targets a cost-effective, intuitive, and fast setup using a single-use robotic technology. After clinical deployment, the slave robot and the associated pneumatic tubing are detached from the valve unit interface in the shielded wall opening of the MR facility. Hence, sterilisation of the platform and tubing becomes obsolete. Due to applied design principles and actuation technology, a direct transition to manufacturing with injection moulding is feasible.

An array of fourteen 5/2-way directional pneumatic valves (MHA2-MS1H-5/2-2, Festo AG, Esslingen, Germany) handles independent piston motion of employed actuators and clamps (see Figure 4.1a, part labelled as the solenoid valve manifold). Valve switching is triggered by a customised real-time valve controller based on two ESP32 controllers (see Section 4.2.1). Both controllers are linked to the common CAN bus and hardware timers on each controller enable independent control of three pneumatic motors with signal sequences described in Section 4.2.4. The primary core is dedicated to monitoring and settings adjustment for signal generation. The secondary core handles bus communication at 100Hz. The actual state of the slave robot is consolidated to

$$\boldsymbol{q}_\mathrm{S} = \left(\boldsymbol{x}_\mathrm{C/G}, \boldsymbol{\theta}_\mathrm{C/G}, \boldsymbol{\gamma}_\mathrm{C/G}\right)^\mathrm{T}, \tag{4.2}$$

where $\boldsymbol{x}_\mathrm{C/G} = (\boldsymbol{x}_\mathrm{C}, \boldsymbol{x}_\mathrm{G})^\mathrm{T}$ is composed of linear platform displacements $\boldsymbol{x}_\mathrm{C} = (x_\mathrm{CC}, x_\mathrm{CR})^\mathrm{T} \in \mathbb{R}^2$ and $\boldsymbol{x}_\mathrm{G} = (x_\mathrm{GC}, x_\mathrm{GR})^\mathrm{T} \in \mathbb{R}^2$ (see Fig. 4.4a), $\boldsymbol{\theta}_\mathrm{C/G} = (\theta_\mathrm{C}, \theta_\mathrm{G})^\mathrm{T} \in \mathbb{R}^2$ describes the angular instrument configuration, and $\boldsymbol{\gamma}_\mathrm{C/G} = (\gamma_\mathrm{C}, \gamma_\mathrm{G})^\mathrm{T} \in \mathbb{R}^2$ is the clamping condition.

### 4.2.4 Control and Navigation

The control architecture integrates master and slave devices with a high-level controller (see Figure 4.1). The latter accommodates the real-time image guidance framework for rendering of haptic feedback.

The high-level control architecture uses a host-target layout with PC (host) and a dedicated real-time controller (target) for algorithmic prototyping. Host and target are linked via Ethernet interface. The main controller is implemented on a real-time FPGA target (compactRIO 9022, National Instruments, TX, USA). The target delegates CAN messages between the master manipulator and the slave valve controller. Beyond that, the controller computes the velocity mapping to the slave kinematics from actual master input. General mapping $\mathbb{R}^2 \rightarrow \mathbb{R}^3$ of the two DoF input to the three DoF slave kinematics is given for each instrument by

$$\dot{\boldsymbol{q}}_\mathrm{S} = \begin{pmatrix} \dot{\boldsymbol{x}}_\mathrm{C/G} \\ \dot{\boldsymbol{\theta}}_\mathrm{C/G} \end{pmatrix} = \begin{pmatrix} 1 & 0 \\ 1 & 0 \\ 0 & 1 \end{pmatrix} \begin{pmatrix} S_\mathrm{t} & 0 \\ 0 & S_\mathrm{a} \end{pmatrix} \begin{pmatrix} \dot{x}_\mathrm{M} \\ \dot{\theta}_\mathrm{M} \end{pmatrix} \in \mathbb{R}^3, \tag{4.3}$$

with adaptive linear and angular input scaling $S_\mathrm{t} \in \mathbb{R}_{>0}$ and $S_\mathrm{a} \in \mathbb{R}_{>0}$. Hence, valve trigger frequencies for linear and angular actuators are computed to $f_\mathrm{t} = \dot{x}_\mathrm{S}/s_\mathrm{t}$ and $f_\mathrm{a} = \dot{\theta}_\mathrm{S}/s_\mathrm{a}$, respectively. Linear and angular step sizes are determined from the actuator design to $s_\mathrm{t} = 0.3\text{mm}$ and $s_\mathrm{a} = 10°$.

Paired signals are offset with constant phase shift $\phi = 0.25$ at duty cycle $\eta = 0.5$. Valve trigger frequencies are

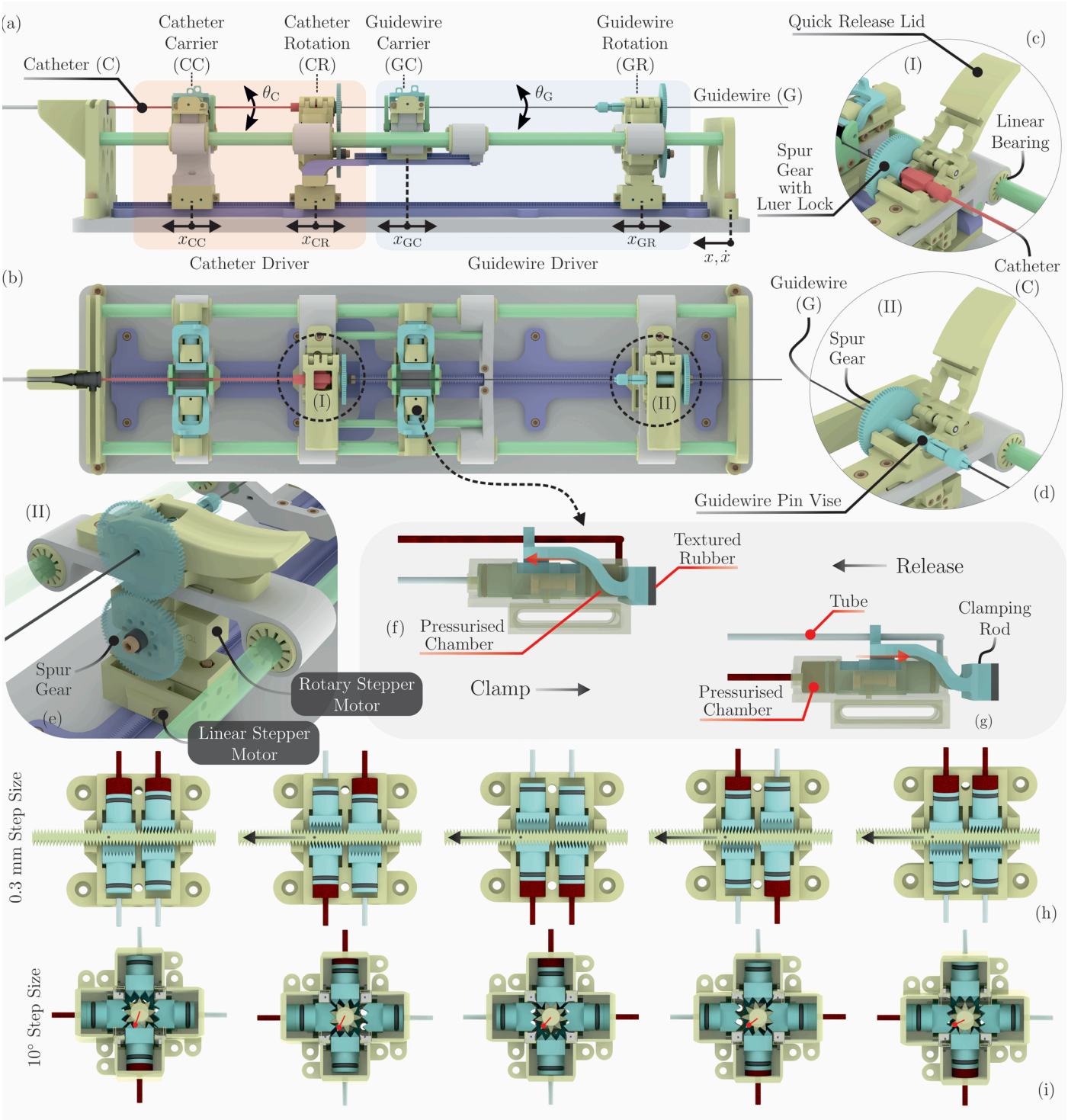



**Figure 4.4:** (a) Slave CAD model with kinematic annotations of the corresponding platforms. (b) Top view of the slave with the two quick release mechanisms (I) and (II) Labelled. (c-d) Inset of the quick release instrumentation mounting for the introduction of rotary motion to the catheter (c) and guidewire (d). (e) Back-sided view of the GR platform. (f-g) Inset of the optimised clamp. (h) Sequence of piston states during the translation of the rack to the left. After four steps the linear motor is back in the first state. The stepper motor has a step-size of 0.3mm. (i) Sequence of piston states during clockwise rotation of the geared axle. After four steps the rotary stepper motor is back in the first state. The rotary motor has a step size of 10°. Acronyms: Catheter (C), guidewire (G), catheter carrier (CC), guidewire carrier (GC), catheter rotation (CR), guidewire rotation (GR), and rotary actuator (RA)

restricted to a maximum of 40Hz. The multi-channel (12×) trigger output for control of six actuators is generated by customised timer modules on two ESP32 boards. Prior to experimental deployment, all actuators are commanded

to a homing procedure using hard stop referencing.

Additionally, an image-based navigation system introduced in [266] was considered for the generation of active constraints rendered through haptic feedback on the master manipulator. In contrast to common teleoperation scenarios with sensing integrated to the slave hardware, this feedback is generated from image metrics and/or user input.

Primarily, the system enables to display the image stream grabbed from the fluoroscope (DVI2USB3, Epiphan Video, Ottawa, Canada) in a customised GUI and to derive parameters for force and torque computation. Instrument tip and vessel walls were tracked in acquired sequences, as described in [266]. The operator observed a viscous friction that increased proportionally with the tip-vessel distance. Thus, a decreasing distance of instrument and vessel causes increased feedback forces and/or torques. The viscous model is given for linear and angular DoF by:

$$\dot{x}_{\mathrm{M}} = \frac{1}{\kappa_{\mathrm{d}}\kappa_{\nu}} I_{\mathrm{M,t}} \tag{4.4}$$

$$\dot{\theta}_{\mathrm{M}} = \frac{1}{\kappa_{\mathrm{d}}\kappa_{\nu}} I_{\mathrm{M,a}}, \tag{4.5}$$

where $I_{\mathrm{M,t}}$ and $I_{\mathrm{M,a}}$ are measured currents of linear and rotary motor when the operator applies a force/torque on the master handle. Parameters $\dot{x}_{\mathrm{M}}$ and $\dot{\theta}_{\mathrm{M}}$ are nominal control outputs and product $\kappa_{\mathrm{d}}\kappa_{\nu} > 0$ sets the damping of virtual contacts. More precisely, the distance of the instrument tip and vessel wall determines $\kappa_{\mathrm{d}}$ and the pose of the tip with respect to the vessel parameter $\kappa_{\nu}$. Algorithmic details are provided in [266, 269].

## 4.3 UserStudy

The device performance was evaluated in a user study with vascular surgeons and senior vascular surgery registrars. This section outlines the experimental setting and workflow. Secondly, evaluation methodologies and statistical considerations are presented.

### 4.3.1 Experimental Setup

The user study was conducted in a research cardiovascular imaging suite using a single-plane fluoroscope (Artis Q ceilinc, Siemens Healthineers, Erlangen, Germany). The latter featured a detector panel size of (30 x 40) cm$^2$ with a sensor array of (1920 x 2480) px resulting in 156$\mu$m resolution. For trials with remote teleoperation, the master manipulator was located in the control room in the proximity of the proprietary user interface of the fluoroscope, as shown in Figure 4.5a. This provided subjects with direct X-ray monitoring of instrument motions in the phantom environment from user inputs to the master manipulator.

Two different anatomical phantoms were considered for simulation of abdominal and thoracic vascular scenarios. The abdominal phantom (A-S-N-003, Elastrat Sàrl, Geneva, Switzerland) is depicted in Figure 4.5c, and comprises the abdominal aorta and iliac arteries with major branch arteries. Percutaneous vascular access was simulated with the placement of an introducer in the femoral artery connector of the model (see Figure 4.5c). The thoracic aorta and supra-aortic branches were simulated by a thoracic phantom (T-S-N-004, Elastrat Sàrl, Geneva, Switzerland), as shown in Figure 4.5d. The abdominal aortic section in this model was substituted by a bespoke aortic section

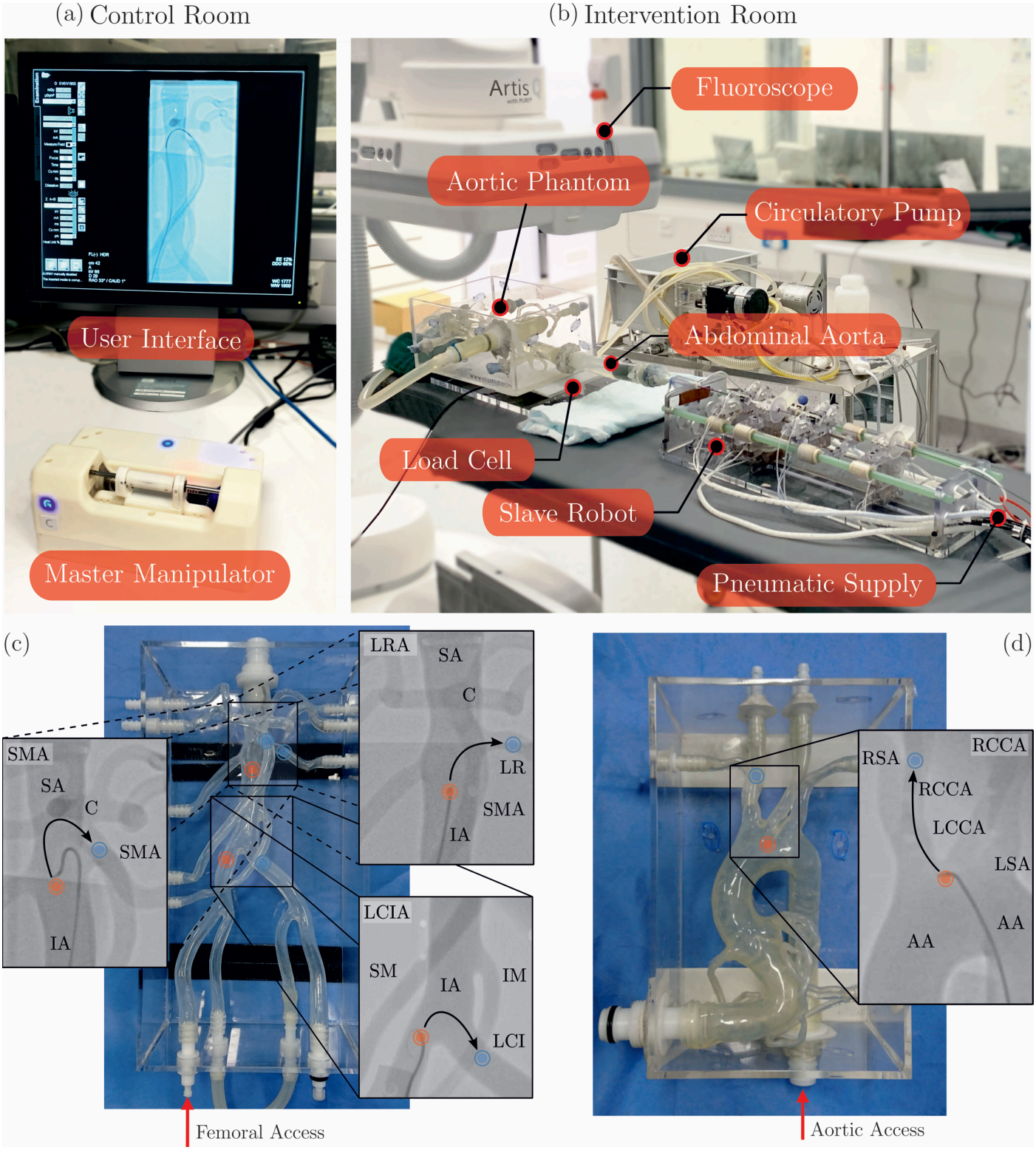



**Figure 4.5:** Experimental setup of user study: (a) Master manipualtor console with user interface in control room and (b) slave robot deployed to phantom installed in fluoroscopic monitoring (c) Phantom setup and task conditions: (c) Abdominal phantom with LCIA, LRA, and SMA tasks. (d) Thoracic phantom with RCCA task. Red markers denote start configurations and blue markers denote the nominal cannulation target of each trial. Acronyms describe: infrarenal aorta (IA), suprarenal aorta (SA), superior mesenteric artery (SMA), inferior mesenteric (IM), celiac artery (C), left subclavian artery (LSA), aortic arch (AA), right subclavian artery (RSA), left subclavian artery (LSA), aortic arch (AA), and left common carotid artery (LCCA).

(see Figure 4.5b) that replicates anatomical distances.

Phantoms are located in the head area of the fluoroscope's floating top table. Models are placed on a radiolucent platform rigidly linked to a load cell (Mini40, ATI Industrial Automation, Apex, NC, USA). This facilitated measurements of interaction forces between phantom and vascular instrumentation. Phantoms were mechanically decoupled from the slave robot with a percutaneous introducer sheath that was inserted to corresponding model inlets.

Both phantoms were connected to a circulatory pump (FAIN Biomedical Inc., Nagoyashi, Japan) to simulate physiological pulsatile blood flow and pressure conditions. A surfactant (Elastrat Sàrl, Geneva, Switzerland) was added to the water tank (30 vol% concentration) according to manufacturer guidelines to adjust the model friction. The heart rate was set to 50bpm and peak systolic pressure to approximately 120mmHg.

The slave robot was placed in the centre of the floating table closely located to the percutaneous introducer. Guidewires and task-specific catheters were installed to the slave device, inserted to the introducer, and advanced to specific starting position in the corresponding phantom prior to each trial (see Figure 4.5c, d). Air compressor (PT15, Bambi Air Ltd, Birmingham, UK) and valve unit were installed in 2m distance to the foot section of the floating table, i.e. a low-risk distance of 4m to the imaging unit taking prospective MRI deployment into consideration.

Kinematics data of master and slave robot, interaction forces, and video streams were acquired from the main controller framework and synchronised based on timestamps. Data was stored at 10Hz, i.e. governed by the maximum frame rate of the fluoroscopic image stream.

### 4.3.2 Study Design

Subjects were recruited from the Department of Vascular Surgery, St Mary's Hospital, London based on Imperial College London (ICL) recruitment guidelines. All participants ($N$ = 7) were either fully qualified vascular surgeons, or senior vascular surgery registrars in the final 1-2 years of training. Subjects received written information, and gave their informed consent for participation and post-experimental data analysis. The study was conducted in accordance with ICL ethics and approved by the ICL research ethics committee (approval 19IC5681). Data was recorded and stored anonymously. Prior to each experimental series, subjects were allowed a 5 min familiarisation period with the robotic teleoperation framework and were provided with an induction to the phantom environment for manual trials.

**Table 4.1:** Catheter and guidewire instruments of the user study.

| **Task** | **Manufacturer** | **Instrument** | Size (Fr) | Length (cm) |
|---|---|---|---|---|
| ‡ | Terumo Corp. | Radifocus Introducer II sheath, B Kit, angled plastic guidewire | 5 | 10 |
| ‡ | Terumo Corp. | Radifocus Guidewire M, 10 mm flexible length, angled, hydrophilic coatin | 2.6 | 180 |
| LCIA | Merit Medical | Impress Catheter, shape RIM, braided | 5 | 65 |
| LRA | Merit Medical | Impress Catheter, shape Cobra 2, braided | 5 | 65 |
| RCCA | Merit Medical | Impress Catheter, shape Berenstein, braided | 5 | 65 |
| SMA | Merit Medical | Impress Catheter, shape Modified Hook 2, braided | 5 | 80 |

‡ The introducer and guidewire were used throughout the study.

Afterwards, each subject conducted tasks 1) to 3) on the abdominal and task 4) on the thoracic phantom with randomised order of manual or robotic execution (each $N$ = 4). The task workflows are derived from instrument handling in angioplasty and involve manipulation of both the catheter and its supporting guidewire. Further instrument details are provided in Table 4.1. With respect to clinical deployment, the task objective is constituted by the catheter motion due its subsequent exchange with a balloon catheter over the guidewire. The objectives are further elaborated in the following list with visual annotations in Figure 4.5c, d:

1. **Left common iliac artery (LCIA)**: The catheter tip is initially located in the right common iliac artery. The tip must traverse the aortic bifurcation and be advanced at least 3 cm (see marker in Figure 4.5c) into the LCIA.
2. **Superior mesenteric artery (SMA)**: The catheter tip is located in the suprarenal aorta and must be advanced from the starting position to a point in the proximal superior mesenteric artery (see marker in Figure 4.5c).
3. **Left renal artery (LRA)**: From a starting position in the infrarenal aorta 3cm inferior the target vessel), the catheter must be advanced 2cm into the left renal artery (see marker in Figure 4.5c) for task completion.
4. **Right common carotid artery (RCCA)**: The task starts with the catheter tip in the aortic arch in proximity to the left common carotid artery (LCCA) origin. To complete the task, the catheter must traverse the brachiocephalic trunk and reach a point in the RCCA 3cm from its origin (see marker in Figure 4.5d).

Subsequent to study participation, subjects were asked to complete the survey listed in Table 4.2. The questionnaire is composed of 16 statements linked to a 20 point ordinal scale that maps the range of $\pm$ 10 from rejection to agreement. The composition relates to NASA task load index protocols [271] and after scenario questionnaires (ASQ) [272].

### 4.3.3 Evaluation Methodology

Acquired visual data of fluoroscopy sequences was post-processed to determine instrument motions. A semi-automatic instrument tracking framework was implemented with pyramidal pattern matching (NI Vision, LabVIEW 2018, National Instruments, TX, USA) and applied to visual data.

Instrument tips of catheter and guidewire were separately delineated and masked in the first valid frames by experienced subjects that were not involved in the study to generate tracking template $\boldsymbol{T}_{\mathrm{C/G}}$. Matching of template $\boldsymbol{T}_{\mathrm{C/G}}$ to current fluoroscopic image frame $\boldsymbol{I}_i$ was implemented with normalised cross-correlation, where the video sample series is denoted by $i = \{1, \ldots, N\}$ with $N$ acquired frames in total. The centre of the matching result denoted the current instrument position $\boldsymbol{p}_{\mathrm{C/G}}(t_i) = (u, v)^{\mathrm{T}} \in \mathbb{R}^2$, where $u$ and $v$ denote pixel coordinates in the image frame. The remainder of frames in the sequence was subsequently processed automatically. Challenging tracking conditions, e.g. from occlusions or weak appearance, were indicated by tracking metrics and complemented by manual intervention.

Each X-ray sequence was further calibrated geometrically using a cylindrical object with known physical dimensions located in the plane of relevant anatomy [273]. This facilitates pixel-to-metric conversion of image-based

measurements. Each pixel coordinate is converted to corresponding metric representation:

$$\boldsymbol{x}_{\mathrm{C/G},i} = \underbrace{\begin{pmatrix} \varepsilon_u & 0 \\ 0 & \varepsilon_v \end{pmatrix}}_{\boldsymbol{\varepsilon}} \boldsymbol{p}_{\mathrm{C/G},i}, \tag{4.6}$$

where $\boldsymbol{\varepsilon} \in \mathbb{R}^{2\times 2}$ denotes the conversion matrix obtained from the calibration procedure.

The accuracy of the tracking algorithm was evaluated on sequences ($N$ = 8) with 589 frames in total which have been selected randomly from study data of manual LCI, LRA, RCCA and SMA tasks. The sequences show various manipulation manoeuvres with different instrument shapes, e.g. retraction and rotation with ambiguous imaging conditions. Each tracking result $\boldsymbol{x}_{\mathrm{C/G},j}$ of frame $j$ was compared to a ground truth $\hat{\boldsymbol{x}}_{\mathrm{C/G},i}$ which was has been acquired from manual data labelling of a trained subject, where $j = 1, ..., N_{\mathrm{T}} = 589$. The overall mean tracking error is given by:

$$e_{\mathrm{T}} = \frac{\sum_{j=1}^{N_{\mathrm{T}}} \|\boldsymbol{x}_{\mathrm{C/G},i+1} - \hat{\boldsymbol{x}}_{\mathrm{C/G},i}\|}{N_{\mathrm{T}}}. \tag{4.7}$$

and was determined to $e_{\mathrm{T}} = (1.42 \pm 1.27)$mm. The following paragraph introduces the study metrics. The *overall distance* of the instrument motion is given by accumulation of Euclidean distances of consecutively tracked tip positions:

$$d_{\mathrm{C/G}} = \sum_{i=1}^{N-1} \|\boldsymbol{x}_{\mathrm{C/G},i+1} - \boldsymbol{x}_{\mathrm{C/G},i}\|. \tag{4.8}$$

The *task completion time* $t_{\mathrm{C/G}}$ is determined from assigned timestamps and describes the duration from commencement to successful termination of the specific task (see criteria in Figure 4.5c, d), i.e. the subject has reached the corresponding vascular landmark.

Interaction of instrumentation and vascular anatomy was described by resultant forces obtained from load cell measurements. The latter are transformed to a resultant sample with:

$$f_i = \sqrt{f_{x,i}^2 + f_{y,i}^2 + f_{z,i}^2}, \tag{4.9}$$

where $f_{x,i}$, $f_{y,i}$, and $f_{z,i}$ are uniaxial measurements of the corresponding load cell axes. Force samples were concatenated to measurement vector $\boldsymbol{f} = (f_1, \ldots, f_N)^{\mathrm{T}}$. Hence, *maximum forces* are given by $\widetilde{f} = \max \boldsymbol{f}$ and trial *mean force* yielded to

$$\bar{f} = \frac{\sum_{i=1}^{N} f_i}{N}. \tag{4.10}$$

### 4.3.4 Statistical Considerations

Inferential statistics were applied to determine the effects of within-subject factors or experimental settings on recorded task metrics. Task metrics are dependent variables of the analysis. The study regards two independent variables: Two-level factor *mode* describes manual or robotic task execution. Factor *measurement* is a four-level

**Table 4.2:** Questionnaire for subjective task evaluation.

| No. | Statement | Score |
|---|---|---|
| 1 | The control system was precise. | ± 10 |
| 2 | The presence of haptic feedback was helpful in completing the tasks. | ± 10 |
| 3 | I felt stressed, irritated or annoyed while using this system during the task. | ± 10 |
| 4 | It was easy to control/use the system. | ± 10 |
| 5 | It was easy to make mistakes with the system. | ± 10 |
| 6 | Contralateral iliac artery cannulation (robot): My performance in the task was satisfactory | ± 10 |
| 7 | Left renal artery cannulation (robot): My performance in the task was satisfactory | ± 10 |
| 8 | Superior mesenteric artery cannulation (robot): My performance in the task was satisfactory | ± 10 |
| 9 | Right common carotid artery cannulation (robot): My performance in the task was satisfactory | ± 10 |
| 10 | The control interface of the system was comfortable for my hand. | ± 10 |
| 11 | Staying focused on what I was doing was easy. | ± 10 |
| 12 | I found the use of this system easy to learn. | ± 10 |
| 13 | The brief verbal introduction was necessary for me to be able to use the system properly. | ± 10 |
| 14 | The system was safe to use. | ± 10 |
| 15 | I would like to use the system again for this kind of task. | ± 10 |
| 16 | I would recommend this system to a colleague. | ± 10 |

representation corresponding to four repeated measurements per task and subject (see Section 4.3.2). Statistics target identification of significant differences within data populations linked to factors. This setting determines the applied methodology to parametric multi-way analysis of variances (ANOVA); more specifically to a two-way ANOVA [274]. However, two fundamental assumptions were assessed for individual data sets: 1) presence of outliers and 2) normal distribution of residuals. If assumption 2) is violated, data transformation, e.g. box cox, is feasible.

## 4.4 Results

This section reports experimental results against the chosen study metrics and the user feedback obtained through questionnaires.

### 4.4.1 Study Metrics

Objective assessment of the experimental procedures is reported in Figure 4.6 and summarised in Table 4.3.

An analysis of this data shows that, considering the defined metrics for performance, manual and robotic cannulation of the selected arteries are overall comparable. Columns *Path Length* report the overall instruments displacement for each cannulation task. Considering the catheter path length $d_{\mathrm{C}}$, it is observed that it is slightly higher in robotic manipulations. More in detail, using the robot, the mean catheter path is $\approx$ 3cm longer when cannulating the LCIA, $\approx$ 9cm longer when cannulating the SMA, $\approx$ 15cm longer when cannulating the LRA, and $\approx$ 16cm longer when cannulating the RCCA. On the other hand, results show an average decrease in the guidewire path when using the robot. In detail: $\approx$ 3cm shorter when cannulating the LCIA, $\approx$ 1cm shorter when cannulating the SMA, $\approx$ 8cm longer when cannulating the LRA, and $\approx$ 1cm shorter when cannulating the RCCA. However, results showed that the guidewire path length is never significantly affected by the experimental condition, i.e. manual or robotic deploy-

ment. The analysis of catheter path length did show significant differences, excluding the LCIA cannulation. The completion time resulted on average slightly more than 1 minute longer when using the robot, namely: 65s when for cannulating the LCIA, 71s for the SMA, 73s for the LRA, and 95s for the RCCA. These results are statistically significant according to the ANOVA test.

The analysis of manipulation forces (i.e. the forces applied to the phantoms during cannulation tasks) resulted lower when using the robot with respect to manual. Examples of force measurements along the instrument paths for robotic LCIA and RCCA cannulation are provided in Figure 4.7a, b and a manual RCCA cannulation in Figure 4.7c. The corresponding robotic displacement is shown in Figure 4.7d, e.

In general, mean forces resulted in 60% lower when cannulating the LCIA, and 25% lower when cannulating the SMA. The values of the mean force were similar during LRA and RCCA cannulation tasks. However, these results are not statistically significant according to the ANOVA test. Maximum forces resulted significantly lower values when cannulating the LCIA with the robot, showing a decrease of 45% with respect to manual. Similarly, maximum forces are lower in robotic cannulation of LRA and RCCA (7% and 8% respectively) although the ANOVA test did not show statistical significance. Manual cannulation of the SMA resulted in slightly lower maximum forces (7%), but again, not statistically significant. Finally, the cannulation success rate using the robot was 90% in LCIA and SMA cannulation, 100% in LRA cannulation, and 97% in RCCA. The cannulation rate during manual tasks was slightly higher, presenting 100% in LCIA, LRA, and RCCA, and 97% in SMA cannulations.

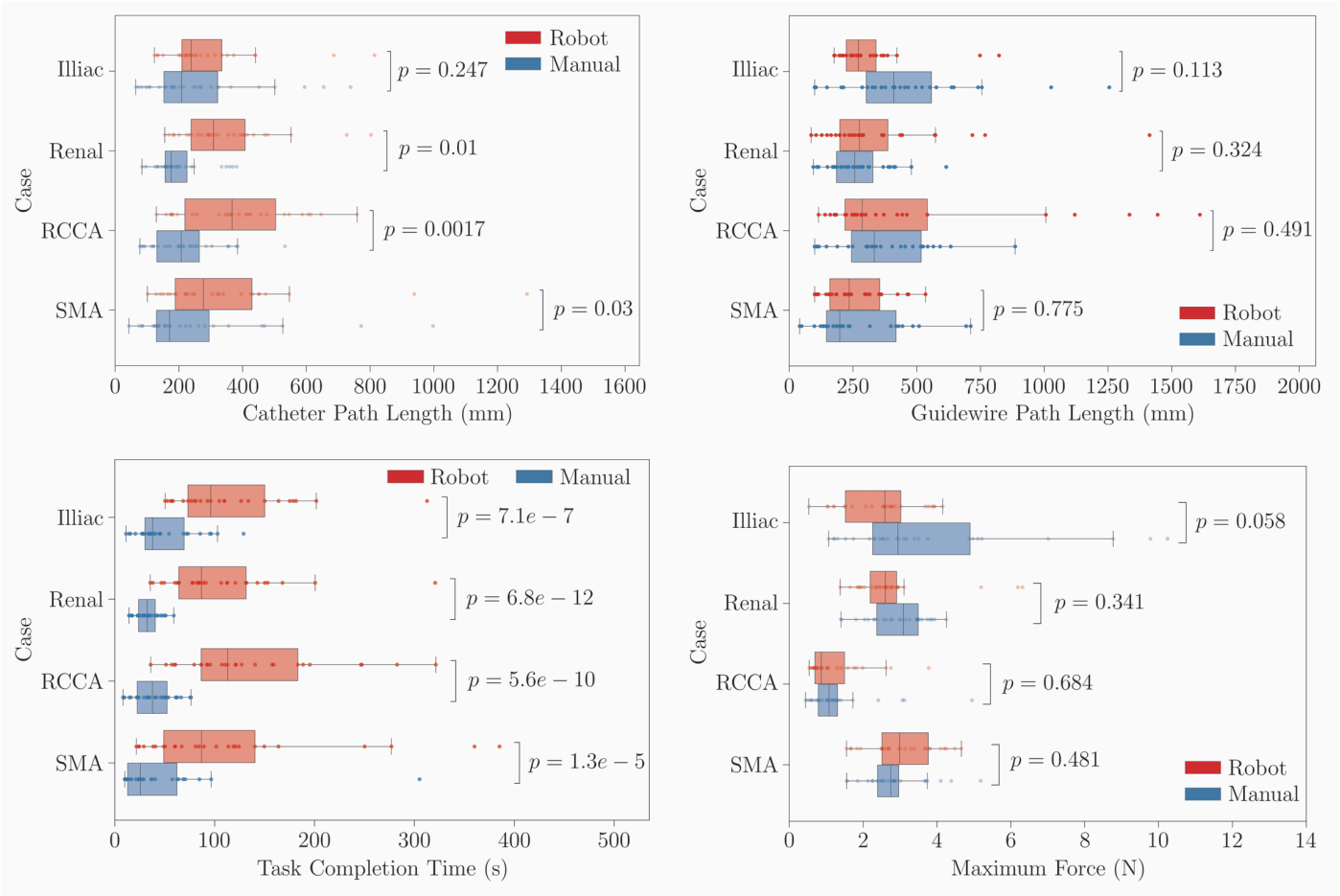



**Figure 4.6:** Boxplots: (a) Catheter path lengths, (b) guidewire path lengths, (c) task completion times, and (d) maximum forces.

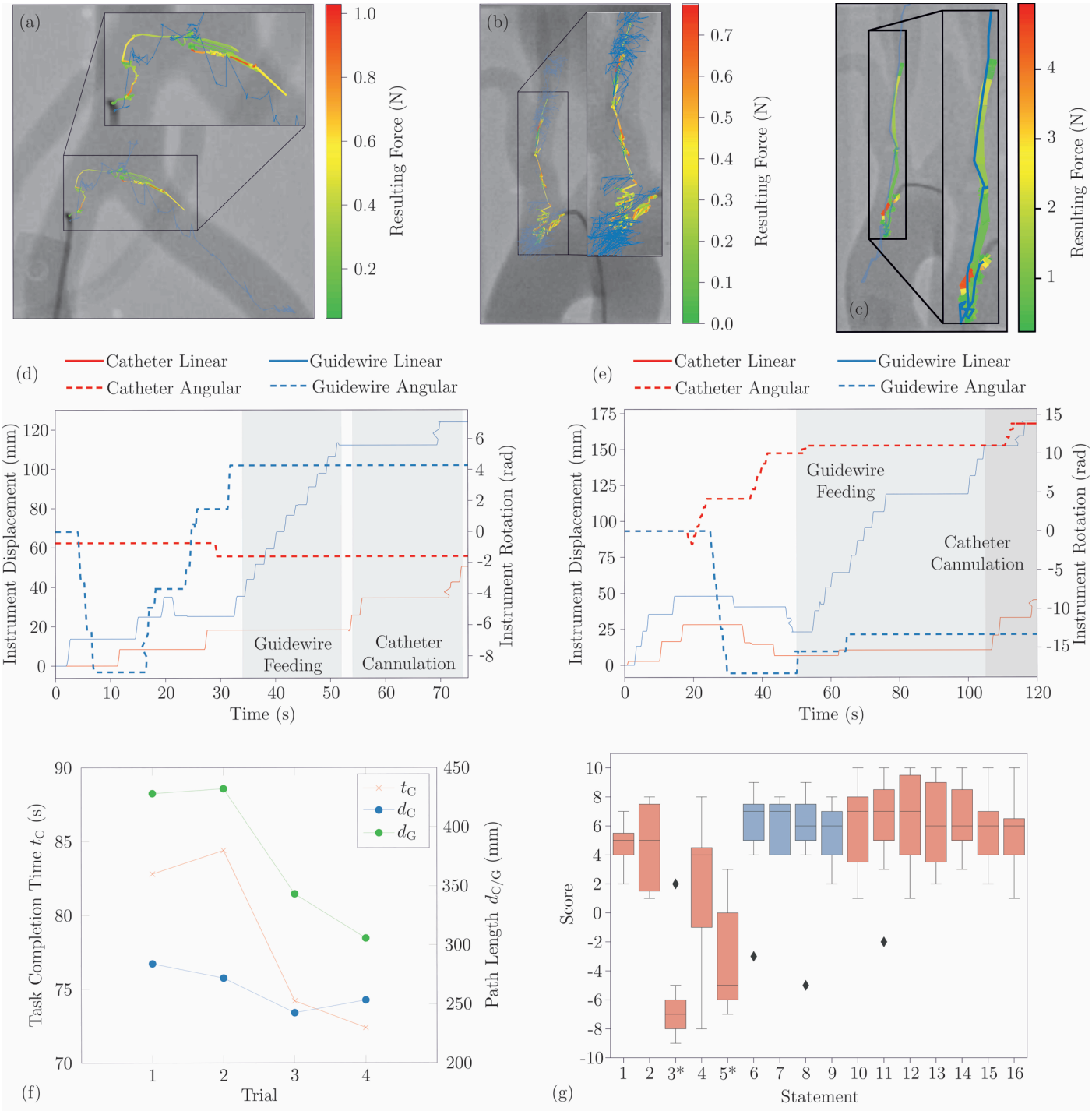



**Figure 4.7:** Forces and kinematics examples: (a) robotic LCIA cannulation, (b) robotic RCCA cannulation, (c) manual RCCA cannulation, (d) kinematics data to task in (a), and (e) kinematics data to task in (b). Colour overlays correlate tracked tip positions and corresponding force measurements. This enables identification of difficult anatomy or catheter handling issues. (f) Completion time and path lengths metrics for a robotic RCCA cannulation over number of study trials. (g) Survey results. Red plots annotate statements related to design and usability. Blue plots denote task specific statements. Marker * indicates negative statements.

As an example, study metrics are reported for trials of an expert RCCA cannulation in Figure 4.7f. In this example, the expert has completed the given task in less time and with less instrument motions for an increasing number of trials. With respect to the protocol of the study series, occasional instrument buckling was present between the introducer and slave root during the user experiments which resulted from the interaction of the instruments and the silicone phantom, i.e. high friction forces from interaction of instruments and model vessels prevented further

**Table 4.3:** User study metrics for cannulation tasks (mean ± SD).

| Task | Condition | Path length $d_C$ (mm) | Path length $d_G$ (mm) | Completion time $t_C$ (s) | Mean force $\bar{f}$ (N) | Max force $\widetilde{f}$ (N) | Cannulation rate $\beta$ (%) |
|---|---|---|---|---|---|---|---|
| LCIA | Manual | 264.9 ± 177.9 | 450.2 ± 267.9 | **49.3 ± 29.9**$^{***}$ | 0.8 ± 0.7 | **3.7 ± 2.5**$^{*}$ | 100 |
| | Robot | 293.8 ± 162.4 | 313.2 ± 157.4 | **115.1 ± 61.4**$^{***}$ | 0.5 ± 0.2 | **2.5 ± 1.1**$^{*}$ | 90 |
| SMA | Manual | **258.3 ± 221.0**$^{*}$ | 268.4 ± 181.2 | **44.8 ± 57.5**$^{***}$ | 1.0 ± 0.3 | 2.8 ± 0.8 | 97 |
| | Robot | **350.0 ± 261.3**$^{*}$ | 261.8 ± 123.8 | **116.4 ± 99.1**$^{***}$ | 0.8 ± 0.3 | 3.0 ± 0.9 | 90 |
| LRA | Manual | **202.5 ± 82.7**$^{**}$ | 271.9 ± 120.6 | **32.4 ± 11.8**$^{***}$ | 0.7 ± 0.2 | 3.0 ± 0.8 | 100 |
| | Robot | **348.2 ± 155.8**$^{**}$ | 355.2 ± 269.4 | **105.1 ± 59.0**$^{***}$ | 0.7 ± 0.3 | 2.8 ± 1.2 | 100 |
| RCCA | Manual | **220.5 ± 109.6**$^{***}$ | 370.7 ± 188.6 | **39.2 ± 20.1**$^{***}$ | 0.4 ± 0.2 | 1.3 ± 1.0 | 100 |
| | Robot | **381.8 ± 173.5**$^{***}$ | 360.2 ± 303.1 | **134.1 ± 73.6**$^{***}$ | 0.4 ± 0.2 | 1.2 ± 0.8 | 97 |

‡ The introducer and guidewire were used throughout the study.

instrument feeding by the robot.

### 4.4.2 Questionnaire

Results (mean ± SD) of the post-experimental survey are summarised for all expert users ($N = 7$) in Figure 4.7g and are discussed as follows. In general, subjects were satisfied with the system control (S4, 3.8 ± 2.5), the precision (S1, 4.7 ± 1.6), and acknowledged the presence of haptic feedback (S2, 4.6 ± 3.0). Beyond that, the task-specific survey outcomes underline quantitative results. Subjects appreciated their performance in LCIA (S6, 5.4 ± 3.7), LRA (S7, 6.0 ± 1.8), SMA (S8, 5.0 ± 4.3), and RCCA (S9, 5.4 ± 2.0) cannulation tasks. Furthermore, subjects have valued the system introduction (S13, 6.1 ± 3.0), the steep learning phase (S12, 6.4 ± 3.2), low stress (S3, -7.2 ± 1.3), and the straightforward procedural workflow (S11, 6.0 ± 3.9). This also addressed ergonomics (S10, 5.9 ± 3.0) and procedural safety (S5, -4.8 ± 4.2, S14, 6.6 ± 2.4). Future work has been motivated by positive statements on frequent use of the system (S15, 5.7 ± 2.5) and recommendation to peers (S16, 5.4 ± 2.7).

## 4.5 Discussion

Experimental results demonstrate the potential of the proposed robotic platform for use in endovascular interventions. Vision and robotics are seamlessly integrated into the clinical workflow to support the clinician in performing the surgical procedure. Medical images (e.g. fluoroscopy) are used to generate visual and haptic feedback for operator guidance. The intuitiveness and ergonomics of the master manipulator allow the operators to fully leverage their endovascular skills with the dexterity and stability provided by the robotic slave. The metrics chosen for the performance evaluation give an account of the usability and safety of the system. Results on these metrics are reported for both robotic manipulation and conventional manual technique. However, any direct comparison of manual vs robotic procedures on these metrics must take into account that the trials were conducted by trained surgeons with relevant experience in manual catheterisation but no training with the robotic platform. Results of manual cannulations are reported to provide a reference for completeness of the work. As reported in Section 4.4.1, surgeons achieved robotic cannulation success rates ranging between 90-100%. In the case of unsuccessful cannulations, two main issues were identified: 1) buckling of the catheter, and 2) finite instrument manipulation stroke. These are both related to hardware and design limitations of the latest slave prototype. Contact forces

related to friction between the catheter, the introducer, and the vascular phantom occasionally resulted in buckling of the catheter from insufficient mechanical support. As a result, the surgeon's motion commands on the master robot, although properly replicated by the slave, did not result in a corresponding movement of the tip of the catheter within the vasculature. Moreover, the current design of the slave robot presents a finite manipulation stroke on the linear actuators that were derived from anatomy. This means that the endovascular instruments can be translated within a limited range. In a few cases, the buckling reported in Section 4.4, combined with the limited stroke of the slave robot, resulted in an 'out-of-workspace' condition which prevented the surgeon from completing the cannulation task. This issue can be fixed by designing a rigid, expandable, support device between the slave robot and the percutaneous introducer, which guides the catheter and prevents buckling of that segment (e.g. patent US8961533B2). The analysis of mean and maximum forces shows that overall there is a reduction of forces exerted to the phantoms when the robot is used. Forces are very relevant clinically, in terms of patient safety: high-force contact between an instrument and the vessel wall may result in injury or embolisation, which may cause bleeding or loss of blood supply to the vital organs. The force results obtained with our system are overall in line with similar experiment with experienced users reported in literature [275], further corroborating the potential clinical applicability of our platform. From a technical point of view, lower forces can be related to the higher manipulation stability and optimised user input for delicate manoeuvers provided by the robot, and specifically to the vision-based haptic guidance, whose role is actually guiding the surgeon through the vasculature while avoiding high-impact contacts between the endovascular instruments and the vessel walls. Unsurprisingly, completion time is higher when the robot is used with respect to manual cannulations. This is due to two factors: 1) the intrinsically lower dynamic of the robotic system, due to the vision-based architecture which slows down the velocity of the robot when the manipulated instruments approach the vessel wall; and 2) the lack of training of the surgeons with our robotic system. However, with an average completion time of less than 2 minutes, the results on this metric are already within a range that would be acceptable in actual clinical use.

It is worth noting that in this study the robot is teleoperated from the control room due to X-ray imaging for the performance assessment. Although prospective use targets MR deployment, concerns among endovascular surgeons of high radiation doses [276] and lifetime exposure are addressed [277].

The robotic platform allows the manipulation of both catheter and guidewire but not simultaneously as in standard manual procedure. Although this was not perceived as a limitation by the users, it may have forced them to find alternative strategies to accomplish the task. The analysis of instrument paths and experimental videos shows that, when performing cannulation tasks with the robot, the surgeons manipulated the catheter more than the guidewire (as measured by distances travelled by the instruments), whereas in manual cannulations, catheter and guidewire manipulation were more equal. This may be explained by the technical limitations of the robot described above, causing surgeons to adapt their behaviour to work around the limitations, as well as experience considerations, as participants were accustomed to manual procedures but were new to using the robot. A learning effect related to the number of trials may be demonstrated by the RCCA example in Section 4.4. However, an in-depth analysis must include expert user and trials to identify significant learning effects. This also addresses effects related to the realised haptic feedback. The latter does not exactly replicate the haptic feedback of manual endovascular procedures as this would include accumulation of tissue-instrument contacts along the instrument bodies and/or introducers. However, the experts acknowledged the transparency of this assistive concept and the study results corroborate the feasibility of this approach. Nevertheless, optimisation of the haptic concept is regarded in future

work. Further experience with the robot and feedback, gained through training, may enable the users to complete the tasks more efficiently.

Despite the comprehensive fluoroscopic image data analysis and its promising results in this study, single-plane fluoroscopy not only exposes patient and operator to ionising radiation but further shows limitations with respect to procedural monitoring, e.g. ambiguous representation of instruments or branches of the vasculature, or recovery of instrument poses for accurate pose control for a transition to semi-automated procedural phases. Those ambiguities may be resolved by consideration of MRI.

Qualitative user feedback (see Figure 4.7g) corroborates the results obtained through objective metrics. Analysis of questionnaire responses shows that the robotic system was well received both in terms of technical design and clinical usability. Further to the data already reported in Section 4.4.2 and summarised in Figure 4.7g, subjects individually appreciated the concept of mimicking manual instrument handling and augmentation of 'transparent' but effective haptic feedback. In contrast, automation of procedural sub-tasks, e.g. larger displacements in non-tortuous vessels, was suggested by users to enhance temporal efficiency. Lastly, drawbacks resulting from potential latencies of the pneumatic principle have not been reported by the expert users.

Overall, this user study demonstrated the feasibility of the proposed robotic system in clinically relevant endovascular tasks. Results provided valuable data for future improvements, highlighting the potential of the robotic platform in clinical translation, but also current limitations. The main technical limitations are related to the catheter buckling and the limited linear operational workspace of the slave robot. While catheter buckling can be easily avoided by adding a guiding slide to front of the robot, the optimisation of the operational workspace will require a redesign of the slave robot. This will need to take into account the specific intended procedures (as the stroke needed to accomplish cannulation must be factored in) but also the usability considerations. While a bigger robot would allow a larger stroke, the integration within the clinical workflow would be negatively impacted by a larger footprint. The new design will need to be a compromise between these two factors. Although the robotic hardware has demonstrated adequate manipulation performances and already enables an application in MR environments, the clinical workflow must be adapted to the needs of MR environments. This, in particular, addresses the integration of the platform to prospective interventional MR suites. Challenges are mainly haptic guidance and advanced user visualisation. Advanced control schemes of the master may include feed forward approaches to compensate for the internal friction. Beyond that, as presented in Chapter 2, MR safe endovascular instrumentation is needed.

While the metrics used in this study were designed to obtain quantitative and qualitative analysis of the system performance and usability, they are not a substitute for actual clinical outcomes data. There are inherent limitations associated with the use of silicon phantoms, as their biomechanical properties differ from real tissues, in particular their response to damage. Future studies should be performed in in vivo models, such as porcine models, to provide more data more closely applicable to a real clinical setting. It would be valuable to assess the endothelial injuries caused by the instrument manipulation (e.g. through histopathology analysis [278]), and ideally correlate it to the exerted forces. In terms of study design, either in vitro or in vivo, future investigations would benefit from a larger number of users and tasks to strengthen the statistical significance. Moreover, in terms of system usability, it would be useful to assess the users learning path on the robotic system, including endovascular clinicians with different levels of robotic experience.

## 4.6 Extended Work: *in-vivo* Animal Trials

To further evaluate the safety and efficacy of the robotic platform, an in-vivo study is performed on four porcine models with the primary objectives of: (i) successfully integrating robotic, imaging and sensing technologies in-vivo; (ii) assessing the feasibility of performing robotics endovascular procedures; and (iii) assessing the safety and clinical usability of the robotic system by comparison with standard manual procedures. The study comprised the following tasks: (1) cannulating the target blood vessel using the robotic system (i.e. navigating through the anatomy by remotely manipulating the catheter and guidewire), followed by (2) the manual exchange of the catheter with a balloon angioplasty catheter by passing it over the guidewire, finally (3) the balloon angioplasty catheter is deployed and inflated. The five target arteries are:

- Left Common Iliac Artery (LCIA) - Figure 4.8c
- Left Renal Artery (LRA) - Figure 4.8d
- Right Renal Artery (RRA) - Figure 4.8e
- Right Common Carotid Artery (RCCA) - Figure 4.8f
- Superior Mesenteric Artery (SMA) - Figure 4.8g

During the course of the experiments, it was not possible to use the dynamic active tracking feature implemented in the phantom studies due to the weak contrast between the vessel walls and surrounding tissue. This shortcoming was resolved by extracting the vessel contour from the image with contrast (i.e. Digital subtraction angiography) and using it as a reference for the navigation system. Cannulation was considered successful when the catheters

| Task | Sheath | Catheter | Guidewire | Balloon |
|---|---|---|---|---|
| LCIA | n/a | Impress 5Fr 65cm RIM[2] | Radifocus Guidewire M Standard type, .035", 180cm, 10mm flexible length, angled. Hydrophilic coating, nitinol core[3] | Mustang 10mm x 20mm, 75cm (6Fr)[4] |
| R/L RA | Flexor Ansel 6Fr x 45cm[1] | Impress 5Fr 65cm Cobra 2[2] | | Mustang 7mm x 20mm, 135cm (5Fr)[4] |
| SMA | Flexor Ansel 6Fr x 45cm[1] | Impress 5Fr 80cm Modified Hook 2[2] | Radifocus Guidewire M Standard type, .035", 260cm, 30mm flexible length, angled. Hydrophilic coating, nitinol core[3] | Mustang 7mm x 20mm, 135cm (5Fr)[4] |
| RCCA | Flexor Shuttle 6Fr x 90cm[1] | Impress 5Fr 100cm VER[2] | | Mustang 7mm x 20mm, 135cm (5Fr)[4] |

**Table 4.4:** Sheaths, catheters, guidewires, balloon catheters used in the animal study.
[1] Cook Medical Europe, Limerick, Ireland
[2] Merit Medical UK, Reading, UK
[3] Terumo UK Ltd., Surrey, UK
[4] Boston Scientific UK, Hemel Hempstead, UK

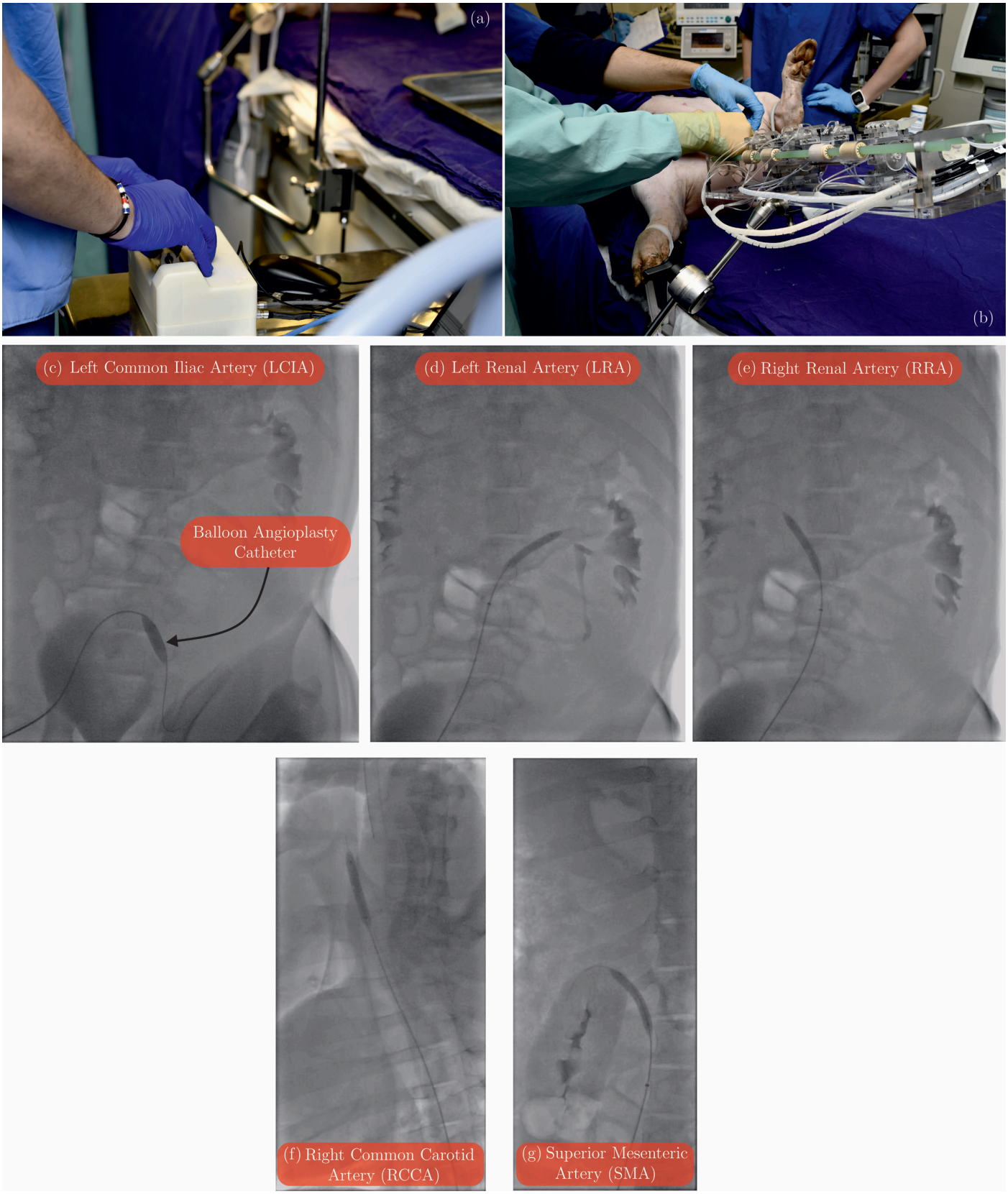



**Figure 4.8:** (a) Operator remotely manipulating the robot using the master manipulator. (b) MR safe slave robot positioned next to the animal using a scope and holding arm (KARL STORZ SE & Co. KG, Tuttlingen, Germany). Acquired fluoroscopy scans of the deployed and inflated balloon catheter in the five different target arteries: (c) Left Common Iliac Artery (LCIA), (d) Left Renal Artery (LRA), (e) Right Renal Artery (RRA), (f) Right Common Carotid Artery (RCCA), (g) Superior Mesenteric Artery (SMA).

were positioned in such a way they were able to deliver therapy (e.g., balloon angioplasty inflation). The performance was objectively evaluated over the following metrics: (i) success rate, (ii) histopathology, and (iii) completion time. Note: Histopathology (tissue damage) was used as a metric for comparison between robotic and manual interventions and not as a blinded study to demonstrate clinical significance.

The results showed a 100% success rate with lower occurrence and severity of injuries (as per the post-mortem histopathological assessment) when the robotic platform was used when compared to the manual intervention. When the robot was used, the histopathology showed a lower incidence and severity of arterial injuries (only 2 sections presented vessel damage (out of 78)), whereas in the case of manual interventions, 21 sections out of 78 presented high-grade injuries. Due to its stability and guidance, the robot allowed the surgeon to navigate the vessels with a higher level of accuracy, thus reducing the damage it causes, as demonstrated by the less significant grade of injuries (complications such as endothelial loss) in the robotic cases versus the manual control. The clinical significance of these results lies in the fact that robot-assisted endovascular interventions can help mitigate the unintentional (yet frequent) contacts between the manually manipulated instruments and the vessel walls, with potential for perforation and fatal haemorrhage [279]. However, it is reasonable to suspect bias due to the non-blinded nature of this study. Moreover, as in the case of the previously described user study, time-wise, the robot-assisted interventions took 20mins more on average when compared to manual interventions. Although this confirms that the robot slightly extends the procedure time – while remaining in an acceptable range for clinical use – this also demonstrates the increased safety for the operator when the procedure is carried out remotely from the control room. In general, this assessment demonstrates the feasibility and safety of different endovascular tasks through the integration of robotics within a standard clinical workflow.

Note: The trials were conducted at the animal research facility of The Griffin Institute, Northwick Park and St Mark's Hospital, Harrow, UK under Home Office License (Project License: XA57A4134) according to the Animal (Scientific Procedures) Act 1986 and Good Laboratory Practice Regulations 1999.

## 4.7 Conclusions

Endovascular interventions are among the most relevant and widely used therapies for cardiovascular diseases. Various robotic technologies were commercialised to assist the procedural workflow for such interventions. However, common deficiencies of state-of-the-art technologies are proprietary instrumentation, non-intuitive master consoles, and, importantly, the X-ray exposure for clinicians and patients. This contribution addresses these challenges, demonstrating that expert vascular surgeons were able to successfully complete all cannulation tasks using the proposed platform. Looking into the future, MRI may replace common X-ray imaging and may be incorporated to the procedural workflow to improve diagnosis, 3D navigation, and eliminate radiation exposure in endovascular applications. Hence, this contribution presents an alternative robotic strategy. In this chapter, the robotic system is further optimised and evaluated with clinical experts in a phantom study and pre-clinically through a comprehensive animal study. Future work should address 1) Incorporation of tailored and dexterous MR safe steerable catheters and guidewires, which is the challenge addressed in the following chapter (Chapter 5), 2) Device integration to state-of-the-art MRI suites, fusion with 2D/3D MRI and subsequent user studies. Further recommendations and potential research avenues are presented in the concluding Chapter 6.

Chapter 5

# Thermally Drawn Steerable Catheter for MR-guided Endovascular Interventions

"Part of this chapter was accepted for publications in the proceedings of ISMRM & SMRT Annual Meeting & Exhibition 2021, under the title "An MR Safe Steerable Catheter for MR-guided Endovascular Interventions".

## 5.1 Contribution

The true impact of the robotic system presented in Chapters 3 and 4 on MR-guided endovascular interventions can be realised iff the issue of the lack of MR compatible instrumentation is addressed. In this chapter, the fibre production technology is leveraged to fulfil this gap in the field of MR-guided endovascular interventions [135, 140]. A thermally drawn catheter equipped with steering capabilities by incorporating MR-visible pull-wires as well as a 3D printed handle allowing remote 4-way manipulation of a flexible distal end were created from bulk polymer materials in our research facility. The proposed new approach allows any design modification in the catheter to be incorporated rapidly. The MR-safe thermally drawn catheter was then successfully demonstrated in both *in-vitro* and *in-vivo* experiments. The translational work proposed here does not only fulfil the instrumentation gap to help adaptation of MR guided interventions into operating theatres, but also introduces a new rapid prototyping approach that will accelerate technology translation in this emerging biomedical engineering field.

# 5.2 Limitations and Requirements

## 5.2.1 Limitations Impeding Development of MR Safe Steerable Catheters

- **Limitations Introduced by Materials under MR**: MRI-guided interventions face a significant challenge due to the presence of a large magnetic field (1.5/3 Tesla), which limits the set of materials suitable for the construction of key instrumentation (sheaths, catheters and guidewires).
  - *(MR Visibility)* The use of ferromagnetic materials introduces localised magnetic field inhomogeneities which lead to the dephasing of adjacent proton spins and a local signal void, which in turn create large magnetic susceptibility artefacts in the acquired MR images. This makes it difficult to visualise the instrument and the surrounding soft tissue structures under MRI.
  - *(MR Safety)* The use of non-ferromagnetic metals (e.g. stainless steel and nitinol), on the other hand, create acceptable susceptibility artefacts. Still, if used in long lengths, it makes the instrument susceptible to radiofrequency (RF)-induced heating under MRI, risking thermal injury. The induced heating is a result of standing wave formation along the conductive parts longer than a quarter wavelength, which corresponds to approximately 12cm in humans at 1.5 Tesla.
  - *(Mechanical Integrity)* Although, using relatively safe polymeric materials instead of ferromagnetic and non-ferromagnetic metals might seem like an obvious alternative, they are difficult to visualise and localise due to their low magnetic susceptibility. Moreover, several reported results indicate that substituting metals with polymers in catheter braiding and guidewire cores lead to a reduction in the desired mechanical performance.
- **Limitations Introduced by Steering Mechanism:** Although the usage of steerable sheaths/catheters contributes to improved manoeuvrability and stability when compared to selective catheters, each of the commonly proposed and developed steering technologies have their own set of challenges.
  - *(Steerability)* For *tendon*-driven catheters (also referred to as pull-wire driven or cable driven), the main challenge lies in the mechanical nonlinearities experienced with an increase in the number of moving components and DOF [21]. Examples of such nonlinearities include friction between tendons and their corresponding catheter lumens; and the backlash caused by tendon slack and moving components of the tendon driving mechanism (e.g. gears). Other challenges include the uncontrolled change in length of tendons caused by the passive bending of catheter shafts while manoeuvring through tortuous anatomies. *Fluidic (Hydraulic)* actuation, on the other hand, presents several drawbacks such as slower response times when compared to tendon-driven catheters; the need for equipment like pumps, valves and pipes; the possibility of leakage which can limit the catheter's efficiency [227]; the need for sophisticated control methods [226, 228]; and difficulty in miniaturisation because of the space occupied by the driving fluid. For *magnetic* steering, on the other hand, the difficulty of achieving precise motions, and the need for customised "interleaved" MRI sequences to simultaneously visualise and steer catheters continue to remain as challenges for MR-actuated catheters. In the case of *Shape memory alloy (SMA)* actuation, SMAs are inherently nonlinear materials exhibiting significant hysteresis, which makes it difficult to control them in a repeatable manner [229, 230].
  - *(Safety)* Steering without posing any risk to the physiological processes and causing any complications to

anatomical structures is crucial for the adoption and commercialisation of steerable catheters [21]. Steerable catheters actuated by tendons, hydraulics and MR (ferromagnetic spheres embodiment), all have the added advantage of not having any long conductive wires, unlike catheters actuated by SMAs and MR (microcoiled embodiment) catheters. The drawback of having long conductive wires is the risk of resistive heating and RF induced heating. Heating leads to heat stress (inability to control the body's internal temperature), induced current burns and contact burns of body tissues. The safety hazard associated with hydraulic actuated catheters is the need for high fluidic pressures which, if not controlled properly, may result in jets of pressurised liquid that could damage soft tissue [226, 233]. The safety concern linked to catheters driven by ferromagnetic spheres is the insertion of ferromagnetic components at the entry region of the MRI bore, where a very strong static gradient of 20 T/m exists. In this region, magnetic forces would be high enough to damage the blood vessel wall [198]. Tendon-driven catheters are generally considered safe; however, catheters with multiple segments should not have any sharp or irregular edges which can damage blood vessel walls and increase the risk of embolisation [21].

### 5.2.2 Requirements for the Development of an MR Safe Steerable Catheter

To overcome the challenges and limitations of MR compatibility (MR visibility and MR safety) and overall mechanical performance (mechanical properties and steerability), the materials used in the construction and manipulation of MR-guided steerable catheters should:

- Ensure that the catheter is ***visible in its entirety*** (proximal shaft and distal tip) without introducing large artefacts that impede the visualisation of surrounding tissue.
- Elimintate the ***risk of resistive heating and RF induced heating*** across the length of the catheter.
- Have ***similar mechanical integrity*** as their MR unsafe equivalents. Generally, the catheter should have sufficient axial rigidity along its shaft to allow force transmission axially for optimal pushability and navigation through the vasculature and be capable of transmitting a high torque in order to achieve rotational control from the proximal end to the distal end. On the other hand, the distal end of the catheter should be relatively and sufficiently flexible and atraumatic to allow smooth motion through the tortuous vessel without perforating the vascular wall.
- Reduce the ***overall complexity*** of steering the distal end of the catheter. This could be achieved by devising an intuitive method of control that does not require any cumbersome hardware and/or software [21]. This not only simplifies the regulatory process of the catheter, but also speeds up the clinician's learning curve, reduces the instrument's cost (aids commercialisation), and increases the overall reliability and safety of the system.
- Enable the ***scalable manufacturing*** of steerable catheters, which also reduces the overall cost and facilitates clinical translation and commercialisation.

In summary, replicating what clinicians would typically see (instrument's visibility) and experience (instrument's mechanical performance) in fluoroscopy-guided endovsacular interventions will facilitate the transition and broader adoption of MRI in interventional radiology and targeted drug therapy.

# 5.3 Steerable Catheter Fabrication

## 5.3.1 Multi-Lumen Tubing

The multi-lumen tubing is the main building block of the steerable catheter; from which **(1) a flexible, yet relatively stiff shaft**, and **(2) a more flexible and a softer distal end** materialise. Inspired by Clogenson et al.'s monolithic approach [2, 175], a subtractive manufacturing technique is employed to enhance the flexibility of the tubing's distal end. Thereby, creating a flexible structure that can be steered when pull-wires *(also referred to as tendons or cables)* running from a proximal handle through the shaft towards the distal end are tensioned.

**State-of-the-art Manufacturing Method**: Although several manufacturing methods have been devised to fabricate multi-lumen tubing for the construction of medical devices (e.g. catheters), the most commonly used method is extrusion. Extrusion is the work-horse of the polymer shaping industry, producing a multitude of semi-finished products such as rods, tubes, and other prismatic sections in a scalable manner [280]. In general, the process of extrusion begins by feeding raw materials (polymeric pellets or granules) into a barrel with one or more rotating screws in a heating chamber. The resulting melt is forced through a shaped die which is either placed collinearly to the extruder screw axis (i.e. in-line extrusion die) or placed perpendicular to the extruder screw axis (i.e. crosshead extrusion die). The extrudate is subsequently pulled using a puller and cooled as it leaves the die using air or water cooling. In the case of multi-lumen tubing extrusion, the crosshead configuration is commonly employed.

The corresponding crosshead extrusion die is a metal conduit comprising several metallic mandrels that make up the desired cross-section of the multi-lumen tubing. The mandrels are embedded with gas injection holes to control the shape accuracy of the lumens, alongside other parameters such as screw speed, die temperature and pulling speed. Although widely adopted, the extrusion of multi-lumen tubing is a difficult process because of associated effects such as extrudate (die) swelling [281]. Extrudate swelling is the expansion of the flowing, continuous viscoelastic polymer melt to a wider conduit, upon exit from a confined flow conduit (die) [282]. Die swell is influenced by the fundamental properties of polymers such as the molecular weight and processing conditions such as the shear rate, shear stress and melt temperature [283]. Tooling design for highly complex and dimensionally challenging tubing is another major challenge that manufacturers face as minimally invasive procedures try to accommodate more components and functionality in tighter spaces. These limitations and challenges make it difficult to balance between achieving the target design and cost effectiveness within a limited *proof-of-concept* budget for companies and research institutes alike.

**Proposed Manufacturing Method**: Herein, we propose a new approach by re-purposing of an unconventional, but a well-established scalable and low cost polymer processing technique that can support the efforts to accelerate research and development in the manufacturing of high aspect ratio medical devices (e.g. catheters). Initially developed for silica glass optical fibres, the thermal fibre drawing process has become a significant tool in the fabrication of scalable and sophisticated multimaterial multifunctional devices. In this new category of fibres, different materials with contrasting thermal and mechanical properties are combined into a single preform (macroscopic structure) and are thermally co-drawn. The first multimaterial fibres were realised by Hart et al. and Temelkuran et al. in 2002, which comprised 21 alternative bi-layer structures of polymer and chalcogenide glass to create a Bragg mirror inside the core of the fibre [284, 285]. This led to a novel way of guiding light that facilitated the transmission of wavelengths not feasible with single material (silica) fibres. In 2004, Bayindir et al. demonstrated

for the first time a metal-insulator-semiconductor structure in a fibre [286] which was used to fabricate a flexible photo-detection fibre which was sensitive to visible and infrared light across its length. Since then, thermal drawing has been used to fabricate fibres for neural interfacing [287], deformation sensing [288], electromechanical actuation [289], artificial muscles [290], additive manufacturing [291], and smart textiles [292], among others [293, 294]. The process starts from a macroscopic, single or multimaterial preform, usually centimetres in diameter and tens of centimetres in length. Preforms can be made by various combinations of techniques, including but not limited to, consolidation of rolled thin-films [295], vacuum hot press/compression moulding of pellets [296], machining of bars and rods, additive manufacturing [297, 298], and stack-and-draw approach (Holey fibres) [299–301]. Examples of preform materials include polymers, glass, metal alloys (amorphous, liquid, low melting point), semiconductors, and dielectrics. Once fabricated, the preform is thermally softened above its glass transition temperature ($T_g$) at a draw tower and pulled in the viscous fluid state to the desired diameter (tens to thousands of micrometres) and length (tens to hundreds of metres); while maintaining the transverse geometry across the fibre length [302].

Figure 5.1 illustrates the custom-draw tower used to fabricate the multi-lumen tubing. The draw tower consists of a three-zone tube furnace (top, middle, and bottom zones), into which the preform is fed at a controlled speed using a linear translation stage. The furnace ensures control of the temperature profile across the length of the preform. The top zone preheats the preform, the middle zone heats the preform to a temperature above the material's $T_g$, and the bottom zone defines the quenching time of the drawn fibre. Once quenched, the outer diameter of the drawn fibre is readily measured using a laser micrometre. After diameter measurement, the fibre is passed through a three-wheel tension senor, which facilitates the real-time calculation of internal stresses inside the fibre. At the lower end of the system, a capstan is used to pull the fibre from the furnace at a constant speed.

***Step 1 (Materials Selection):*** As discussed in 5.2.2, the biocompatible materials used in the construction of the multi-lumen tubing should not only achieve the desired mechanical properties (flexibility, pushability and torquability), but also resist kinking, preserve lumen patency, tolerate physical sterilisation, and enable ease of fabrication. Comparing different thermally drawable thermoplastics, we identified polycabronate (PC) and polyetherimide (PEI) as good candidates for the aforementioned requirements. Both polymers are amorphous thermoplastics with biocompatible grades, high mechanical strength, excellent dimensional stability, and good resistance to heat and impact. In this investigation, we opted for commercially acquired Medical/Life Science Grade (LSG) polymeric rods (Mitsubishi Chemical Advanced Materials UK Ltd., Lancashire, United Kingdom) as the raw materials for fabricating the preforms.

***Step 2 (Preform Design and Fabrication):*** The multi-lumen tubing fabrication process commences by defining the size and geometry of the macroscopic preform. As indicated in the previously described device requirements, the target steerable catheter should be able to accommodate a 0.014" microguidewire (0.36mm in diameter) and four (0.26mm in diameter) pull-wires. Unlike previous work where high strength synthetic fibres (Dyneema®, Kevlar®, Spectra®) were utilised, the pull-wires herein are also passively MR visible, which makes the steerable catheter also visible over its full length.

The pull-wires incorporated into our steerable catheters are micropultruded rods used in the fabrication of MR safe MaRVis guidewires (MaRVis Interventional GmbH, Krün, Germany). The micropultruded rods (referred to as MaRVis rods) are thin rod-shaped composite materials, composed of non-metallic high strength synthetic fibres (glass and/or aramid fibres) impregnated by a high temperature resistant epoxy resin. The epoxy resin is doped with

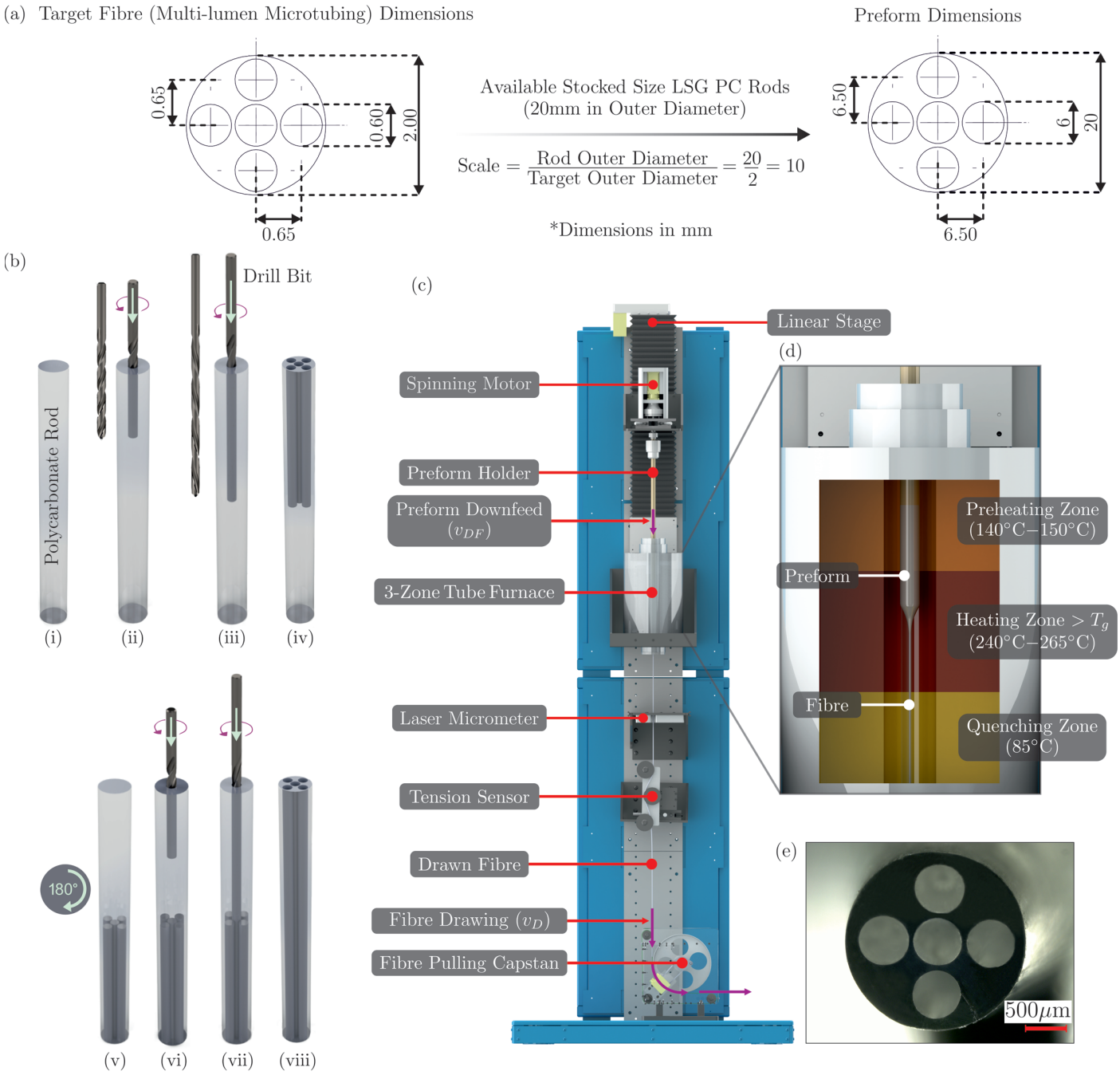



**Figure 5.1:** (a) Fibre to preform calculation. (b) Preform fabrication by peck drilling a polymeric rod from both ends. The preform was drilled from both ends to minimise the vibrations and drifting experienced while drilling across long lengths. (c) CAD rendering of the fibre draw tower. (d) Cross-sectional inset of the three-zone tube furnace with the corresponding preheating, heating and quenching temperatures.(e) A microscopic view of the thermally drawn fibre (multi-lumen tubing).

iron microparticles as passive-negative markers which cause susceptibility artefacts [7]. As a result of its passive-negative nature, the distance between the MR visible pull-wires and neighbouring water molecules influences the sharpness and intensity of the artefacts. In other words, the thicker the layer of polymer enveloping the pull-wires (i.e. pull wires closer to the centre), the sharper the signal will be [157]. This in turn, impacts the preform/fibre design and the positioning of pull-wires with respect to the central axis of the steerable catheter. Bearing this in mind, the preform was designed to incorporate five through-holes: a central hole dedicated for microguidewire insertion and contrast agent injection, and four lateral holes to accommodate the pull-wires. Figure 5.1a illustrates the workflow

adopted to calculate the diameters of the preform through-holes. Based on these designs, the preforms were fabricated by peck drilling through-holes through the PC (20mm) and PEI (3/4") rods as illustrated in 5.1b.

***Step 3 (Fibre "Multi-lumen tubing" Thermal Drawing)***: The preform is fed into the draw tower's three-zone tube furnace at the downfeed speed of $v_{DF}$ = 1 mm/min. The preheating top zone is set to $140°$C for PC and to $220°$C for PEI. The middle zone temperature is set above the glass transition temperature of PC ($T_g$ = $145°$C, set temperature = $240°$C) and PEI ($T_g$ = $215°$C, set temperature = $340°$C). The bottom zone temperature is set to $85°$C and $95°$C for PC and PEI, respectively. An initial weight of 142 grams (5 ounces) was utilised to facilitate the neck down of the preform into a fibre. Once the fibre is quenched, a capstan is used to pull the fibre at a constant draw speed ($v_D$). The fibre is constantly monitored by a laser micrometre (measures outer diameter) and a three-wheel tension sensor (measures tension on fibre). The draw speed ($v_D$) is derived using the conservation of mass (continuity) equation:

$$\underbrace{A_P \cdot v_{DF}}_{\text{Into Furnace - Preform}} = \underbrace{A_F \cdot v_D}_{\text{Out of Furnace - Fibre}} \tag{5.1}$$

where $A_P$ is the cross-sectional area of the preform and $A_F$ is the cross-sectional area of the fibre (multi-lumen tubing).

$$\frac{1}{4} \cdot \pi \cdot D^2 \cdot v_{DF} = \frac{1}{4} \cdot \pi \cdot d^2 \cdot v_D \tag{5.2}$$

where $D$ is the outer diameter of the preform and $d$ is the outer diameter of the targetted fibre (multi-lumen tubing). Rearrange equation 5.2 to compute the required draw speed ($v_D$):

$$\boxed{v_D = \left(\frac{D}{d}\right)^2 \cdot v_{DF}} \tag{5.3}$$

Tension is also an important parameter which provides feedback to tune the draw parameters, mainly the three-zone furnace temperatures. Low tensions may indicate that the draw temperature is high, which could lead to fibres with collapsed lumina (channels). Conversely, high tensions may indicate that the fibre might break due to colder draw temperatures. Ideally fibres are pulled at a constant tension around 100g. In the following section 5.3.2, an additional degree of freedom is added to the drawing process to create axially asymmetric fibres (multi-lumen tubing) which can suppress undesirable mechanical non-linearities.

### 5.3.2 Multi-lumen tubing with a Twist

Three phenomena experienced during the manipulation of flexible pull-wire driven instruments, which are important, yet often not addressed in literature *(with exceptions such as the patent by Bogusky et al.* [303] ), primarily due to limitations and complexities in conventional manufacturing processes are listed below as follows:

1. The unreliable and uncontrollable catheter tip deflections experienced while navigating through non-linear and tortuous anatomies and pathways.**This phenomenon is not caused by the controlled tensioning of the pull-wire as the other two phenomena.*
2. The undesirable lateral motion of the catheter shaft and distal end as a result of tensioning the pull-wire. This is referred to as the muscling phenomenon [303].

3. The undesirable rotational motion of the catheter shaft and distal end as a result of tensioning the pull-wire. This is referred to as the curve alignment phenomenon [303].

***Passive Tip Deflection Phenomenon***: The passive deflections experienced by steerable catheters while navigating through non-linear pathways, results in the uncontrollable lengthening and shortening of the incorporated pull-wires to accommodate the non-linear bends. The pull-wires lengthen if extension forces exist on the lumen and shorten if compressive forces exist on the lumen, as depicted in 5.2a-g. These forces exist because the distance along the external bend is longer than the neutral axis, and the distance along the internal bend is shorter than the neutral axis. Consequently, since the pull-wires are locked/fixed at the proximal end to a manual handle/robotic system, the aforementioned changes in lengths lead to the unreliable and uncontrollable deflection of the *free* and *flexible* distal end of the catheter (unless compensated for by a passive or an active mechanism).

***Muscling Phenomenon***: In the ideal scenario of catheter steering, the tensioning of the pull-wire should deflect only the flexible distal end. Conversely, the catheter's shaft should remain straight along the catheter's neutral axis. One way of achieving this is by having a significantly stiffer shaft which is unsusceptible to bending. However, in practice, it is undesirable to do so, because a very stiff shaft might lead to a high traumatic action in the vessel wall. Hence, tensioning of the peripherally-placed pull-wires results in a cumulative bending moment along the neutral axis of the catheter. This causes the flexible, yet relatively stiff catheter shaft to also laterally bend in the same direction as the distal end (as illustrated in 5.2)h-k.

***Curve Alignment Phenomenon***: As illustrated in Figure 5.2l-o, in this scenario, to articulate the distal end opposite to the direction of the catheter's resting passive bent state, the opposing pull-wire is tensioned. Tensioning the pull-wire applies a compressive load along the external bend, which is opposite to the extension loads applied for bending the catheter in its "current" resting state. Moreover, the tensioned pull-wire will try to return to its lowest energy state, i.e. where the compressive load rests in the catheter's internal bend. This causes the shaft to undesirably rotate so that the tensioned pull-wire rests in the internal bend, thereby, articulating the distal end opposite to the direction intended.

**Proposed Solution**: Inspired by the twisting and coiling of wires to enhance the flexibility, and freedom of movement of flexible devices, Bogusky et al. [303] proposed the adoption of helically routed side lumina (pull-wires) along the catheter shaft to overcome the aforementioned undesirable phenomena. This in turn, radially distributes the compressive loads from a single pull-wire around the catheter. The tensioning of a helically routed pull-wire allows it to transmit the compressive load in several directions around the catheter's neutral axis. Moreover, the bending moments applied on the shaft are also symmetrically distributed around the longitudinal axis of the catheter shaft, which counterbalances opposing compressive and tensile forces. Furthermore, this minimises the net bending (muscling) and rotational forces (curve alignment) by creating a lowest energy state for the pull-wires parallel to the neutral axis. The use of helically routed pull-wires also helps overcome the uncontrolled change in pull-wire length as the catheter navigates through tortuous non-linear pathways. This is also as a result of the exposure of the pull-wires to the counterbalanced extension and compression forces experienced by the hosting lumen, which minimises the changes in pull-wire length. However, helically routed pull-wires create several drawbacks. Helical lumina require compensation for higher frictional forces as the pull-wire travels through the lumen for longer distances [303]. Employing helical lumina that travel longer distances might also adversely affect the mechanical integrity of the multi-lumen tubing due to the reduction in the volume ratio of *enveloping polymer* to *empty lumina*

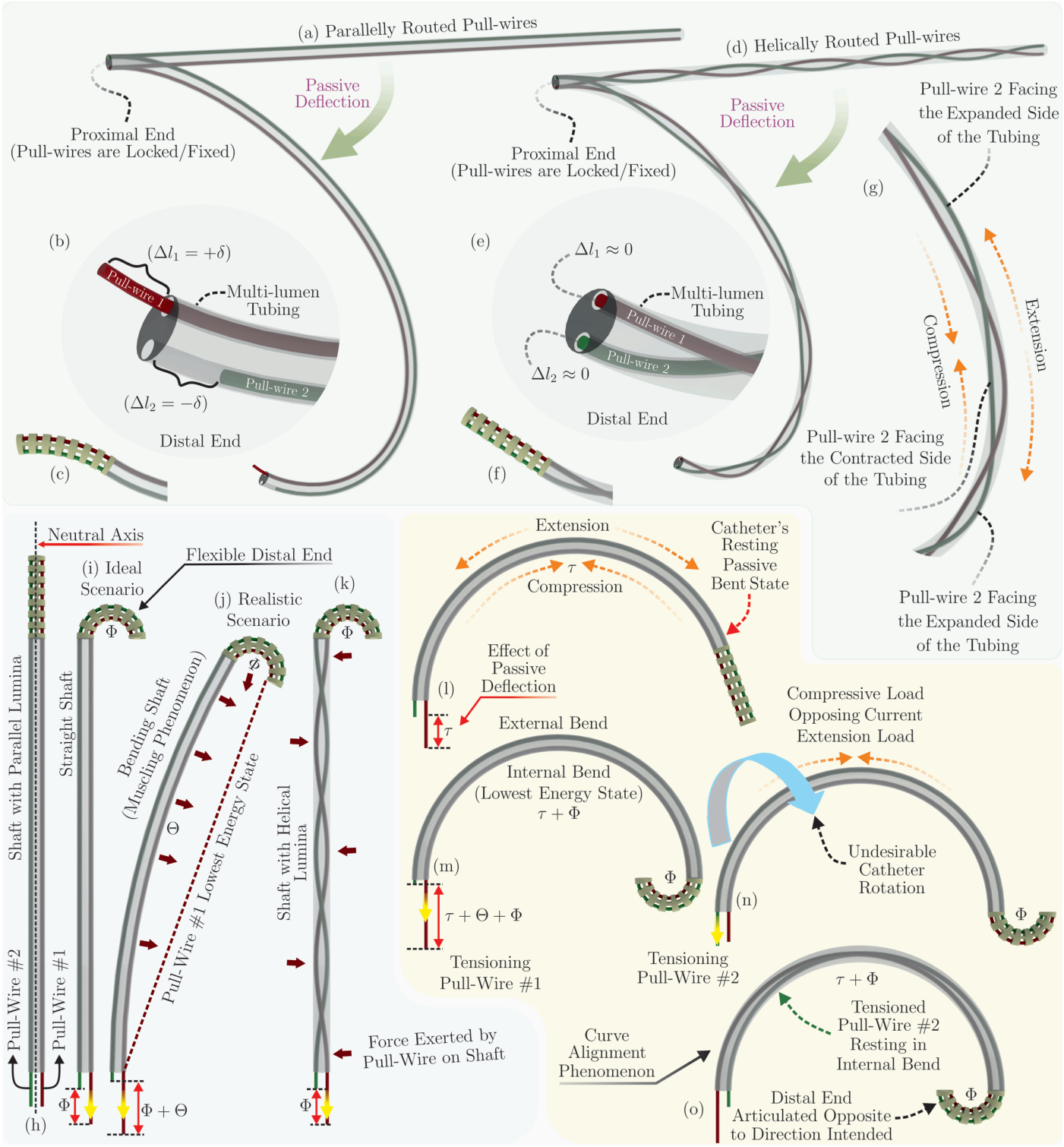



**Figure 5.2:** Three Phenomena experienced during the manipulation of flexible instruments through tortuous anatomies. (a-b) Uncontrollable lengthening (+$\delta$) and shortening (-$\delta$) of the pull-wires as a result of the passive deflection of a flexible shaft with parallelly routed pull-wires. (c) Consequent undesirable bending of the relatively flexible distal end of the catheter to which the pull-wires are anchored. (d-f) Pull-wires routed in helical lumina are exposed to counterbalanced extension and compression forces, which minimises the change in pull-wires length ($\delta \approx 0$). (h-k) muscling phenomenon. (h) Neutral axis of the catheter. (i) Ideal catheter steering, where pull-wire tensioning deflects only the flexible distal end by $\phi$. (j) Realistic catheter steering, where the tensioning of the pull-wire deflects the shaft by $\theta$, for a total catheter deflection of $\phi + \theta$. (k) Counterbalancing of opposing compressive and tensile forces minimises the muscling phenomenon. (l-o) curve alignment phenomenon. (l) Catheter in resting passive bent state with a radius angle of curvature $\tau$. (m) Tensioning of the pull-wire along the internal bend results in the cumulative bending of $\tau + \theta + \phi$. (n) Subsequent tensioning of the opposing pull-wire applies a compressive load which opposes the current extension loads applied for bending the catheter in its current resting state. (o) Undesirable rotation of the shaft as the tensioned pull-wires tries to rest in the internal bend.

across the same length of tubing.

**Previously Proposed Fabrication Method**: To fabricate helically routed channels, Bogusky et al. proposed the following example [303]:

- A main process mandrel is selected to create a cavity in the catheter/endoscope for a central lumen which may function as the working channel.
- Similarly, supplemental mandrels are also selected to create cavities for the (helically routed) pull-wire lumina. *Mandrels can be constructed from PTFE coated metals or thermoset polymers for ease of removal upon completion of subsequent braiding and over-extrusion/polymer coating processes.
- The main process mandrel is fed/advanced through the central hole of a rotating nose cone. Simultaneously, the supplement mandrels are fed through supplemental side holes in the rotating nose cone. As the nose cone rotates, the supplemental mandrels are applied in a helical pattern around the pulled main process mandrel. Thereby creating the cavities for the helical lumina.
- Upon completion, a polymer coating or jacket is sheathed, heated and bonded to the mandrel composite.
- After adding the polymer coating, the main process mandrel is removed from the composite to create a central lumen (or) working channel, and the supplemental mandrels are removed to create the lumina for the pull-wires.

**Proposed Fabrication Method**: Unlike the proposed multi-step fabrication process proposed by Bogusky et al. [303], herein, we propose a new approach which utilises the thermal drawing process by spinning the preform while drawing to fabricate multi-lumen tubing with helically routed channel/lumina in a single step. Spinning of preforms while drawing to create axially asymmetric fibres, have been previously investigated in the fabrication of twisted single-mode fibres [304], helically twisted photonic crystal fibres [305], and spatially expandable multifunctional fiber-based probes for mapping and modulating brain activities [306].

As illustrated in Figure 5.1c, a spinning motor is attached to the linear stage (preform downfeed), and is directly coupled to the Jacob's chuck holding the preform holder/preform assembly. During the draw, the motor spins the preform at a few hundred to thousand revolutions per minute (rpm) in conjunction with the preform downfeed ($v_{DF}$) and fibre drawing ($v_D$). This approach has the advantage that long lengths of multi-lumen tubing (fibres) with helical channels with pitch sizes ranging from a few millimetres to tens of centimetres, can be readily fabricated. Moreover, it is also be possible to control the spinning motor speed $\omega$ and draw speed $v_D$ to vary the pitch of the helical channels across the length of the fibre. Figure 5.3a,b illustrates the process by which straight and helical lumina can be readily fabricated by controlling the spinning motor.

The angular velocity ($\omega$) required to achieve a desired pitch can be calculated as follows. The time period for one complete spinning motor revolution is given by:

$$\omega = \frac{2 \cdot \pi}{T} \Rightarrow T = \frac{2 \cdot \pi}{\omega} \tag{5.4}$$

where $\omega$ is the angular velocity of the spinning motor and $T$ is the time period. Simultaneously, for the same time

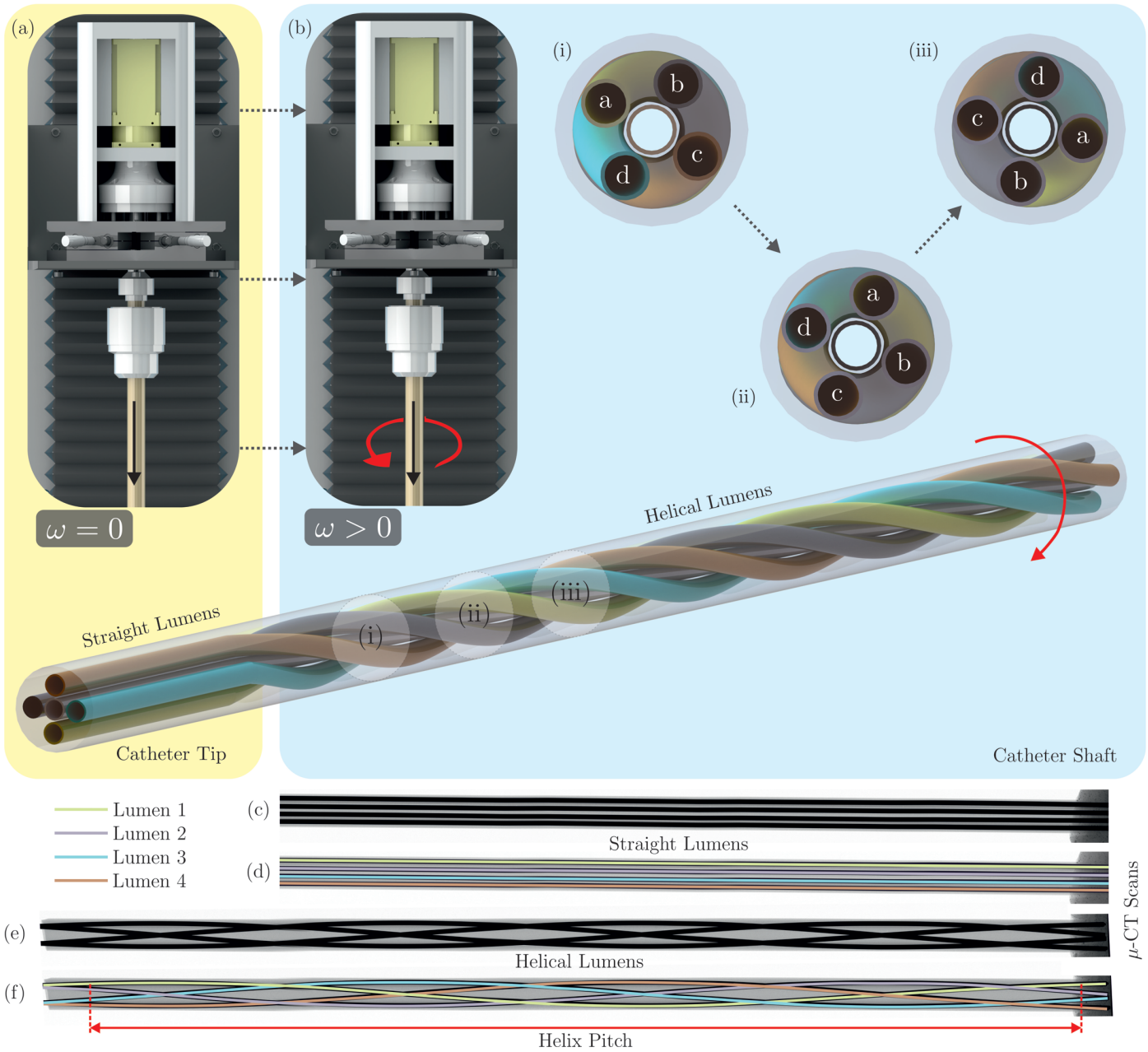



**Figure 5.3:** CAD renderings of the thermal drawing of multi-lumen tubing (fibres) with parallel and helical lumina. (a) Parallel lumina of the distal end of the catheter are fabricated by switching off the spinning motor $\omega = 0$, where $\omega$ is the angular velocity of the spinning motor. (b) Helical lumina of the catheter shaft are fabricated by switching on the spinning motor $\omega > 0$. (b-i). (b-ii), (b-iii) are cross-sectional insets of the fibre across the helically routed catheter shaft. (c-d) $\mu$-CT scan of a multi-lumen tubing (fibre) with parallel channels embedded with four 0.4mm nitinol wires to visualise the lumina. (e-f) $\mu$-CT scan of a multi-lumen tubing (fibre) with helical channels and a pitch size of 50mm.

period $T$, the fibre is drawn/pulled at the draw speed $v_D$:

$$v_D = \frac{l_f}{T} \tag{5.5}$$

where $l_f$ is the length of fibre drawn while the spinning motor completes one revolution. Since the preform is spun from its top end and fibres are pulled from its bottom end simultaneously, the fibre length pulled $l_f$ is equivalent to the helix pitch $p_f$ of the helical channels/lumina created across the length of the drawn fibre (multi-lumen tubing).

Equation 5.5 is rewritten as:

$$v_D = \frac{p_f}{T} \Rightarrow T = \frac{p_f}{v_D} \tag{5.6}$$

Equating 5.5 and 5.6 results in:

$$\frac{2 \cdot \pi}{\omega} = \frac{p_f}{v_D} \Rightarrow \boxed{\omega = \frac{2 \cdot \pi \cdot v_D}{p_f}} \tag{5.7}$$

Knowing the predetermined draw speed $v_D$ (calculated using equation 5.3), and desired helix pitch $p_f$, the motor's angular velocity $\omega$ can be computed.

**Pitch Determination**: As illustrated in Figure 5.2, the lengthening and shortening of pull-wires which results in the undesired tip deflection is non-linear and dependant on the path undertaken by the flexible steerable catheter. Moreover, in a real scenario, the true benefits of helically routed lumina/pull-wires are realised when the constant (or) variable pitch of the helices is optimised towards one or more personalised interventional path(s). However, the aim here is not to optimise the pitch for a specific interventional path, but to propose thermal drawing as an alternative single step process and to perform a preliminary comparative study between thermally drawn multi-lumen tubing with parallel and helical lumina.

Bearing this in mind, several multi-lumen tubing with arbitrarily chosen pitches were thermally drawn, and qualitatively assessed by evaluating the friction between the post-fed pull-wires (MaRVis rods) and the helically routed lumina. Based on these initial qualitative investigations, the smallest helical pitches which did not exert high frictional forces for a one metre long tubing, were 50 $\mathrm{mm}$ and 60 $\mathrm{mm}$ respectively. Prior to performing subsequent testing and characterisation, a Finite-Element (FE) analysis of both configurations is performed to investigate the uncontrolled tip steering as a result of passively deflecting a 100mm shaft by 5mm (ANSYS 2020 R2). The tip and shaft materials were set to PC with the following physical/mechanical properties: Density = 1200 $\mathrm{Kg/m^3}$, Young's Modulus (E) = 2380 $\mathrm{MPa}$, Poisson's Ratio = 0.399, Tensile Yield Strength = 6.21 $\mathrm{MPa}$. The pull-wire on the other hand, is set to stainless-steel with the following physical/mechanical properties: Density = 7500 $\mathrm{Kg/m^3}$, Young's Modulus (E) = 1.93E+05 $\mathrm{MPa}$, Poisson's Ratio = 0.31, Tensile Yield Strength = 207 $\mathrm{MPa}$. The pull-wires are fixed at both ends of the catheter and the interfacing plane between the proximal end of the tip and the distal end of the shaft is also fixed. A passive deflection of 5mm is applied to the shaft midway (50mm) from its proximal end. Figure 5.4a,b,c shows the total deformations of the parallelly routed pull-wire configuration and Figure 5.4d,e,f shows the total deformations of the helically routed pull-wire configuration.

### 5.3.3 Post-Processing of Multi-Lumen Tubing

Once drawn, the fibres (multi-lumen tubing) are cut to length and post-processed as described below.

***Step 1 (Over-braiding)***: To further enhance the mechanical properties of the thermally drawn multi-lumen tubing, additional braid reinforcement are added along its length (excluding the distal end) as illustrated in Figure 5.5a. Braid reinforcement improves torquability, reduces whip, and improves kink resistance, without a significant increase in the catheter's wall thickness and outer diameter. Thus, the same mechanical characteristics of thick-walled catheters can be achieved with thin-walled and smaller catheters.

***Catheter Whip***: is an undesirable behaviour which occurs when the distal end of the catheter does not respond as the proximal hub/handle of the catheter is rotated. In this event, the catheter builds up energy and then releases

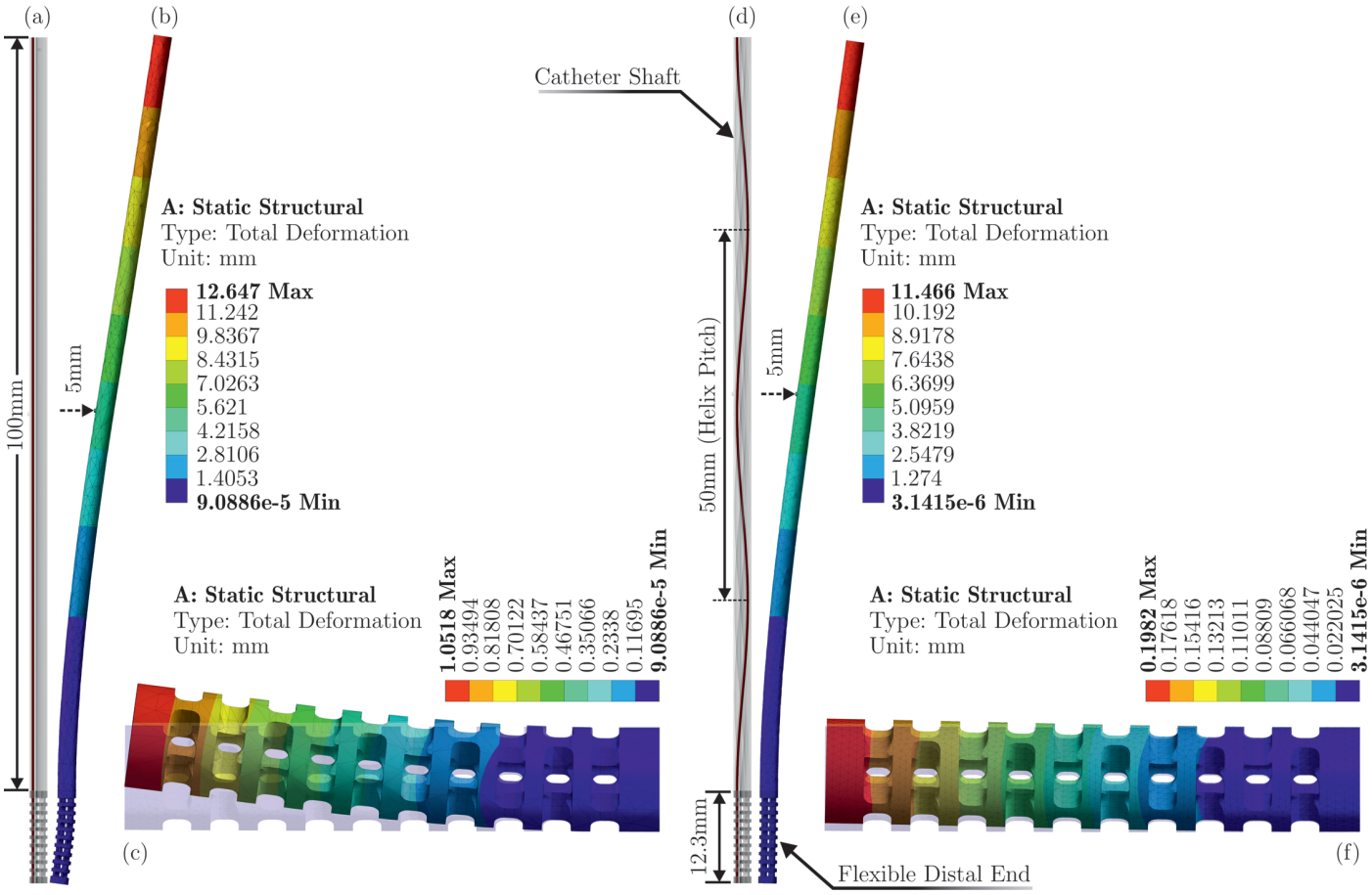



**Figure 5.4:** FEM static structural analysis (a-b) Steerable catheter with a flexible distal end and a parallelly routed pull-wire which is anchored at both ends of the catheter. The catheter shaft was subjected to a passive deflection (displacement) of 5mm midway to simulate passive deflection. (c) Total deformation contours of the flexible distal end for the parallel case. (d-e) Steerable catheter with a flexible distal end and a helically routed pull-wire which is also anchored at both ends. The catheter is subjected to the same boundary conditions and loads. (f) Total deformation analysis of the flexible distal end for the helical case. Note: The proximal end of the flexible distal end is fixed. Simulation settings and parameters: catheter material: Polycarbonate (PC), pull-wire material: stainless steel, coefficient of friction between the pull-wire and catheter: 0.2.

that energy causing the catheter to suddenly whip (rotate with high acceleration) within the vessel.

Over-braiding is the process of intertwining three or more metallic wires and/or monofilament/multifilament yarns diagonally over a mandrel in a pre-established fashion to create the desired braid architecture [307]. The reinforcement was added using a vertical Maypole type braider (Herzog RU 2/16-80, HERZOG GmbH, Germany). The braiding process commences by transferring the commercially acquired yarns from the as supplied bobbin to bobbins or spools which are then fitted on carriers. Carriers move in a pseudo-sinusoidal fashion on the braider track plate with the help of horn gears. Half of the carriers move clockwise (green carriers in Figure 5.5a) whereas the other half move in opposite direction (red carriers in Figure 5.5a). When a carrier meets the horn gear moving in the opposite direction, it switches to the latter by a mechanism similar to a railway switch. To prevent slack or loosening of the yarn, the carries are equipped with a tension adjustment spring system to keep the yarn uniformly under tension while being driven along its path [307–309].

When each yarn passes over and below one other yarn, the resulting braid is 1/1, or a diamond braid (Figure C.1a). When each yarn passes over and below two other yarns, the resulting braid is 2/2 or a regular braid (Figure C.1b).

In the case where each yarn passes above and below three other yarns, it is referred to as 3/3 or a Hercules braid (Figure C.1c). Examples of commonly used braid materials in the field of catheter manufacturing include: stainless-steel (e.g. 304V, 304L, and 316L grades), and nitinol. Since using metals in MR environments increases the risk of resistive heating and RF induced heating; high strength synthetic/glass fibres are used herein as a comparable substitute. The two MR safe alternatives include: Kevlar®49 yarns (DuPont, Delaware, United States), and Liquid Crystal Polymer (LCP) 50$\mu$m monofilament yarns (Zeus Industrial Products Inc, Orangeburg, United States). Sixteen bobbins/spools of the aforementioned polymeric materials were loaded onto the carriers and interlaced over the thermally drawn multi-lumen tubing in a 1/1 diamond fashion.

***Step 2 (Laser-Profiling)***: After adding the braid reinforcement, the non-braided distal end of the tubing is laser cut as illustrated in Figures 5.5c,d,e and f. Laser cutting the distal end increases its flexibility in relation to the proximal shaft, which in turn, enables the steering of the catheter tip and its atraumatic introduction into tortuous vessels. A thorough investigation of the different types of cutting profiles (joint designs) and laser micromachining processes were made prior to this post-processing step. While a body of literature exists on the development and optimisiation of joint designs for the distal ends of deflectable catheters/endoscopes, Jelínek et al's review paper served as the basis for determining the optimal design to pursue [310]. The type of joints adopted in this study are the 2 DOF perpendicular compliant flexure hinge joints. These joints approximately act as hinges due to flexural bending [311], and are formed by cutting notches out of the distal end of the thermally drawn multi-lumen tubing. This choice was made for several reasons, including its simplistic design, ease of miniaturisation/fabrication, and its inherent capabilities of preventing slip, spin, and transverse/axial split or disconnection of joint segments (with respect to the catheter's shaft). However, this design operates within the limits of the material's elastic region, beyond which the material plastically deforms.

In order to optimise the flexure hinge design and to avoid undesirable plastic deformation, a computational design tool (detasFLEX) was employed to rapidly analyse various hinge designs prior to fabrication (Figure C.1f). The tool developed in MATLAB uses a non-linear analytical approach for large deflections of rod like structures to compute the elasto-kinematic flexure hinge proprieties by numerically solving a system of differential equations [312]. The first step in using the software is to specify the materials' (PC and PEI) Young's moduli (E), and their corresponding admissible elastic strains ($\varepsilon_{ad}$) as follows:

- PC $\Rightarrow$ E : 2400 MPA, $\varepsilon_{ad}$ : $5\%$
- PEI $\Rightarrow$ E : 3500 MPa, $\varepsilon_{ad}$ : $6\%$

This was followed by specifying the geometry of the corner-filleted hinge contour and the maximum load (bending moment) on the flexure hinge. A set of arbitrary initial hinge dimensions were assigned to start the iterative analysis process. The maximum bending moment on the other hand was computed by multiplying the estimated maximum pull-wire tension ($\approx 10$ N) by the perpendicular distance between the pull-wire axis (side lumen axis) and the central axis of the multi-lumen tubing. The target of this analysis is to achieve the desired catheter tip total deflection of $90°$ without exceeding the admissible elastic strains. Once designed, a CAD model of the optimised structure/profile is generated for the subsequent subtractive micromachinging process.

After careful consideration of the various micromachining techniques (e.g. conventional micromilling/microdrilling, Focused Ion Beam (FIB) milling, Electrical Discharge Machining (EDM), laser micromachining), we opted for laser

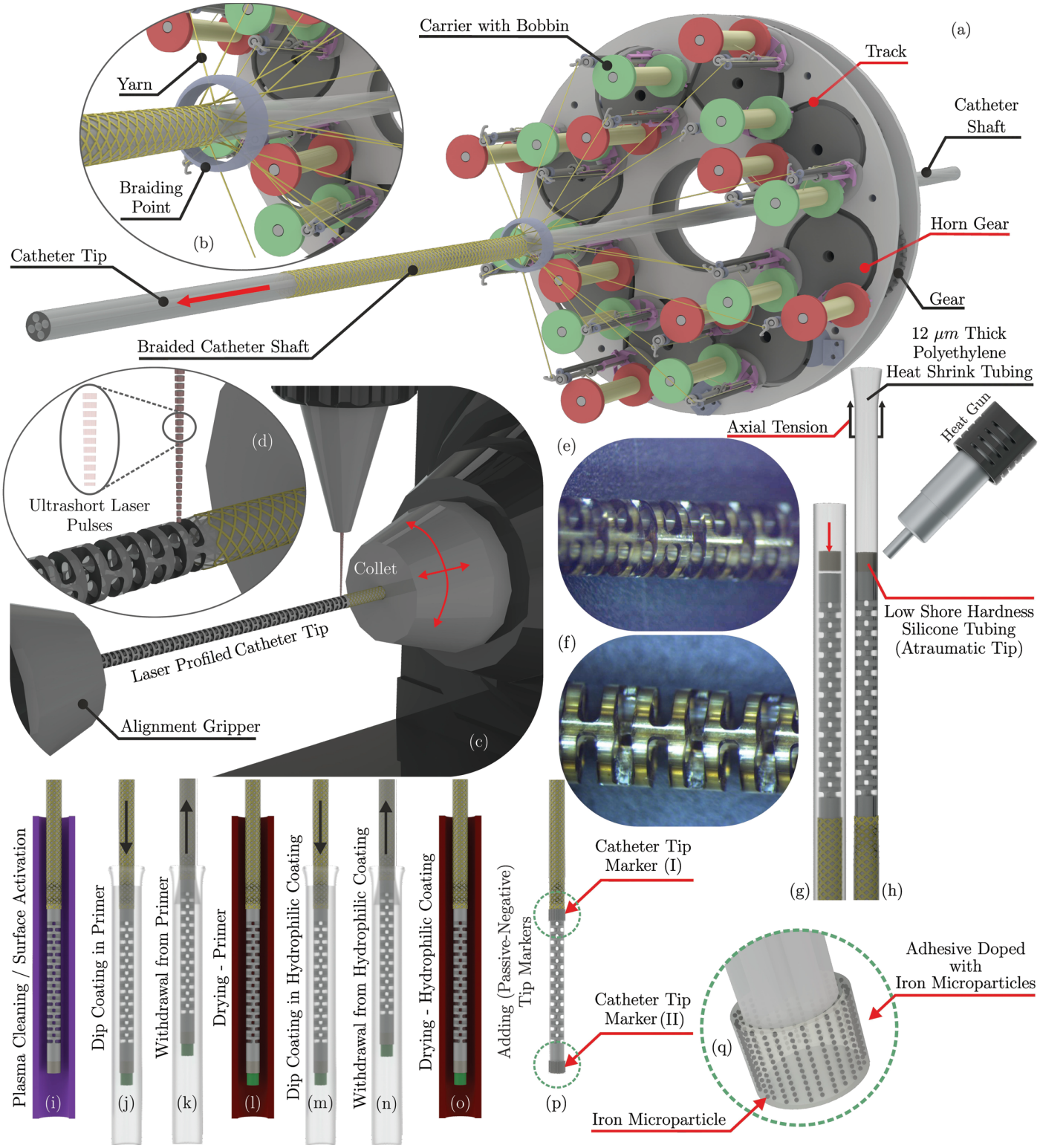



**Figure 5.5:** (a) CAD rendering of the Maypole braider used to overbraid the bare thermally drawn multi-lumen tubing (fibre). Note: The distal end of the tubing is left non-braided to facilitate subsequent laser profiling. (b) Inset of the yarns braiding point. (c) CAD rendering of the laser profiling setup. (d) Inset of the ultrashort laser pulses used to non-thermally ablate the polymeric substrate. (e-f) optical images of the laser cut samples with laser cut notches. (g-h) CAD renderings of covering the overbraided and laser cut multi-lumen tubing (fibre) with heat shrink tubing. (i) Plasma cleaning and surface activation of the catheter assembly. (j) Dip coating the assembly in primer (Note: A blocker (indicated in green) is added at the distal most point to prevent the coating material from infiltrating and blocking the lumina. (k) Withdrawal from the primer. (l) Primer-coated assembly is dried for 5 minutes at 80°C. (m) Dip coating the assembly in a hydrophilic coating. (n) Withdrawal from the hydrophilic coating. (o) Hydrophilic-coated assembly is dried for 8 hours at 80°C. (p) Adding the passive negative tip markers for visualisation under MR. (q) Inset of the tip marker.

micromachining because it is better able to handle more intricate and complex 3D cutting profiles on polymeric substrates. Moreover, several laser parameters affect the micromachining outcome, most prominently the choice of pulse width. The laser's pulse width affect the precision, throughput, quality, and economics of the process [313]. Pulsed lasers with pulse widths in the nanosecond to femtosecond range are commonly employed for the precision micromachining of various materials.

***Laser Ablation:*** The two main mechanisms used in the laser ablation of materials are thermal and non-thermal ablations. For thermal ablation, upon the irradiation of a continuous laser beam or a pulsed laser beam with pulse length down to nanoseconds, the laser pulse interacts with the solid target, which excites and heats the electrons to a high temperature by the absorption of laser energy. In this case, the laser pulse has enough time to excite the lattice vibrations and heat it to the vaporisation temperature. On the contrary, for ultrashort laser pulses (e.g. femtosecond pulsed), energy is transferred to the electrons on a time scale much faster than the transfer time of this energy to the lattice of the material. Thus allowing material machining with minimal thermal damage or without heat-affected zones, i.e. suppressing the melting or carbonisation phenomenon [314, 315].

The distal end micromachining was performed using the LML-femto2000 ultrafast laser micromachining tool (Laser Micromachining, St. Asaph, United Kingdom). The machine comprises a Pharos femtosecond laser system (Pharos SP-HP, Light Conversion, Vilnius Lithuania) which is capable of producing three wavelengths from three separate output ports: 1030nm (infrared), 515nm (visible), and 343nm (ultraviolet). The multi-lumen tubing was machined using the using the ultraviolet femtosecond laser. The multi-lumen tubing is held by the collet chuck of a lathe stage (LaserTurn1, Aerotech, Inc., Pennsylvania, United States) to laser cut the notches in the object as illustrated in Figure 5.5d-f.

***Step 3 (Covering, Coating & Tip Marking)***: To encapsulate the braid reinforcement and suppress the thrombogenesis of the laser cut catheter tip, the post-processed assembly is covered by two polyethylene heat shrink tubing with a wall thickness of 6$\mu$m (103-0042, Nordson MEDICAL, New Hampshire, United States), as illustrated in Figure 5.5g,h. Prior to activating the heat shrink tubing, a short section of a low shore hardness platinum cured silicone tubing with similar outer diameter (SFM3-2050, Polymer Systems Technology Ltd, High Wycombe, United Kingdom) is mechanically held against the distal most point of the catheter inside the expanded heat shrink. Once heated, the shrink tubing collapses and adheres/joins both components together to form an atraumatic tip. This minimises the risk of vessel perforation or dissection while manoeuvring the catheter through tortuous anatomies.

In order to reduce the surface friction and improve the catheter's manoeuvrability, an additional layer of hydrophilic polymer coating is added to the encapsulated assembly (as illustrated in Figure 5.5i-o). The hydrophilic coating's ability makes the catheter more lubricious and easier to navigate through tortuous anatomies. The coating process commences by wiping the catheter samples with isopropanol, followed by placing the catheter in an oxygen plasma oven (Atto, Diener electronic GmbH & Co. KG, Ebhausen, Germany) for 5 minutes to clean and activate the catheter's outer layer surface which improves its adhesion characteristics (Figure 5.5i). Next the plasma cleaned assembly is dip coated in a urethane-based primer (Primer 5-017, Coatings2Go, Massachusetts, United States) to further promote the outer surface's adhesion to the subsequent hydrophilic top coat. Once dried for 5 minutes at 80°C, the assembly is dip coated in a water-based hydrophilic coating (Patented Hydrophilic Coating 8-3C, Coatings2Go, Massachusetts, United States). This post-processing step is concluded by drying the coated catheter inside the draw tower's 3-zone tube furnace for 8 hours at 80°C. At the distal end of the catheter, two additional passive

negative markers (adhesive doped with iron microparticles) were added: one at the distal most point of the catheter and the other at the proximal end of the deflectable tip. These markers, alongside the aforementioned MR visible pull-wires enable the physician to enchance the visibility of the catheter tip and ensure that it is present in the projected MR image slice.

## 5.4 Bench-top Mechanical Characterisation

As described in 5.2.2, MR safe catheters should have similar mechanical integrity as their MR unsafe counterparts. To better gauge and evaluate key mechanical performance parameters of our in-house fabricated catheter shafts against commercial catheter shafts, the following characterisation setups were devised. Note: The catheter samples used in these experiments are listed in B.

### 5.4.1 Flexural Rigidity

Flexural rigidity, also known as the bending stiffness (in the case of beams), is the reciprocal of flexibility, which reflects the stiffness of the material when subjected to bending. The purpose of this characterisation is to measure the force required to bend a specific length of the catheter shaft. In general, it is desirable for the catheter shaft to have sufficient flexural rigidity to guide and support other intravascular devices. Conversely, the flexible distal end should have a relatively lower flexural rigidity to facilitate safe, atraumatic navigation through tortuous anatomies. Herein, the catheter shafts fabricated in-house (parallel/helical lumina, and braided/non-braided) are benchmarked against commercially available fluoroscopy-guided selective and steerable catheters.

The bending is modelled as the deflection of a cantilever beam using the Euler-Bernoulli beam theory. This theory assumes small deflections when the beam is loaded in the lateral direction [316]. Using the Euler-Bernoulli equation, the maximum deflection of the catheter $\delta$ is defined as follows:

$$\delta = \frac{FL^3}{3EI} \Rightarrow EI = \frac{FL^3}{3\delta} \tag{5.8}$$

where $L$ is the length of the catheter shaft sample, and $\delta$ is the maximum deflection produced by the lateral force F exerted at the free end of the catheter shaft sample (Figure 5.6d). The product of the modulus of elasticity of the catheter material ($E$) and the moment inertia of the cross-section of the catheter with respect to its neutral axis ($I$) are usually grouped and referred to as flexural rigidity ($EI$). Flexural rigidity is independent of the experimental setup, such that if other values for $L$ and $\delta$ are chosen, the ($EI$) value remains the same [317].

#### 5.4.1.1 Methodology

*Experiment 1-1:* The catheter shaft sample protrudes $L$ = 20mm from the pin vise and a push rod located just above the free end is used to apply a force that leads to a relatively small deflection $\delta$ of 5mm. The other end of the push rod is fixed to a force/torque sensor (ATI F/T Sensor Nano43, ATI Industrial Automation, North Carolina, United States) which measures the force required to push the sample. To achieve high positioning resolution, the push rod/sensor assembly is mounted to a linear stage (M4004M, Parker, Pennsylvania, United States) which in turn is coupled to a servo motor (Dynamixel MX-106T, Robosavvy, London, United Kingdom). Figure 5.6b,c,d) illustrate the flexural rigidity experimental setup. The push rod moves with a constant speed until the sample is deflected by

5mm. Subsequently, the deflected sample is held at the same position for 12 seconds and released as the push rod retracts at the same constant speed back to the home position. Thirteen[1] different types of catheter shafts were examined. Five samples of each shaft were tested once, i.e., five times for each type of catheter shaft.

*Experiment 1-2:* It is likely that the stiffness of the catheter would decrease *in-vivo* due to the effect of body temperature and moisture absorption [318]. This, in turn, adversely affects the mechanical integrity of the catheter during intervention. To evaluate the effect of temperature and moisture on flexural rigidity, the catheter samples are immersed in a simulated intravascular environment with water at 37.4°C for 30 minutes. This is followed by repeating *Experiment 1-1* in a tank with water circulating at a constant temperature of 37.4°C $\pm$ 0.5°C. Each catheter shaft sample was tested four times.

*Experiment 1-3:* During catheterisation, catheters can be held in a bent state for some time (usually 10 to 15 minutes) while performing subsequent treatment or therapy through its working channel. During which, the polymers that make up the catheter display stress relaxation, which results in the reduction of the shaft's flexural rigidity over time [318]. Stress relaxation is the change in stress, i.e. reaction force, that occurs to a material due to a constant strain over time. To characterise this property, using the same setup, the push rod moves with a constant speed until the sample is deflected by $5\mathrm{mm}$. Subsequently, the deflected sample is held at the same position for 900 seconds (15 minutes) during which the force is recorded. Each type of catheter was tested once.

### 5.4.1.2 Results and Discussion

Figure 5.6a shows the flexural rigidities ($EI$) for *Experiments 1-1* and *1-2*, after an elapsed time of 12 seconds for the different types of catheter shafts before and after immersion in warm water at 37.4°C and their corresponding drop in $EI$ (expressed in percentage). For *Experiment 1-3*, the recorded flexural rigidities ($EI$) for the entire time period of 15 minutes, are shown in Figure 5.6e.

*Experiment 1-1*: For the catheter shafts fabricated in-house, under dry conditions, the $EI$ of PEI non-braided shafts with parallel and helical lumina demonstrate higher flexural rigidities (974.6Nmm$^2$ to 877.2Nmm$^2$) when compared to their PC counterparts (653.1Nmm$^2$ to 532.8Nmm$^2$). In terms of lumina, catheter shafts with helical lumina have lower $EI$s as opposed to shafts with parallel lumina. For example: non-braided PC shafts with parallel lumina demonstrate 8.48% higher $EI$ than PC shafts with parallel lumina. This is due to the fact that shafts with helical lumina have a smaller volume ratio of *enveloping polymer* to *empty lumina* across the same length of tubing. The presence of braiding contributes to an increase in $EI$. In the case of PC shafts with parallel lumina, braiding increase the catheter shaft's $EI$ by 10.85%. Similarly, for PC shafts with helical lumina, braiding increase the catheter shaft's $EI$ by 8.27%. In general, the in-house fabricated catheter shafts have shown comparable flexural rigidities to the commercial selective and steerable catheters. Among all the test samples, PEI catheter shafts (parallel and helical) have the highest flexural rigidities, with the Magellan™guide catheter shaft trailing behind in third with an EI of 669.8Nmm$^2$. The ablation catheter shaft from Biosense Webster®, shows a similar $EI$ (545.1Nmm$^2$) to the non-braided PC catheter shaft with helical lumina (532.8Nmm$^2$). The $EI$ of the other three PC catheter shafts lie in between 669.8Nmm$^2$ (Magellan™guide catheter shaft's $EI$) and 545.1Nmm$^2$ (Biosense Webster® ablation catheter shaft's $EI$).

[1]Magellan™lead catheter has three segments of different materials along the length of the catheter shaft. Each segment is treated and tested as a separate shaft

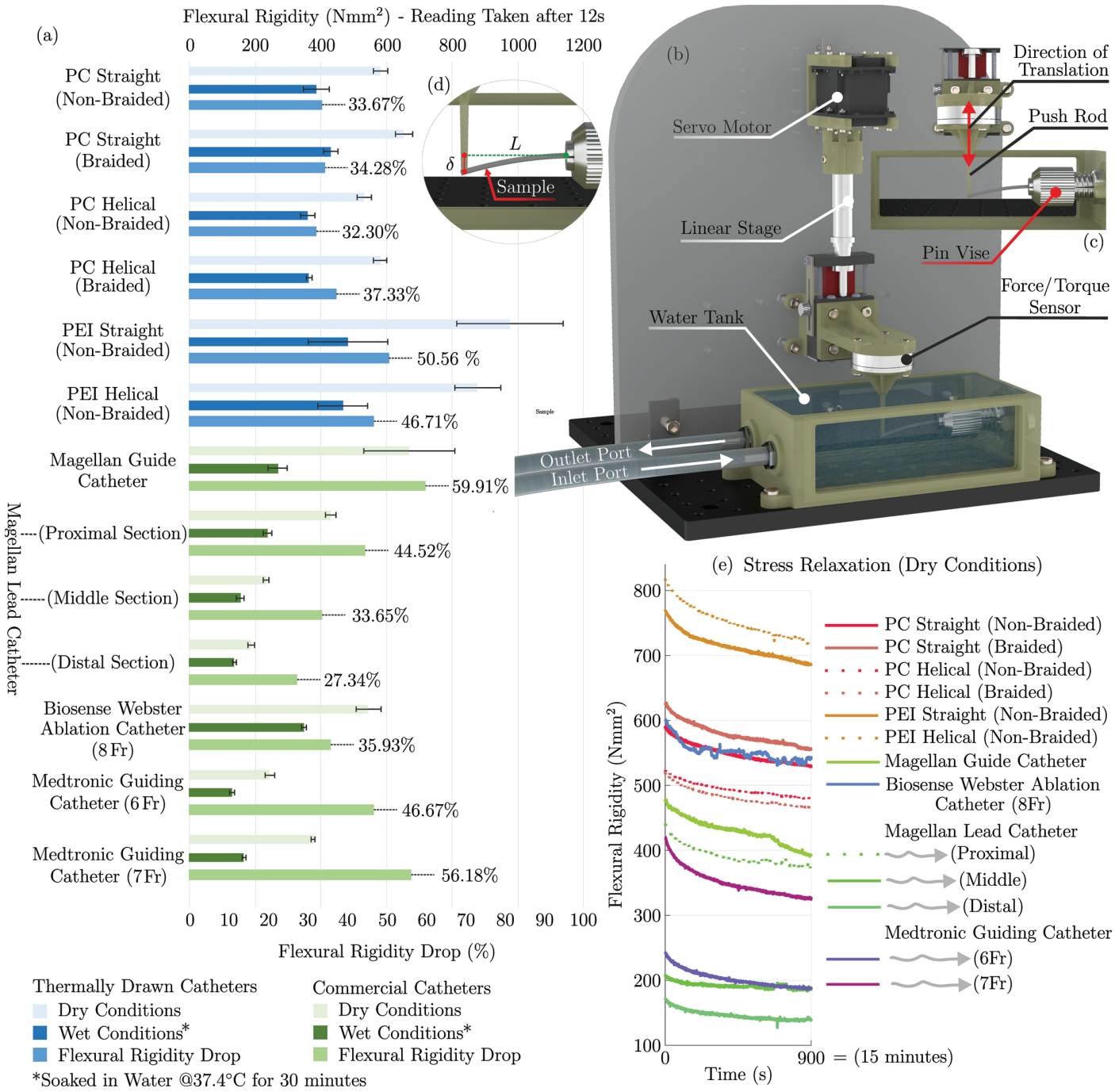



**Figure 5.6:** Flexural Rigidity - Experimental Setup and Results. (a) *Experiment 1-1* and *1-2* results. (b) CAD renderings of the experimental setup. (c) Inset of the direction of translation of the push rod and force/torque assembly. (d) Inset illustrating the maximum deflection $\delta$ and the length of the sample $L$. (e) *Experiment 1-3* Stress relaxation results.

*Experiment 1-2*: After fully immersing the samples in 37.4°C water for 30 minutes, their $EI$ decrease considerably, and the percentage of decrease is correlated with the $EI$ value under dry conditions. The smallest drop in $EI$ is in the case of the distal part of the Magellan™lead catheter shaft (27.34%). Conversely, the flexural rigidity of the PEI catheter decreases to about half of its dry condition values: from 974.6Nmm$^2$ to 481.82Nmm$^2$) for shafts with parallel lumina and from 877.24Nmm$^2$ to 467.52Nmm$^2$ for shafts with helical lumina. Despite the fact that the $EI$s of the proposed embodiments of the MR safe catheters are significantly lower than dry conditions, they are still comparable to their commercial counterparts.

| **Catheter Shaft Sample** | $EI$ $t = 0$s (Nmm$^2$) | $EI$ $t = 900$s (Nmm$^2$) | Drop (%) |
|---|---|---|---|
| PC Parallel (Non-Braided) | 587.72 | 528.96 | 10 |
| PC Parallel (Braided) | 626.40 | 557.83 | 10.95 |
| PC Helical (Non-Braided) | 521.05 | 478.85 | 8.10 |
| PC Helical (Braided) | 518.65 | 464.80 | 10.38 |
| PEI Parallel (Non-Braided) | 767.89 | 685.89 | 10.68 |
| PEI Helical (Non-Braided) | 815.08 | 717.73 | 11.94 |
| Magellan Guide Catheter | 474.82 | 391.78 | 17.49 |
| Magellan Lead Catheter - Proximal Part | 439.68 | 376.34 | 14.41 |
| Magellan Lead Catheter - Middle Part | 207.23 | 186.70 | 9.91 |
| Magellan Lead Catheter - Distal Part | 172.26 | 139.15 | 19.22 |
| Biosense Webster Ablation Catheter | 601.53 | 538.45 | 10.49 |
| Medtronic Guiding Catheter 6Fr | 241.33 | 186.98 | 22.52 |
| Medtronic Guiding Catheter 7Fr | 420.31 | 325.80 | 22.49 |

**Table 5.1:** Percentage drop in $EI$ of the 13 catheter shaft samples when immersed in warm water at 37.4°C

*Experiment 1-3*: For the stress relaxation experiment, the flexural rigidities of all samples are seen to decay as a function of time. The largest drop in $EI$ is in the case of the Medtronic Guiding Catheters (6Fr & 7Fr) with an average drop of 22.5%. On the other hand, the PC catheter shaft with helical lumina have shown the smallest drop in $EI$ over the 15 minutes preiod (8.10%). On average, the in-house fabricated catheter shafts demonstrate an average drop of 10.34%. Table 5.1 reports the % drop in $EI$ for all 13 in-house fabricate and commercial samples.

Based on these experimental results, it can be concluded that the in-house fabricated catheters have similar flexural rigidities when compared to their commercial fluoroscopy-guided counterparts. Despite these encouraging findings, they also revealed some room for improvement in the experimental methodology. First, the experiments were conducted in a non-temperature-controlled laboratory, and changes in room temperature may have also had an impact on the results of the experiments. Therefore, a temperature and humidity controlled environment may improve the accuracy of these measurements. Second, to distinguish between the effect of moisture and temperature, the samples could be weighed before and after their immersion in warm water. This can give a better view of the effect of moisture on the bending stiffness of the samples. Moreover, due to the limited number of samples, it is unavoidable that the same sample would be used multiple times which might lead to a cumulative deformation effect.

### 5.4.2 Pushability

Pushability reflects the capability of the catheter to transmit forces in the axial direction. Adequate pushability is desirable in catheter shafts because it allows more force to be transmitted along the shaft of the catheter, thus enabling smooth (buckling-free) advancement through the vasculature. This experiment is designed to examine the pushability of different catheter shafts, by estimating their axial rigidity ($EA$). $E$ is the modulus of elasticity of the catheter material, and $A$ is cross-sectional area of the sample (modelled as a beam). Using Hooke's law, the following equation is used to derive $EA$:

$$EA = \frac{PL}{\delta} \tag{5.9}$$

where, $L$ is the length of the catheter shaft sample and $P$ is the force required to push one end of the sample a displacement of $\delta$ after securing the other end of the sample.

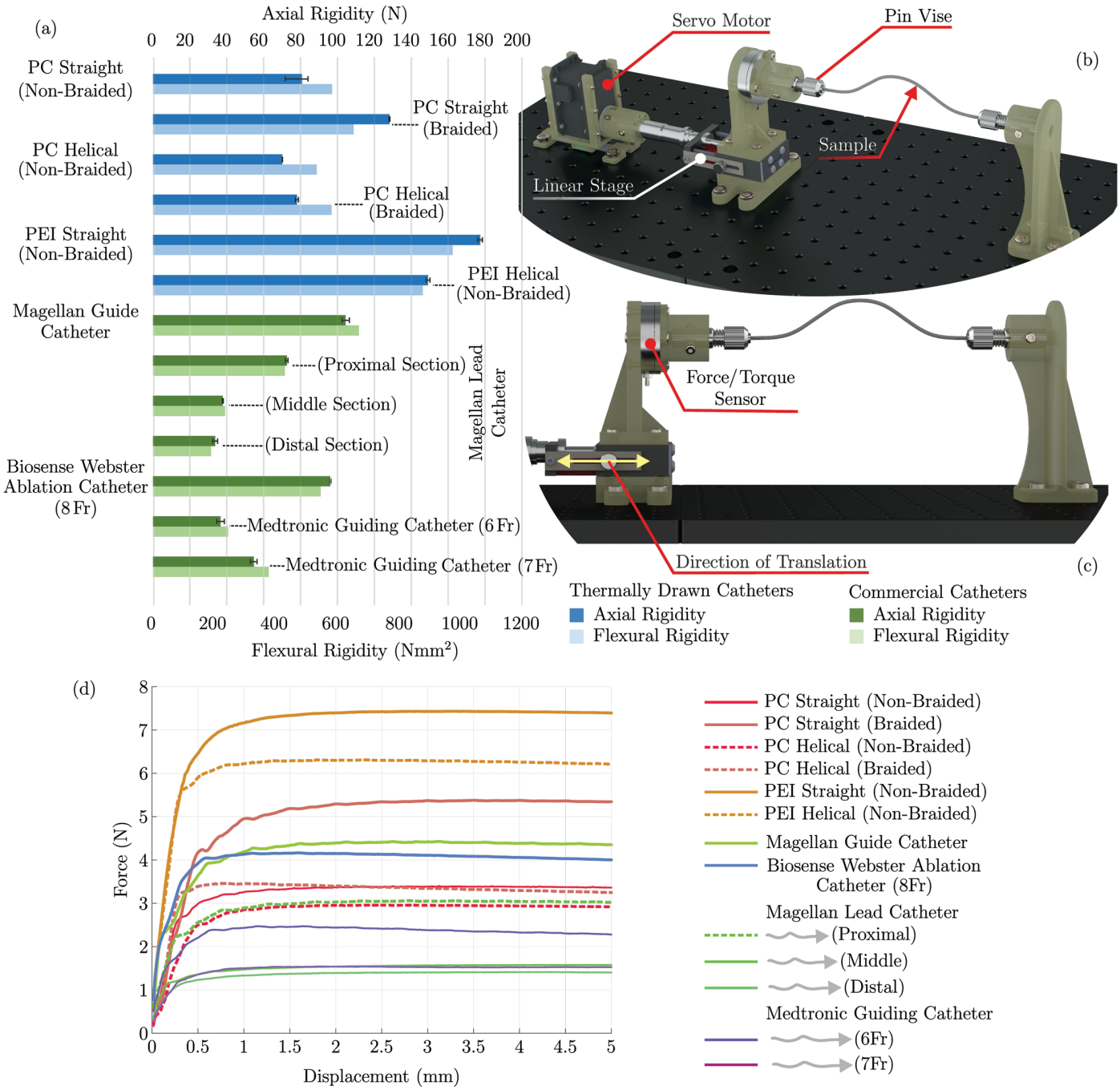



**Figure 5.7:** Experiment 2: Pushability - (a) Results, (b-c) CAD renderings of the experimental setup. (d) Force versus displacement .

### 5.4.2.1 Methodology

*Experiment 2:* In this experiment, as shown in Figure 5.7b,c, the catheter shaft sample is held in place with two pin vises spaced $L$ = 120mm apart. One pin vise is fixed to a force/torque sensor (ATI F/T Sensor Nano43, ATI Industrial Automation, North Carolina, United States) to measure the reaction force $P$ required to push the catheter shaft sample a displacement $\delta$ = 5mm. The pin vise and force/torque sensor assembly is mounted to a linear stage (M4004M, Parker, Pennsylvania, United States) coupled to a servo motor (Dynamixel MX-106T, Robosavvy, London, United Kingdom) to produce the aforementioned displacement. Each catheter shaft sample was tested for at least three times.

#### 5.4.2.2 Results and Discussion

Figure 5.7d shows the force-displacement curves for each catheter shaft sample, from which it is evident that after a certain force value is reached, all samples are incapable of transmitting greater forces due to buckling. In general, the stiffer the catheter (i.e. higher flexural rigidity), the greater axial force it can transmit (as indicated in Figure 5.7a). Similar to the flexural rigidity results, the PEI catheter shafts demonstrate the highest axial rigidity out of all the samples (149.07N to 177.39N). By comparing the different configurations of PC catheter shafts, over-braiding increases the the samples' $EA$ by 37.06% in the case of parallel lumina and 10.17% in the case of helical lumina. Furthermore, catheter shafts with helical lumina have lower axial rigidities when compared to shafts with parallel lumina. For example: PC non-braided catheter shafts demonstrate a drop of 13.14%. On the contrary, PC braided catheter shafts show a larger drop in $EA$ of 39.14%. Apart from the braided PC catheter shaft with parallel lumina, which has a relatively high $EA$, the other three PC catheters shafts show pushability similar to that of the commercial catheters (Magellan™guide catheter, proximal part of Magellan™lead catheter, Biosense Webster®, and 7Fr Medtronic™guide catheter), with a maximum transferable force of approximately 3N to 4.3N.

Based on these experimental results, it is sufficient to draw the conclusion that in-house fabricated catheter shafts have comparable axial rigidities to their commercial counterparts. However, similar to what has been observed from the flexural rigidity experiments, carrying out the pushability experiments in a temperature and humidity controlled environment may improve the overall accuracy of the measurements. Moreover, conducting further experiments in a simulated intravascular environment would help account for the effect of body temperature and moisture absorption on the axial rigidity of the catheter shaft samples.

### 5.4.3 Torquability

Torquability evaluates the torque transmission ability of the catheter from its proximal end to its distal end. In general, high torquability is desirable to accurately control the distal end of the catheter whilst navigating through tortuous anatomies. The product of the shear modulus or modulus of rigidity ($G$) and the polar moment of inertia of the shaft ($J$), i.e. the torsional rigidity ($GJ$), is often used as a metric to quantify the torquability of a device. The torsional rigidity ($GJ$) is obtained using the following equation [319]:

$$GJ = \frac{TL}{\phi} \tag{5.10}$$

where $L$ is the length of the catheter shaft, and $T$ is the torque required to rotate the catheter by $\phi$ (angle in rad).

#### 5.4.3.1 Methodology

*Experiment 3-1:* As shown in Figure 5.8b, the catheter shaft sample is clamped by two pin vises at a distance of $L$ = 120mm. One of the pin vises is mounted to a servo motor (Dynamixel MX-106T, Robosavvy, London, United Kingdom) to subject the sample to a torque around its axis, with an angle of twist ($\phi$ = $2\pi$). The other pin vise is attached to a static force/torque sensor (ATI F/T Sensor Nano43, ATI Industrial Automation, North Carolina, United States) to measure the torque $T$. Each catheter shaft sample is tested for at least five times. Torque is measured at the 12$^{th}$ second after the catheter shaft sample is twisted about its axis.

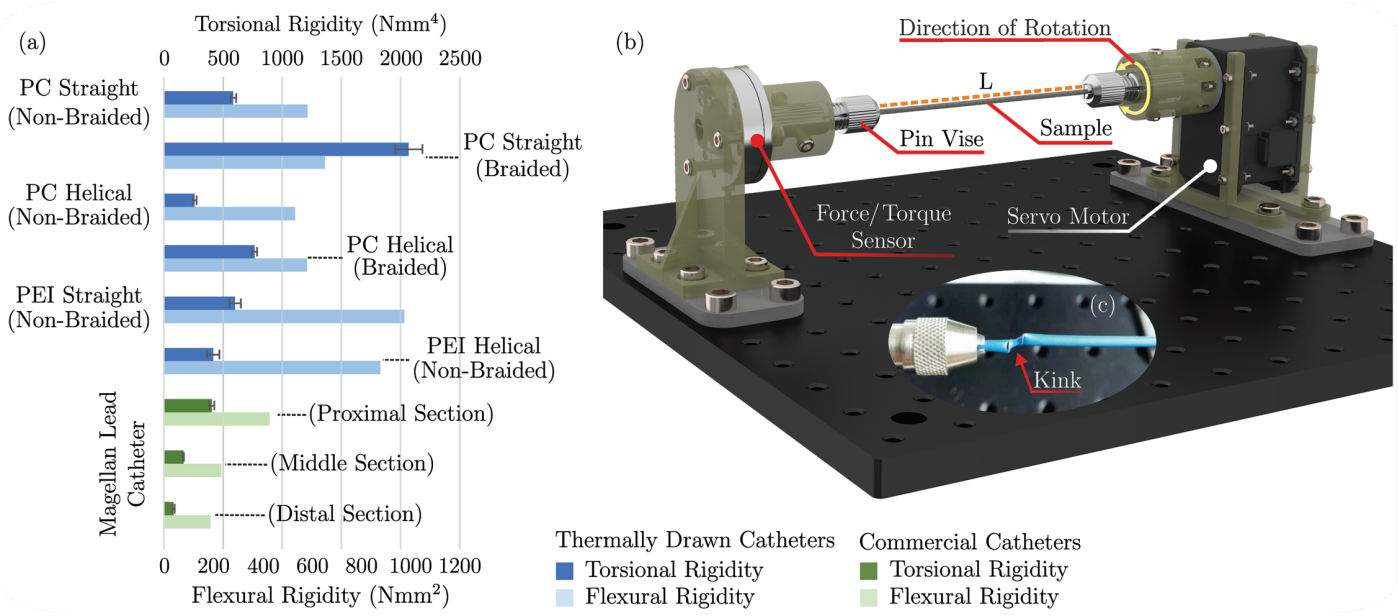


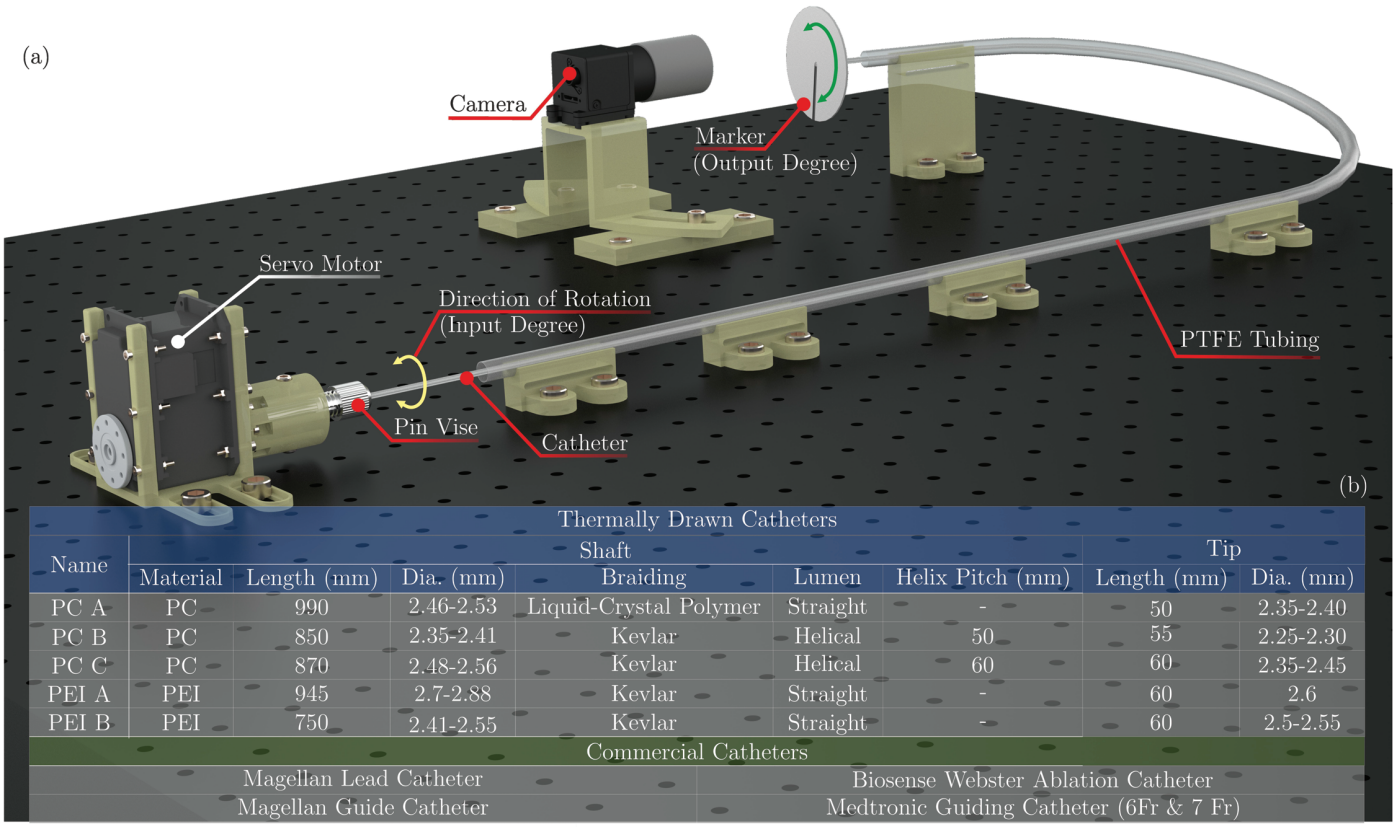

**Figure 5.8:** *Experiment 3-1*: Torsional Rigidity - (b) CAD renderings of the experimental setup and (a) Results. (c) Kinked catheter sample.

*Experiment 3-2:* The experimental setup shown in Figure 5.9, inspired by Yildirim et al [141], targets to measure the torque response by placing the catheter shaft samples in an a low-friction PTFE vessel phantom, which mimicked the trajectory of a transfermoral catheter across the the aortic arch and the descending thoracic aorta. The proximal end of the catheter shaft is firmly clamped to a pin vise, which is connected to a servo motor (Dynamixel MX-106T, Robosavvy, London, United Kingdom). Rotation of the motor causes the catheter to twist, simulating the motion of a surgeon rotating the catheter's proximal handle/hub during intervention. A marker is attached at the distal end of the sample to track its corresponding twist using a high-sensitivity USB 3.0 CMOS camera (DCC3240M, Thorlabs GmbH, Bergkirchen, Germany). The experiment was repeated at a minimum of four times for each catheter shaft sample.

### 5.4.3.2 Results and Discussion

*Experiment 3-1*: Figure 5.8a displays the $GJ$ values in the form of a bar chart for the different types of catheter shafts that did not kink. Samples with parallel lumina demonstrate higher torsional rigidity than the samples with helical lumina. As expected, braiding improves the torsional rigidity of the in-house fabricated catheter samples by approximately 71.6% for PC catheter shafts with parallel lumina, and 65.87% for PC catheter shafts with helical lumina. On the contrary to flexural rigidity $EI$, PEI-based catheter shafts did not show significantly higher $GJ$s when compared to the PC-based catheter shafts. Nevertheless, the torsional rigidities of in-house fabricated catheter shafts are comparable to their commercial metal-braided counterparts. Several commercial catheters "kinked" during the course of Experiment 3-1 (Figure 5.8)c, so their $GJ$ values are not presented. The adoption of very thin walls in commercial selective catheters (e.g. 6Fr and 7Fr Medtronic™guide catheters) is one possible reason behind the kinking of the shaft samples.

*Experiment 3-2*: The purpose of this experiment is to investigate whether a passively bent catheter can transmit the torque to the distal end from the proximal end. As shown from the input-output curves (Figure 5.9c), catheters shafts with relatively higher flexural rigidity (e.g. in-house fabricated PEI catheter shafts, commercial Biosense




(b)

| Name | Shaft | | | | | | Tip | |
|---|---|---|---|---|---|---|---|---|
| | Material | Length (mm) | Dia. (mm) | Braiding | Lumen | Helix Pitch (mm) | Length (mm) | Dia. (mm) |
| **Thermally Drawn Catheters** | | | | | | | | |
| PC A | PC | 990 | 2.46-2.53 | Liquid-Crystal Polymer | Straight | - | 50 | 2.35-2.40 |
| PC B | PC | 850 | 2.35-2.41 | Kevlar | Helical | 50 | 55 | 2.25-2.30 |
| PC C | PC | 870 | 2.48-2.56 | Kevlar | Helical | 60 | 60 | 2.35-2.45 |
| PEI A | PEI | 945 | 2.7-2.88 | Kevlar | Straight | - | 60 | 2.6 |
| PEI B | PEI | 750 | 2.41-2.55 | Kevlar | Straight | - | 60 | 2.5-2.55 |
| **Commercial Catheters** | | | | | | | | |
| Magellan Lead Catheter | | | | Biosense Webster Ablation Catheter | | | | |
| Magellan Guide Catheter | | | | Medtronic Guiding Catheter (6Fr & 7 Fr) | | | | |

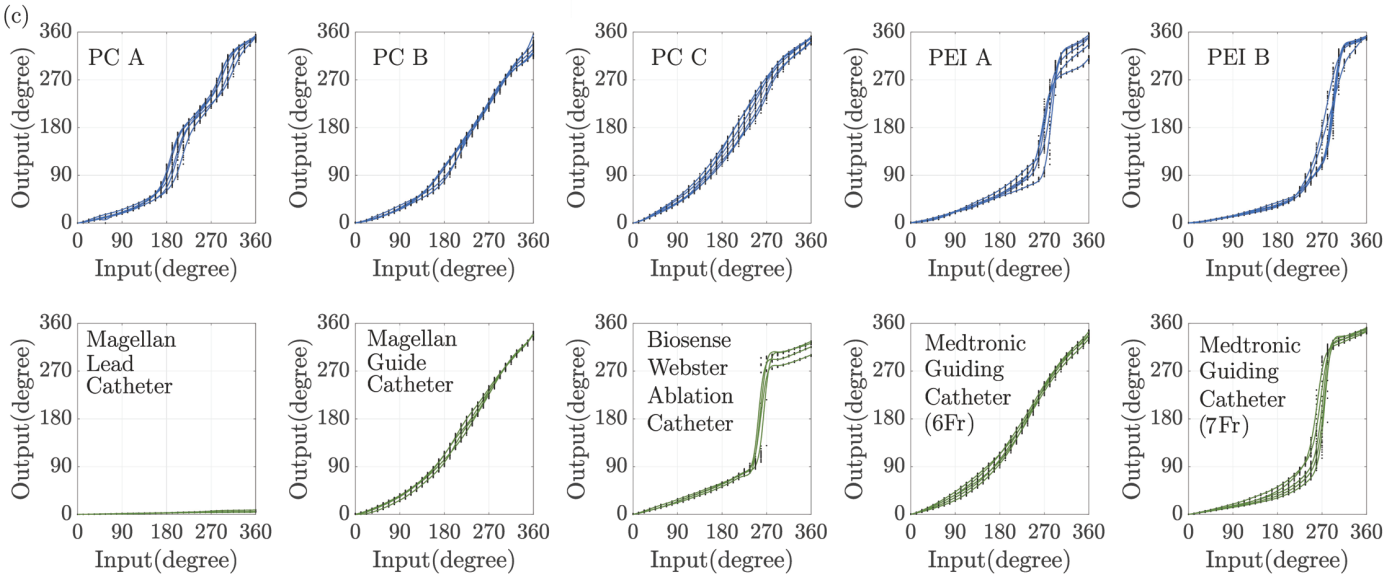



**Figure 5.9:** *Experiment 3-2*: Torque Response - (a) CAD renderings of the experimental setup, (b) List of catheter samples used in this experiment, (c) Results of the angular response (input angle versus output angle).

Webster® ablation catheter) are poorly capable of linearly transmitting the torque to the distal end, and demonstrate the undesirable catheter whip phenomenon (indicated by the large slope) after an input twist angle of 250° is applied. Conversely, the torque transmission of the PC-based catheters and the two commercial catheters (Medtronic 6Fr guide catheter and the Magellan™guide catheter) are approximately linearly related and have a smoother torque transmission across the length of the passively bent catheter shaft.

Based on these experimental results, it can be concluded that the in-house fabricated catheter shafts have comparable torsional rigidities and torque responses to the commercial selective and steerable catheters. However, as

in the case of the axial rigidity characterisation, performing the torquability experiments in a more sophisticated simulated intravascular environment with water at 37.4°C can help account for the effects of body temperature and moisture absoprtion. Furthermore, due to the limited number of samples, it is unavoidable that using the same sample might lead to a cumulative deformation effect. Moreover, for catheter shafts with helical lumina, the samples were twisted in the same direction as the helices's direction of rotation. Whether twisting the samples against the helices's direction of rotation would affect the performance of the catheter is something that could be characterised in further experiments.

# 5.5 Manual Handle and Catheter Integration

This section introduces the design and integration of an additively manufactured handle with the thermally-drawn, characterised, and post-processed multi-lumen tubing.

## 5.5.1 Manual Handle Design

### 5.5.1.1 Design Requirements

Based on our initial tests, MR safety requirements and extensive literature review, the following handle design requirements are formulated:

The handle design should:

1. Be MR safe, i.e. composed of non-metallic, non-magnetic, and non-conductive materials.
2. Be able to control the steerable distal end of the catheter independently in all four directions.
3. Be compact in size, easy-to-grip, and operatable with one hand.
4. Have a locking mechanism to lock the shape of the distal end of the catheter.
5. Have a Luer lock port for fluid injection (e.g. contrast agent) and micro-guidewire insertion.
6. Minimise backlash in the pull-wire driven mechanism.
7. Be integrative into an MR safe robotic system; to facilitate the seamless switching between remote (robot-assisted) and manual intervention.

### 5.5.1.2 Handle Designs (State-of-Art)

Selecting the appropriate handle design is critical to realising the requirements above. After carefully reviewing literature and patents, the handles used for controlling steerable catheters can be classified into the following three main categories:

*Slider:* The distal end of the catheter is deflected by moving a thumb-slide proximally or distally within a guide slot [320, 321]. The thumb-slide, in turn, is connected to the pull-wire. This handle design is commonly adopted in steerable catheters that bend in one direction (1/2 Degree of Freedom (DOF)). Similarly, the slide can be in the form a short slidable sleeve that wraps around the handle housing as demonstrated by Clogenson et al. [175].

*Piston:* The distal end of the catheter is steered by the axial displacement of a piston mounted in a piston chamber [322–324]. This handle design is widely used in uni-directional (1/2 DOF), and sometimes bi-directional steerable catheters (1 DOF).

*Dial/Knob:* The distal end is deflected by rotating a knob/dial. The knob/dial's axis of rotation can be either (a) in-line with the handle's axis of rotation [325, 326], or (b) orthogonal to the handle's axis of rotation [327–329]. This handle design employs a mechanism that transforming the rotary motion of the knob/dial into either: (1) linear motion of an internal slider(s) through a lead screw or gear mechanism, or (2) a lever structure that simultaneously tensions and releases opposing pull-wires. This handle design is often utilised for bi-directional steering (1 DOF). Moreover, two in-line knobs/dials can also enable quad-directional (four-way, 2 DOF) steering, i.e. each knob steers the distal end in two directions. This embodiment is adopted in the commercially available ultrasound catheter ACUSON AcuNav™. In general, for handle designs that allow for bi-directional or multi-directional steering, when one of the two antagonistic pull-wires is tensioned, the other is simultaneously released to ensure that the tip bends.

#### 5.5.1.3 Proposed Handle Design

After taking into consideration the design requirements and previous designs, we decided to opt for a dial/knob-based design (as illustrated in Figure 5.10). The handle comprises two dials located on both sides of the handle to control the distal end's four-way bending. As in the case of the ACUSON AcuNav™catheter, each dial deflects the distal end in two directions (1 DOF). The catheter steering is achieved by transforming the dial's rotary motion to linear motion using a double-rack and pinion mechanism. The pinion is fixed concentrically to the dial and engages with the pair of racks, to which a pair of pull-wires controlling the same DOF are anchored separately. As illustrated in Figure 5.10e, as the dial rotates, the pinion rotates and drives the two racks to move linearly in opposite directions, thereby tensioning one pull-wire while releasing the other. This results in the bending of the flexible distal end towards the tensioned pull-wire. The dial is designed to have involute contours as it offers several benefits, such as ensuring a better grip due to the increased surface friction between the operator's slippery gloves and the dial's jagged profile. Furthermore, the dial's gear-like profile enables it to mesh with other gears of the same module, enhancing the handle's potential for seamless and direct integration to robotics. Moreover, a dial with such a profile facilitates a more robust locking mechanism by utilising the meshing of gears to fix the dial in place (as illustrated in Figure 5.10f) . A pin vice is also mounted at the handle's proximal end to fine-tune the anchored pull-wires' tensioning (with respect to the catheter) during assembly. A universal Luer lock port is placed at the rear of the handle to facilitate fluid injection and the insertion of a microguidewire into the central lumen of the catheter.

### 5.5.2 Catheter Integration

Since the polymer-only based catheter is invisible under MR images, the passively MR visible MaRVis rods [158] are employed as pull-wires to enable catheter visualisation over its full length (as illustrated in Figure 5.10b, c, d and Figure 5.14c). These pull wires have high tensile strength but poor compressive strength, making them more susceptible to kinking while steering. Therefore, it is important to ensure smooth force transmission along the pull-wire, thus minimising kinking and subsequent backlash. Figure 5.10b) presents the internal components and mechanism of the additively manufactured handle. A Fused Deposition Modelling (FDM) printer (FORTUS 400mc, Stratasys Ltd., Eden Prairie, MN, USA) was employed to print most of the main components using a biocompatible Acrylonitrile Butadiene Styrene (ABS) grade (ABS-M30i, Stratasys Ltd., Eden Prairie, MN, USA). This excludes the plastic screws (PEEK and Glass Reinforced Resin Screws, Misumi Europa GmbH, Frankfurt, Germany), bearings (Linear Plain bearing GSM-0608-04, Igus, Northampton, United Kingdom) and pinion (0.5 Mod x 13 Tooth Metric

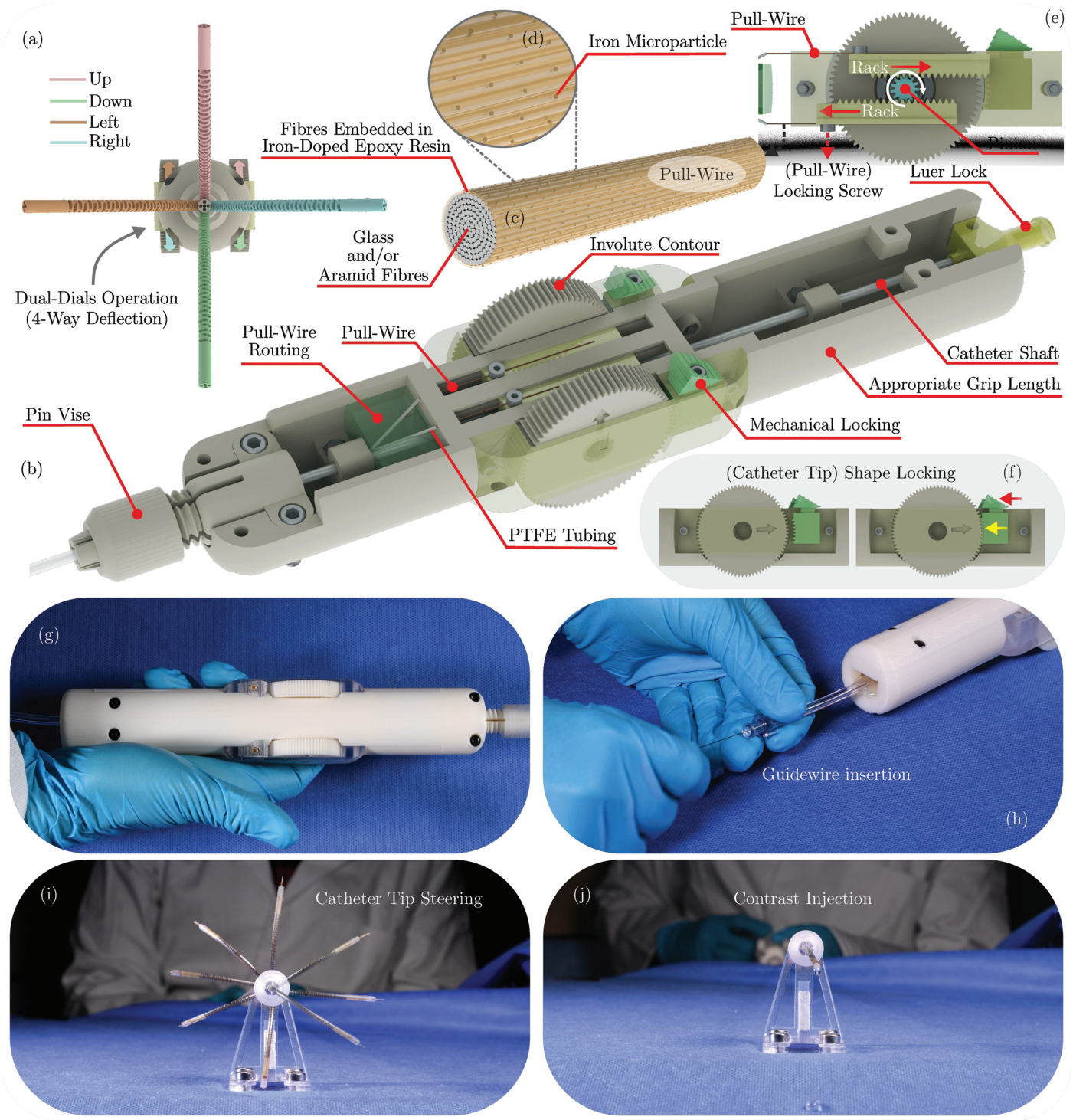



**Figure 5.10:** Manual handle overview. CAD renderings of: (a) 4-way deflection using the dual dial knobs. The different colours indicate the different directions of bending. (b) Isometric view of the catheter handle assembly (top cover removed). (c) MR visible pull-wires. (d) Zoomed-in (inset) of the doped iron microparticles. (e) Dual rack and pinion mechanism. (f) Shape locking mechanism. Images of the (g) catheter-handle assembly (top view), (h) guidewire insertion (back view), (i) catheter tip steering (images of 8 configurations are superimposed) and (j) contrast (fluid) injection.

Spur Gear In Hostaform, Bearingboys, Norwich, United Kingdom).

The integration commences by inserting the catheter into the handle through a pin vice, followed by a series of guide channels (to suppress the lateral motion of the shaft) and a pull-wire routing block (to prevent the crosstalk

and fiberisation of the pull-wires). Once mounted, the shaft is fixed in place by tightening the vice's nut. Next, four small-diameter polytetrafluoroethylene (PTFE) tubing (0.4 x 0.6, Iwase, Kanagawa, Japan) are advanced through the pull-wire routing block, followed by further advancing the PTFE tubing through four skived side holes that grant side access to the four lateral lumina of the shaft. Once completed, four pre-lubricated pull-wires[2] are fed through the PTFE tubing guide created in the previous step and are further advanced through the distal end of the catheter. Once protruded, the pull-wires are anchored to the distal end of the catheter by passing them through small segments of fused silica capillary (TSP450670, CM Scientific, Keighley, United Kingdom), and subsequently securing them to the capillary with cyanoacrylate glue (Loctite 416, Henkel, Düsseldorf, Germany). The capillary has an outer diameter larger than the catheter lateral lumen, allowing it to act as a stopper when the pull-wire is tensioned.

The loose proximal ends of the pull-wires are equally tensioned and fixed to their corresponding racks using a combination of a locking screw and Loctite 416 cyanoacrylate adhesive. Once fixed, the racks are held in place by the knob/pinion assembly which is, in turn, mounted to the handle using an external cover embedded with a mechanical lock. As previously described, one knob/dial controls two racks that simultaneously tension and release the antagonistic pull-wires (as illustrated in Figure 5.10e). To minimise backlash, the pull-wire routing block is fixed in place using hot melt adhesive to suppress any unwanted displacement of the pull-wires. The catheter integration process is wrapped up by connecting a Luer lock port at the catheter shaft's proximal-most point. The Luer lock gains access only to the central lumen of the catheter shaft for microguidewire insertion 5.10h and contrast injection 5.10j.

### 5.5.3 Discussion

Four handle-catheter assemblies were completed following the assembly protocol described in the previous section. The handle design requirements were met through functional testing of the handle, i.e., four-way steering of the catheter tip, locking mechanism, fluid injection, and guidewire insertion. Although extensive work has been attempted to eliminate backlash, the backlash cannot be avoided entirely. One way to suppress backlash is by covering/coating the pull-wires with PTFE heat shrink tubing and add PTFE liners to the inside diameter of the catheter lumina. Reducing friction makes it easier for the pull-wires to slide with reduced friction along the tubing interior. Proper pre-tensioning of all four pull-wires is also crucial to eliminate backlash. Pre-tensioning can also be improved by measuring the tensile forces applied on the four pull-wires during assembly using an array of force sensors.

[2] Pull-wires wiped with a lubricant (Griffon Unilube Lubricant, 3DGBIRE, Lancashire, United Kingdom)

# 5.6 Steerability

Steerability is the quality of a catheter's ability to deflect the catheter's distal end. This section investigates the steerability of the integrated catheter-handle assembly in terms of repeatability and torque required to turn the knob to demonstrate its steering performance.

## 5.6.1 Methodology

*Experiment 4-1:* To assess the steerability of the catheter's distal end, an experimental setup is devised to evaluate the catheter workspace and positioning accuracy (as illustrated in Figure 5.11). The experiment commences by securing the distal end of the catheter from its proximal end using a pin vice. Followed by securing the proximal handle in place as illustrated in Figure 5.11a. The experiments are conducted by removing one of the handle's external covers and connecting a servo motor (Dynamixel MX-106T, Robosavvy, London, United Kingdom) in-line with the knob. In between the knob and motor lies a force/torque sensor (ATI F/T Sensor Mini40, ATI Industrial Automation, North Carolina, United States) and a coupling that connects the rotating force/torque sensor (driving mechanism) to the knob (driven mechanism), as illustrated in Figure 5.11b. The coupling comprises an internal gear with the same diameter and modulus as the knob. The force/torque sensor measures the torque required to turn the knob.

Driven by the motor, the knob is initially turned 90° in one direction, causing the catheter tip to bend (stroke I - Forward Steering); then the motor is turned in the opposite direction, returning the knob and catheter tip to its initial position (stroke II - Backward Steering); followed by a further 90° in the opposite direction, causing the catheter tip to bend in the other direction (stroke III - Forward Steering); and finally the knob is turned back to its initial home position (stroke IV - Backward Steering). Each 90° rotation is completed in eight equal steps, with the motor rotating 11.25° increments. The deflection of the catheter tip is recorded by a high-sensitivity USB 3.0 CMOS camera (DCC3240M, Thorlabs GmbH, Bergkirchen, Germany) perpendicular to the plane of motion (Figure 5.11)a. Also, to facilitate the tracking and depicting the shape of the catheter tip using computer vision methods, four dark markers were equidistantly affixed along the catheter tip. The degrees of freedom (up/down and left/right steering) of the catheter tip were tested separately.

*Experiment 4-2:* As the catheter navigates through the vascular network, passive bending is inevitable. Maintaining the effectiveness of steering after passive bending is critical. To evaluate the steering performance after bending, a fixed pulley is placed in the middle of the catheter shaft, resulting in a 90° bend of the catheter (Figure 5.12). After adjusting the knob to straighten the catheter tip and compensate for passive tip deflections, the same experimental protocol described above (*Experiment 4-1*) is repeated in this bent configuration.

## 5.6.2 Results and Discussion

*Repeatability:* Figures 5.11e,f,g and 5.12d,e,f show the forward and backward steering of the distal end of catheter PC A for five iterations. For this catheter sample, the standard deviation is less than 1mm for a deflection of approximately 30mm, which is similar to what has been reported in previous work [177]. For all four samples, the standard deviation is less than 5mm. The PEI A catheter with straight lumina (see D.11, D.12, D.9, D.10), has the second-best repeatability, with a standard deviation of less than 2mm. However, the catheter sample with helical

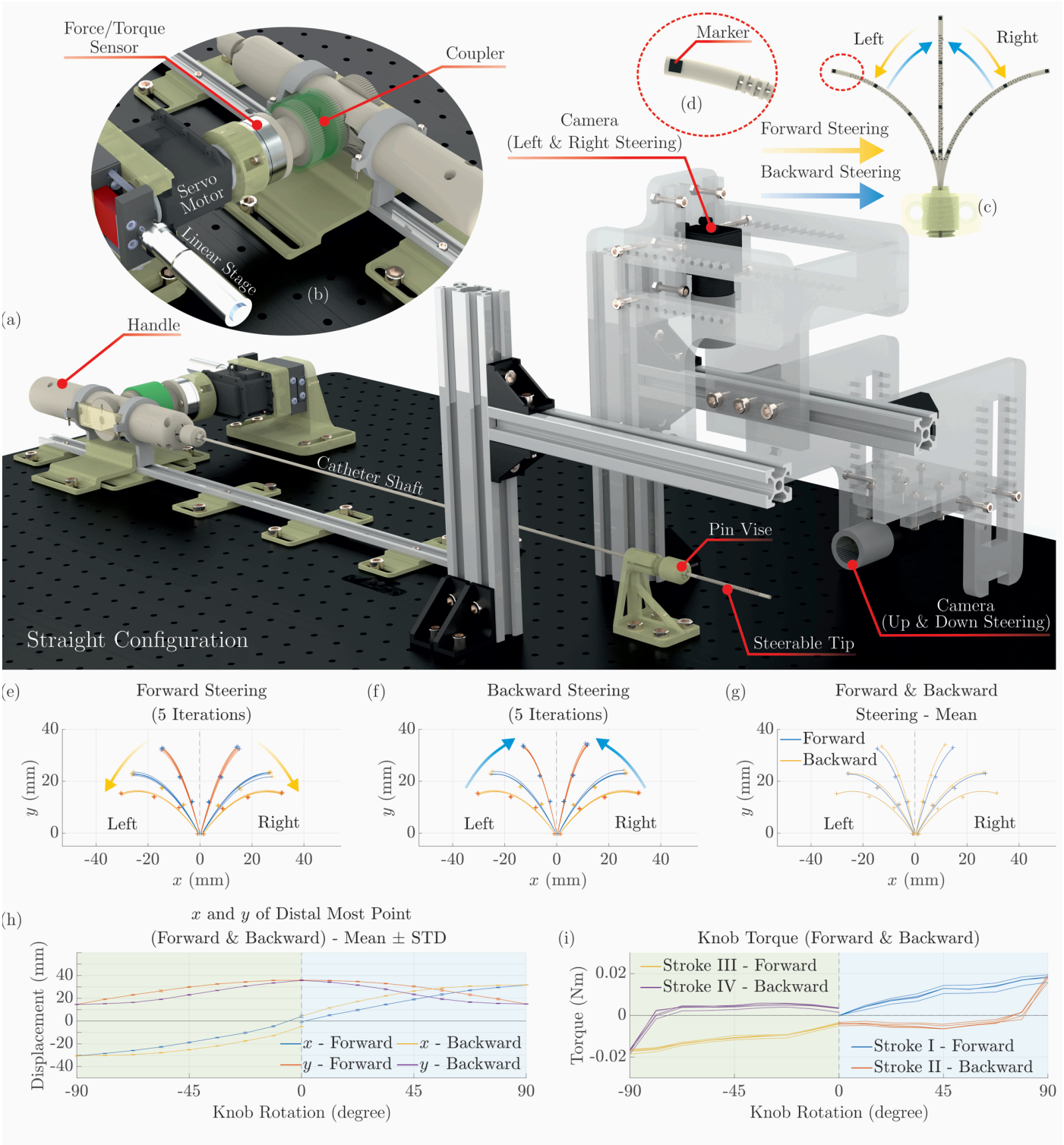



**Figure 5.11:** Experiment 4-1: **PC A** Catheter Steering in a Straight Configuration. (a-b) CAD renderings of the experimental setup. (c) Forward and backward steering definitions. (d) Markers added to the distal end for tracking purposes. Steerability results of the left and right steering of PC A catheter: (e) and (f) indicate the geometry of the catheter tip for each trial when the catheter is subjected to forward steering (Stroke I and Stroke III) and backward steering (Stroke II and Stroke IV) respectively. (g) Averaged catheter tip positions over five trials. The difference between the catheter tip positions corresponding to the same knob angle position during the forward and backward steering indicate backlash. For better visualisation, only the catheter tip shapes for knob rotation angles ±22.5°, ±56.25° and ±90°, are represented. (h) Average $x$ and $y$ coordinates (with standard deviation) of the distal most point of the catheter over the course of the experiment. (e) Torque applied to the knob during the experiments.

lumina (see D.7, D.8, D.5, D.6) demonstrates the lowest repeatability in its movement, primarily due to the presence of a relatively larger backlash.

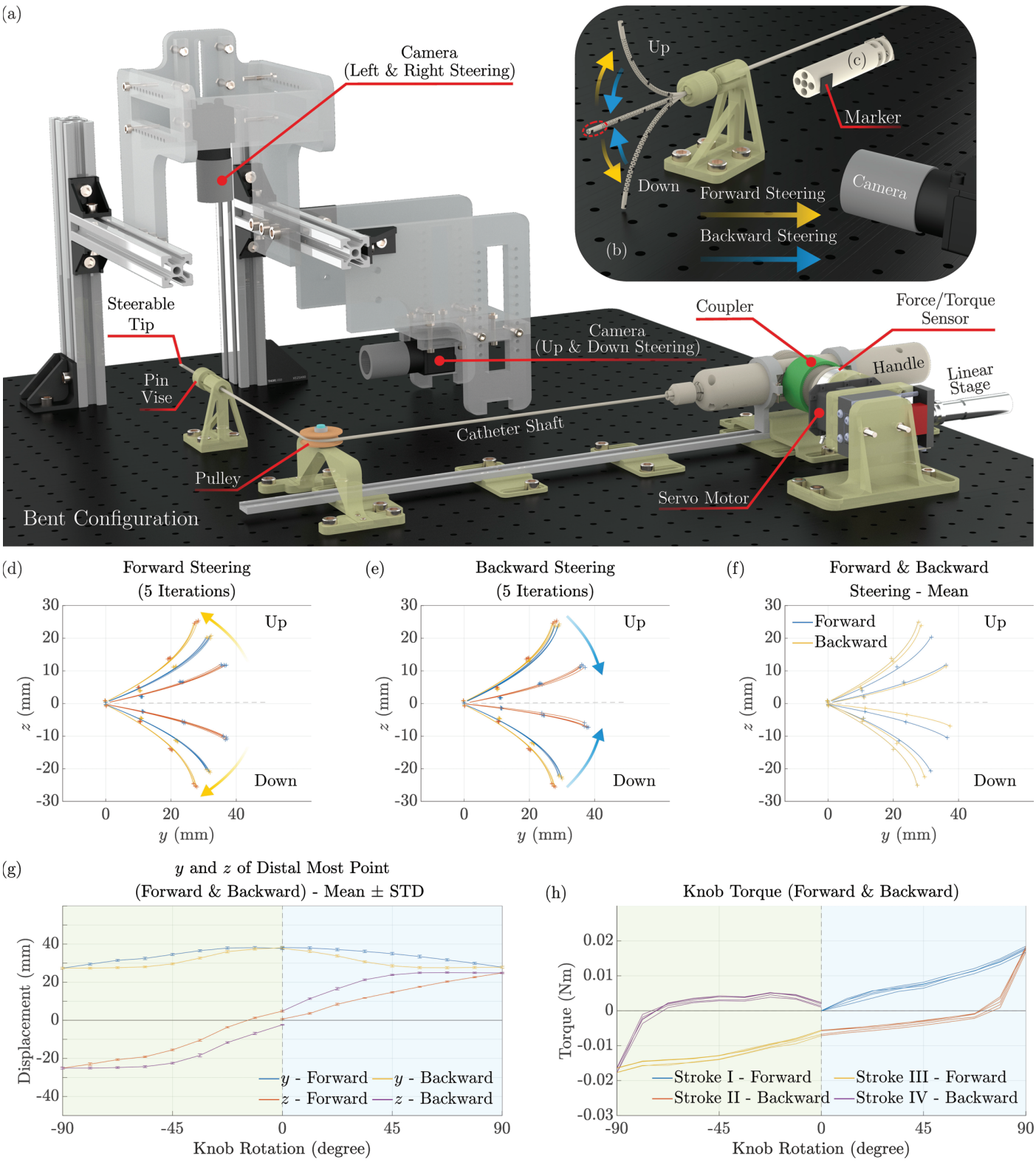



**Figure 5.12:** Experiment 4-2: **PC A** Catheter Steering in a Bent Configuration. (a) CAD renderings of the experimental setup. (b) Forward and backward steering definitions. (c) Marker added to the distal end for tracking purposes. Steerability results of the up and down steering of PC A catheter: (d) and (e) indicate the geometry of the catheter for each trial when the catheter is subjected to forward steering (Stroke I and Stroke III) and backward steering (Stroke II and Stroke IV) respectively. (g) Averaged catheter tip positions over five trials. The difference between the catheter tip positions corresponding to the same knob angle position during the forward and backward steering indicate backlash. For better visualisation, only the catheter tip shapes for knob rotation angles $\pm 22.5°$, $\pm 56.25°$ and $\pm 90°$, are represented. (h) Average $x$ and $y$ coordinates (with standard deviation) of the distal most point of the catheter over the course of the experiment. (e) Torque applied to the knob during the experiments.

*Backlash:* The trajectory of PC A's distal-most point during the forward and backward steering is also shown in Figures 5.11h and 5.12g. The difference in positioning between forward and backward steering when the knob is turned to the same angle indicates the backlash within the catheter-handle assembly. Based on the results of all four samples, catheters with straight lumina PC A, PEI A and PEI B all have a similar sized backlash of about 5mm on average; however, the catheter with helical lumina PC C demonstrates a larger backlash of about 10mm. Furthermore, backlash increases when catheters with straight lumina are bent. Conversely, this increase in backlash is not apparent when the catheter with helical lumina is bent. Moreover, as previously discussed in section 5.5.2, backlash is caused by the improper pretensioning during assembly, poor pull-wire compressive strength, and friction between the pull-wire and their corresponding lumina. Solutions to these challenges are addressed in the previous Section 5.5.3. Other causes of backlash may also include the improper meshing between the handle's rack and pinion, or possible wear of these plastic components. One possible way of eliminating mechanical play is either by (1) shortening the distance between the rack and pinion's centres, (2) spring-load one against the other, so they stay tightly meshed, (3) substituting the additively manufactured racks with injection moulded or precision machined racks, or (4) Using polymeric materials with more superior wear resistance.

*Knob Torque:* Figures 5.11i and 5.12h demonstrate the torques required to turn the knob 90° clock-wise and 90° counter clockwise for catheter PC A. The torque required to guide the catheter at the knob is predominately within the range of $\pm$ 0.02Nm (20 Nmm), i.e. the tangential force at the 40mm knob is around $\pm$ 1N. The torque measured reflects the forces required to deflect the catheter tip, the friction forces between the pull-wire and catheter lumen, and friction between the handle's moving components (e.g. rack). Moreover, another cause for variation in the torque measurements could also be the low dimensional tolerances of the 3D printed components.

Although *Experiments 4-1* and *4-2* are conducted to characterise the catheter's 2 DOF steerability, further experiments could also be conducted by investigating the 3 DOF steerability of the tip by turning both knobs simultaneously (see Figure 5.10i for tip steering in all directions).

# 5.7 Helical Compensation

As previously described in Section 5.3.2, conventional pull-wire driven catheters suffer from three undesirable phenomena during interventions, namely: passive tip deflection, muscling and curve alignment. In this section, as proposed in Section 5.3.2, the suppression of passive tip deflections using helically routed pull-wires is investigated.

## 5.7.1 Methodology

*Experiment 5:* The purpose of this experiment is to test the effectiveness of helically routed pull-wires in compensating passive deflections. This is achieved by passively bending the catheter shaft around a pivot point. i.e. a vee-grooved pulley (RS Part No. 352-0664, RS Components, Corby, United Kingdom) as illustrated in Figure 5.13a. The experiment commences by mounting the integrated catheter handle assembly onto a sliding carriage (NW-02-17, Igus, Northampton, United Kingdom). In turn, the carriage is mounted on a linear rail (NS-01-17-300, Igus, Northampton, United Kingdom) which is fixed to a 3D printed rotating beam. This part of the setup allows the catheter handle assembly to freely slide along the rail as it simultaneously rotates around the pivot point. At one

end of the beam, lies an additively manufactured spur gear attached to a passive rotary stage (PR01/M, Thorlabs GmbH, Bergkirchen, Germany). At the top of this gear lies the pivoting pulley, which also guides and keeps the catheter shaft aligned within its grooves as the catheter-handle assembly rotates. The spur gear is driven by another gear directly connected to a servo motor (Dynamixel MX-106T, Robosavvy, London, United Kingdom). At the distal end, the catheter's flexible tip is held in place by clamping it from its proximal end using a pin vice. Driven by the motor, the catheter shaft on the beam rotates around the pulley and forms a 90° as indicated by the yellow arrow in Figure 5.13a. Next, the beam returns to the initial home position to conclude the experiment. In parallel, the catheter tip movement is recorded by tracking a marker placed at its distal-most point. The tip motion is recorded using a high-sensitivity USB 3.0 CMOS camera (DCC3240M, Thorlabs GmbH, Bergkirchen, Germany). In this experiment, five catheter-handle assemblies (two helical and three parallel lumina) were tested. Each catheter assembly was tested for four times.

## 5.7.2 Results and Discussion

Figure 5.13c-i depicts the trajectory of the passive tip deflections obtained during the experiment (indicated by the blue lines), and the radius of the red circles which quantify the maximum passive tip deflection. As observed from the results, catheters with parallel lumina demonstrate considerably larger deflections (ranging from 5.6mm

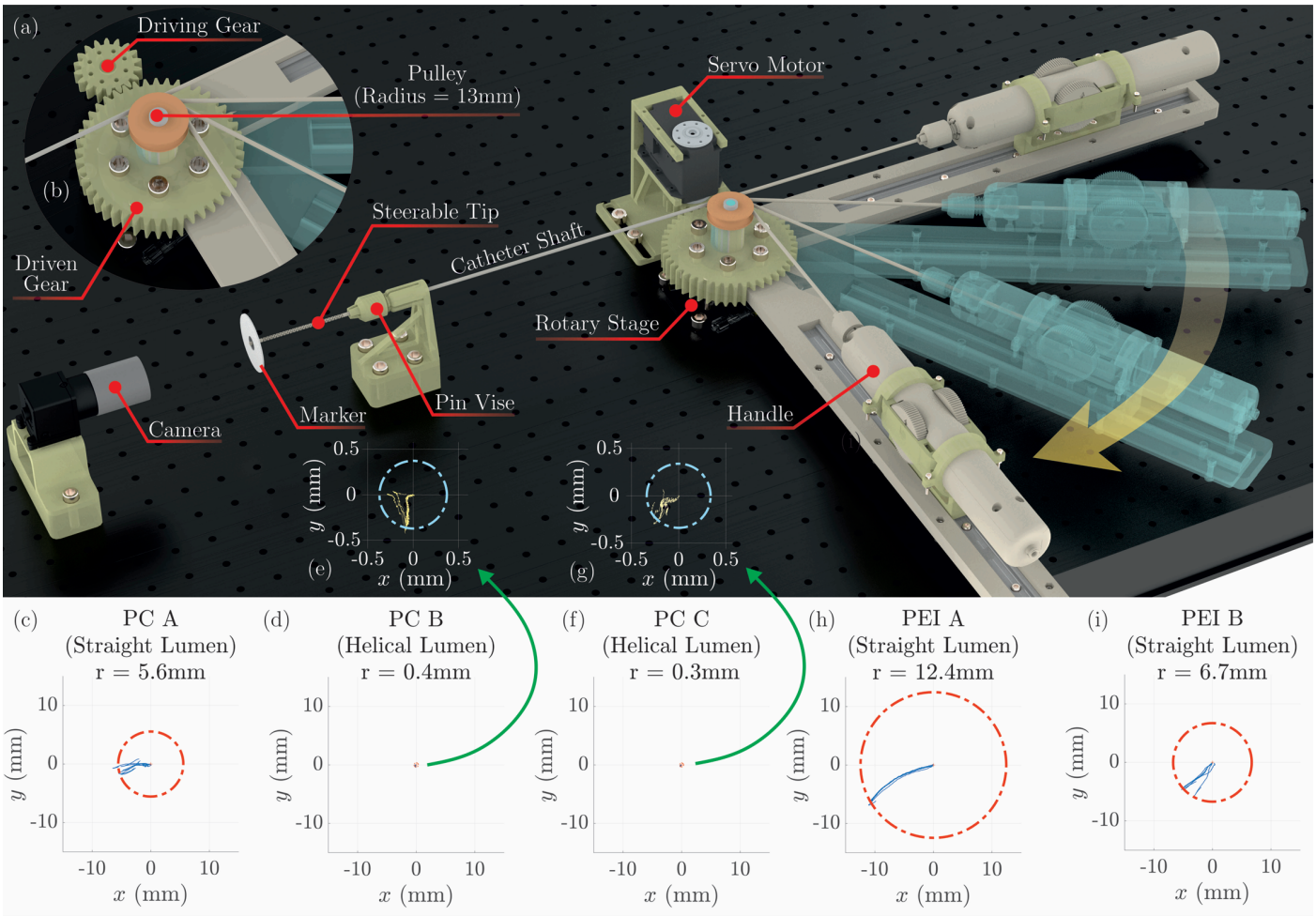



**Figure 5.13:** Experiment 5: (a-b) CAD renderings of the experimental setup. (c, d, f, h, i) Uncontrolled deflection of the catheter tip as a result of the 90° catheter shaft deflection. (e, g) Zoomed-in plots of the catheters with helically routed pull-wires.

to 12.4mm) when compared to their helical lumina counterparts (ranging from 0.3mm to 0.4mm). The difference in magnitude between the parallel lumina samples may be caused due to slight variations in their outer diameters. For instance, PEI A has a larger outer diameter ranging from 2.7 to 2.88mm, when compared to the other parallel lumina samples PC A and PEI B, with outer diameters ranging from 2.41mm to 2.55mm. Furthermore, in the case of PEI A, due to its relatively larger outer diameter, the pull-wires are placed further away from the neutral axis, which leads to larger passive tip deflections. Moreover, large tip deflections reduce the catheter steering's overall accuracy and may also lead to adverse effects such as trauma to the surrounding tissue and vessel wall.

## 5.8 *In-Vitro* and *In-Vivo* Studies

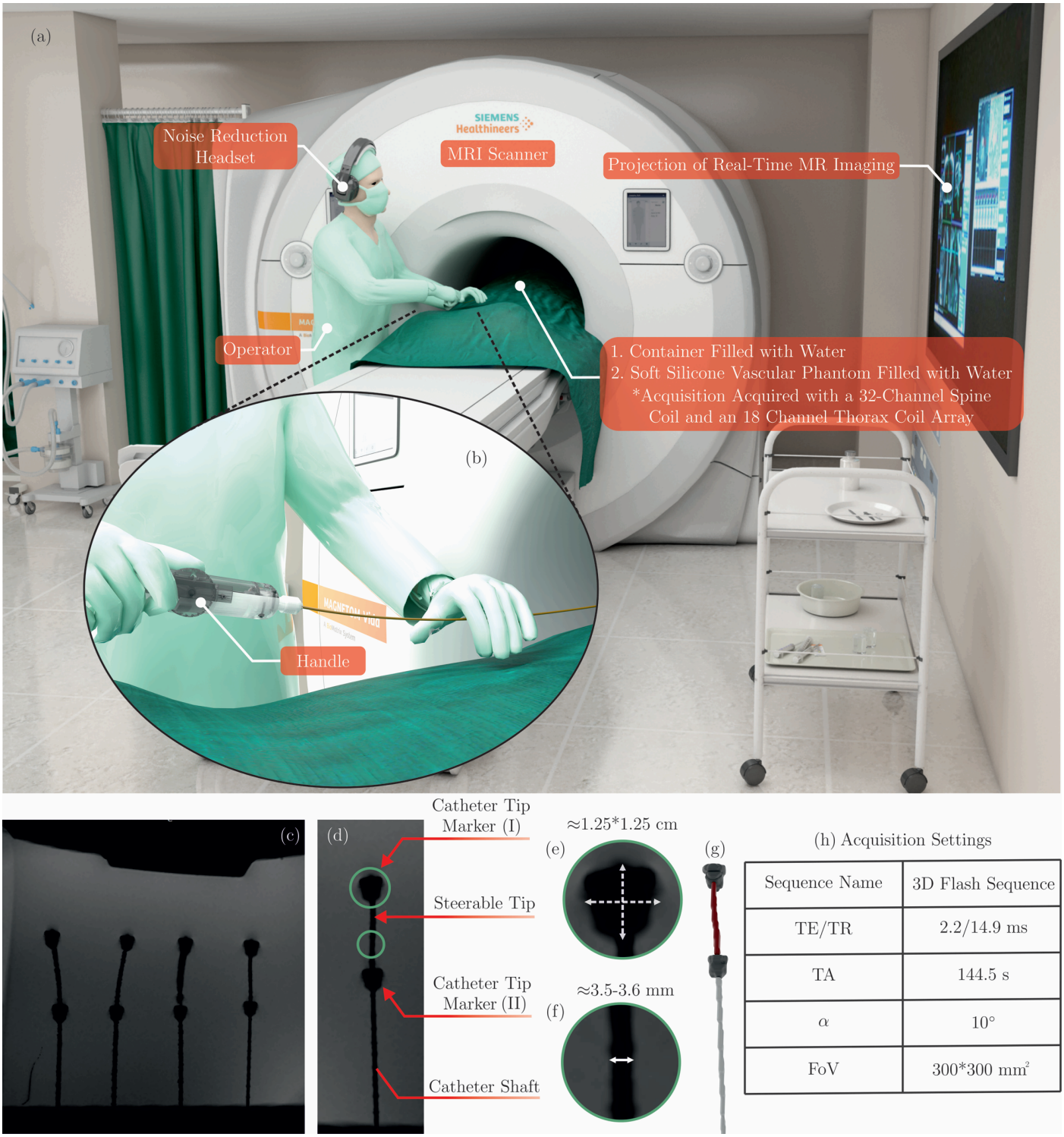
### 5.8.1 *In-Vitro* MR Compatibility and Phantom Study

This section presents the experimental setups and methods undertaken to evaluate the mechanical efficacy and MR visibility of the catheter in a number of simulated clinical scenarios; which involved a series of arterial cannulation manoeuvres performed by a novice under real-time MR guidance in a clinical 3T MR scanner equipped with a 32-channel spine coil and an 18 channel thorax coil array (as visualised in Figure 5.14a, b).

*MR Visibility and Artefact Evaluation*: Four in-house fabricated and assembled steerable catheters are placed in a water-filled container for acquiring high-resolution MR images in a clinical 3 Tesla MR system (Magnetom Prisma, Siemens) using a 3D FLASH sequence (TE/TR = 2.2/14.9ms, TA = 144.5s, $\alpha$ = 10°, FoV = 300*300mm$^2$). Figure 5.14c shows the acquired image from the 3D FLASH sequence. Figure 5.14d, e, f shows the size of the artefacts of the shaft and the catheter tip markers. The size of artefacts is comparable to previous work [158] with guidewires, which comprise an MR visible rod, as a continuous susceptibility artefact with a mean diameter of 2mm ± 0.2 along the shaft. Using four MR visible pull-wires for steering did not increase the artefact size significantly. The average thickness of the shaft artefacts is 3.55mm, and the size of the tip marker is approximately 1.25cm by 1.25cm. Figure 5.14g illustrates a segmented 3-dimensional model of the acquired high-resolution MR images (5.14c) using a simple thresholding technique.

*Phantom Studies*: Phantom experiments are performed under real-time MR image guidance to evaluate the mechanical efficacy and steerability of the catheter. A soft silicone commercial vascular phantom of a normal adult abdominal aorta (Elastrat Sarl, Geneva, Switzerland) is filled with water, and the steerable catheter is introduced to three main target vascular structures, namely: right renal artery, left renal artery, and coeliac trunk. Real-time images were acquired using a 2D FLASH sequence with the following parameters: TE/TR = 2.2/319.6ms, TA/image = 320ms, $\alpha$ = 8°, FoV = 289*289mm$^2$. Figure 5.15 shows the 2D Flash sequence of the successful probing by a novice of the right and left renal arteries, which was followed by contrast agent injection for post-assessment. Similarly, Figure 5.15a, b, c, d shows the 2D Flash sequence of the successful probing by a novice of the coeliac trunk, which was also followed by contrast agent injection for post-assessment.

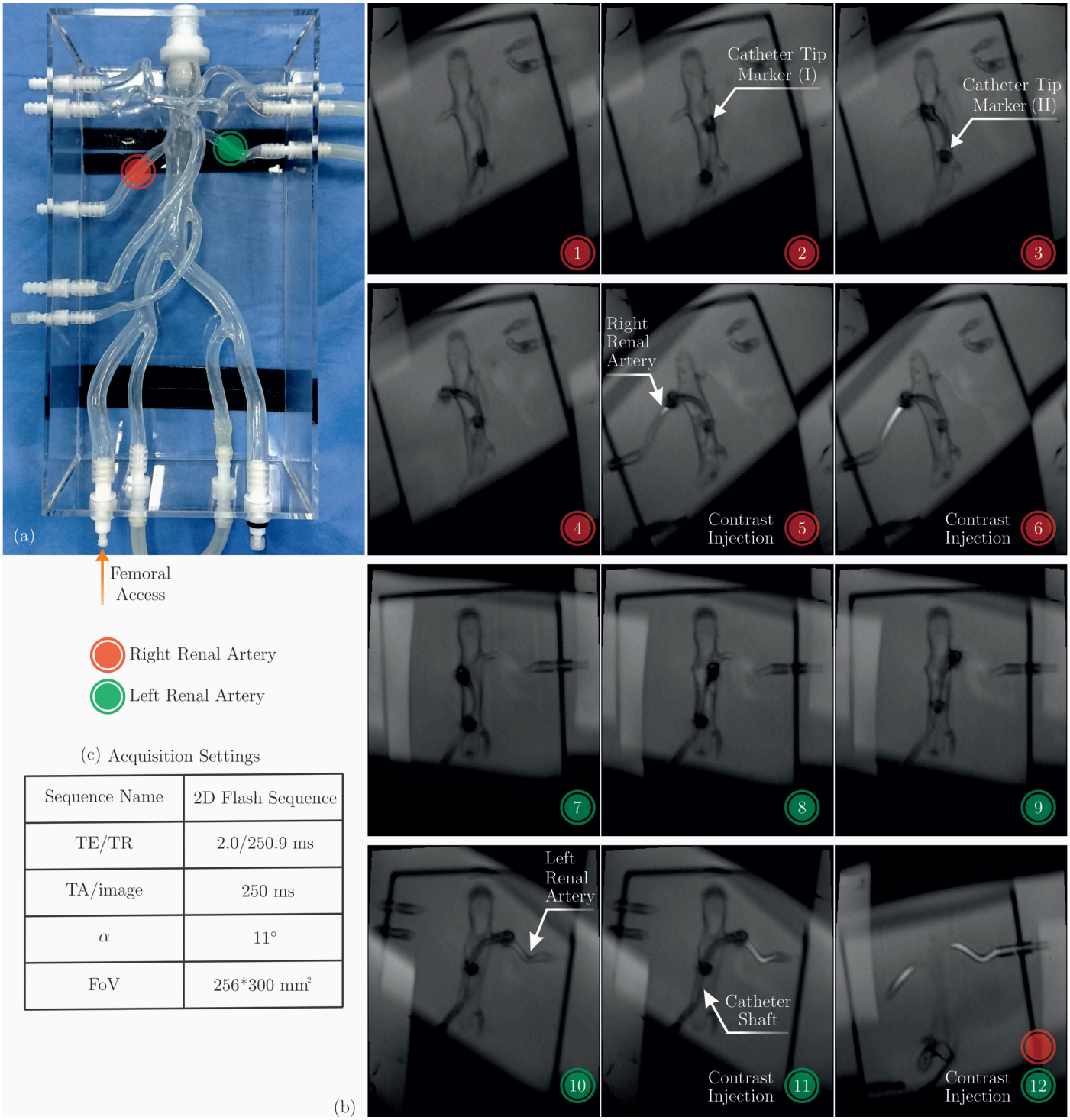
*Four-way Steering*: Figure 5.16e-k demonstrates the four way steering of the catheter. Since it is difficult to demonstrate the catheter's quad-directional steering in a single projected plane, herein, two projected planes are acquired simultaneously to observe the (1) transverse plane at the distal-most point of the catheter tip, and (2) frontal plane which covers the entire length of the catheter. For example, in Figure 5.16e, as the catheter is steered to the left, the tip marker moves up. The same is repeated for the remaining three directions. Figure 5.16j shows a superimposed




| Sequence Name | 3D Flash Sequence |
|---|---|
| TE/TR | 2.2/14.9 ms |
| TA | 144.5 s |
| $\alpha$ | 10° |
| FoV | 300*300 mm$^2$ |

**Figure 5.14:** (a) CAD rendering of the *in-vitro* experimental setup in an MR suite. (b) Inset of the operator's handling of the steerable catheter's manual handle. (c) Imaging artefacts of four steerable catheters acquired using a 3D Flash sequence in a 3T MRI scanner. (d) Labelling of the artefacts. (e) Inset of the catheter tip marker artefacts and its dimensions. (f) Inset of the catheter shaft artefacts and its dimensions. (g) Reconstructed 3D model of the steerable catheter from the acquired scan. (h) Acquisition settings of the MRI scanner.

post-processed image of the catheter tip's steering in four directions.




(c) Acquisition Settings

| Sequence Name | 2D Flash Sequence |
|---|---|
| TE/TR | 2.0/250.9 ms |
| TA/image | 250 ms |
| $\alpha$ | 11° |
| FoV | 256*300 mm$^2$ |

**Figure 5.15:** (a) Abdominal phantom with left and right renal artery (LRA & RRA) targets. (b) 2D Flash sequence illustrating the probing of the LRA and RRA in an abdominal phantom (Elastrat, Geneva, Switzerland) using the steerable catheter under real-time MR-guidance. (c) Acquisition settings of the MRI scanner.

## 5.8.2 *In-Vivo Animal Study*

For the in-vivo trial, the catheter was tested in a porcine model under general anaesthesia in a clinical 3T Magnetom Prisma (Siemens Healthineers, Erlangen, Germany): The cardiologist used a commercially available non-magnetic and RF-shielded in-room screen to monitor the position of the catheter via real-time MRI while performing the intervention. The catheter was introduced into the arterial system through a femoral access sheath (10F), which was implanted beforehand. A 2D real-time radial GRE sequence (TE/TR: 1.3/2.1 ms, spokes: 105, FA: 10°, FoV: 289 ×

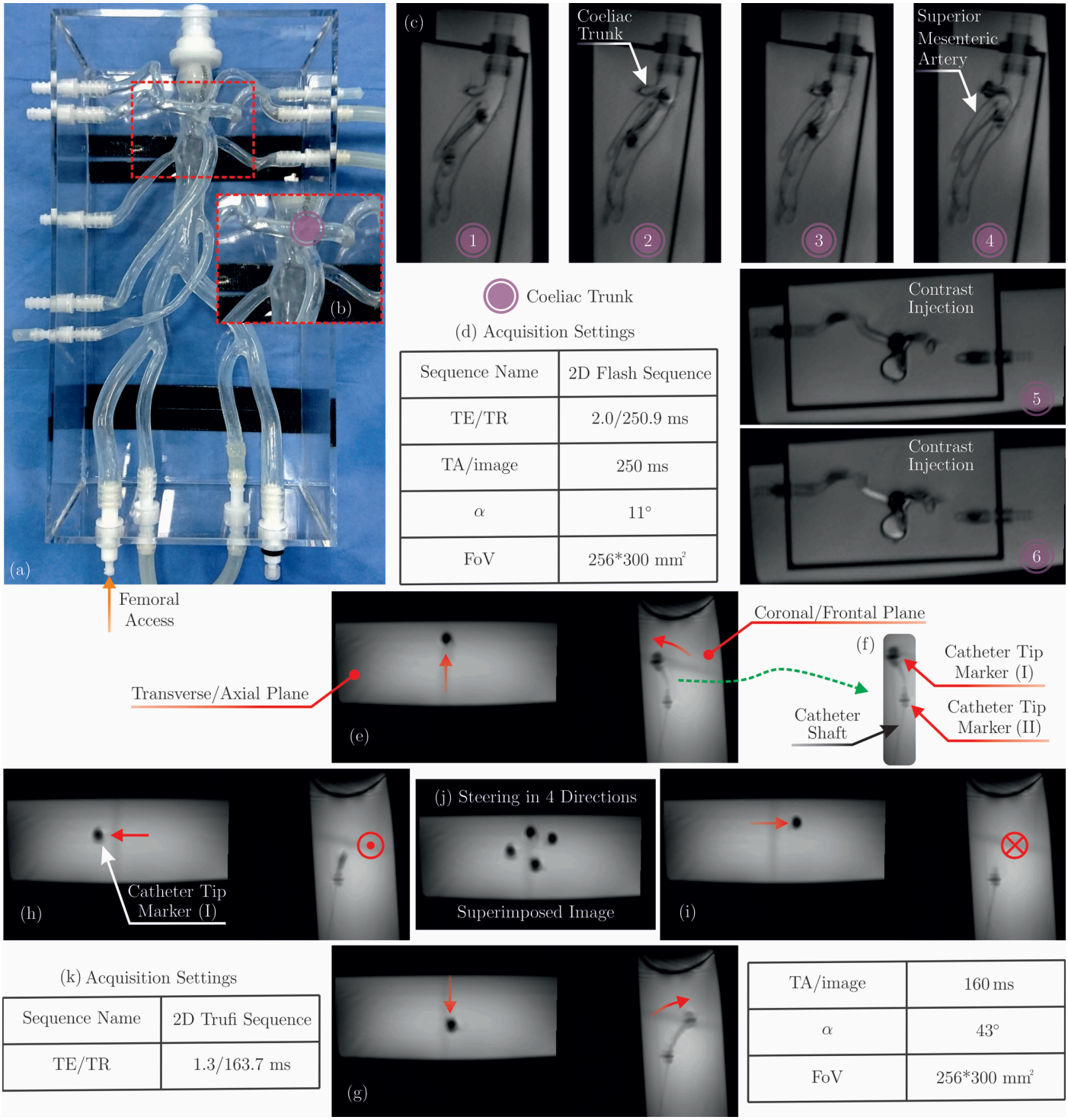



**Figure 5.16:** (a) Abdominal phantom with coeliac trunk artery target. (b) Zoomed-in inset of the coeliac trunk artery. (c) 2D Flash sequence illustrating the probing of the coeliac in an abdominal phantom (Elastrat, Geneva, Switzerland) using the steerable catheter under real-time MR-guidance. (d) Acquisition settings of the MRI scanner. (e-g) Four-way steering of the catheter. The images were simultaneously acquired in two different planes (transverse plane (TP) and frontal plane (FP)). (e) Catheter is steered to the left in the FP and the distal most tip marker moves up in the TP. (f) Labelled inset of the steerable catheter. (g) Catheter is steered to the right in the FP and the distal most tip marker moves down in the TP. (h) Catheter is steered out of the FP and the distal most tip marker moves to the left in the TP. (i) Catheter is steered into the FP the frontal plane and the distal most tip marker moves to the right in the TP. (j) Superimposed image of the steering in four different directions. (k) Acquisition settings of the MRI scanner.

289× 8 $mm^3$, matrix: 192 × 192, fat saturation) was used to display the anatomy and the catheter, for full coverage of the vascular system a 32-channel spine coil and an 18-channel thorax coil array was used. Steerability was tested by attempting to intubate the carotid artieries as well as crossing the aortic arch towards the heart, both of which were successful. Figures 5.17 and 5.18 show the acquired *in-vivo* MRI scans. Note: The experiments were approved by the local ethics committee of Freiburg University and the regional council of Freiburg, Baden-Wuerttemberg, Germany (licence numbers 35–9185.81/G-15/156 and 35-9185.81/G-16/78). Experiments were conducted in accordance with FELASA, GV-SOLAS standards for animal welfare.

# 5.9 Catheter Robot Integration

## 5.9.1 Robotic Catheterisation

As pointed out in Chapters 1 and 2, there are still some challenges associated with manual procedures conducted within an MR environment. The challenges include:

- Limited accessibility to the patient (especially paediatric patients), which can increase the surgeon's risk of developing musculoskeletal injury and increase the possibility of medical errors and risk for the patient [16].
- Uncomfortable acoustic noise generated while operating MR systems which may lead to hearing impairment [17].

Moreover, to benefit from teleoperation, robotic catheterisation could potentially help overcome these challenges. To utilise the full potential of the work presented in Chapters 3 and 4 on the robotic manipulation of off-the-shelf instruments, herein, the pneumatically actuated MR slave robot is extended to accommodate the in-house fabricated steerable catheter. This section introduces an MR safe actuation unit that utilises the optimised designs of the pneumatic linear and rotary stepper motors presented in Section 4.2.2.

## 5.9.2 Actuation Unit

### 5.9.2.1 Design Requirements

To robotically control the steerable catheter, the actuation unit should meet the following requirements:

- Safe for use in MR environments, i.e. MR Safe.
- Have a quick and simple method to dock and release the catheter-handle assembly for seamless switching between remote (robot-assisted) and manual operations.
- Control the four-way deflection of the catheter tip and translate the catheter-handle assembly.

### 5.9.2.2 Proposed Design

*Actuation Unit*: The actuation unit comprises two main components, an upper case and a lower case, hinged together at one lateral side. When closed, the two cases form a cavity with the same shape as the handle. Two quick release locks are adopted on either side to facilitate the quick docking/releasing of the handle. In the bottom case, two pneumatic rotary stepper motors are integrated to rotate the two handle knobs respectively. Each rotary

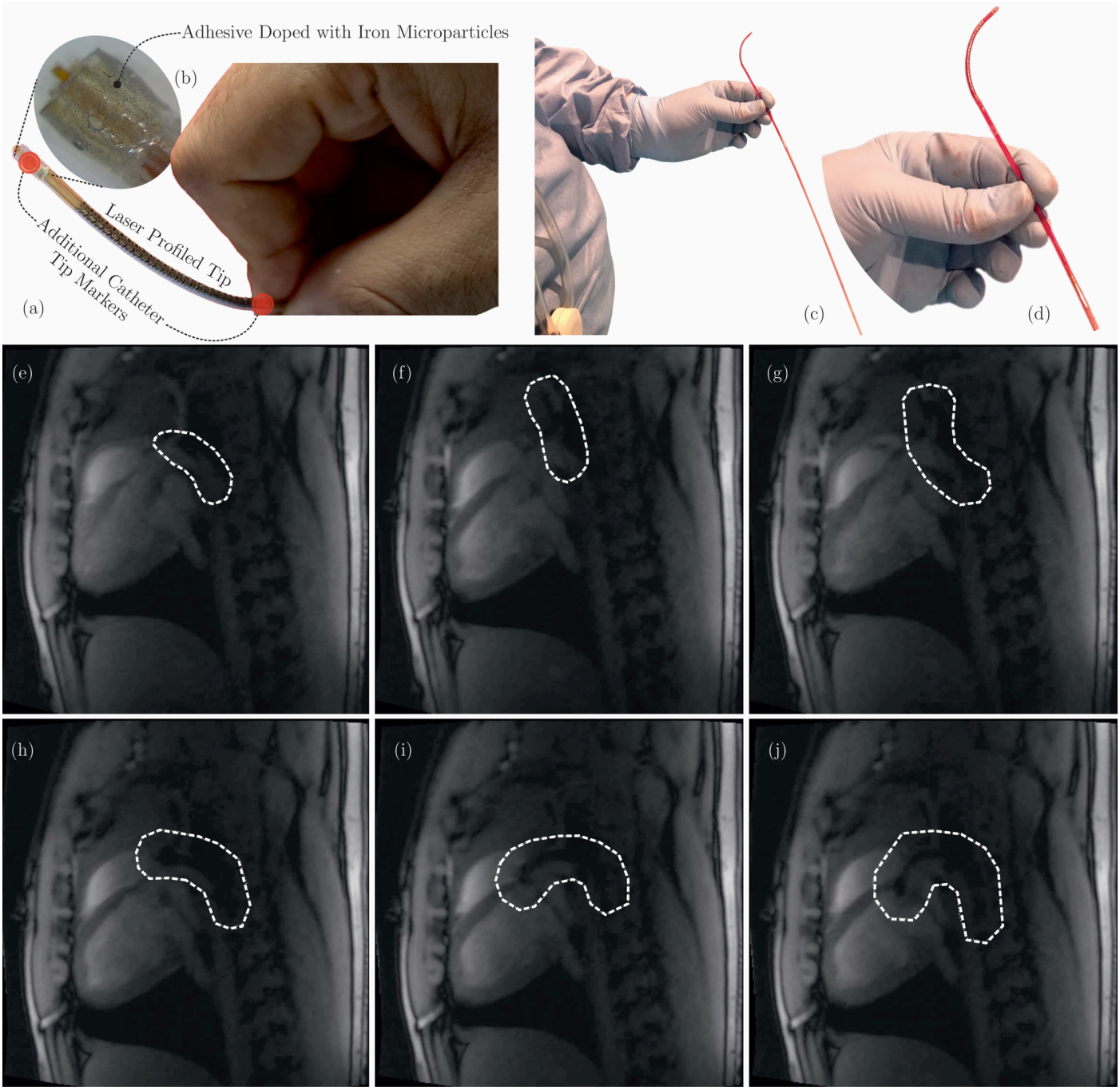



**Figure 5.17:** (a) Laser profiled catheter tip with the positions of the additional tip markers labelled. (b) Optical image of the catheter tip marker. (c-d) Steerable catheter after the *in-vivo* animal trial. Acquired *in-vivo* MRI scans of the steerable catheter manipulation in a clinical 3T MR system (Magnetom Prisma, Siemens) using a GRE sequence (TE/TR: 1.3/2.1 ms, spokes: 105, FA: 10°, FoV: 289 × 289× 8 $mm^3$, matrix: 192 × 192, fat saturation) for real-time guidance. Dotted lines are added to mark the distal end of the catheter. (e) Catheter is advanced towards the aortic arch. (f) Catheter is steered towards the carotid artery. (g) Carotid artery is succeffuly intubated. (h-i) Catheter is retracted back and steered towards the aortic arch. (j) Catheter crosses the aortic arch towards the heart.

stepper motor is coupled to a drive gear which shares the same module as the knobs (M = 0.5). The drive gear engages with the gear-shaped knob on the handle when the handle is placed in the actuator box. Two idle gears on the upper box mesh with the knob and hold the knob securely in place when the upper box is closed and locked by the quick release locks. Each rotary motor is independently operated by a pair of 5/2-way directional control valves MHA2-MS1H-5/2-2 (FESTO AG and CO. KG, Esslingen, Germany). A linear motor is fixed to the bottom of

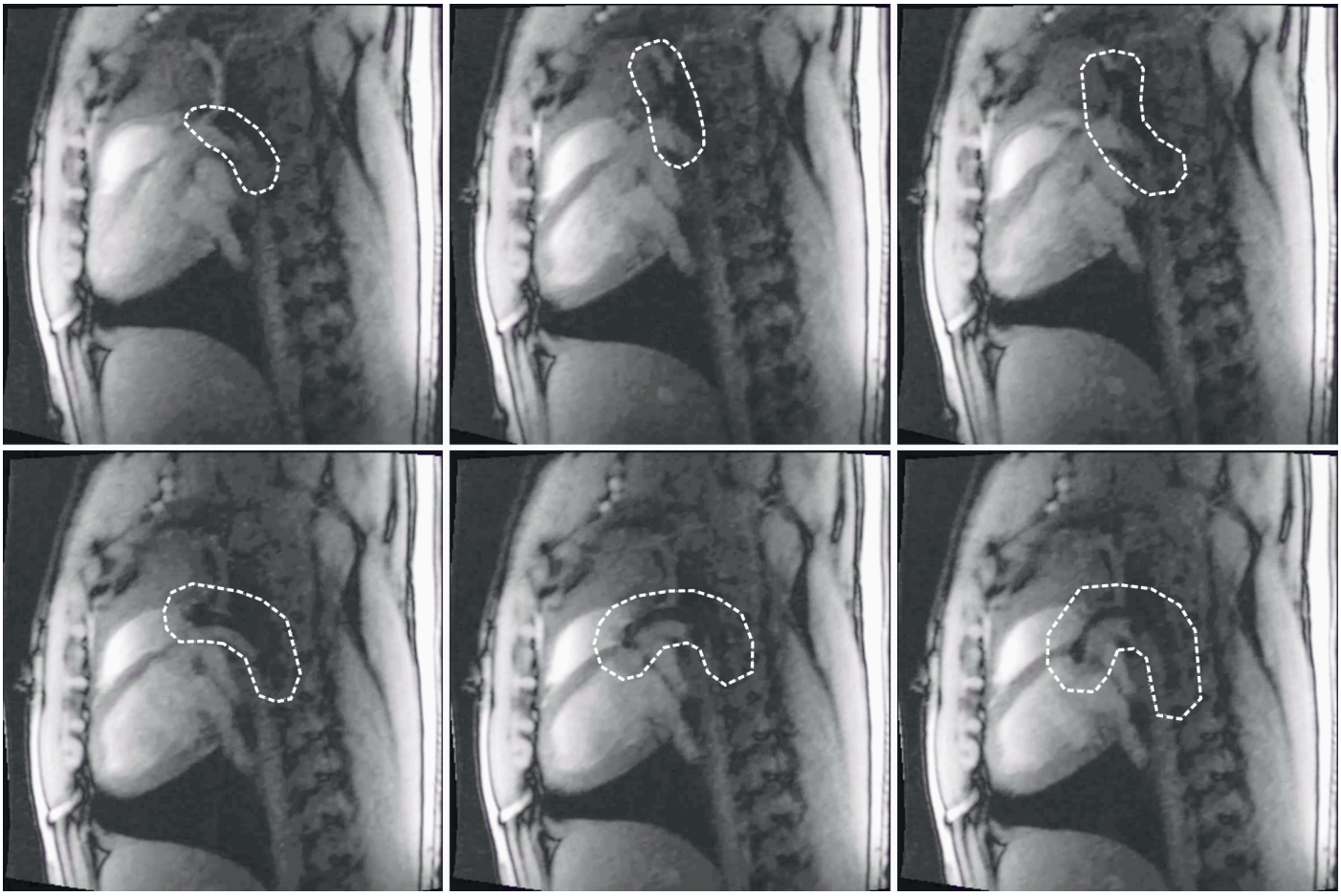


**Figure 5.18:** (light and contrast enhanced) acquired *in-vivo* MRI scans of the steerable catheter manipulation.

the actuator box to advance and retract the actuation unit (i.e. steerable catheter). The linear motor's dual acting pistons act on a geared rack to achieve the translation motion.

### 5.9.3 Preliminary Test

The basic functionalities of the actuation unit (i.e. 4-way steering and translational motion) are tested. The actuation unit is controlled via a pneumatic valve manifold, where each stepper motor (linear and rotary) is connected to a pair of solenoid actuated directional control valves. Valve switching is triggered by a real-time controller (compactRIO 9022, National Instruments, Austin, TX, USA) to run the control the control algorithm of the actuation unit. Due to the unavailability of an MR facility to evaluate the system over the last year, it was not possible to test the system further. In terms of future work, the system needs to be revised and combined with the robotic platform presented in Chapters 3 and 4, and should go through a detailed *in-vitro* (pilot & user), and *in-vivo* validation under MR-guidance with clear clinical targets to assess the overall system performance, navigation accuracy and downstream commercialisation issues.

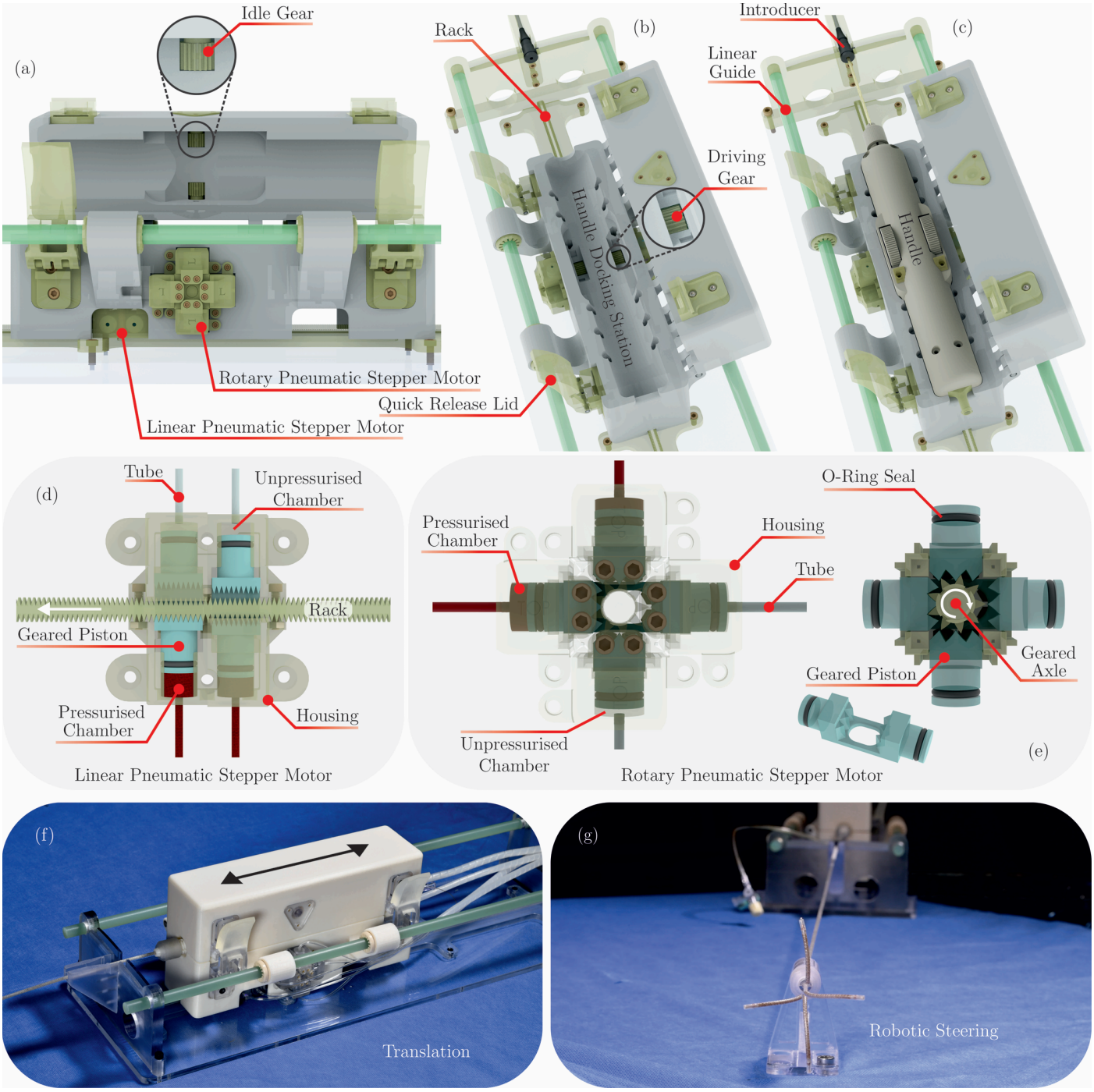



**Figure 5.19:** CAD renderings of the (a) Side view of the actuation unit, (b) Isometric view of the actuation unit (without the manual handle), (c) Isometric view of the actuation unit (with the manual handle docked), (d) Linear pneumatic stepper motor with o-rings sealing (Chapter 4). (e) Rotary pneumatic stepper motor with o-rings sealing (Chapter 4). Actuation unit performing its functions of (f) translational motion and (g) 4-way tip steering (where four images of where superimposed).

## 5.10 Conclusions

In an attempt to address the lack of MR-compatible instruments and to complement the work presented in Chapters 3 and 4, this chapter presented a thermally drawn steerable catheter for MR-guided endovascular interventions. The fibre drawing technique to fabricate catheters allows for a low-cost rapid prototyping which can lower the cost and accelerate research. While allowing miniaturisation to desired dimensions and axially asymmetry (i.e. helical

channels), this approach still results in fabrication at long length scales for scalable manufacturing. The in-house polymer-only based catheters show comparable mechanical properties (flexural rigidity, torquability, pushability) when compared to their commercially available metal-reinforced counterparts.

Subsequently, an additively manufactured manual handle was designed and fabricated to steer the compliant distal end of the catheter in four different directions. The integration between the catheter and the handle was also explored and optimised to minimise backlash. The steerability and repeatability evaluations show an accuracy of 1mm for a deflection of approximately 30mm. Added to that, catheters with helically routed pull-wires show better compensation to passive shaft deflections when compared to catheters with parallelly routed pull-wires. The *in-vitro* and *in-vivo* experiments demonstrate that the catheter is visible in its entirety and can be effectively manipulated in the vessel anatomy without obscuring the surrounding tissue. The size of artefacts is comparable to previous work [158] with guidewires, which comprise an MR visible rod, as a continuous susceptibility artefact with a mean diameter of 2mm $\pm$ 0.2 along the shaft. Using four MR visible pull-wires for steering did not increase the artefact size significantly. The steerable catheter was also integrated with a pneumatically actuated actuation unit to pave the way for robot-assisted MR-guided endovascular interventions.

A limitation observed over the course of the *in-vitro* and *in-vivo* trials, is the difficulty to cannulate vessels which would normally require catheters with several curves in their distal ends (e.g. Simmons2 (SIM)). One way to overcome this challenge is by developing an MR safe steerable sheath with an independently controlled deflectable segment through which the steerable catheter is telescopically manipulated. This facilitates the recreation of a wider selection of common selective catheter shapes. In other instances, the radius of curvature of the flexible distal end (currently 30mm) was found to be large to perform cannulations of specific blood vessels (e.g. superior mesenteric artery (SMA) artery). Therefore, the length of the laser profiled distal end needs further optimisation to facilitate safer cannulations. Although the visibility of the catheter was satisfactory, it was difficult at times to track the catheter tip when it is out of the projected imaging plane. Although the passive negative markers used are simple, safe and low cost, other hybrid tracking solutions could also be investigated to achieve optimal visibility under MR-guidance (e.g. indirect active tip markers and passive negative MR visible pull-wires).

In terms of follow-up work, future iterations of the steerable catheter could be extended from pure navigational purposes to navigation and subsequent treatments where MR-guidance can provide a competitive advantage over fluoroscopy-guidance (e.g. ventricular tachycardia [255]). In addition, the thermal drawing process can be employed to incorporate functional elements at the preform level to fabricate catheters with sensing capabilities without adding significant post-processing steps. For robotic catheterisation, the platform needs to be further tested and evaluated *in-vitro* and *in-vivo* in MR environments. In the following chapter, the thesis is drawn to a final conclusion, the contributions by each chapter are outlined and the limitations of each study are presented. Some directions and recommendations for future research are also offered.

Chapter 6

# Conclusion and Future Work

This chapter consolidates previous discussions, presenting the contributions made throughout this thesis to develop robotic tools and instrumentation by employing existing, scalable and unconventional fabrication methods to further the on-going research in the field of MR-guided endovascular interventions. Additionally, study limitations and potential directions for the future research are also presented. This concluding chapter summarises the overall research, key findings and limitations in section , and finally, in section 6.2 directions for future research are highlighted.

# 6.1 Conclusions and Limitations

**(Chapter 3) An MR-Safe Endovascular Robotic Platform: Pilot Study**

**A** The first iteration of a master-slave robotic platform and a navigation framework with image-based haptic feedback has been developed to remotely manipulate standard endovascular instruments (selective catheters and guidewires) in different imaging modalities, namely X-ray fluoroscopy and MRI.

**B** The system was evaluated under X-ray fluoroscopy guidance by catheterising three target vessels (LSA, LCCA and RCCA) in a simulated clinical scenario, i.e. a vascular silicone phantom of a normal adult human aortic arch connected to a pulsatile pump. The *in-vitro* study was conducted by a trained vascular surgeon with experience in manual interventions but no formal training with robotic systems.

**C** The image-based haptic feedback incorporated within the navigation framework, contributed towards the reduction in the mean overall forces exerted on the phantom when the robotic system is used, when compared to manual interventions. Thus, increasing the overall safety of the procedure.

**D** Based on the temporal analysis of the pilot study, while using the robot, a considerable amount of time is spent navigating the descending aorta and the aortic arch. These relatively simpler tasks can be done more quickly manually. However, when a more complex task such as cannulation of the RCCA was performed, the robotic procedure time was comparable with the manual. This suggests that the robot can be potentially employed in complex phases of the procedure, while manual manipulation can continue to be used for less critical phases. The proposed slave robot lends itself to this approach, given its capability of seamlessly switching between robotic and manual manipulation.

**E** The system was tested in a 3T MRI scanner by manipulating an MR conditional guidewire. As a result of its polymeric nature and pneumatic-based actuation, the slave robot did not introduce imaging artefacts which alters the ability of the operator to reliably perform the remote manipulation. The adoption of robotic catheterisation under MR guidance alleviates the difficulties of manual MR-guided interventions, such as the risk of developing musculoskeletal injury due to limited accessibility and hearing impairment due to acoustic noise.

**(Chapter 4) An MR-Safe Endovascular Robotic Platform: User Study**

**A** The second optimised iteration of the robotic platform was developed based on the end-user feedback received from the pilot study. The master manipulator was modified to improve and support its scalability prospects through the adoption of embedded real-time controllers to acquire and process the control signs. Similarly, the redesigned and optimised pneumatic stepper motors employed in the slave robot were able to achieve lower chamber pressure losses from only 10% to 23% with respect to the nominal pressure of 0.35MPa.

**B** The system was further evaluated under X-ray fluoroscopy guidance by conducting a user study with 7 clinical experts to demonstrate the performance characteristics of the optimised platform against manual interventions. In this study, the clinicians were asked to probe four different vessels in two different vascular silicone phantoms manually and robotically.

**C** Considering the defined metrics for performance, manual and robotic cannulations of the selected arteries are overall comparable. The catheter path length is slightly higher in robotic manipulation. On the other hand, the guidewire path length shows an average decrease when manipulated using the robot. As in the case with the pilot study, the task completion time, which is the time taken to cannulate the corresponding blood vessel, is higher when the robot is used. This is due to two factors the intrinsically lower dynamics

of the robotic system and the lack of surgical training with our robotic system. However, with an average completion time of less than 2 minutes, the results on this metric are already within a range that would be acceptable in actual clinical use.

**D** The cannulation rate during manual tasks was 5% higher when compared to the robotic tasks. Unsuccessful robotic catheterisations were primarily due to hardware and design limitations of the latest slave prototype. The two main issues identified were the occasional buckling of the catheter between the abdominal phantom's introducer and the slave robot, and the finite instrument manipulation stroke. Contact forces related to friction between the catheter, the introducer, and the vascular phantom occasionally resulted in buckling of the catheter due to the insufficient mechanical support.

**E** The mean and maximum forces show that overall there is a reduction of forces exerted to the phantoms when the robot is used, further corroborating the benefit of the image-based haptic feedback.

**F** Qualitative user feedback supports the results obtained through objective metrics. Analysis of questionnaire responses shows that the robotic system was well received both in terms of technical design and clinical usability. Users appreciated the concept of mimicking manual instrument handling and the augmentation of 'transparent' but effective haptic feedback. Conversely, several users suggested automating procedural sub-tasks, e.g. larger displacements in non-tortuous vessels to enhance temporal efficiency. Lastly, drawbacks resulting from potential latencies of the pneumatic principle have not been reported by the expert users.

**G** In the *in-vivo* animal study, an expert endovascular surgeon cannulated and performed angioplasty tasks in five target blood vessels. The tasks were performed manually (2 pigs) and robotically (2 pigs). The metrics used for evaluation included the success rate, fluoroscopy time, completion time, and histopathology. The dynamic active tracking feature implemented in the phantom study was not applicable with the animal trials due to the weak contrast of the vessel walls and surrounding tissue. This shortcoming was resolved by extracting the vessel contour from the image with contrast (i.e. Digital subtraction angiography). When the robot was used, the histopathology showed a lower incidence and severity of arterial injuries (only 2 sections presented vessel damage out of 78), whereas in the case of manual interventions, 21 sections out of 78 presented high-grade injuries. As expected, the robot-assisted interventions took 20mins longer on average when compared to manual interventions.

**(Chapter 5) Thermally Drawn Steerable Catheter for MR-Guided Endovascular Interventions**

**A** The scalable thermal fibre drawing process was leveraged to fabricate the main building block of an MR safe, pull-wire driven steerable catheter, i.e. multi-lumen tubing with parallely routed and helically routed lumina. Helically routed lumina were investigated to passively compensate for several undesirable effects experienced during the manipulation of flexible instrumentation.

**B** The thermally drawn multi-lumen tubing were subsequently post-processed by (1) overbraiding the tubing to enhance its torquability and kink resistance, (2) laser profiling the non-braided distal end to increase its flexibility to facilitate its steering and the atraumatic introduction of the catheter into tortuous vessels, (3) covering the assembly by heat shrink tubing to encapsulate the braid reinforcement and to suppress the thrombogenesis of the laser cut tip, (4) coating the encapsulated assembly with hydrophilic coating to improve the catheter's manoeuvrability and reduce the surface friction, (5) adding passive-negative tip markers to better visualise the distal end of the steerable catheter tip.

**C** To better gauge and evaluate key mechanical performance parameters (flexural rigidity, torquability, axial rigidity) of the in-house fabricated polymer-based catheter shafts against commercial metal-reinforced catheter shafts, several characterisation setups were fabricated and assembled. Based on the thorough

characterisation, it was concluded that the thermally drawn polymeric catheters have comparable mechanical properties to their metal-reinforced counterparts.

**D** An additively manufactured manual handle was developed to steer the distal end of the catheter in 4 directions. The handle comprised 1) a locking mechanism to lock the shape of the distal end, 2) a luer lock port for fluid injection and guidewire insertion, 3) dials with involute contours to ensure a better grip and to facilitate the handle's meshing with other gears of the same module for robotic integration. Since the polymer-only based catheter is invisible under MR images, passively MR visible pull-wires were employed to enable catheter visualisation over its full length. The steerability performance of the catheter-handle assembly was objectively evaluated and it was able to achieve an accuracy of 1mm for an approximate deflection of 30mm.

**E** A unique characterisation setup was designed and fabricated to evaluate the effectiveness of helically routed pull-wires in compensating passive deflections. The study showed that catheters with parallelly routed pull-wires demonstrate considerably larger deflections when compared to their helically router counterparts. Based on these results, it was concluded that multi-lumen tubing with helical lumina can improve the overall accuracy of catheter tip steering, especially when robotically controlled.

**F** *in-vitro* phantom experiments were performed in a clinical 3T MR scanner using image guidance to evaluate the mechanical efficacy and steerability of the catheter. The experiments demonstrate that the polymer-only catheter can be visualised over its lengths while being manipulated in the vessel anatomy without obscuring the surrounding tissue. The size of artefacts were comparable to previous work [158]. Using MR visible pull-wires for steering did not increase the artefact size significantly, with an average thickness of the shaft artefacts of 3.55mm, and tip marker artefact size of approximately 1.25cm by 1.25cm.

**G** During the course of the *in-vitro* trials, it was difficult to cannulate vessels which would normally require catheter with several curves in their distal ends. Furthemore, in other instances, the radius of curvature of the flexible distal end was found to be large (currently 30mm) to perform cannulations of specific blood vessels (e.g. superior mesenteric artery (SMA) artery).

**H** The catheter was tested in a pig model (*in-vivo*) under general anaesthesia in a clinical 3T MRI scanner using a 2D real-time imaging sequence. The steerability of the catheter was tested by attempting to intubate the carotid arteries as well as crossing the aortic arch towards the heart, both of which were successful. The visibility of the catheter shaft and tip markers *in-vivo* were also satisfactory.

**I** The pneumatically actuated robotic platform was extended to accommodate the thermally drawn steerable catheter assembly. The basic functionalities of the actuation unit were successfully evaluated by testing the remote 4-way steering and translation of the steerable catheter. By fulfilling the lack of MR safe instrumentation through the development of an MR safe steerable catheter and by integrating it with an MR actuation unit, the combined system paves the way for robot-assisted MR-guided endovascular interventions.

## 6.2 Future Work

The proposed future research and technical challenges are summarised below:

**Master-Slave Robotic Platform**

**A** Optimising the existing mechatronic design of the robotic platform to overcome the limitations and challenges experienced and observed during the previously described pilot (Chapter 3) and user (Chapter 4) studies. Future iterations of the slave robot should consider the following improvements:

- an anti-buckling system to eliminate the occasional instrument buckling between the introducer and slave robot. This issue can be resolved by designing a rigid, expandable, support device between the slave robot and the percutaneous introducer, which guides the catheter and prevents buckling of the device [330–332].
- an infinite guidewire manipulation stroke to eliminate the limited linear operational workspace of the slave robot without compromising the overall footprint of the robot. This can be achieved by employing the classical roller-based mechanism [122].
- safety components such as emergency stop buttons, visual alerts and a watchdog system to disable the system and suspend the pneumatic pressure in case of emergencies [333].
- a side injection port to facilitate the injection of contrast medium or the flushing of selective or steerable catheters.
- the additional capability of remotely manipulating therapeutic catheters (e.g. stent/balloon catheters).
- an extended reach arm for the seamless integration with different medical imaging suites (X-ray fluoroscopy and MRI).

**B** Similarly, based on the feedback received from some of the clinicians during the user study (Chapter 4), future iterations of the master manipulator should also consider the following optimisations:

- introduce an infinite stroke length for the manual handle instead of the currently employed automated homing feature. Several users noted that the automated homing introduces additional delays to the task completion time.
- introduce additional features such as: (1) the simultaneous manipulation of the catheter and guidewire as in standard manual procedures, and (2) instrument oscillation as it advances to prevent prolapses in tortuous anatomies during navigation.
- develop a master manipulator with two manual handles to independently control two instruments simultaneously as in standard manipulations. This, according to one of the users, would eliminate the time taken to switch between instruments (using the capacitive touch sensors) and could potentially further enhance the learning curve of the user.

**Steerable Catheter (Instrumentation)**

Future iterations of the catheter should consider the following suggestions:

**A** Covering or coating the MR visible pull-wires with PTFE heat shrink tubing and incorporating PTFE liners into the central and lateral channels to further alleviate the friction which may lead to backlash. As described in the filed patent (see E), the latter can be achieved by co-feeding etched PTFE liners during the thermal drawing process of the multi-lumen tubing without adding additional steps. Moreover, adding liners to helically routed lumina would mitigate the relatively higher frictional forces experienced by the pull-wires in unlined helical channels (see Section 5.3.2).

**B** Developing an MR safe steerable sheath with an independently controlled deflectable segment through which the steerable catheter is telescopically advanced or retracted. This not only increases the DOFs, but also facilitates the recreation of a wider selection of common selective catheter shapes.

**C** Sensing functionalities can be integrated directly into the steerable catheter without also adding significant post-processing steps to its fabrication process, underlining the value of employing the thermal fibre drawing process to fabricate functional catheters. Sensing can be achieved by integrating functional elements

at the preform level and their co-processing concertedly with the aforementioned PTFE liners. A particularly promising functionality, especially with robotic catheterisation, is the assessment of mechanical interactions between the device and the surrounding tissue, to avoid tissue damage and ease of operation of the device. The functionality can be activated exclusively at the tip or throughout the entire length of the device. For MR-guided endovascular interventions, incorporating soft and elastic optical fibres can be employed for this purpose [334]. In this case, the light guiding is sensitively influenced by geometrical shape changes of the deformable fibre which can be translated to contact force measurements. Incorporating sensing at the instrument level can possibly replace the image-based haptic feedback employed in this thesis.

**D** Adopting alternative catheter designs by doping the polymeric material used to fabricate the multi-lumen tubing with iron microparticles (at the preform level) to achieve the desired passive MR visibility of the catheter shaft. This would minimise the reliance on the relatively thick commercially acquired MR visible pull-wires, which, in turn, facilitates the use of thinner pull-wires (e.g. high synthetic fibres) and the further miniaturisation of the catheter.

**E** Investigating other tip marker tracking methods (e.g. indirect active tip marking) to track the distal end of the catheter instead of the passive negative tip markers used in this thesis [7]. In the case of indirect active tip marking, co-axial cables could be co-fed at the preform level during the draw to create multi-lumen tubing embedded with the cable in a single step fabrication process. This also highlights the benefit of using the fibre drawing technology.

**F** Exploring anatomy-specific design and fabrication of helically routed multi-lumen tubing for the passive compensation of the undesirable phenomena which were thoroughly described in section 5.3.2. This could be achieved by using preoperative scans of the patient from which the centrelines of different interventional paths could be extracted. Followed by computing the optimal constant or variable pitch size of the helices to compensate for the different phenomena across the desired path(s).

**G** Leveraging the lessons learned from the work described in Chapter 5, to extend the functionalities of the MR steerable catheter from pure navigational purposes to navigation and ablation (MR safe or MR conditional steerable ablation catheter) for the treatment of a diseases where MR-guidance can provide a competitive advantage over fluoroscopy-guidance (e.g. ventricular tachycardia [255]).

**H** Future characterisation setups should carefully explore the effect of moisture and temperature on the various mechanical properties. Ideally the setups should be designed in accordance with medical standards, such as ISO 25539-1 and ISO 25539-2. These guidelines and standards will ensure that the final outcome is inline with regulatory requirements for subsequent clinical investigation and commercialisation.

**I** Perform detailed *in-vitro* (pilot & user), and *in-vivo* studies under real-time MR-guidance with clear clinical targets to assess the overall system performance, navigation accuracy and downstream commercialisation issues. It would also be crucial to consider adding evaluation of the treatment to the study to uniquely demonstrate the strengths of MR-guidance.

In addition to the aforementioned future directions, as pointed out in Chapter 2, further systematic communication and collaboration among researchers (engineers, physicists, radiologists, physicians) are still needed to create a true impact on the field of MR-guided endovascular interventions. The work presented in this thesis attempted to stimulate such conversations and collaborations through the development of tools that could potentially facilitate the wider adoption of MR-guided interventions in interventional radiology and targeted therapy.

Finally, as our research and understanding of MRI and MR-related technologies move forward, great strides can be made towards improving the quality and safety of patient healthcare.

# References


[1] Kaplan, J. A., Augoustides, J. G. T., Manecke, G. R., et al. *Kaplan's Cardiac Anesthesia : for Cardiac and Noncardiac Surgery*. Amsterdam, the Netherlands: Elsevier, 2017. ISBN: 9780323393782 0323393780 9780323463010 0323463010.

[2] Clogenson, H. C. M. "MRI-Compatible Endovascular Instruments: Improved Maneuverability during Navigation". PhD Thesis. Delft University of Technology, Netherlands, Sept. 2014.

[3] Piorkowski, C., Kottkamp, H., Gerds-Li, J.-H., et al. "Steerable Sheath Catheter Navigation for Ablation of Atrial Fibrillation: A Case-Control Study". In: *Pacing and Clinical Electrophysiology* 31.7 (2008), pp. 863–873. ISSN: 0147-8389. DOI: 10.1111/j.1540-8159.2008.01101.x.

[4] Matsuo, S., Yamane, T., Tokuda, M., et al. "Prospective randomized comparison of a steerable versus a nonsteerable sheath for typical atrial flutter ablation". In: *EP Europace* 12.3 (2010), pp. 402–409. ISSN: 1099-5129. DOI: 10.1093/europace/eup434.

[5] Piorkowski, C., Eitel, C., Rolf, S., et al. "Steerable Versus Nonsteerable Sheath Technology in Atrial Fibrillation Ablation". In: *Circulation: Arrhythmia and Electrophysiology* 4.2 (2011), pp. 157–165. DOI: 10.1161/CIRCEP.110.957761.

[6] Matsuo, S., Yamane, T., Date, T., et al. "Completion of Mitral Isthmus Ablation Using a Steerable Sheath: Prospective Randomized Comparison With a Nonsteerable Sheath". In: *Journal of Cardiovascular Electrophysiology* 22.12 (2011), pp. 1331–1338. ISSN: 1045-3873. DOI: 10.1111/j.1540-8167.2011.02112.x.

[7] Heidt, T., Reiss, S., Krafft, A. J., et al. "Real-time magnetic resonance imaging – guided coronary intervention in a porcine model". In: *Scientific Reports* 9.1 (2019), p. 8663. ISSN: 2045-2322.

[8] Venneri, L., Rossi, F., Botto, N., et al. "Cancer risk from professional exposure in staff working in cardiac catheterization laboratory: insights from the National Research Council's Biological Effects of Ionizing Radiation VII Report". In: *American heart journal* 157.1 (2009), pp. 118–124.

[9] Razavi, R., Hill, D. L. G., Keevil, S. F., et al. "Cardiac catheterisation guided by MRI in children and adults with congenital heart disease". In: *The Lancet* 362.9399 (2003), pp. 1877–1882. ISSN: 0140-6736.

[10] Bock, M. and Wacker, F. K. "MR-guided intravascular interventions: Techniques and applications". In: *Journal of Magnetic Resonance Imaging* 27.2 (2008), pp. 326–338. ISSN: 1053-1807. DOI: 10.1002/jmri.21271.

[11] Kuehne, T., Saeed, M., Higgins, C. B., et al. "Endovascular Stents in Pulmonary Valve and Artery in Swine: Feasibility Study of MR Imaging–guided Deployment and Postinterventional Assessment". In: *Radiology* 226.2 (2003), pp. 475–481. ISSN: 0033-8419. DOI: 10.1148/radiol.2262011639.

[12] Deng, J., Miller, F. H., Rhee, T. K., et al. "Diffusion-weighted MR imaging for determination of hepatocellular carcinoma response to yttrium-90 radioembolization". In: *J Vasc Interv Radiol* 17.7 (2006), pp. 1195–200. ISSN: 1051-0443 (Print) 1051-0443. DOI: 10.1097/01.Rvi.0000227234.81718.Eb.

[13] Ratnayaka, K., Faranesh, A. Z., Hansen, M. S., et al. "Real-time MRI-guided right heart catheterization in adults using passive catheters". In: *European Heart Journal* 34.5 (2012), pp. 380–389. ISSN: 0195-668X. DOI: 10.1093/eurheartj/ehs189.

[14] Grothoff, M., Gutberlet, M., Hindricks, G., et al. "Magnetic resonance imaging guided transatrial electrophysiological studies in swine using active catheter tracking–experience with 14 cases". In: *European radiology* 27.5 (2017), pp. 1954–1962.

[15] Sommer, P., Grothoff, M., Eitel, C., et al. "Feasibility of real-time magnetic resonance imaging-guided electrophysiology studies in humans". In: *Europace* 15.1 (2013), pp. 101–108.

[16] Fernández Gutiérrez, F., Martinez, S., Rube, M., et al. "Comparative ergonomic workflow and user experience analysis of MRI versus fluoroscopy-guided vascular interventions: an iliac angioplasty exemplar case study". In: *International journal of computer assisted radiology and surgery* 10 (Oct. 2015), pp. 1639–1650. DOI: 10.1007/s11548-015-1152-y.

[17] McJury PhD, M. and Shellock PhD, F. G. "Auditory noise associated with MR procedures: a review". In: *Journal of Magnetic Resonance Imaging* 12.1 (2000), pp. 37–45.

[18] Groenhuis, V. and Stramigioli, S. "Rapid Prototyping High-Performance MR Safe Pneumatic Stepper Motors". In: *IEEE/ASME Transactions on Mechatronics* 23.4 (Aug. 2018), pp. 1843–1853. ISSN: 1083-4435. DOI: 10.1109/TMECH.2018.2840682.

[19] Groenhuis, V., Siepel, F., and Stramigioli, S. "Dual-Speed MR Safe Pneumatic Stepper Motors". In: *Robotics: Science and Systems 2018*. June 2018.

[20] Dagnino, G., Liu, J., Abdelaziz, M. E. M. K., et al. "Haptic Feedback and Dynamic Active Constraints for Robot-Assisted Endovascular Catheterization". In: *2018 IEEE/RSJ International Conference on Intelligent Robots and Systems (IROS)*. Oct. 2018, pp. 1770–1775. DOI: 10.1109/IROS.2018.8593628.

[21] Ali, A., Plettenburg, D. H., and Breedveld, P. "Steerable Catheters in Cardiology: Classifying Steerability and Assessing Future Challenges". In: *IEEE Transactions on Biomedical Engineering* 63.4 (2016), pp. 679–693. ISSN: 1558-2531.

[22] Gupta, V. US20190192828A1. 2019.

[23] Tóth, G. G., Yamane, M., and Heyndrickx, G. R. "How to select a guidewire: technical features and key characteristics". In: *Heart* 101.8 (2015), pp. 645–652. ISSN: 1355-6037. DOI: 10.1136/heartjnl-2013-304243. eprint: https://heart.bmj.com/content/101/8/645.full.pdf.

[24] Buller, C. "Coronary guidewires for chronic total occlusion procedures: Function and design". In: *Interventional Cardiology* 5 (Oct. 2013), pp. 533–540. DOI: 10.2217/ica.13.63.

[25] Truckai, C. WO9737713A1. 1997.

[26] Parisi, M., Willard, M., Wang, Y., et al. US6648874B2. 2003.

[27] Opolski, M. P. US6238799B1. 2001.

[28] Horrigan, J. B. and Riopel, M. C. Patent US5792124A. 1998.

[29] Wang, J. C. US5533985A. 1996.

[30] To, J. T. US2009043330A1. 2009.

[31] Ebnesajjad, S. *Fluoroplastics, Volume 1: Non-Melt Processible Fluoropolymers - The Definitive User's Guide and Data Book (2nd Edition)*. Amsterdam, the Netherlands: Elsevier, 2014.

[32] Raeder-Devens, J. E., Shelso, S. I., Hemerick, J. F., et al. US8535369B2. 2013.

[33] Peterson, A. A., Logan, J. B., Patel, M. R., et al. US5836926A. 1998.

[34] Moore, P. "MRI-guided congenital cardiac catheterization and intervention: The future?" In: *Catheterization and Cardiovascular Interventions* 66.1 (2005), pp. 1–8. ISSN: 1522-1946.

[35] Rothmore, P. "Lead aprons, radiographers, and discomfort: A pilot study". In: *Journal of Occupational Health and Safety - Australia and New Zealand* 18 (2002), pp. 357–365.

[36] Journy, N., Dreuil, S., Rage, E., et al. "Projected Future Cancer Risks in Children Treated With Fluoroscopy-Guided Cardiac Catheterization Procedures". In: *Circulation: Cardiovascular Interventions* 11.11 (2018), e006765. DOI: 10.1161/CIRCINTERVENTIONS.118.006765.

[37] Vandenberghe, W. and Hoste, E. "Contrast-associated acute kidney injury: does it really exist, and if so, what to do about it?" In: *F1000Research* 8.753 (2019).

[38] Roy, K., Gomez-Pulido, F., and Ernst, S. "Remote Magnetic Navigation for Catheter Ablation in Patients With Congenital Heart Disease: A Review". In: *Journal of Cardiovascular Electrophysiology* 27.S1 (2016), S45–S56. ISSN: 1045-3873. DOI: 10.1111/jce.12903.

[39] Rafii-Tari, H., Payne, C. J., and Yang, G.-Z. "Current and Emerging Robot-Assisted Endovascular Catheterization Technologies: A Review". In: *Annals of Biomedical Engineering* 42.4 (Apr. 2014), pp. 697–715. ISSN: 1573-9686.

[40] Antoniou, G. A., Riga, C. V., Mayer, E. K., et al. "Clinical applications of robotic technology in vascular and endovascular surgery". In: *Journal of vascular surgery* 53.2 (2011), pp. 493–499.

[41] Riga, C., Bicknell, C., Cheshire, N., et al. "Initial clinical application of a robotically steerable catheter system in endovascular aneurysm repair". In: *Journal of Endovascular Therapy* 16.2 (2009), pp. 149–153.

[42] Riga, C. V., Bicknell, C. D., Rolls, A., et al. "Robot-assisted fenestrated endovascular aneurysm repair (FEVAR) using the Magellan system". In: *Journal of Vascular and Interventional Radiology* 24.2 (2013), pp. 191–196.

[43] Granada, J. F., Delgado, J. A., Uribe, M. P., et al. "First-in-human evaluation of a novel robotic-assisted coronary angioplasty system". In: *JACC: Cardiovascular Interventions* 4.4 (2011), pp. 460–465.
[44] Al Nooryani, A. and Aboushokka, W. "Rotate-on-retract procedural automation for robotic-assisted percutaneous coronary intervention: first clinical experience". In: *Case reports in cardiology* 2018 (2018).
[45] Patel, T. M., Shah, S. C., and Pancholy, S. B. "Long distance tele-robotic-assisted percutaneous coronary intervention: a report of first-in-human experience". In: *EClinicalMedicine* 14 (2019), pp. 53–58.
[46] Saliba, W., Reddy, V. Y., Wazni, O., et al. "Atrial fibrillation ablation using a robotic catheter remote control system: initial human experience and long-term follow-up results". In: *Journal of the American College of Cardiology* 51.25 (2008), pp. 2407–2411.
[47] Di Biase, L., Wang, Y., Horton, R., et al. "Ablation of atrial fibrillation utilizing robotic catheter navigation in comparison to manual navigation and ablation: Single-center experience". In: *Journal of cardiovascular electrophysiology* 20.12 (2009), pp. 1328–1335.
[48] Knight, B., Ayers, G. M., and Cohen, T. J. "Robotic positioning of standard electrophysiology catheters: a novel approach to catheter robotics". In: *Journal of Invasive Cardiology* 20.5 (2008), p. 250.
[49] Khan, E. M., Frumkin, W., Ng, G. A., et al. "First experience with a novel robotic remote catheter system: Amigo™ mapping trial". In: *Journal of Interventional Cardiac Electrophysiology* 37.2 (2013), pp. 121–129.
[50] Datino, T., Arenal, A., Pelliza, M., et al. "Comparison of the safety and feasibility of arrhythmia ablation using the Amigo Robotic Remote Catheter System versus manual ablation". In: *The American journal of cardiology* 113.5 (2014), pp. 827–831.
[51] López-Gil, M., Salgado, R., Merino, J. L., et al. "Cavo-tricuspid isthmus radiofrequency ablation using a novel remote navigation catheter system in patients with typical atrial flutter". In: *Europace* 16.4 (2014), pp. 558–562.
[52] Shaikh, Z. A., Eilenberg, M. F., and Cohen, T. J. "The Amigo™ Remote Catheter System: From Concept to Bedside". In: *The Journal of Innovations in Cardiac Rhythm Management* 8.8 (2017), p. 2795.
[53] Wutzler, A., Wolber, T., Parwani, A. S., et al. "Robotic ablation of atrial fibrillation with a new remote catheter system". In: *Journal of Interventional Cardiac Electrophysiology* 40.3 (2014), pp. 215–219.
[54] Ernst, S., Ouyang, F., Linder, C., et al. "Initial experience with remote catheter ablation using a novel magnetic navigation system: magnetic remote catheter ablation". In: *Circulation* 109.12 (2004), pp. 1472–1475.
[55] Ernst, S., Ouyang, F., Linder, C., et al. "Modulation of the slow pathway in the presence of a persistent left superior caval vein using the novel magnetic navigation system Niobe". In: *EP Europace* 6.1 (2004), pp. 10–14.
[56] Pappone, C., Vicedomini, G., Manguso, F., et al. "Robotic magnetic navigation for atrial fibrillation ablation". In: *Journal of the American College of Cardiology* 47.7 (2006), pp. 1390–1400.
[57] Chun, J. K.-R., Ernst, S., Matthews, S., et al. "Remote-controlled catheter ablation of accessory pathways: results from the magnetic laboratory". In: *European heart journal* 28.2 (2007), pp. 190–195.
[58] Di Biase, L., Fahmy, T. S., Patel, D., et al. "Remote magnetic navigation: human experience in pulmonary vein ablation". In: *Journal of the American College of Cardiology* 50.9 (2007), pp. 868–874.
[59] Carpi, F. and Pappone, C. "Stereotaxis Niobe® magnetic navigation system for endocardial catheter ablation and gastrointestinal capsule endoscopy". In: *Expert review of medical devices* 6.5 (2009), pp. 487–498.
[60] Atmakuri, S. R., Lev, E. I., Alviar, C., et al. "Initial experience with a magnetic navigation system for percutaneous coronary intervention in complex coronary artery lesions". In: *Journal of the American College of Cardiology* 47.3 (2006), pp. 515–521.
[61] Thornton, A. S. and Jordaens, L. J. "Remote magnetic navigation for mapping and ablating right ventricular outflow tract tachycardia". In: *Heart rhythm* 3.6 (2006), pp. 691–696.
[62] Choi, M. S., Oh, Y.-S., Jang, S. W., et al. "Comparison of magnetic navigation system and conventional method in catheter ablation of atrial fibrillation: is magnetic navigation system is more effective and safer than conventional method?" In: *Korean Circulation Journal* 41.5 (2011), p. 248.
[63] Kiemeneij, F., Patterson, M. S., Amoroso, G., et al. "Use of the Stereotaxis Niobe® magnetic navigation system for percutaneous coronary intervention: Results from 350 consecutive patients". In: *Catheterization and Cardiovascular Interventions* 71.4 (2008), pp. 510–516.

[64] Armacost, M. P., Adair, J., Munger, T., et al. "Accurate and reproducible target navigation with the stereotaxis Niobe® magnetic navigation system". In: *Journal of Cardiovascular Electrophysiology* 18 (2007), S26–S31.
[65] Gang, E. S., Nguyen, B. L., Shachar, Y., et al. "Dynamically shaped magnetic fields: initial animal validation of a new remote electrophysiology catheter guidance and control system". In: *Circulation: Arrhythmia and Electrophysiology* 4.5 (2011), pp. 770–777.
[66] Nguyen, B. L., Merino, J. L., Shachar, Y., et al. "Non-fluoroscopic transseptal catheterization during electrophysiology procedures using a remote magnetic navigation system". In: *Journal of atrial fibrillation* 6.4 (2013).
[67] Filgueiras-Rama, D., Estrada, A., Shachar, J., et al. "Remote magnetic navigation for accurate, real-time catheter positioning and ablation in cardiac electrophysiology procedures". In: *Journal of visualized experiments: JoVE* 74 (2013).
[68] Saliba, W., Cummings, J. E., Oh, S., et al. "Novel Robotic Catheter Remote Control System: Feasibility and Safety of Transseptal Puncture and Endocardial Catheter Navigation". In: *Journal of Cardiovascular Electrophysiology* 17.10 (2006), pp. 1102–1105.
[69] Khan, E. M., Frumkin, W., Ng, G. A., et al. "First experience with a novel robotic remote catheter system: Amigo™ mapping trial". In: *Journal of Interventional Cardiac Electrophysiology* 37.2 (Aug. 2013), pp. 121–129. ISSN: 1572-8595.
[70] Cercenelli, L., Marcelli, E., and Plicchi, G. "Initial experience with a telerobotic system to remotely navigate and automatically reposition standard steerable EP catheters". In: *ASAIO J.* 53.5 (2007), pp. 523–529.
[71] Marcelli, E., Cercenelli, L., and Plicchi, G. "A novel telerobotic system to remotely navigate standard electrophysiology catheters". In: *2008 Computers in Cardiology*. Sept. 2008, pp. 137–140. DOI: 10.1109/CIC.2008.4748996.
[72] Cercenelli, L., Bortolani, B., and Marcelli, E. "CathROB: A Highly Compact and Versatile Remote Catheter Navigation System". In: *Appl Bionics Biomech* 2017 (2017), p. 2712453.
[73] Moon, Y. and Choi, J. "A tele-operated robotic platform for cardiovascular catheter intervention with haptic guidance". In: *2014 14th International Conference on Control, Automation and Systems (ICCAS 2014)*. Oct. 2014, pp. 299–303. DOI: 10.1109/ICCAS.2014.6988007.
[74] Fu, Y., Gao, A., Liu, H., et al. "Development of a novel robotic catheter system for endovascular minimally invasive surgery". In: *The 2011 IEEE/ICME International Conference on Complex Medical Engineering*. May 2011, pp. 400–405. DOI: 10.1109/ICCME.2011.5876772.
[75] Fu, Y., Gao, A., Liu, H., et al. "The master-slave catheterisation system for positioning the steerable catheter". In: *International Journal of Mechatronics and Automation* 1.3-4 (2011), pp. 143–152. DOI: 10.1504/IJMA.2011.045271. eprint: https://www.inderscienceonline.com/doi/pdf/10.1504/IJMA.2011.045271.
[76] Park, J. W., Choi, J., Pak, H.-N., et al. "Development of a Force-Reflecting Robotic Platform for Cardiac Catheter Navigation". In: *Artificial Organs* 34.11 (Nov. 2010), pp. 1034–1039. DOI: 10.1111/j.1525-1594.2010.01142.x. eprint: https://onlinelibrary.wiley.com/doi/pdf/10.1111/j.1525-1594.2010.01142.x.
[77] Tavallaei, M. A., Thakur, Y., Haider, S., et al. "A Magnetic-Resonance-Imaging-Compatible Remote Catheter Navigation System". In: *IEEE Transactions on Biomedical Engineering* 60.4 (Apr. 2013), pp. 899–905. ISSN: 0018-9294. DOI: 10.1109/TBME.2012.2229709.
[78] Tavallaei, M. A., Gelman, D., Lavdas, M. K., et al. "Design, development and evaluation of a compact telerobotic catheter navigation system". In: *The International Journal of Medical Robotics and Computer Assisted Surgery* 12.3 (2015), pp. 442–452. DOI: 10.1002/rcs.1711. eprint: https://onlinelibrary.wiley.com/doi/pdf/10.1002/rcs.1711.
[79] Ganji, Y., Janabi-Sharifi, F., and Cheema, A. N. "Robot-assisted catheter manipulation for intracardiac navigation". In: *Int J Comput Assist Radiol Surg* 4.4 (June 2009), pp. 307–315.
[80] Lee, K., Fu, K. C. D., Guo, Z., et al. "MR Safe Robotic Manipulator for MRI-Guided Intracardiac Catheterization". In: *IEEE/ASME Transactions on Mechatronics* 23.2 (2018), pp. 586–595.
[81] Bismuth, J., Duran, C., Stankovic, M., et al. "A first-in-man study of the role of flexible robotics in overcoming navigation challenges in the iliofemoral arteries". In: *Journal of Vascular Surgery* 57.2 (Feb. 2013), 14S–19S. ISSN: 0741-5214.

[82] Robocath. *R-One™ robotic platform*. 2018. URL: https://www.robocath.com/en/produits/ (visited on 11/15/2018).

[83] Granada, J. F., Delgado, J. A., Uribe, M. P., et al. "First-in-Human Evaluation of a Novel Robotic-Assisted Coronary Angioplasty System". In: *JACC: Cardiovascular Interventions* 4.4 (2011), pp. 460–465. ISSN: 1936-8798. DOI: https://doi.org/10.1016/j.jcin.2010.12.007.

[84] Bian, G., Xie, X., Feng, Z., et al. "An enhanced dual-finger robotic Hand for Catheter manipulating in vascular intervention: A preliminary study". In: *2013 IEEE International Conference on Information and Automation (ICIA)*. 2013, pp. 356–361.

[85] Feng, Z., Bian, G., Xie, X., et al. "Design and evaluation of a bio-inspired robotic hand for percutaneous coronary intervention". In: *2015 IEEE International Conference on Robotics and Automation (ICRA)*. May 2015, pp. 5338–5343. DOI: 10.1109/ICRA.2015.7139944.

[86] Srimathveeravalli, G., Kesavadas, T., and Li, X. "Design and fabrication of a robotic mechanism for remote steering and positioning of interventional devices". In: *The International Journal of Medical Robotics and Computer Assisted Surgery* 6.2 (2010), pp. 160–170. DOI: 10.1002/rcs.301. eprint: https://onlinelibrary.wiley.com/doi/pdf/10.1002/rcs.301.

[87] Mi, J., He, Y., Zhang, P., et al. "A vascular intervention assisted robot based on master-slave control mode". In: *2014 IEEE International Conference on Mechatronics and Automation*. Aug. 2014, pp. 1276–1281. DOI: 10.1109/ICMA.2014.6885883.

[88] Cha, H.-J., Yi, B.-J., and Won, J. Y. "An assembly-type master–slave catheter and guidewire driving system for vascular intervention". In: *Proceedings of the Institution of Mechanical Engineers, Part H: Journal of Engineering in Medicine* 231.1 (2017). PMID: 28097937, pp. 69–79. DOI: 10.1177/0954411916679328. eprint: https://doi.org/10.1177/0954411916679328.

[89] Wang, K., Chen, B., Lu, Q., et al. "Design and Performance Evaluation of Real-time Endovascular Interventional Surgical Robotic System with High Accuracy". In: *The International Journal of Medical Robotics and Computer Assisted Surgery* 14.5 (2018), e1915.

[90] Bao, X., Guo, S., Xiao, N., et al. "A cooperation of catheters and guidewires-based novel remote-controlled vascular interventional robot". In: *Biomedical Microdevices* 20.1 (Feb. 2018), p. 20. ISSN: 1572-8781. DOI: 10.1007/s10544-018-0261-0.

[91] Bao, X., Guo, S., Xiao, N., et al. "Operation evaluation in-human of a novel remote-controlled vascular interventional robot". In: *Biomedical Microdevices* 20.2 (Apr. 2018), p. 34. ISSN: 1572-8781. DOI: 10.1007/s10544-018-0277-5.

[92] Zhang, P., Yu, S., Hu, Y., et al. "Design of a novel master-slave robotic system for minimally intravascular invasive surgery". In: *2011 IEEE International Conference on Mechatronics and Automation*. Aug. 2011, pp. 259–264. DOI: 10.1109/ICMA.2011.5985667.

[93] Omisore, O. M., Han, S. P., Ren, L. X., et al. "Towards Characterization and Adaptive Compensation of Backlash in a Novel Robotic Catheter System for Cardiovascular Interventions". In: *IEEE Transactions on Biomedical Circuits and Systems* 12.4 (Aug. 2018), pp. 824–838. ISSN: 1932-4545. DOI: 10.1109/TBCAS.2018.2825359.

[94] Guo, S., Kondo, H., Wang, J., et al. "A New Catheter Operating System for Medical Applications". In: *2007 IEEE/ICME International Conference on Complex Medical Engineering*. May 2007, pp. 82–86. DOI: 10.1109/ICCME.2007.4381697.

[95] Guo, S., Yamaji, H., Kita, Y., et al. "A novel active catheter system for Ileus treatment". In: *2008 IEEE International Conference on Automation and Logistics*. Sept. 2008, pp. 67–72. DOI: 10.1109/ICAL.2008.4636121.

[96] Xiao, N., Guo, J., Guo, S., et al. "A novel type of catheter operating system with force monitoring". In: *IEEE/ICME International Conference on Complex Medical Engineering*. July 2010, pp. 11–16. DOI: 10.1109/ICCME.2010.5558879.

[97] Feng, W., Chi, C., Wang, H., et al. "Highly Precise Catheter Driving Mechanism for Intravascular Neurosurgery". In: *2006 International Conference on Mechatronics and Automation*. June 2006, pp. 990–995. DOI: 10.1109/ICMA.2006.257760.

[98] Che Zakaria, N. A., Komeda, T., Low, C. Y., et al. "Development of foolproof catheter guide system based on mechatronic design". In: *Production Engineering* 7.1 (Jan. 2013), pp. 81–90. ISSN: 1863-7353. DOI: 10.1007/s11740-012-0430-6.

[99] Wang, T., Zhang, D., and Da, L. "Remote-controlled vascular interventional surgery robot". In: *The International Journal of Medical Robotics and Computer Assisted Surgery* 6.2 (2010), pp. 194–201. DOI: 10.1002/rcs.306. eprint: https://onlinelibrary.wiley.com/doi/pdf/10.1002/rcs.306.

[100] Zhao, H. and Duan, X. "Design of a Catheter Operating System with Active Supporting Arm for Vascular Interventional Surgery". In: *2011 Third International Conference on Intelligent Human-Machine Systems and Cybernetics*. Vol. 1. Aug. 2011, pp. 169–172. DOI: 10.1109/IHMSC.2011.47.

[101] Zhao, H., Duan, X., Huang, Q., et al. "Mechanical design and control system of vascular interventional robot". In: *The 2011 IEEE/ICME International Conference on Complex Medical Engineering*. May 2011, pp. 357–362. DOI: 10.1109/ICCME.2011.5876765.

[102] Kong, X., Duan, X., Zhao, H., et al. "An active medical supporting manipulator and experiments for vascular interventional robot". In: *2012 IEEE International Conference on Mechatronics and Automation*. Aug. 2012, pp. 617–622. DOI: 10.1109/ICMA.2012.6283178.

[103] Thakur*, Y., Bax, J. S., Holdsworth, D. W., et al. "Design and Performance Evaluation of a Remote Catheter Navigation System". In: *IEEE Transactions on Biomedical Engineering* 56.7 (2009), pp. 1901–1908.

[104] Kesner, S. B. and Howe, R. D. "Design and control of motion compensation cardiac catheters". In: *2010 IEEE International Conference on Robotics and Automation*. May 2010, pp. 1059–1065. DOI: 10.1109/ROBOT.2010.5509250.

[105] Meng, C., Guan, S., Sun, S., et al. "A novel catheter operating robot for vascular interventional surgery". In: *2016 IEEE Workshop on Advanced Robotics and its Social Impacts (ARSO)*. July 2016, pp. 304–309. DOI: 10.1109/ARSO.2016.7736300.

[106] Meng, C. "A New Design of Two-Fingered Catheter Operating Robot for Vascular Interventional Surgery". In: 2 (July 2017), pp. 1–8.

[107] Arai, F., Fujimura, R., Fukuda, T., et al. "New catheter driving method using linear stepping mechanism for intravascular neurosurgery". In: *Proceedings 2002 IEEE International Conference on Robotics and Automation (Cat. No.02CH37292)*. Vol. 3. May 2002, 2944–2949 vol.3. DOI: 10.1109/ROBOT.2002.1013679.

[108] Guo, S., Guo, J., Shao, L., et al. "Performance evaluation of the novel grasper for a robotic catheter navigation system". In: *2014 IEEE International Conference on Information and Automation (ICIA)*. July 2014, pp. 339–344. DOI: 10.1109/ICInfA.2014.6932678.

[109] Guo, S., Qin, M., Xiao, N., et al. "High precise haptic device for the robotic catheter navigation system". In: *2016 IEEE International Conference on Mechatronics and Automation*. 2016, pp. 2524–2529.

[110] Guo, J., Guo, S., Shao, L., et al. "Design and performance evaluation of a novel robotic catheter system for vascular interventional surgery". In: *Microsystem Technologies* 22.9 (Sept. 2016), pp. 2167–2176. ISSN: 1432-1858. DOI: 10.1007/s00542-015-2659-4.

[111] He, C., Wang, S., and Zuo, S. "A linear stepping endovascular intervention robot with variable stiffness and force sensing". In: *International Journal of Computer Assisted Radiology and Surgery* 13.5 (May 2018), pp. 671–682. ISSN: 1861-6429. DOI: 10.1007/s11548-018-1722-x.

[112] Guo, J., Guo, S., Xiao, N., et al. "Characteristics evaluation of the novel robotic catheter system". In: *2011 IEEE International Conference on Robotics and Biomimetics*. Dec. 2011, pp. 258–262. DOI: 10.1109/ROBIO.2011.6181295.

[113] Bao, X., Guo, S., Xiao, N., et al. "Design and evaluation of a novel guidewire navigation robot". In: *2016 IEEE International Conference on Mechatronics and Automation*. Aug. 2016, pp. 431–436. DOI: 10.1109/ICMA.2016.7558602.

[114] Jayender, J., Azizian, M., and Patel, R. V. "Autonomous robot-assisted active catheter insertion using image guidance". In: *2007 IEEE/RSJ International Conference on Intelligent Robots and Systems*. Oct. 2007, pp. 889–894. DOI: 10.1109/IROS.2007.4399251.

[115] Yang, G.-Z., Cambias, J., Cleary, K., et al. "Medical robotics—Regulatory, ethical, and legal considerations for increasing levels of autonomy". In: *Science Robotics* 2.4 (2017). DOI: 10.1126/scirobotics.aam8638.

[116] Zakaria, N. A. C., Komeda, T., Low, C. Y., et al. "Development of foolproof catheter guide system based on mechatronic design". In: *Production Engineering* 7.1 (2013), pp. 81–90.
[117] Sankaran, N. K., Chembrammel, P., Siddiqui, A., et al. "Design and development of surgeon augmented endovascular robotic system". In: *IEEE Transactions on Biomedical Engineering* 65.11 (2018), pp. 2483–2493.
[118] Feng, Z.-Q., Bian, G.-B., Xie, X.-L., et al. "Design and evaluation of a bio-inspired robotic hand for percutaneous coronary intervention". In: *2015 IEEE International Conference on Robotics and Automation (ICRA)*. 2015.
[119] Tavallaei, M. A., Lavdas, M. K., Gelman, D., et al. "Magnetic resonance imaging compatible remote catheter navigation system with 3 degrees of freedom". In: *International Journal of Computer Assisted Radiology and Surgery* 11.8 (Aug. 2016), pp. 1537–1545. ISSN: 1861-6429.
[120] Thakur, Y., Bax, J. S., Holdsworth, D. W., et al. "Design and Performance Evaluation of a Remote Catheter Navigation System". In: *IEEE Transactions on Biomedical Engineering* 56.7 (July 2009), pp. 1901–1908. ISSN: 0018-9294. DOI: 10.1109/TBME.2009.2017203.
[121] Song, Y., Guo, S., Zhang, L., et al. "Haptic feedback in robot-assisted endovascular catheterization". In: *2017 IEEE International Conference on Mechatronics and Automation, ICMA 2017* (2017), pp. 404–409. ISSN: 18616429. DOI: 10.1109/ICMA.2017.8015851.
[122] Bian, G., Xie, X., Feng, Z., et al. "An enhanced dual-finger robotic Hand for Catheter manipulating in vascular intervention: A preliminary study". In: *2013 IEEE International Conference on Information and Automation, ICIA 2013* (2013), pp. 356–361.
[123] Guo, S., Qin, M., Xiao, N., et al. "High precise haptic device for the robotic catheter navigation system". In: *2016 IEEE International Conference on Mechatronics and Automation, IEEE ICMA 2016*. 2016. ISBN: 9781509023943. DOI: 10.1109/ICMA.2016.7558963.
[124] Wang, K., Chen, B., Lu, Q., et al. "Design and Performance Evaluation of Real-time Endovascular Interventional Surgical Robotic System with High Accuracy". In: *The International Journal of Medical Robotics and Computer Assisted Surgery* 14.5 (2018).
[125] Lee, K., Fu, K. C. D., Guo, Z., et al. "MR Safe Robotic Manipulator for MRI-Guided Intracardiac Catheterization". In: *IEEE/ASME Transactions on Mechatronics* 23.2 (2018), pp. 586–595. ISSN: 1941-014X. DOI: 10.1109/TMECH.2018.2801787.
[126] Hwang, J., Kim, J.-y., and Choi, H. "A review of magnetic actuation systems and magnetically actuated guidewire-and catheter-based microrobots for vascular interventions". In: *Intelligent Service Robotics* 13.1 (2020), pp. 1–14.
[127] Jolesz, F. A. and Blumenfeld, S. M. "Interventional use of magnetic resonance imaging". In: *Magn Reson Q* 10.2 (1994), pp. 85–96. ISSN: 0899-9422 (Print) 0899-9422.
[128] Lufkin, R. B. "Interventional MR imaging". In: *Radiology* 197.1 (1995), pp. 16–18.
[129] Rogers, T., Ratnayaka, K., and Lederman, R. J. "MRI Catheterization in Cardiopulmonary Disease". In: *Chest* 145.1 (2014), pp. 30–36. ISSN: 0012-3692.
[130] Rogers, T. and Lederman, R. J. "Interventional CMR: Clinical applications and future directions". In: *Current Cardiology Reports* 17.5 (2015), p. 31. ISSN: 1523-3782.
[131] Hanson, L. G. "Is quantum mechanics necessary for understanding magnetic resonance?" In: *Concepts in Magnetic Resonance Part A* 32A.5 (2008), pp. 329–340. ISSN: 1546-6086. DOI: 10.1002/cmr.a.20123.
[132] Brown, R. W., N.Cheng, Y., Haacke, E. M., et al. *Magnetic Resonance Imaging: Physical Principles and Sequence Design, Second Edition*. Hoboken, NJ, USA: John Wiley & Sons, Inc., 2014. ISBN: 9780323393782 0323393780 9780323463010 0323463010.
[133] Plewes, D. B. and Kucharczyk, W. "Physics of MRI: A primer". In: *Journal of Magnetic Resonance Imaging* 35.5 (2012), pp. 1038–1054. ISSN: 1053-1807. DOI: 10.1002/jmri.23642.
[134] Elster, A. D. and Burdette, J. H. *Questions & Answers in Magnetic Resonance Imaging (2nd Edition)*. Maryland Heights, MO, US: Mosby, 2001. ISBN: 9780323393782 0323393780 9780323463010 0323463010.
[135] Pushparajah, K., Chubb, H., and Razavi, R. "MR-guided Cardiac Interventions". In: *Topics in Magnetic Resonance Imaging* 27.3 (2018), pp. 115–128. ISSN: 1536-1004.
[136] Mahnken, A. H., Wilhelm, K. E., and Ricke, J. *CT- and MR-Guided Interventions in Radiology*. Berlin, Germany: Springer, 2013.

[137] Thomsen, H. S. "Nephrogenic systemic fibrosis: a serious late adverse reaction to gadodiamide". In: *European Radiology* 16.12 (2006), pp. 2619–2621. ISSN: 1432-1084.

[138] Kos, S., Huegli, R., Hofmann, E., et al. "MR-compatible polyetheretherketone-based guide wire assisting MR-guided stenting of iliac and supraaortic arteries in swine: Feasibility study". In: *Minimally Invasive Therapy & Allied Technologies* 18.3 (2009), pp. 181–188. ISSN: 1364-5706.

[139] Rogers, T., Ratnayaka, K., Karmarkar, P., et al. "Real-Time Magnetic Resonance Imaging Guidance Improves the Diagnostic Yield of Endomyocardial Biopsy". In: *JACC: Basic to Translational Science* 1.5 (2016), pp. 376–383. ISSN: 2452-302X. DOI: https://doi.org/10.1016/j.jacbts.2016.05.007.

[140] Mukherjee, R. K., Chubb, H., Roujol, S., et al. "Advances in Real-Time MRI–Guided Electrophysiology". In: *Current Cardiovascular Imaging Reports* 12.2 (2019), p. 6. ISSN: 1941-9074.

[141] Yildirim, K. D., Basar, B., Campbell-Washburn, A. E., et al. "A cardiovascular magnetic resonance (CMR) safe metal braided catheter design for interventional CMR at 1.5T: freedom from radiofrequency induced heating and preserved mechanical performance". In: *Journal of Cardiovascular Magnetic Resonance* 21.1 (2019), p. 16. ISSN: 1532-429X.

[142] Abu Hazeem, A. A., Dori, Y., Whitehead, K. K., et al. "X-ray magnetic resonance fusion modality may reduce radiation exposure and contrast dose in diagnostic cardiac catheterization of congenital heart disease". In: *Catheterization and Cardiovascular Interventions* 84.5 (2014), pp. 795–800. ISSN: 1522-1946. DOI: 10.1002/ccd.25473.

[143] *ASTM F2503-20 Standard Practice for Marking Medical Devices and Other Items for Safety in the Magnetic Resonance Environment*. Report. 2020.

[144] Elmar, S., Alexander, R., Tobias, S., et al. "Magnetic Resonance-Guided Coronary Artery Stent Placement in a Swine Model". In: *Circulation* 105.7 (Feb. 2002), pp. 874–879. DOI: 10.1161/hc0702.104165.

[145] Elgort, D. R., Hillenbrand, C. M., Zhang, S., et al. "Image-guided and -monitored renal artery stenting using only MRI". In: *Journal of Magnetic Resonance Imaging* 23.5 (2006), pp. 619–627. DOI: 10.1002/jmri.20554. eprint: https://onlinelibrary.wiley.com/doi/pdf/10.1002/jmri.20554.

[146] Buecker, A., Spuentrup, E., Schmitz-Rode, T., et al. "Use of a Nonmetallic Guide Wire for Magnetic Resonance-Guided Coronary Artery Catheterization". In: *Investigative Radiology* 39.11 (2004). ISSN: 0020-9996.

[147] Mekle, R., Hofmann, E., Scheffler, K., et al. "A polymer-based MR-compatible guidewire: A study to explore new prospects for interventional peripheral magnetic resonance angiography (ipMRA)". In: *J. Magn. Reson. Imaging* 23.2 (Feb. 2006), pp. 145–155. ISSN: 1053-1807. DOI: 10.1002/jmri.20486.

[148] Clogenson, H. C. M., Dankelman, J., and Dobbelsteen, J. J. van den. "Steerable Guidewire for Magnetic Resonance Guided Endovascular Interventions". In: *J. Med. Devices* 8.2 (Mar. 2014). ISSN: 1932-6181. DOI: 10.1115/1.4026560.

[149] Bakker, C. J., Smits, H. F., Bos, C., et al. "MR-guided balloon angioplasty: in vitro demonstration of the potential of MRI for guiding, monitoring, and evaluating endovascular interventions." eng. In: *Journal of magnetic resonance imaging : JMRI* 8 (1 Jan. 1998), pp. 245–50.

[150] Kos, S., Huegli, R., Hofmann, E., et al. "Feasibility of Real-Time Magnetic Resonance-Guided Angioplasty and Stenting of Renal Arteries in Vitro and in Swine, Using a New Polyetheretherketone-Based Magnetic Resonance-Compatible Guidewire". In: *Investigative Radiology* 44.4 (2009). ISSN: 0020-9996.

[151] Krueger, S., Schmitz, S., Weiss, S., et al. "An MR guidewire based on micropultruded fiber-reinforced material." eng. In: *Magnetic resonance in medicine* 60 (5 Nov. 2008), pp. 1190–6.

[152] Aphrodite, T., Krombach Gabriele, A., Nils, K., et al. "Magnetic Resonance-Guided Cardiac Interventions Using Magnetic Resonance-Compatible Devices". In: *Circulation: Cardiovascular Interventions* 3.6 (Dec. 2010), pp. 585–592. DOI: 10.1161/CIRCINTERVENTIONS.110.957209.

[153] Kos, S., Huegli, R., Hofmann, E., et al. "First Magnetic Resonance Imaging-Guided Aortic Stenting and Cava Filter Placement Using a Polyetheretherketone-Based Magnetic Resonance Imaging-Compatible Guidewire in Swine: Proof of Concept". In: *CardioVascular and Interventional Radiology* 32.3 (2009), pp. 514–521. ISSN: 1432-086X. DOI: 10.1007/s00270-008-9483-5.

[154] Krämer, N. A., Krüger, S., Schmitz, S., et al. "Preclinical Evaluation of a Novel Fiber Compound MR Guidewire In Vivo". In: *Investigative Radiology* 44.7 (2009). ISSN: 0020-9996.

[155] Pushparajah, K., Tzifa, A., and Razavi, R. "Cardiac MRI catheterization: A 10-year single institution experience and review". In: *Interventional Cardiology* 6 (June 2014), pp. 335–346. DOI: 10.2217/ica.14.28.

[156] Basar, B., Rogers, T., Ratnayaka, K., et al. "Segmented nitinol guidewires with stiffness-matched connectors for cardiovascular magnetic resonance catheterization: preserved mechanical performance and freedom from heating". In: *Journal of Cardiovascular Magnetic Resonance* 17.1 (2015), p. 105. ISSN: 1532-429X. DOI: 10.1186/s12968-015-0210-5.

[157] Klaus Düring, J. G. P. US20170232158A1. 2017.

[158] Massmann, A., Buecker, A., and Schneider, G. K. "Glass-Fiber-based MR-safe Guidewire for MR Imaging-guided Endovascular Interventions: In Vitro and Preclinical in Vivo Feasibility Study". In: *Radiology* 284.2 (Mar. 2017), pp. 541–551. ISSN: 0033-8419. DOI: 10.1148/radiol.2017152742.

[159] Wolska-Krawczyk, M., Rube, M. A., Immel, E., et al. "Heating and safety of a new MR-compatible guidewire prototype versus a standard nitinol guidewire". In: *Radiological Physics and Technology* 7.1 (2014), pp. 95–101. ISSN: 1865-0341.

[160] Wolska-Krawczyk, M. "Evaluation of liver tumor perfusion by intraarterial transcatheter magnetic resonance angiography during transarterial chemoembolization in patients with hepatocellular carcinoma: Preclinical instrument validation in vascular models and clinical study". PhD Thesis. Saarland University, Germany, 2013.

[161] Brecher, C., Emonts, M., Brack, A., et al. "New concepts and materials for the manufacturing of MR-compatible guide wires". English. In: *Biomedical Engineering / Biomedizinische Technik* 59.2 (), pp. 147–151. DOI: 10.1515/bmt-2013-0027.

[162] Van de Velde, K. and Kiekens, P. "Thermoplastic pultrusion of natural fibre reinforced composites". In: *Composite Structures* 54.2 (2001), pp. 355–360. ISSN: 0263-8223. DOI: 10.1016/S0263-8223(01)00110-6.

[163] Veeram Reddy, S. R., Arar, Y., Zahr, R. A., et al. "Invasive cardiovascular magnetic resonance (iCMR) for diagnostic right and left heart catheterization using an MR-conditional guidewire and passive visualization in congenital heart disease". In: *Journal of Cardiovascular Magnetic Resonance* 22.1 (2020), p. 20. ISSN: 1532-429X. DOI: 10.1186/s12968-020-0605-9.

[164] Rube, M. A., Fernandez-Gutierrez, F., Cox, B. F., et al. "Preclinical feasibility of a technology framework for MRI-guided iliac angioplasty". In: *International Journal of Computer Assisted Radiology and Surgery* 10.5 (2015), pp. 637–650. ISSN: 1861-6429. DOI: 10.1007/s11548-014-1102-0.

[165] Bietenbeck, M., Florian, A., Chatzantonis, G., et al. "Introduction of a CMR-conditional cardiac phantom simulating cardiac anatomy and function and enabling training of interventional CMR procedures". In: *Scientific Reports* 9.1 (2019), p. 19852. ISSN: 2045-2322. DOI: 10.1038/s41598-019-56506-8.

[166] Williams, J. C. "Evaluating EPflex MRline Guidewire for Endovascular Interventions Guided by MRI at 3T vs. X-ray Fluoroscopy". MSc Thesis. University of California, USA, 2019.

[167] Knight, D. S., Kotecha, T., Martinez-Naharro, A., et al. "Cardiovascular magnetic resonance-guided right heart catheterization in a conventional CMR environment - predictors of procedure success and duration in pulmonary artery hypertension". In: *Journal of Cardiovascular Magnetic Resonance* 21.1 (2019), p. 57. ISSN: 1532-429X. DOI: 10.1186/s12968-019-0569-9.

[168] Settecase, F., Martin, A. J., Lillaney, P., et al. "Magnetic Resonance–Guided Passive Catheter Tracking for Endovascular Therapy". In: *Magnetic Resonance Imaging Clinics of North America* 23.4 (2015), pp. 591–605. ISSN: 1064-9689. DOI: https://doi.org/10.1016/j.mric.2015.05.003.

[169] Schenck, J. F. "The role of magnetic susceptibility in magnetic resonance imaging: MRI magnetic compatibility of the first and second kinds". In: *Medical Physics* 23.6 (1996), pp. 815–850. ISSN: 0094-2405. DOI: 10.1118/1.597854.

[170] Li, X., Perotti, L. E., Martinez, J. A., et al. "Real-time 3T MRI-guided cardiovascular catheterization in a porcine model using a glass-fiber epoxy-based guidewire". In: *PLOS ONE* 15.2 (Feb. 2020), e0229711. DOI: 10.1371/journal.pone.0229711.

[171] Carey, J., Fahim, A., and Munro, M. "Design of braided composite cardiovascular catheters based on required axial, flexural, and torsional rigidities". In: *Journal of Biomedical Materials Research Part B: Applied Biomaterials* 70B.1 (2004), pp. 73–81. ISSN: 1552-4973.

[172] Sonmez, M., Saikus, C. E., Bell, J. A., et al. "MRI active guidewire with an embedded temperature probe and providing a distinct tip signal to enhance clinical safety". In: *Journal of Cardiovascular Magnetic Resonance* 14.1 (2012), p. 38. ISSN: 1532-429X. DOI: 10.1186/1532-429X-14-38.
[173] Bell, J. A., Saikus, C. E., Ratnayaka, K., et al. "A deflectable guiding catheter for real-time MRI-guided interventions". In: *Journal of Magnetic Resonance Imaging* 35.4 (2012), pp. 908–915. ISSN: 1053-1807.
[174] Yao, W., Schaeffter, T., Seneviratne, L., et al. "Developing a Magnetic Resonance-Compatible Catheter for Cardiac Catheterization". In: *Journal of Medical Devices* 6.4 (2012). ISSN: 1932-6181.
[175] Clogenson, H. C. M., Lith, J. Y. van, Dankelman, J., et al. "Multi-selective catheter for MR-guided endovascular interventions". In: *Medical Engineering & Physics* 37 (2015), pp. 623–630. ISSN: 1350-4533.
[176] Dupont, P. E., Lock, J., Itkowitz, B., et al. "Design and Control of Concentric-Tube Robots". In: *IEEE Transactions on Robotics* 26.2 (2010), pp. 209–225. ISSN: 1941-0468.
[177] Ataollahi, A., Karim, R., Fallah, A. S., et al. "Three-Degree-of-Freedom MR-Compatible Multisegment Cardiac Catheter Steering Mechanism". In: *IEEE Transactions on Biomedical Engineering* 63.11 (2016), pp. 2425–2435. ISSN: 1558-2531.
[178] Ataollahi, A., Althoefer, K., Schaeffter, T. R., et al. US9675781B2. 2017.
[179] Haga, Y., Muyari, Y., Mineta, T., et al. "Small diameter hydraulic active bending catheter using laser processed super elastic alloy and silicone rubber tube". In: *Proceedings of 2005 IEEE/EMBS Special Topic Conference on Microtechnology in Medicine and Biology*. Oahu, HI, USA, 2005, pp. 245–248.
[180] Ikuta, K., Ichikawa, H., Suzuki, K., et al. "Safety active catheter with multi-segments driven by innovative hydro-pressure micro actuators". In: *Proceedings of The Sixteenth Annual International Conference on Micro Electro Mechanical Systems*. Kyoto, Japan, 2003, pp. 130–135.
[181] Ikuta, K., Ichikawa, H., Suzuki, K., et al. "Multi-degree of freedom hydraulic pressure driven safety active catheter". In: *Proceedings of 2006 IEEE International Conference on Robotics and Automation (ICRA)*. Orlando, FL, USA, 2006, pp. 4161–4166.
[182] Ikuta, K., Matsuda, Y., Yajima, D., et al. "Precise bending angle control of hydraulic active catheter by pressure pulse drive". In: *Proceedings of 2010 IEEE International Conference on Robotics and Automation (ICRA)*. Anchorage, Alaska, 2010, pp. 5588–5593.
[183] De Boer, J. US2007060997A1. 2007/03/15/ 2007.
[184] Johansen, J. A., Yee, C. E., and Neet, J. M. US6951554B2. 2005.
[185] Skerven, G. J. US20100168665A1. 2010.
[186] Caenazzo, A. and Althoefer, K. "Hypertonic Saline Solution for Signal Transmission and Steering in MRI-Guided Intravascular Catheterisation". In: *Proceedings of 2018 TAROS: 19th Annual Conference Towards Autonomous Robotic Systems*. Bristol, UK, 2018, pp. 284–290.
[187] Muller, L., Saeed, M., Wilson, M. W., et al. "Remote control catheter navigation: options for guidance under MRI". In: *J Cardiovasc Magn Reson* 14 (2012), p. 33. ISSN: 1097-6647.
[188] Roberts, T., Hassenzahl, W., Hetts, S., et al. "Remote control of catheter tip deflection: An opportunity for interventional MRI". In: *Magnetic Resonance in Medicine* 48.6 (2002), pp. 1091–1095. ISSN: 0740-3194. DOI: 10.1002/mrm.10325.
[189] Bernhardt, A., Wilson, M. W., Settecase, F., et al. "Steerable Catheter Microcoils for Interventional MRI: Reducing Resistive Heating". In: *Academic Radiology* 18.3 (2011), pp. 270–276. ISSN: 1076-6332. DOI: https://doi.org/10.1016/j.acra.2010.09.010.
[190] Malba, V., Maxwell, R., Evans, L. B., et al. "Laser-Lathe Lithography—a Novel Method for Manufacturing Nuclear Magnetic Resonance Microcoils". In: *Biomedical Microdevices* 5.1 (2003), pp. 21–27. ISSN: 1572-8781. DOI: 10.1023/A:1024407231584.
[191] Moftakhar, P., Lillaney, P., Losey, A. D., et al. "New-Generation Laser-lithographed Dual-Axis Magnetically Assisted Remote-controlled Endovascular Catheter for Interventional MR Imaging: In Vitro Multiplanar Navigation at 1.5 T and 3 T versus X-ray Fluoroscopy". In: *Radiology* 277.3 (2015), pp. 842–852. DOI: 10.1148/radiol.2015142648.

[192] Lillaney, P. V., Yang, J. K., Losey, A. D., et al. "Endovascular MR-guided Renal Embolization by Using a Magnetically Assisted Remote-controlled Catheter System". In: *Radiology* 281.1 (2016), pp. 219–228. DOI: 10.1148/radiol.2016152036.

[193] Liu, T., Lombard Poirot, N., Greigarn, T., et al. "Design of a Magnetic Resonance Imaging Guided Magnetically Actuated Steerable Catheter". In: *Journal of Medical Devices* 11.2 (2017). ISSN: 1932-6181. DOI: 10.1115/1.4036095.

[194] Greigarn, T., Poirot, N. L., Xu, X., et al. "Jacobian-Based Task-Space Motion Planning for MRI-Actuated Continuum Robots". In: *IEEE Robotics and Automation Letters* 4.1 (2019), pp. 145–152. ISSN: 2377-3766. DOI: 10.1109/LRA.2018.2881987.

[195] Mathieu, J. B., Soulez, G., Beaudoin, G., et al. "Abstract No. 76: Steering and Tracking of Magnetic Catheters Using MRI Systems". In: *Journal of Vascular and Interventional Radiology* 19.2 (2008), S31. ISSN: 1051-0443. DOI: 10.1016/j.jvir.2007.12.085.

[196] Lalande, V., Gosselin, F. P., and Martel, S. "Catheter steering using a Magnetic Resonance Imaging system". In: *Proceedings of 2010 Annual International Conference of the IEEE Engineering in Medicine and Biology*. Buenos Aires, Argentina, 2010, pp. 1874–1877.

[197] Gosselin, F. P., Lalande, V., and Martel, S. "Characterization of the deflections of a catheter steered using a magnetic resonance imaging system". In: *Medical Physics* 38.9 (2011), pp. 4994–5002. ISSN: 0094-2405. DOI: 10.1118/1.3622599.

[198] Zhang, K., Krafft, A. J., Umathum, R., et al. "Real-time MR navigation and localization of an intravascular catheter with ferromagnetic components". In: *Magnetic Resonance Materials in Physics, Biology and Medicine* 23.3 (2010), pp. 153–163. ISSN: 1352-8661. DOI: 10.1007/s10334-010-0214-y.

[199] Erin, O., Boyvat, M., Tiryaki, M. E., et al. "Magnetic Resonance Imaging System–Driven Medical Robotics". In: *Advanced Intelligent Systems* 2.2 (2020), p. 1900110. ISSN: 2640-4567. DOI: 10.1002/aisy.201900110.

[200] Erin, O., Makower, J., Tsai, L., et al. "Design and Actuation of a Magnetic Millirobot under a Constant Unidirectional Magentic Field". In: *IEEE International Conference on Robotics and Automation (ICRA)*. 2017. ISBN: 9788578110796. arXiv: arXiv:1011.1669v3.

[201] Erin, O., Gilbert, H. B., Tabak, A. F., et al. "Elevation and Azimuth Rotational Actuation of an Untethered Millirobot by MRI Gradient Coils". In: *IEEE Transactions on Robotics* 35.6 (2019), pp. 1323–1337. ISSN: 19410468. DOI: 10.1109/TRO.2019.2934712.

[202] Folio, D., Dahmen, C., Wortmann, T., et al. "MRI magnetic signature imaging, tracking and navigation for targeted micro/nano-capsule therapeutics". In: *IEEE International Conference on Intelligent Robots and Systems* (2011), pp. 1297–1303. DOI: 10.1109/IROS.2011.6048651.

[203] Dahmen, C., Belharet, K., Folio, D., et al. "MRI-based dynamic tracking of an untethered ferromagnetic microcapsule navigating in liquid". In: *International Journal of Optomechatronics* 10.2 (2016), pp. 73–96. ISSN: 15599620. DOI: 10.1080/15599612.2016.1166305.

[204] Mathieu, J. B. and Martel, S. "Steering of aggregating magnetic microparticles using propulsion gradients coils in an MRI scanner". In: *Magnetic Resonance in Medicine* 63.5 (2010), pp. 1336–1345. ISSN: 15222594. DOI: 10.1002/mrm.22279.

[205] Pouponneau, P., Leroux, J. C., and Martel, S. "Magnetic nanoparticles encapsulated into biodegradable microparticles steered with an upgraded magnetic resonance imaging system for tumor chemoembolization". In: *Biomaterials* 30.31 (2009), pp. 6327–6332. ISSN: 01429612. DOI: 10.1016/j.biomaterials.2009.08.005.

[206] Bigot, A., Tremblay, C., Soulez, G., et al. "Magnetic resonance navigation of a bead inside a three-bifurcation PMMA phantom using an imaging gradient coil insert". In: *IEEE Transactions on Robotics* 30.3 (2014), pp. 719–727. ISSN: 15523098. DOI: 10.1109/TRO.2014.2300591.

[207] Latulippe, M. and Martel, S. "Dipole field navigation for targeted drug delivery". In: *Proceedings of the IEEE RAS and EMBS International Conference on Biomedical Robotics and Biomechatronics* 1 (2014), pp. 320–325. ISSN: 21551774. DOI: 10.1109/biorob.2014.6913796.

[208] Latulippe, M. and Martel, S. "Dipole field navigation: Theory and proof of concept". In: *IEEE Transactions on Robotics* 31.6 (2015), pp. 1353–1363. ISSN: 15523098. DOI: 10.1109/TRO.2015.2489518.

[209] Becker, A. T., Felfoul, O., and Dupont, P. E. "Toward tissue penetration by MRI-powered millirobots using a self-assembled Gauss gun". In: *Proceedings - IEEE International Conference on Robotics and Automation* 2015-June.June (2015), pp. 1184–1189. ISSN: 10504729. DOI: 10.1109/ICRA.2015.7139341.

[210] Wilkes, K. E., Liaw, P. K., and Wilkes, K. E. "The fatigue behavior of shape-memory alloys". In: *JOM* 52.10 (2000), pp. 45–51. ISSN: 1543-1851. DOI: 10.1007/s11837-000-0083-3.

[211] Lim, G., Park, K., Sugihara, M., et al. "Future of active catheters". In: *Sensors and Actuators A: Physical* 56.1 (1996), pp. 113–121. ISSN: 0924-4247. DOI: https://doi.org/10.1016/0924-4247(96)01279-4.

[212] Fu, Y., Li, X., Wang, S., et al. "Research on the axis shape of an active catheter". In: *The International Journal of Medical Robotics and Computer Assisted Surgery* 4.1 (2008), pp. 69–76. ISSN: 1478-5951. DOI: 10.1002/rcs.172.

[213] Chang, J. K., Chung, S., Lee, Y., et al. "Development of endovascular microtools". In: *Journal of Micromechanics and Microengineering* 12.6 (2002), pp. 824–831. ISSN: 0960-1317. DOI: 10.1088/0960-1317/12/6/313.

[214] Mineta, T., Mitsui, T., Watanabe, Y., et al. "Batch fabricated flat meandering shape memory alloy actuator for active catheter". In: *Sensors and Actuators A: Physical* 88.2 (2001), pp. 112–120. ISSN: 0924-4247. DOI: https://doi.org/10.1016/S0924-4247(00)00510-0.

[215] Namazu, T., Komatsubara, M., Nagasawa, H., et al. "Titanium-Nickel Shape Memory Alloy Spring Actuator for Forward-Looking Active Catheter". In: *Journal of Metallurgy* 2011 (2011), p. 685429. ISSN: 1687-9465. DOI: 10.1155/2011/685429.

[216] Fukuda, T., Shuxiang, G., Kosuge, K., et al. "Micro active catheter system with multi degrees of freedom". In: *Proceedings of 1994 IEEE International Conference on Robotics and Automation (ICRA)*. San Diego, CA, USA, 1994, pp. 2290–2295.

[217] Takizawa, H., Tosaka, H., Ohta, R., et al. "Development of a microfine active bending catheter equipped with MIF tactile sensors". In: *In Proceedings of The Twelfth IEEE International Conference on Micro Electro Mechanical Systems*. Orlando, FL, USA, 1999, pp. 412–417.

[218] Crews, J. H. and Buckner, G. D. "Design optimization of a shape memory alloy–actuated robotic catheter". In: *Journal of Intelligent Material Systems and Structures* 23.5 (2012), pp. 545–562. DOI: 10.1177/1045389x12436738.

[219] Couture, T. and Szewczyk, J. "Design and Experimental Validation of an Active Catheter for Endovascular Navigation". In: *Journal of Medical Devices* 12.1 (2017). ISSN: 1932-6181. DOI: 10.1115/1.4038334.

[220] Wiest, J. H. and Buckner, G. D. "Path optimization and control of a shape memory alloy actuated catheter for endocardial radiofrequency ablation". In: *Robotics and Autonomous Systems* 65 (2015), pp. 88–97. ISSN: 0921-8890. DOI: https://doi.org/10.1016/j.robot.2014.10.019.

[221] Langelaar, M. and Keulen, F. van. "Modeling of a Shape Memory Alloy Active Catheter". In: *Proceedings of The 45th AIAA/ASME/ASCE/AHS/ASC Structures, Structural Dynamics & Materials Conference*. Palm Springs, California, 2004.

[222] Langelaar, M., Yoon, G. H., Gurav, S., et al. "Modeling and design of shape memory alloy actuators". In: *Proceedings of the 6th International Conference on Thermal, Mechanial and Multi-Physics Simulation and Experiments in Micro-Electronics and Micro-Systems*. 2005, pp. 626–633. DOI: 10.1109/ESIME.2005.1502878.

[223] Langelaar, M. and Keulen, F. van. "Gradient-based Design Optimization of Shape Memory Alloy Active Catheters". In: *48th AIAA/ASME/ASCE/AHS/ASC Structures, Structural Dynamics, and Materials Conference*. Structures, Structural Dynamics, and Materials and Co-located Conferences. American Institute of Aeronautics and Astronautics, 2007. DOI: doi:10.2514/6.2007-174410.2514/6.2007-1744.

[224] Tung, A. T., Park, B.-H., Liang, D. H., et al. "Laser-machined shape memory alloy sensors for position feedback in active catheters". In: *Sensors and Actuators A: Physical* 147.1 (2008), pp. 83–92. ISSN: 0924-4247. DOI: https://doi.org/10.1016/j.sna.2008.03.024.

[225] Sheng, J., Wang, X., Dickfeld, T. L., et al. "Towards the Development of a Steerable and MRI-Compatible Cardiac Catheter for Atrial Fibrillation Treatment". In: *IEEE Robotics and Automation Letters* 3.4 (2018), pp. 4038–4045. ISSN: 2377-3766. DOI: 10.1109/LRA.2018.2861011.

[226] Runciman, M., Darzi, A., and Mylonas, G. P. "Soft Robotics in Minimally Invasive Surgery". In: *Soft Robotics* 6.4 (2019), pp. 423–443. ISSN: 2169-5172. DOI: 10.1089/soro.2018.0136.

[227] De Greef, A., Lambert, P., and Delchambre, A. "Towards flexible medical instruments: Review of flexible fluidic actuators". In: *Precision Engineering* 33.4 (2009), pp. 311–321. ISSN: 0141-6359. DOI: https://doi.org/10.1016/j.precisioneng.2008.10.004.

[228] Bertetto, A. M. and Ruggiu, M. "A Novel Fluidic Bellows Manipulator". In: *Journal of Robotics and Mechatronics* 16.6 (2004), pp. 604–612. DOI: 10.20965/jrm.2004.p0604.

[229] Mohd Jani, J., Leary, M., Subic, A., et al. "A review of shape memory alloy research, applications and opportunities". In: *Materials & Design (1980-2015)* 56 (2014), pp. 1078–1113. ISSN: 0261-3069. DOI: https://doi.org/10.1016/j.matdes.2013.11.084.

[230] Selden, B., Cho, K., and Asada, H. H. "Segmented shape memory alloy actuators using hysteresis loop control". In: *Smart Materials and Structures* 15.2 (2006), pp. 642–652. ISSN: 0964-1726 1361-665X. DOI: 10.1088/0964-1726/15/2/048.

[231] The International Commission on Non-Ionizing Radiation, P. "AMENDMENT TO THE ICNIRP "STATEMENT ON MEDICAL MAGNETIC RESONANCE (MR) PROCEDURES: PROTECTION OF PATIENTS"". In: *Health Physics* 97.3 (2009). ISSN: 0017-9078.

[232] Shellock, F. G. "Radiofrequency Energy-Induced Heating During MR Procedures: A Review". In: *Journal of Magnetic Resonance Imaging* 12.1 (2000), pp. 30–36. ISSN: 1053-1807. DOI: 10.1002/1522-2586(200007)12:1⟨30::AID-JMRI4⟩3.0.CO;2-S.

[233] Le, H. M., Do, T. N., and Phee, S. J. "A survey on actuators-driven surgical robots". In: *Sensors and Actuators A: Physical* 247 (2016), pp. 323–354. ISSN: 0924-4247. DOI: https://doi.org/10.1016/j.sna.2016.06.010.

[234] Duerk, J. L., Wong, E. Y., and Lewin, J. S. "A brief review of hardware for catheter tracking in magnetic resonance imaging". In: *Magnetic Resonance Materials in Physics, Biology and Medicine* 13.3 (2001), p. 199. ISSN: 1352-8661. DOI: 10.1007/BF02678597.

[235] Maes, R. M., Lewin, J. S., Duerk, J. L., et al. "Combined use of the intravascular blood-pool agent, gadomer, and carbon dioxide: A novel type of double-contrast magnetic resonance angiography (MRA)". In: *Journal of Magnetic Resonance Imaging* 21.5 (2005), pp. 645–649. ISSN: 1053-1807. DOI: 10.1002/jmri.20304.

[236] Miquel, M. E., Hegde, S., Muthurangu, V., et al. "Visualization and tracking of an inflatable balloon catheter using SSFP in a flow phantom and in the heart and great vessels of patients". In: *Magnetic Resonance in Medicine* 51.5 (2004), pp. 988–995. ISSN: 0740-3194. DOI: 10.1002/mrm.20041.

[237] Omary, R. A., Unal, O., Koscielski, D. S., et al. "Real-Time MR Imaging-guided Passive Catheter Tracking with Use of Gadolinium-filled Catheters". In: *Journal of Vascular and Interventional Radiology* 11.8 (2000), pp. 1079–1085. ISSN: 1051-0443. DOI: https://doi.org/10.1016/S1051-0443(07)61343-8.

[238] Unal, O., Korosec, F. R., Frayne, R., et al. "A rapid 2D time-resolved variable-rate k-space sampling MR technique for passive catheter tracking during endovascular procedures". In: *Magnetic Resonance in Medicine* 40.3 (1998), pp. 356–362. ISSN: 0740-3194. DOI: 10.1002/mrm.1910400304.

[239] Unal, O., Li, J., Cheng, W., et al. "MR-visible coatings for endovascular device visualization". In: *Journal of Magnetic Resonance Imaging* 23.5 (2006), pp. 763–769. ISSN: 1053-1807. DOI: 10.1002/jmri.20555.

[240] Tirotta, I., Dichiarante, V., Pigliacelli, C., et al. "19F Magnetic Resonance Imaging (MRI): From Design of Materials to Clinical Applications". In: *Chemical Reviews* 115.2 (2015), pp. 1106–1129. ISSN: 0009-2665. DOI: 10.1021/cr500286d.

[241] Kozerke, S., Hegde, S., Schaeffter, T., et al. "Catheter tracking and visualization using 19F nuclear magnetic resonance". In: *Magnetic Resonance in Medicine* 52.3 (2004), pp. 693–697. ISSN: 0740-3194. DOI: 10.1002/mrm.20202.

[242] Magnusson, P., Johansson, E., Månsson, S., et al. "Passive catheter tracking during interventional MRI using hyperpolarized 13C". In: *Magnetic Resonance in Medicine* 57.6 (2007), pp. 1140–1147. ISSN: 0740-3194. DOI: 10.1002/mrm.21239.

[243] Kuehne, T., Weiss, S., Brinkert, F., et al. "Catheter Visualization with Resonant Markers at MR Imaging–guided Deployment of Endovascular Stents in Swine". In: *Radiology* 233.3 (2004), pp. 774–780. ISSN: 0033-8419. DOI: 10.1148/radiol.2333031710.

[244] Felfoul, O., Mathieu, J., Beaudoin, G., et al. "In Vivo MR-Tracking Based on Magnetic Signature Selective Excitation". In: *IEEE Transactions on Medical Imaging* 27.1 (2008), pp. 28–35. ISSN: 1558-254X. DOI: 10.1109/TMI.2007.897375.

[245] Weiss, S., Kuehne, T., Brinkert, F., et al. "In vivo safe catheter visualization and slice tracking using an optically detunable resonant marker". In: *Magnetic Resonance in Medicine* 52.4 (2004), pp. 860–868. ISSN: 0740-3194. DOI: 10.1002/mrm.20214.

[246] Glowinski, A., Adam, G., Bücker, A., et al. "Catheter visualization using locally induced, actively controlled field inhomogeneities". In: *Magnetic Resonance in Medicine* 38.2 (1997), pp. 253–258. ISSN: 0740-3194. DOI: 10.1002/mrm.1910380214.

[247] Xiao, X., Huang, Z., Rube, M. A., et al. "Investigation of active tracking for robotic arm assisted magnetic resonance guided focused ultrasound ablation". In: *The International Journal of Medical Robotics and Computer Assisted Surgery* 13.3 (2017), e1768. ISSN: 1478-5951. DOI: 10.1002/rcs.1768.

[248] Bartels, L. W. and Bakker, C. J. G. "Endovascular interventional magnetic resonance imaging". In: *Physics in Medicine and Biology* 48.14 (2003), R37–R64. ISSN: 0031-9155 1361-6560. DOI: 10.1088/0031-9155/48/14/201.

[249] Serfaty, J.-M., Yang, X., Aksit, P., et al. "Toward MRI-guided coronary catheterization: Visualization of guiding catheters, guidewires, and anatomy in real time". In: *J. Magn. Reson. Imaging* 12.4 (Oct. 2000), pp. 590–594. ISSN: 1053-1807. DOI: 10.1002/1522-2586(200010)12:4⟨590::AID-JMRI11⟩3.0.CO;2-3.

[250] Kocaturk, O., Kim, A. H., Saikus, C. E., et al. "Active two-channel 0.035 guidewire for interventional cardiovascular MRI". In: *J. Magn. Reson. Imaging* 30.2 (Aug. 2009), pp. 461–465. ISSN: 1053-1807. DOI: 10.1002/jmri.21844.

[251] Alipour, A., Meyer, E. S., Dumoulin, C. L., et al. "MRI Conditional Actively Tracked Metallic Electrophysiology Catheters and Guidewires With Miniature Tethered Radio-Frequency Traps: Theory, Design, and Validation". In: *IEEE Transactions on Biomedical Engineering* 67.6 (2020), pp. 1616–1627. ISSN: 1558-2531. DOI: 10.1109/TBME.2019.2941460.

[252] Krueger Julia, J., Ewert, P., Yilmaz, S., et al. "Magnetic Resonance Imaging–Guided Balloon Angioplasty of Coarctation of the Aorta". In: *Circulation* 113.8 (2006), pp. 1093–1100. DOI: 10.1161/CIRCULATIONAHA.105.578112.

[253] Tzifa, A., Krombach Gabriele, A., Krämer, N., et al. "Magnetic Resonance–Guided Cardiac Interventions Using Magnetic Resonance–Compatible Devices". In: *Circulation: Cardiovascular Interventions* 3.6 (2010), pp. 585–592. DOI: 10.1161/CIRCINTERVENTIONS.110.957209.

[254] Clogenson, H. and Dobbelsteen, J. "Catheters and Guidewires for Interventional MRI: Are We There Yet?" In: *Imaging in Medicine* 8 (2016), pp. 4–8.

[255] Mukherjee, R. K., Costa, C. M., Neji, R., et al. "Evaluation of a real-time magnetic resonance imaging-guided electrophysiology system for structural and electrophysiological ventricular tachycardia substrate assessment". In: *Europace* 21.9 (Sept. 2019), pp. 1432–1441. ISSN: 1099-5129. DOI: 10.1093/europace/euz165.

[256] Abdelaziz, M. E. M. K., Kundrat, D., Pupillo, M., et al. "Toward a Versatile Robotic Platform for Fluoroscopy and MRI-Guided Endovascular Interventions: A Pre-Clinical Study". In: *Proceedings of 2019 IEEE/RSJ International Conference on Intelligent Robots and Systems (IROS)*. Macau, China, 2019, pp. 5411–5418. DOI: 10.1109/IROS40897.2019.8968237.

[257] Saliba, W., Cummings, J. E., Oh, S., et al. "Novel robotic catheter remote control system: feasibility and safety of transseptal puncture and endocardial catheter navigation". In: *J. Cardiovasc. Electrophysiol.* 17.10 (Oct. 2006), pp. 1102–1105.

[258] Khan, E. M., Frumkin, W., Ng, G. A., et al. "First experience with a novel robotic remote catheter system: Amigo™ mapping trial". In: *Journal of Interventional Cardiac Electrophysiology* 37.2 (Aug. 2013), pp. 121–129. ISSN: 1572-8595.

[259] Bismuth, J., Duran, C., Stankovic, M., et al. "A first-in-man study of the role of flexible robotics in overcoming navigation challenges in the iliofemoral arteries". In: *Journal of Vascular Surgery* 57.2, Supplement (2013), 14S–19S. ISSN: 0741-5214.

[260] Granada, J. F., Delgado, J. A., Uribe, M. P., et al. "First-in-Human Evaluation of a Novel Robotic-Assisted Coronary Angioplasty System". In: *JACC: Cardiovascular Interventions* 4.4 (2011), pp. 460–465. ISSN: 1936-8798.

[261] Muller, L., Saeed, M., Wilson, M. W., et al. "Remote control catheter navigation: options for guidance under MRI". In: *Journal of Cardiovascular Magnetic Resonance* 14.1 (June 2012), p. 33. ISSN: 1532-429X.

[262] Whiting, N., Hu, J., Shah, J. V., et al. "Real-Time MRI-Guided Catheter Tracking Using Hyperpolarized Silicon Particles". In: *Scientific Reports* 5 (Aug. 2015).

[263] Payne, C. J., Rafii-Tari, H., and Yang, G. "A force feedback system for endovascular catheterisation". In: *2012 IEEE/RSJ International Conference on Intelligent Robots and Systems*. Oct. 2012, pp. 1298–1304. DOI: 10.1109/IROS.2012.6386149.

[264] Rafii-Tari, H., Payne, C. J., Bicknell, C., et al. "Objective Assessment of Endovascular Navigation Skills with Force Sensing". In: *Annals of Biomedical Engineering* 45.5 (May 2017), pp. 1315–1327. ISSN: 1573-9686.

[265] Moore, W. S. "Arterial Access; Guidewires, Catheters, and Sheaths; and Balloon Angioplasty Catheters". In: *Vascular and Endovascular Surgery: A Comprehensive Review*. Saunders, 2013. Chap. 17, pp. 306–309.

[266] Dagnino, G., Liu, J., Abdelaziz, M. E. M. K., et al. "Haptic Feedback and Dynamic Active Constraints for Robot-Assisted Endovascular Catheterization". In: *2018 IEEE/RSJ International Conference on Intelligent Robots and Systems (IROS)*. 2018, pp. 1770–1775.

[267] Kundrat, D., Dagnino, G., Kwok, T. M. Y., et al. "An MR-Safe Endovascular Robotic Platform: Design, Control, and Ex-Vivo Evaluation". In: *IEEE Transactions on Biomedical Engineering* (2021), pp. 1–1. DOI: 10.1109/TBME.2021.3065146.

[268] Groenhuis, V. and Stramigioli, S. "Rapid Prototyping High-Performance MR Safe Pneumatic Stepper Motors". In: *IEEE/ASME Transactions on Mechatronics* 23.4 (2018), pp. 1843–1853.

[269] Abdelaziz, M. E. M. K., Kundrat, D., Pupillo, M., et al. "Toward a Versatile Robotic Platform for Fluoroscopy and MRI-Guided Endovascular Interventions: A Pre-Clinical Study". In: *2019 IEEE/RSJ International Conference on Intelligent Robots and Systems (IROS)*. 2019, pp. 5411–5418.

[270] Groenhuis, V. and Stramigioli, S. "Laser-Cutting Pneumatics". In: *IEEE/ASME Transactions on Mechatronics* 21.3 (2016), pp. 1604–1611.

[271] Hart, S. G. and Staveland, L. E. "Development of NASA-TLX (Task Load Index): Results of Empirical and Theoretical Research". In: *Human Mental Workload*. Ed. by Hancock, P. A. and Meshkati, N. Vol. 52. Advances in Psychology. North-Holland, 1988, pp. 139–183.

[272] Lewis, J. R. "AN AFTER-SCENARIO QUESTIONNAIRE FOR USABILITY STUDIES: PSYCHOMETRIC EVALUATION OVER THREE TRIALS". In: *SIGCHI Bull.* 23.4 (Oct. 1991), p. 79. ISSN: 0736-6906.

[273] Schumann, S., Thelen, B., Ballestra, S., et al. "X-ray image calibration and its application to clinical orthopedics". In: *Medical Engineering & Physics* 36.7 (2014), pp. 968–974. ISSN: 1350-4533.

[274] MacFarland, T. *Two-Way Analysis of Variance: Statistical Tests and Graphics Using R*. SpringerBriefs in Statistics. Springer New York, 2011. ISBN: 9781461421337.

[275] Rafii-Tari, H., Payne, C. J., Bicknell, C., et al. "Objective Assessment of Endovascular Navigation Skills with Force Sensing". en. In: *Annals of Biomedical Engineering* 45.5 (May 2017), pp. 1315–1327. ISSN: 0090-6964, 1573-9686. DOI: 10.1007/s10439-017-1791-y.

[276] Ho, P., Cheng, S. W. K., Wu, P. M., et al. "Ionizing radiation absorption of vascular surgeons during endovascular procedures." In: *Journal of vascular surgery* 46 3 (2007), pp. 455–9.

[277] Kirkwood, M. L., Guild, J. B., Arbique, G. M., et al. "Surgeon radiation dose during complex endovascular procedures". In: *Journal of Vascular Surgery* 62.2 (2015), pp. 457–463. ISSN: 0741-5214. DOI: https://doi.org/10.1016/j.jvs.2015.02.050.

[278] Duran, C., Lumsden, A. B., and Bismuth, J. "A randomized, controlled animal trial demonstrating the feasibility and safety of the Magellan™ endovascular robotic system". eng. In: *Annals of Vascular Surgery* 28.2 (Feb. 2014), pp. 470–478. ISSN: 1615-5947. DOI: 10.1016/j.avsg.2013.07.010.

[279] *S.-L. Lee, M. Constantinescu, W. Chi, G.-Z. Yang, "Devices for Endovascular Interventions: technical advances and translational challenges" (White paper, National Institute for Health Research and Clinical Research Network, UK, White Paper)*. Report. 2017.

[280] Kazmer, D. O., Grosskopf, C. M., Rondeau, D., et al. "Design and Evaluation of General Purpose, Barrier, and Multichannel Plasticating Extrusion Screws". In: *Polymer Engineering & Science* 60.4 (2020), pp. 752–764.
[281] Jin, G.-B., Wang, M.-J., Zhao, D.-Y., et al. "Design and experiments of extrusion die for polypropylene five-lumen micro tube". In: *Journal of Materials Processing Technology* 214.1 (2014), pp. 50–59.
[282] Papanastasiou, T. C., Kiriakidis, D. G., and Nikoleris, T. G. "Extrudate swelling: Physics, models, and computations". In: (1995).
[283] Mehrjerdi, A. K., Bashir, T., and Skrifvars, M. "Melt rheology and extrudate swell properties of talc filled polyethylene compounds". In: *Heliyon* 6.5 (2020), e04060.
[284] Hart, S. D., Maskaly, G. R., Temelkuran, B., et al. "External reflection from omnidirectional dielectric mirror fibers". In: *Science* 296.5567 (2002), pp. 510–513.
[285] Temelkuran, B., Hart, S. D., Benoit, G., et al. "Wavelength-scalable hollow optical fibres with large photonic bandgaps for CO 2 laser transmission". In: *Nature* 420.6916 (2002), pp. 650–653.
[286] Bayindir, M., Sorin, F., Abouraddy, A. F., et al. "Metal–insulator–semiconductor optoelectronic fibres". In: *Nature* 431.7010 (2004), pp. 826–829.
[287] Canales, A., Jia, X., Froriep, U. P., et al. "Multifunctional fibers for simultaneous optical, electrical and chemical interrogation of neural circuits in vivo". In: *Nature biotechnology* 33.3 (2015), pp. 277–284.
[288] Qu, Y., Nguyen-Dang, T., Page, A. G., et al. "Superelastic multimaterial electronic and photonic fibers and devices via thermal drawing". In: *Advanced Materials* 30.27 (2018), p. 1707251.
[289] Khudiyev, T., Clayton, J., Levy, E., et al. "Electrostrictive microelectromechanical fibres and textiles". In: *Nature communications* 8.1 (2017), pp. 1–7.
[290] Kanik, M., Orguc, S., Varnavides, G., et al. "Strain-programmable fiber-based artificial muscle". In: *Science* 365.6449 (2019), pp. 145–150.
[291] Loke, G., Yuan, R., Rein, M., et al. "Structured multimaterial filaments for 3D printing of optoelectronics". In: *Nature communications* 10.1 (2019), pp. 1–10.
[292] Zhang, T., Li, K., Zhang, J., et al. "High-performance, flexible, and ultralong crystalline thermoelectric fibers". In: *Nano Energy* 41 (2017), pp. 35–42.
[293] Yan, W., Dong, C., Xiang, Y., et al. "Thermally drawn advanced functional fibers: New frontier of flexible electronics". In: *Materials Today* (2020).
[294] Yan, W., Page, A., Nguyen-Dang, T., et al. "Advanced multimaterial electronic and optoelectronic fibers and textiles". In: *Advanced materials* 31.1 (2019), p. 1802348.
[295] Temelkuran, B., Hart, S. D., Benoit, G., et al. "Wavelength-scalable hollow optical fibres with large photonic bandgaps for CO 2 laser transmission". In: *Nature* 420.6916 (2002), pp. 650–653.
[296] Lu, C., Park, S., Richner, T. J., et al. "Flexible and stretchable nanowire-coated fibers for optoelectronic probing of spinal cord circuits". In: *Science advances* 3.3 (2017), e1600955.
[297] Talataisong, W., Ismaeel, R., Marques, T. H., et al. "Mid-IR Hollow-core microstructured fiber drawn from a 3D printed PETG preform". In: *Scientific reports* 8.1 (2018), pp. 1–8.
[298] Cook, K., Canning, J., Leon-Saval, S., et al. "Air-structured optical fiber drawn from a 3D-printed preform". In: *Optics letters* 40.17 (2015), pp. 3966–3969.
[299] Yaman, M., Khudiyev, T., Ozgur, E., et al. "Arrays of indefinitely long uniform nanowires and nanotubes". In: *Nature materials* 10.7 (2011), pp. 494–501.
[300] Brilland, L., Smektala, F., Renversez, G., et al. "Fabrication of complex structures of holey fibers in chalcogenide glass". In: *Optics Express* 14.3 (2006), pp. 1280–1285.
[301] Désévédavy, F., Renversez, G., Brilland, L., et al. "Small-core chalcogenide microstructured fibers for the infrared". In: *Applied Optics* 47.32 (2008), pp. 6014–6021.
[302] Sorin, F. "Multimaterial Multifunctional Fiber Devices". Thesis. 2008.
[303] Bogusky, J. D. and Romo, E. Patent US9844412B2. 2017.
[304] Barlow, A., Ramskov-Hansen, J., and Payne, D. "Birefringence and polarization mode-dispersion in spun single-mode fibers". In: *Applied Optics* 20.17 (1981), pp. 2962–2968.
[305] Russell, P. S. J., Beravat, R., and Wong, G. "Helically twisted photonic crystal fibres". In: *Philosophical Transactions of the Royal Society A: Mathematical, Physical and Engineering Sciences* 375.2087 (2017), p. 20150440.

[306] Jiang, S., Patel, D. C., Kim, J., et al. "Spatially expandable fiber-based probes as a multifunctional deep brain interface". In: *Nature communications* 11.1 (2020), pp. 1–14.
[307] Del Rosso, S. "Micro-scale Hybrid Fibres for Low Cost Polymer Armours". Thesis. 2014.
[308] Lee, S. M. *Handbook of composite reinforcements*. John Wiley & Sons, 1992.
[309] Brunnschweiler, D. "Braids and braiding". In: *Journal of the Textile Institute proceedings* 44.9 (1953), P666–P686.
[310] Jelınek, F., Arkenbout, E. A., Henselmans, P. W., et al. "Classification of joints used in steerable instruments for minimally invasive surgery—A review of the state of the art". In: *Journal of Medical Devices* 9.1 (2015).
[311] Linß, S., Henning, S., and Zentner, L. "Modeling and design of flexure hinge-based compliant mechanisms". In: *Kinematics-Analysis and Applications*. IntechOpen, 2019.
[312] Henning, S., Linß, S., and Zentner, L. "detasFLEX–A computational design tool for the analysis of various notch flexure hinges based on non-linear modeling". In: *Mechanical Sciences* 9.2 (2018), pp. 389–404.
[313] Meijer, J., Du, K., Gillner, A., et al. "Laser machining by short and ultrashort pulses, state of the art and new opportunities in the age of the photons". In: *CIRP Annals* 51.2 (2002), pp. 531–550.
[314] Petkov, P. "Laser milling: surface integrity, removal strategies and process accuracy". PhD thesis. Cardiff University, 2011.
[315] Zhai, Z., Wang, F., and Duan, H. "Experimental study on 800 nm femtosecond laser cutting of polyamide in air". In: *Optik* 194 (2019), p. 163080.
[316] Boresi, A. P. and Schmidt, R. J. *Advanced mechanics of materials*. Wiley, 2018.
[317] Stenqvist, O., Curelaru, I., Linder, L., et al. "Stiffness of Central Venous Catheters". In: *Acta Anaesthesiologica Scandinavica* 27.2 (1983), pp. 153–157. ISSN: 13996576. DOI: 10.1111/j.1399-6576.1983.tb01926.x.
[318] Bersten, A. D. and Williams Phillips, D. R. "Central venous catheter stiffness and its relation to vascular perforation". In: *Anaesthesia and Intensive Care* 16.3 (1988), pp. 342–351. ISSN: 0310057X. DOI: 10.1177/0310057x8801600317.
[319] Carey, J., Emery, D., and McCracken, P. "Buckling test as a new approach to testing flexural rigidities of angiographic catheters". In: *Journal of Biomedical Materials Research Part B: Applied Biomaterials: An Official Journal of The Society for Biomaterials, The Japanese Society for Biomaterials, and The Australian Society for Biomaterials and the Korean Society for Biomaterials* 76.1 (2006), pp. 211–218.
[320] Shockey, R. L., McFarlin, W. A., and Blakemore, S. M. US5275151A. 1991.
[321] Morrill, R. J. US20120158021A1. 2011.
[322] Hunjan, K. S., Koblish, J. V., and Coen, T. P. US5656030A. 1997.
[323] Nguyen, F. US6522933B2. 2001.
[324] Romoscanu, A. I. US9095682B2. 2013.
[325] Bednarek, M. C., Wilkowske, E. J., Stehr, R. E., et al. US20190015633A1. 2018.
[326] Tegg, T. T. US20180207402A1. 2017.
[327] Selkee, T. V. US9861790B2. 2016.
[328] Kanemasa, K., Harata, S., Abe, Y., et al. US10363397B2. 2014.
[329] Rosenman, D., Kayser, D., Keleher, M., et al. US20150314106A1. 2015.
[330] Stahler, G. J., Romo, E., and Weiss, A. M. US8961533B2. 2015.
[331] Sargent, B., Butler, J., Seymour, K., et al. "An Origami-Based Medical Support System to Mitigate Flexible Shaft Buckling". In: *Journal of Mechanisms and Robotics* 12.4 (2020).
[332] Falb, P., Young, A., Bagley, K., et al. US20200324084A1. 2020.
[333] Stoianovici, D., Kim, C., Petrisor, D., et al. "MR safe robot, FDA clearance, safety and feasibility of prostate biopsy clinical trial". In: *IEEE/ASME Transactions on Mechatronics* 22.1 (2016), pp. 115–126.
[334] Qu, Y., Bartolomei, N., Lagier, M., et al. "Stretchable Optical Fibers via Thermal Drawing". In: *Specialty Optical Fibers*. Optical Society of America. 2018, SoW1H–3.

# Appendices

Chapter A

# Fibre Draw Tower




**Figure A.1:** The Hamlyn Centre's fibre draw tower. Note: The tower was assembled by yours truly in my second year of PhD.

Chapter B

# Catheter Samples' Dimensions

**Table B.1:** Segmented Thermally Drawing Catheter Samples

| Sample No. | Material | Lumen | Braiding | Outer Diameter (mm) | | Length (mm) | Experiments |
|---|---|---|---|---|---|---|---|
| | | | | min | max | | |
| 1-1 | PC | Straight | - | 2.02 | 2.09 | ∼50 | 1-1; 1-3; |
| 1-2 | | | | 1.98 | 2.05 | | 1-1; 1-2; |
| 1-3 | | | | 1.87 | 1.97 | | |
| 1-4 | | | | 1.92 | 2.00 | | |
| 1-5 | | | | 1.94 | 1.97 | | |
| 1-6 | | | | 1.94 | 2.03 | ∼160 | 2-1; |
| 1-7 | | | | 1.95 | 1.98 | | 3-1; |
| 2-1 | PC | Straight | Kevlar | 1.90 | 2.04 | ∼50 | 1-1; 1-3; |
| 2-2 | | | | 2.13 | 2.16 | | 1-1; 1-2; |
| 2-3 | | | | 2.09 | 2.10 | | |
| 2-4 | | | | 2.13 | 2.17 | | |
| 2-5 | | | | 2.14 | 2.18 | | |
| 2-6 | | | | 2.27 | 2.40 | ∼160 | 2-1; 3-1 |
| 3-1 | PC | Helical | - | 1.98 | 2.06 | ∼50 | 1-1; 1-3; |
| 3-2 | | | | 1.95 | 2.00 | | 1-1; 1-2; |
| 3-3 | | | | 1.96 | 2.05 | | |
| 3-4 | | | | 1.93 | 2.03 | | |
| 3-5 | | | | 1.92 | 2.02 | | |
| 3-6 | | | | 1.96 | 2.01 | ∼160 | 2-1; 3-1 |
| 3-7 | | | | 1.95 | 1.99 | | 3-1; |
| 4-1 | PC | Helical | Kevlar | 2.04 | 2.13 | ∼50 | 1-1; 1-3; |
| 4-2 | | | | 2.04 | 2.12 | | 1-1; 1-2; |
| 4-3 | | | | 2.04 | 2.13 | | |
| 4-4 | | | | 2.04 | 2.10 | | |
| 4-5 | | | | 2.04 | 2.11 | | |
| 4-6 | | | | 1.83 | 2.15 | ∼160 | 2-1; 3-1 |
| 5-1 | PEI | Straight | - | 2.19 | 2.27 | ∼50 | 1-1; 1-3; |
| 5-2 | | | | 2.13 | 2.18 | | 1-1; 1-2; |
| 5-3 | | | | 1.92 | 1.95 | | |
| 5-4 | | | | 1.95 | 1.98 | | |
| 5-5 | | | | 1.94 | 1.95 | | |
| 5-6 | | | | 2.14 | 2.38 | ∼160 | 2-1; 3-1 |
| 5-7 | | | | 2.18 | 2.27 | | 3-1; |
| 6-1 | PEI | Straight | - | 1.98 | 2.02 | ∼50 | 1-1; 1-3; |
| 6-2 | | | | 1.95 | 1.98 | | 1-1; 1-2; |
| 6-3 | | | | 2.06 | 2.11 | | |
| 6-4 | | | | 2.02 | 2.06 | | |
| 6-5 | | | | 2.06 | 2.12 | | |
| 6-6 | | | | 1.76 | 1.88 | ∼160 | 3-1; |
| 6-7 | | | | 1.88 | 1.93 | | 2-1; |
| 6-8 | | | | 2.18 | 2.38 | | 3-1; |

**Table B.2:** Segmented Commercial Catheter Samples

| Sample No. | Product Name | Outer-Diameter (mm) | | Length (mm) | Experiments |
|---|---|---|---|---|---|
| | | min | max | | |
| 7-1 | Magellan Guide Catheter | 1.95 | 2.02 | ∼50 | 1-1; 1-3; |
| 7-2 | | 2.95 | 3.11 | | 1-1; 1-2; |
| 7-3 | | 2.84 | 3.12 | | |
| 7-4 | | 2.96 | 3.09 | | |
| 7-5 | | 2.93 | 2.96 | | |
| 7-6 | | 3.10 | 3.16 | ∼160 | 2-1; 3-1 |
| 8-1 | Magellan Lead Catheter - Middle Part | 2.09 | 2.12 | ∼50 | 1-1; 1-3; |
| 8-2 | | 2.03 | 2.05 | | 1-1; 1-2; |
| 8-3 | | 2.01 | 2.02 | | |
| 8-4 | | 1.97 | 2.03 | | |
| 8-5 | | 2.07 | 2.13 | | |
| 8-6 | | 2.06 | 2.13 | ∼160 | 2-1; 3-1 |
| 9-1 | Magellan Lead Catheter - Proximal Part | 2.14 | 2.15 | ∼50 | 1-1; 1-3; |
| 9-2 | | 2.14 | 2.17 | | 1-1; 1-2; |
| 9-3 | | 2.16 | 2.18 | | |
| 9-4 | | 2.14 | 2.16 | | |
| 9-5 | | 2.14 | 2.17 | | |
| 9-6 | | 2.15 | 2.17 | ∼160 | 2-1; 3-1 |
| 10-1 | Magellan Lead Catheter - Distal Part | 1.93 | 1.94 | ∼50 | 1-1; 1-3; |
| 10-2 | | 1.94 | 2.02 | | 1-1; 1-2; |
| 10-3 | | 1.91 | 1.96 | | |
| 10-4 | | 1.92 | 1.98 | | |
| 10-5 | | 1.94 | 1.98 | | |
| 10-6 | | 2.15 | 2.16 | ∼160 | 2-1; 3-1 |
| 11-1 | Biosense Webster Ablation Catheter | 2.41 | 2.50 | ∼50 | 1-1; 1-3; |
| 11-2 | | 2.49 | 2.51 | | 1-1; 1-2; |
| 11-3 | | 2.42 | 2.45 | | |
| 11-4 | | 2.48 | 2.54 | | |
| 11-5 | | 2.44 | 2.52 | | |
| 11-6 | | 2.33 | 2.47 | ∼160 | 3-1; Kinked |
| 11-7 | | 2.42 | 2.45 | | 2-1; |
| 12-1 | Medtronic Guide Catheter 6Fr | 2.03 | 2.08 | ∼50 | 1-1; 1-3; |
| 12-2 | | 1.94 | 1.98 | | 1-1; 1-2; |
| 12-3 | | 2.25 | 2.32 | | |
| 12-4 | | 1.96 | 2.05 | | |
| 12-5 | | 1.98 | 2.05 | | |
| 12-6 | | 1.95 | 2.03 | ∼160 | 3-1; Kinked |
| 12-7 | | 1.93 | 2.05 | | 3-1; Kinked |
| 12-8 | | 2.25 | 2.32 | | 21 |
| 13-1 | Medtronic Guide Catheter 7Fr | 2.22 | 2.33 | ∼50 | 1-1; 1-3; |
| 13-2 | | 2.25 | 2.37 | | 1-1; 1-2; |
| 13-3 | | 2.25 | 2.31 | | |
| 13-4 | | 2.04 | 2.10 | | |
| 13-5 | | 2.32 | 2.46 | | |
| 13-6 | | 2.25 | 2.33 | ∼160 | 3-1; Kinked |
| 13-7 | | 2.31 | 2.36 | | 3-1; Kinked |
| 13-8 | | 2.28 | 2.35 | | 3-1; Kinked |
| 13-9 | | 2.28 | 2.34 | | 2-1; |

Chapter C

# Catheter Post-Processing

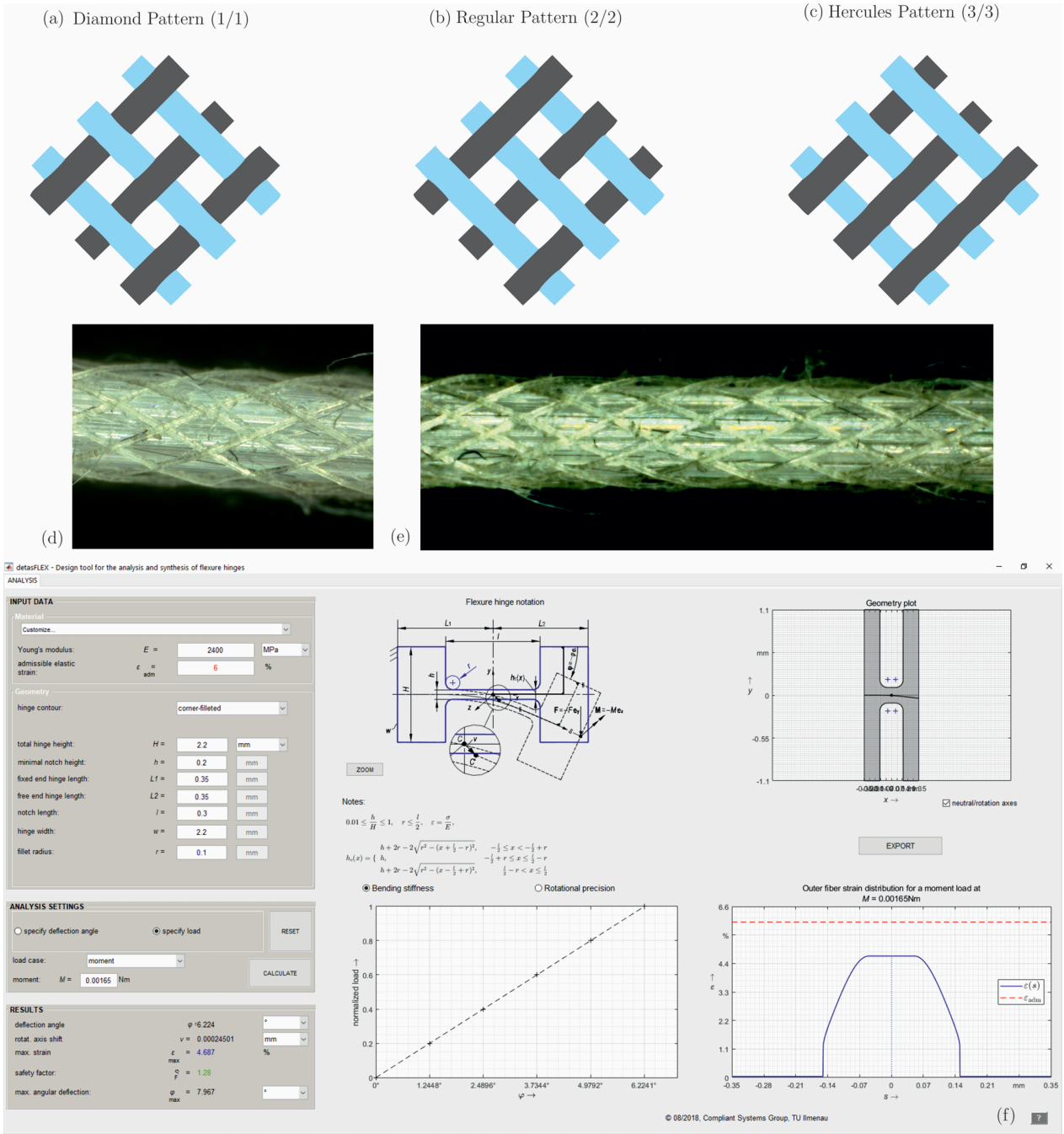



**Figure C.1:** (a-c) Examples of the three braiding patterns that can be produced using a Maypole braider: Diamond (1/1), Regular (2/2) and Hercules (3/3). (d-e) Optical images of overbraided thermally drawn polycarbonate fibres (multi-lumen tubing). The braiding pattern employed here is the diamond pattern. Liquid Crystal Polymer (LCP) 50$\mu$m monofilament yarns (Zeus Industrial Products Inc, Orangeburg, United States) is the braiding material. (f) Computational design tool (detasFLEX) developed by the Compliant Systems Group, TU Ilmenau [312].

Chapter D

# Steerability Results

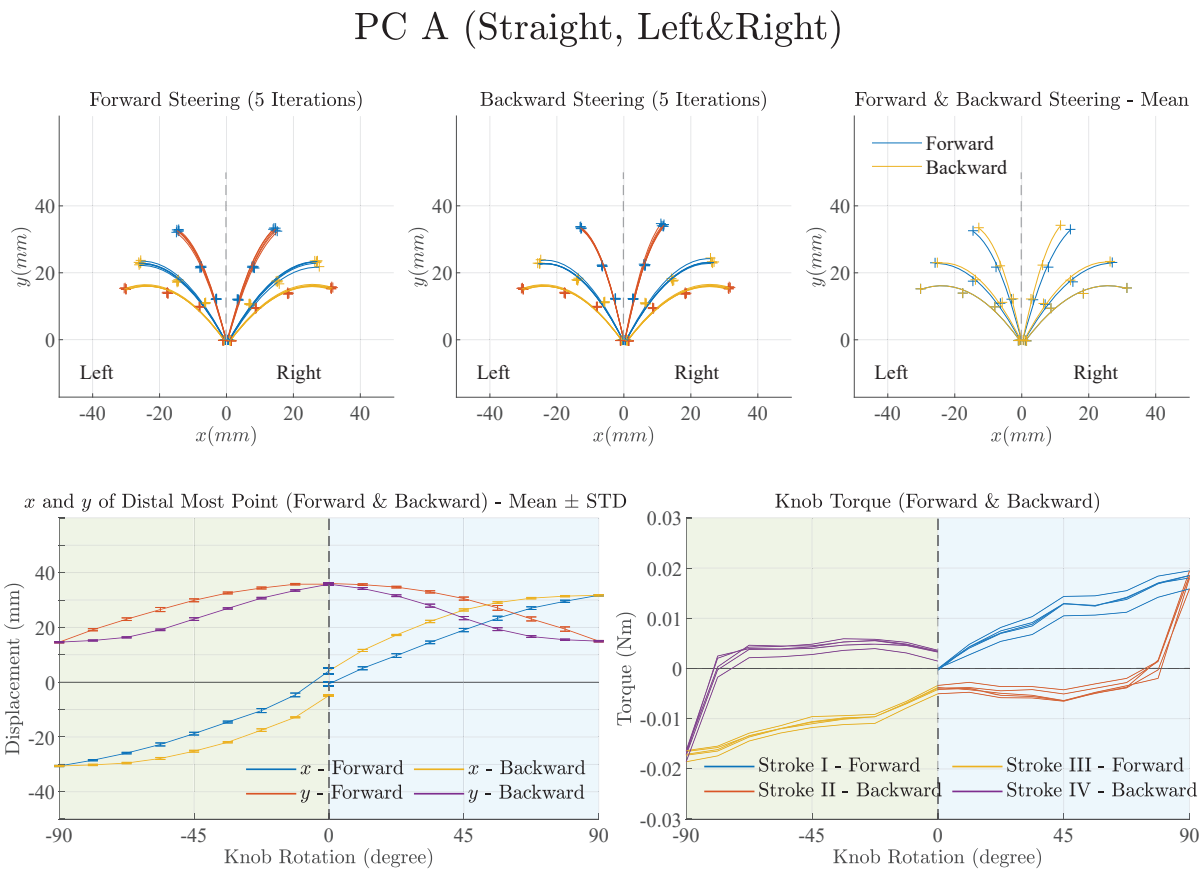



**Figure D.1:** Steerability results of the left and right steering of PC A catheter in a straight configuration: Top left & middle plots indicate the geometry of the catheter tip for each trial when the catheter is subjected to forward steering (Stroke I and Stroke III) and backward steering (Stroke II and Stroke IV) respectively. Top right plot is the average catheter tip positions over five trials. The difference between the catheter tip positions corresponding to the same knob angle position during the forward and backward steering indicate backlash. For better visualisation, only the catheter tip shapes for knob rotation angles $\pm 22.5°$, $\pm 56.25°$ and $\pm 90°$, are represented. Bottom left plot is the average $x$ and $y$ coordinates (with standard deviation) of the distal most point of the catheter over the course of the experiment. Bottom right plot is the torque applied to the knob during the experiments.

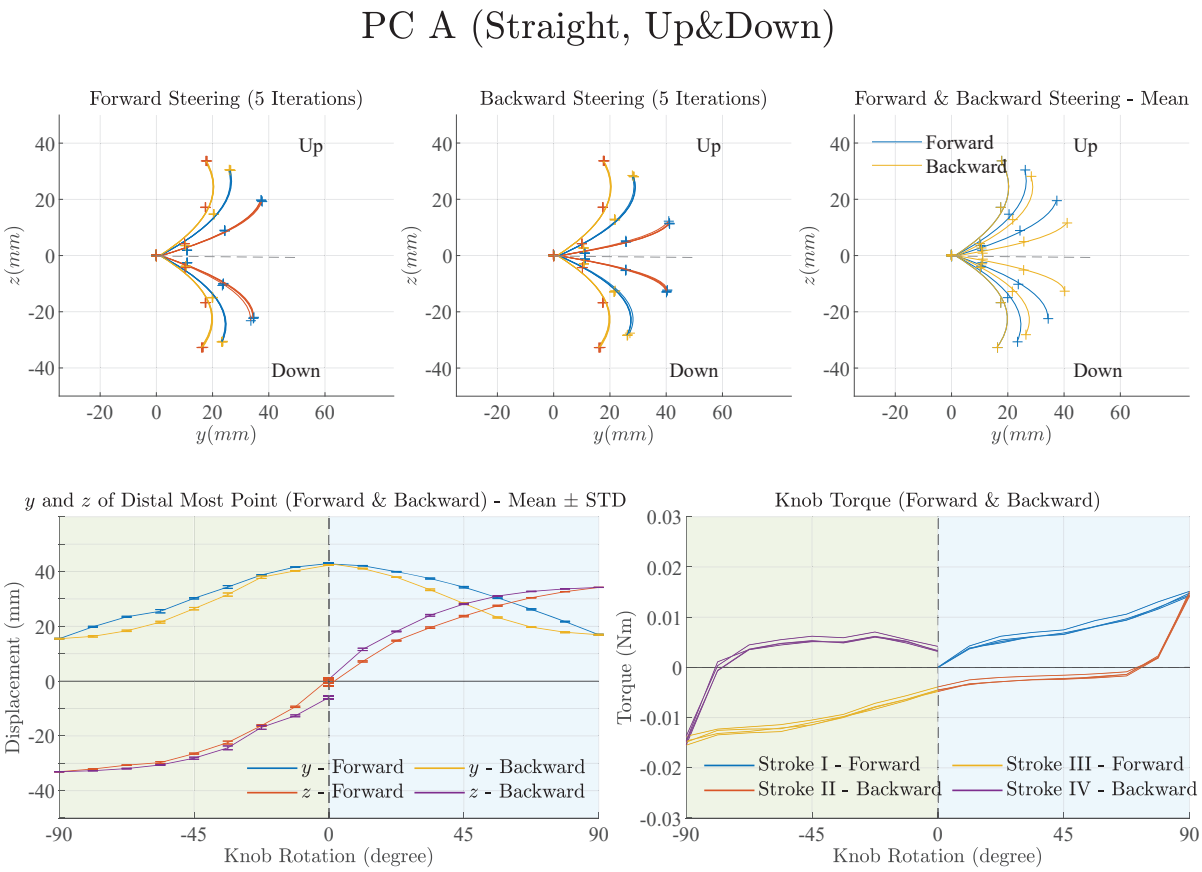



**Figure D.2:** Steerability results of the up and down steering of PC A catheter in a straight configuration: Top left & middle plots indicate the geometry of the catheter tip for each trial when the catheter is subjected to forward steering (Stroke I and Stroke III) and backward steering (Stroke II and Stroke IV) respectively. Top right plot is the average catheter tip positions over five trials. The difference between the catheter tip positions corresponding to the same knob angle position during the forward and backward steering indicate backlash. For better visualisation, only the catheter tip shapes for knob rotation angles $\pm 22.5°$, $\pm 56.25°$ and $\pm 90°$, are represented. Bottom left plot is the average $x$ and $y$ coordinates (with standard deviation) of the distal most point of the catheter over the course of the experiment. Bottom right plot is the torque applied to the knob during the experiments.

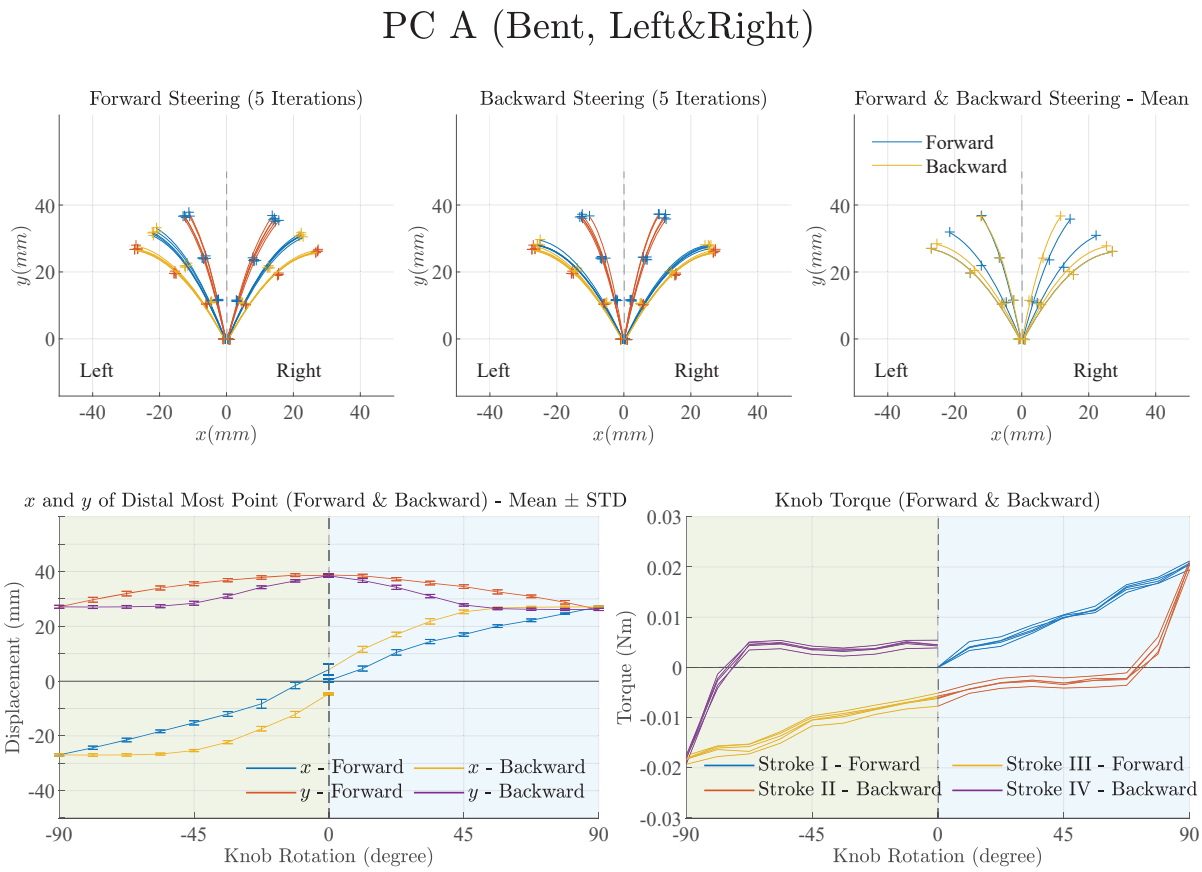



**Figure D.3:** Steerability results of the left and right steering of PC A catheter in a bent configuration: Top left & middle plots indicate the geometry of the catheter tip for each trial when the catheter is subjected to forward steering (Stroke I and Stroke III) and backward steering (Stroke II and Stroke IV) respectively. Top right plot is the average catheter tip positions over five trials. The difference between the catheter tip positions corresponding to the same knob angle position during the forward and backward steering indicate backlash. For better visualisation, only the catheter tip shapes for knob rotation angles $\pm 22.5°$, $\pm 56.25°$ and $\pm 90°$, are represented. Bottom left plot is the average $x$ and $y$ coordinates (with standard deviation) of the distal most point of the catheter over the course of the experiment. Bottom right plot is the torque applied to the knob during the experiments.

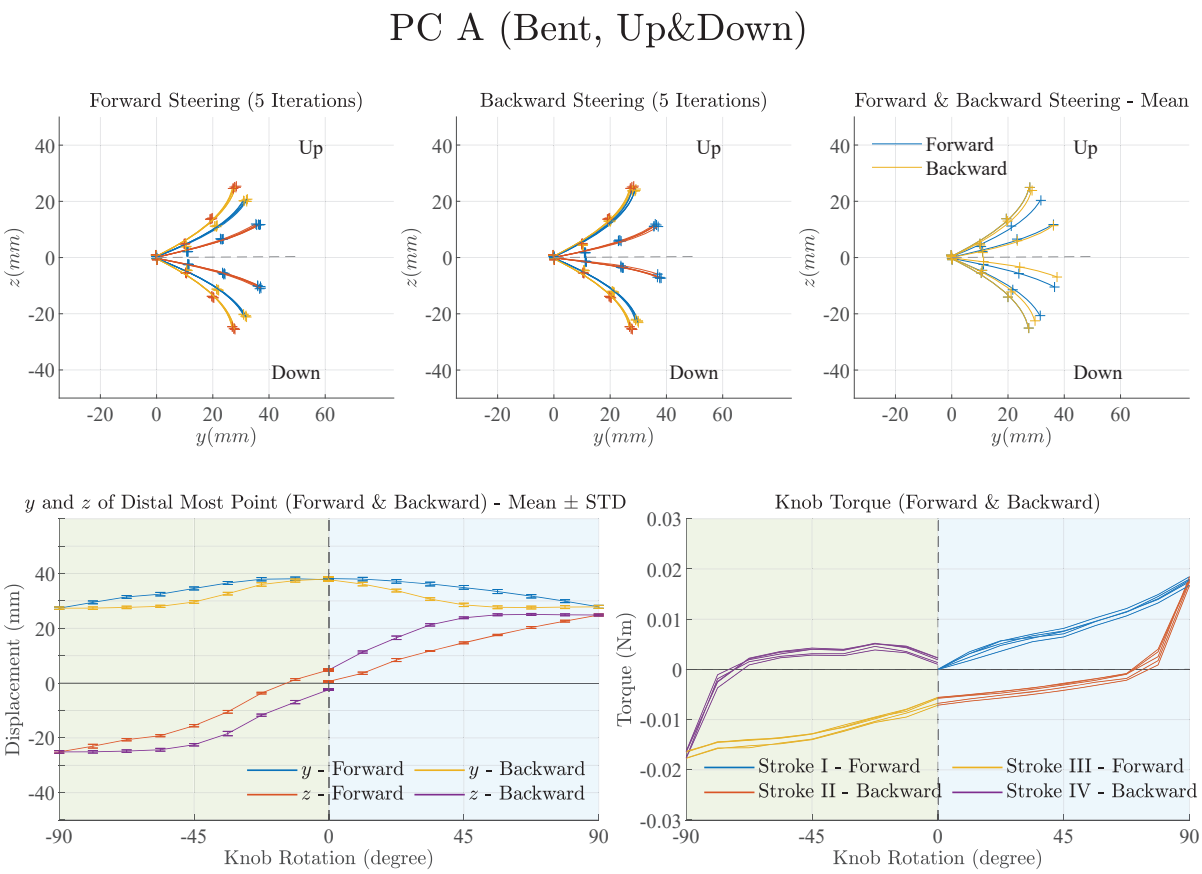



**Figure D.4:** Steerability results of the up and down steering of PC A catheter in a bent configuration: Top left & middle plots indicate the geometry of the catheter tip for each trial when the catheter is subjected to forward steering (Stroke I and Stroke III) and backward steering (Stroke II and Stroke IV) respectively. Top right plot is the average catheter tip positions over five trials. The difference between the catheter tip positions corresponding to the same knob angle position during the forward and backward steering indicate backlash. For better visualisation, only the catheter tip shapes for knob rotation angles $\pm 22.5°$, $\pm 56.25°$ and $\pm 90°$, are represented. Bottom left plot is the average $x$ and $y$ coordinates (with standard deviation) of the distal most point of the catheter over the course of the experiment. Bottom right plot is the torque applied to the knob during the experiments.

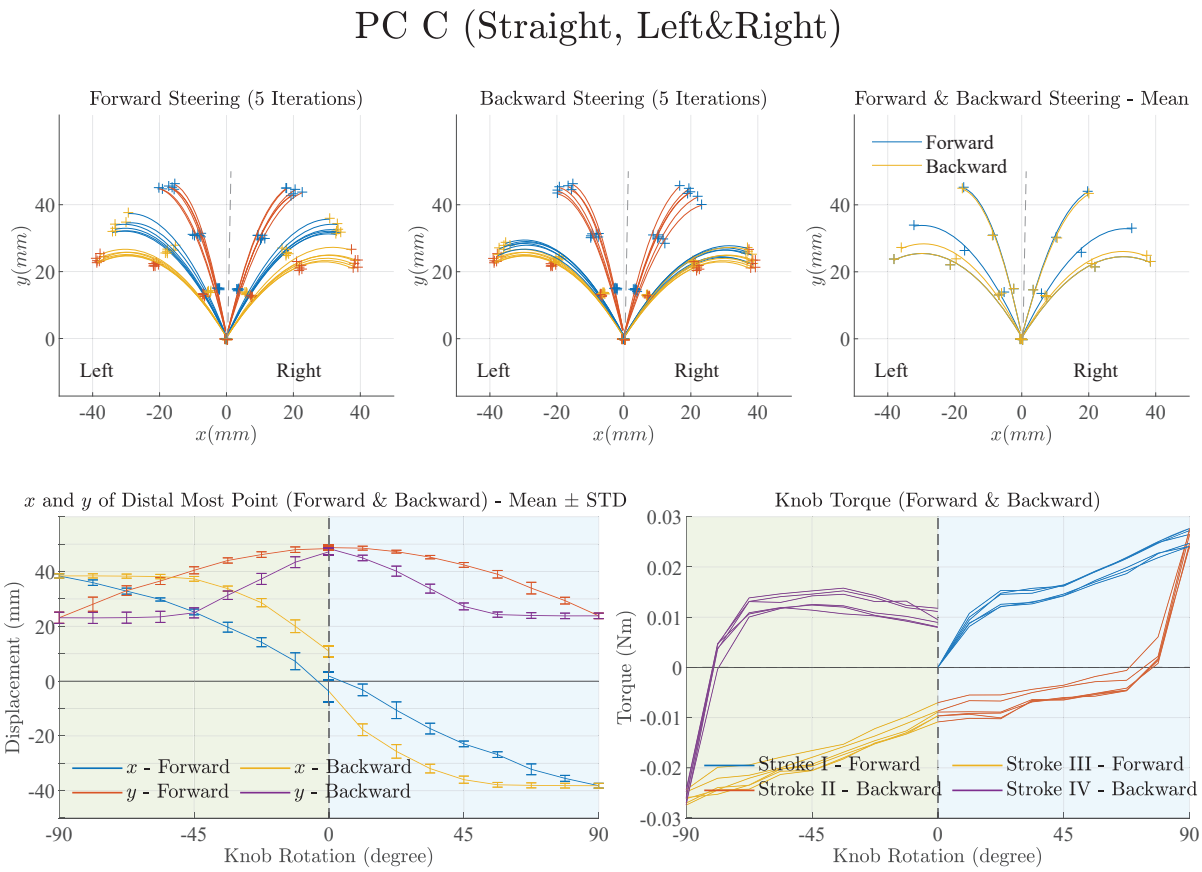



**Figure D.5:** Steerability results of the left and right steering of PC C catheter in a straight configuration: Top left & middle plots indicate the geometry of the catheter tip for each trial when the catheter is subjected to forward steering (Stroke I and Stroke III) and backward steering (Stroke II and Stroke IV) respectively. Top right plot is the average catheter tip positions over five trials. The difference between the catheter tip positions corresponding to the same knob angle position during the forward and backward steering indicate backlash. For better visualisation, only the catheter tip shapes for knob rotation angles $\pm 22.5°$, $\pm 56.25°$ and $\pm 90°$, are represented. Bottom left plot is the average $x$ and $y$ coordinates (with standard deviation) of the distal most point of the catheter over the course of the experiment. Bottom right plot is the torque applied to the knob during the experiments.

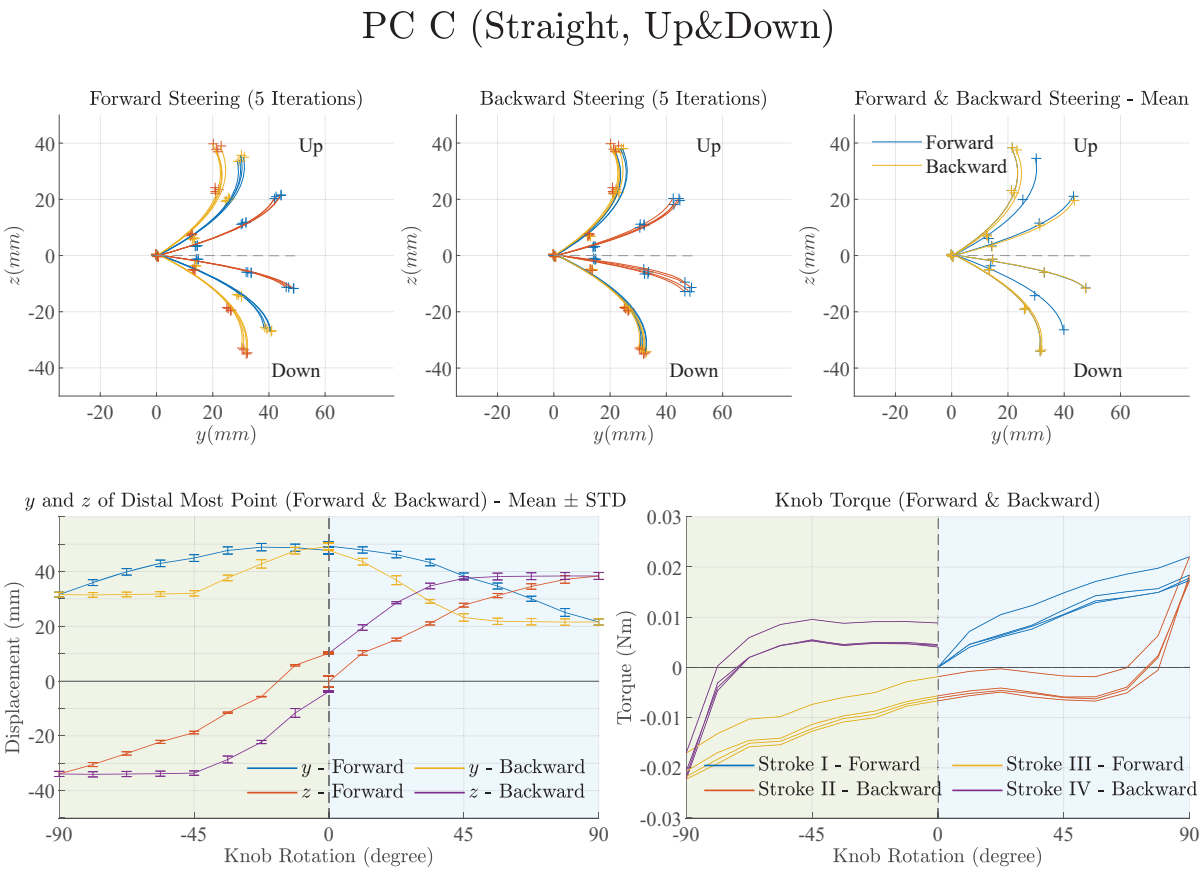



**Figure D.6:** Steerability results of the up and down steering of PC C catheter in a straight configuration: Top left & middle plots indicate the geometry of the catheter tip for each trial when the catheter is subjected to forward steering (Stroke I and Stroke III) and backward steering (Stroke II and Stroke IV) respectively. Top right plot is the average catheter tip positions over five trials. The difference between the catheter tip positions corresponding to the same knob angle position during the forward and backward steering indicate backlash. For better visualisation, only the catheter tip shapes for knob rotation angles $\pm 22.5°$, $\pm 56.25°$ and $\pm 90°$, are represented. Bottom left plot is the average $x$ and $y$ coordinates (with standard deviation) of the distal most point of the catheter over the course of the experiment. Bottom right plot is the torque applied to the knob during the experiments.

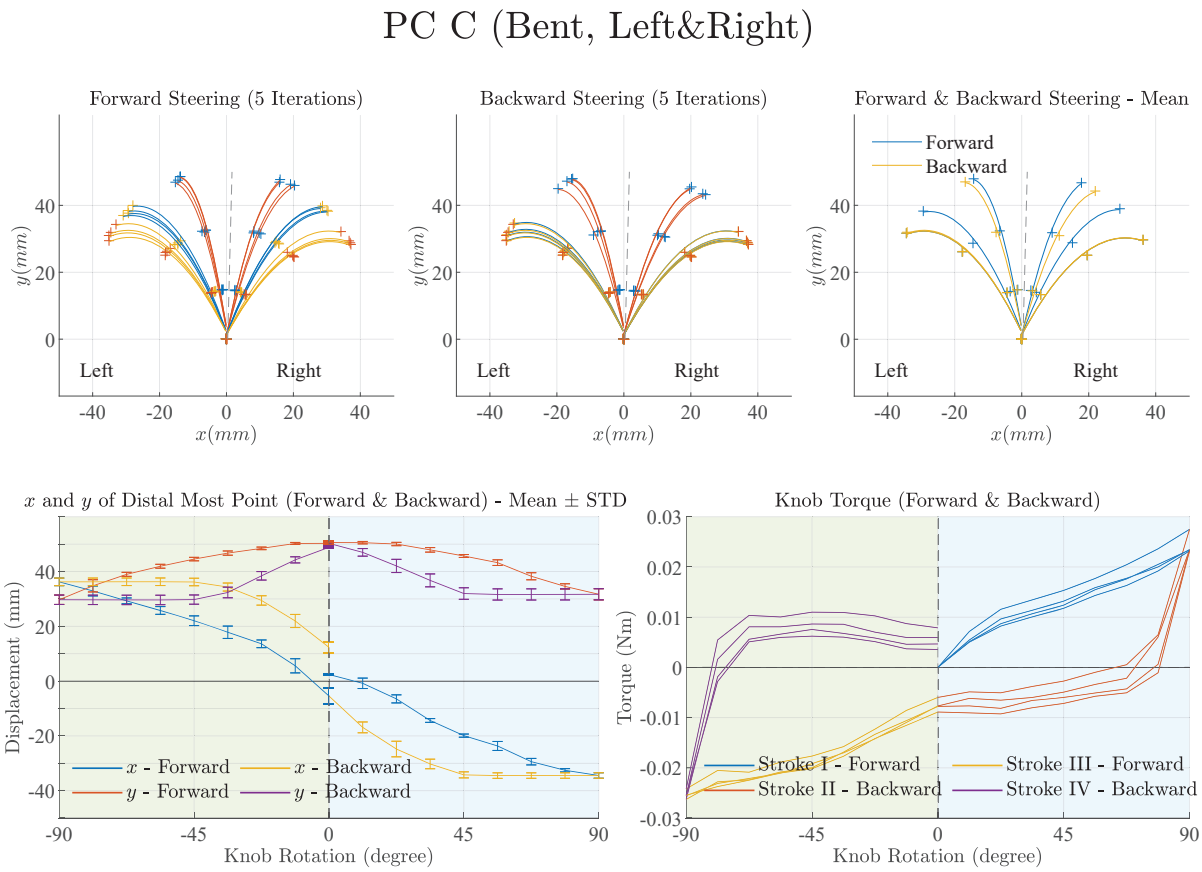



**Figure D.7:** Steerability results of the left and right steering of PC c catheter in a bent configuration: Top left & middle plots indicate the geometry of the catheter tip for each trial when the catheter is subjected to forward steering (Stroke I and Stroke III) and backward steering (Stroke II and Stroke IV) respectively. Top right plot is the average catheter tip positions over five trials. The difference between the catheter tip positions corresponding to the same knob angle position during the forward and backward steering indicate backlash. For better visualisation, only the catheter tip shapes for knob rotation angles $\pm 22.5°$, $\pm 56.25°$ and $\pm 90°$, are represented. Bottom left plot is the average $x$ and $y$ coordinates (with standard deviation) of the distal most point of the catheter over the course of the experiment. Bottom right plot is the torque applied to the knob during the experiments.

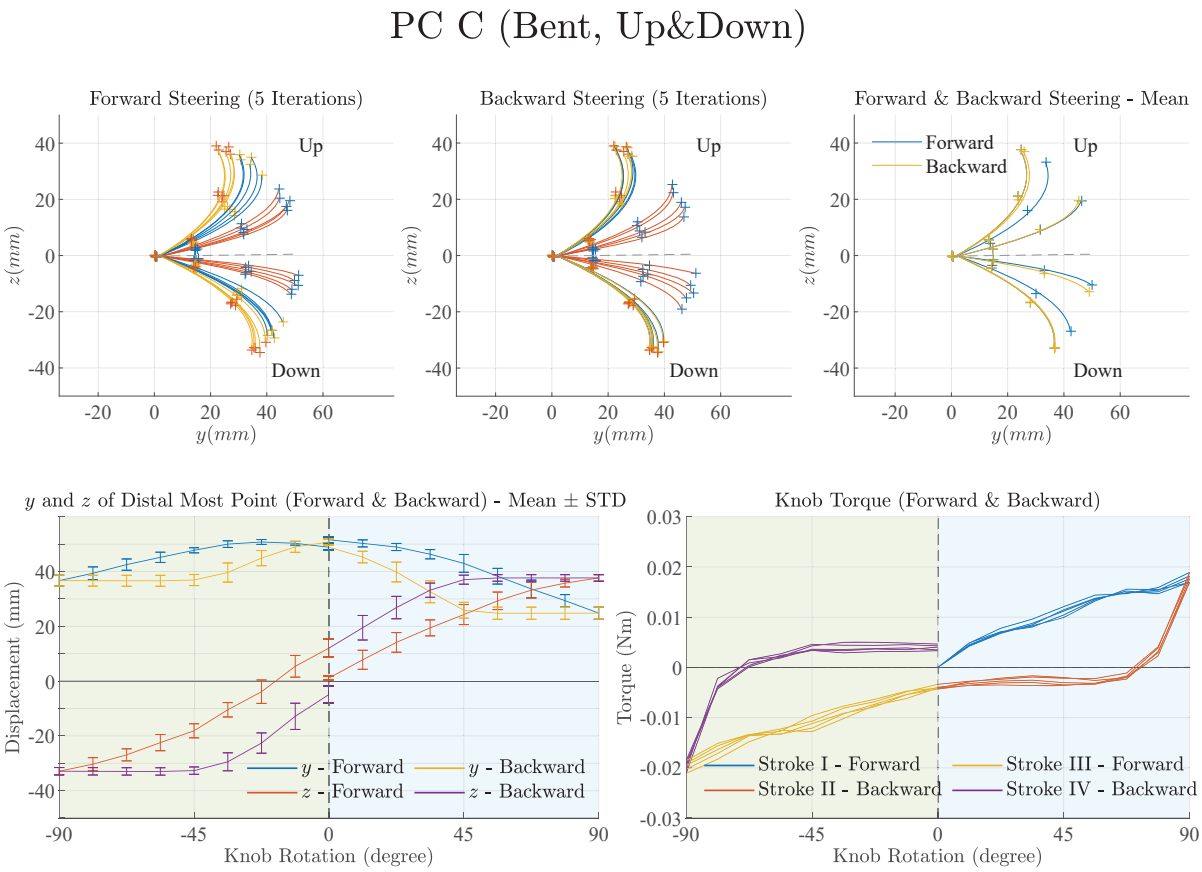



**Figure D.8:** Steerability results of the up and down steering of PC C catheter in a bent configuration: Top left & middle plots indicate the geometry of the catheter tip for each trial when the catheter is subjected to forward steering (Stroke I and Stroke III) and backward steering (Stroke II and Stroke IV) respectively. Top right plot is the average catheter tip positions over five trials. The difference between the catheter tip positions corresponding to the same knob angle position during the forward and backward steering indicate backlash. For better visualisation, only the catheter tip shapes for knob rotation angles $\pm 22.5°$, $\pm 56.25°$ and $\pm 90°$, are represented. Bottom left plot is the average $x$ and $y$ coordinates (with standard deviation) of the distal most point of the catheter over the course of the experiment. Bottom right plot is the torque applied to the knob during the experiments.

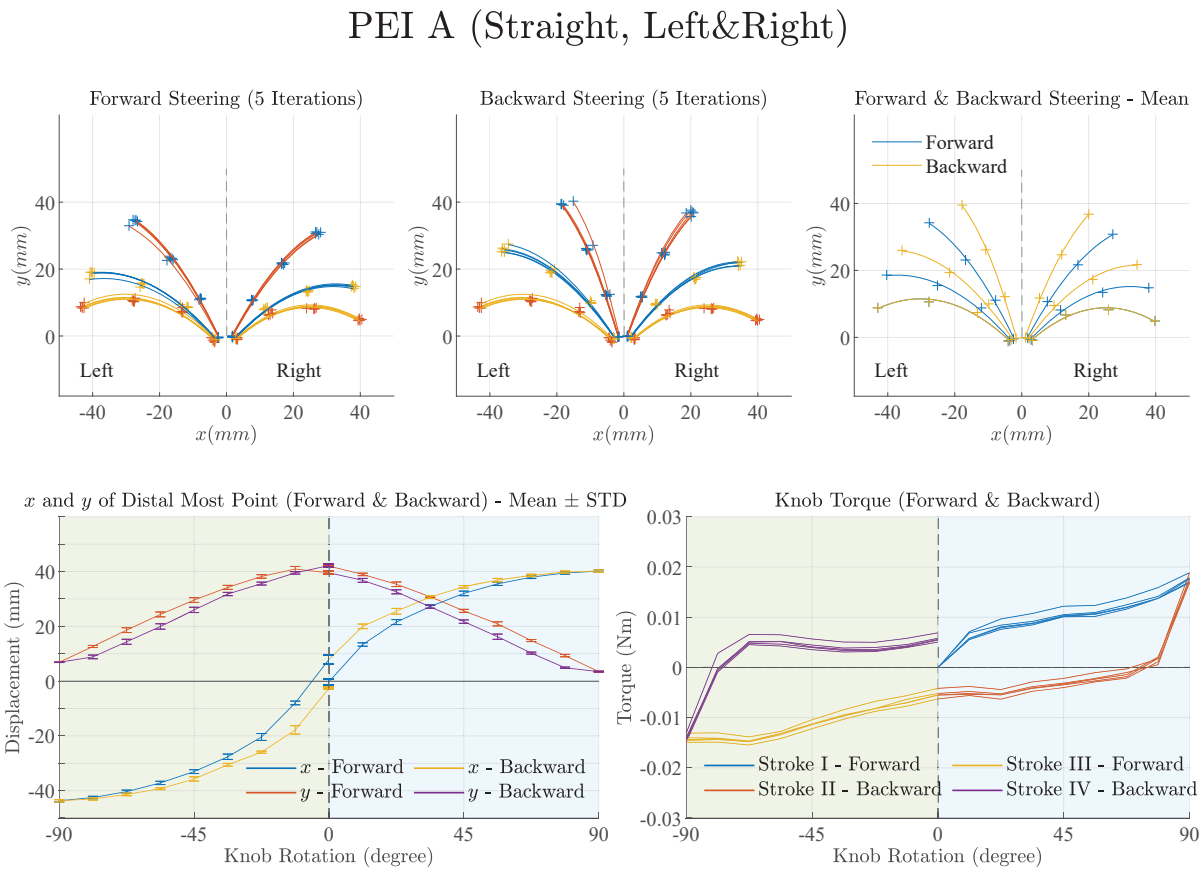



**Figure D.9:** Steerability results of the left and right steering of PEI A catheter in a straight configuration: Top left & middle plots indicate the geometry of the catheter tip for each trial when the catheter is subjected to forward steering (Stroke I and Stroke III) and backward steering (Stroke II and Stroke IV) respectively. Top right plot is the average catheter tip positions over five trials. The difference between the catheter tip positions corresponding to the same knob angle position during the forward and backward steering indicate backlash. For better visualisation, only the catheter tip shapes for knob rotation angles $\pm 22.5°$, $\pm 56.25°$ and $\pm 90°$, are represented. Bottom left plot is the average $x$ and $y$ coordinates (with standard deviation) of the distal most point of the catheter over the course of the experiment. Bottom right plot is the torque applied to the knob during the experiments.

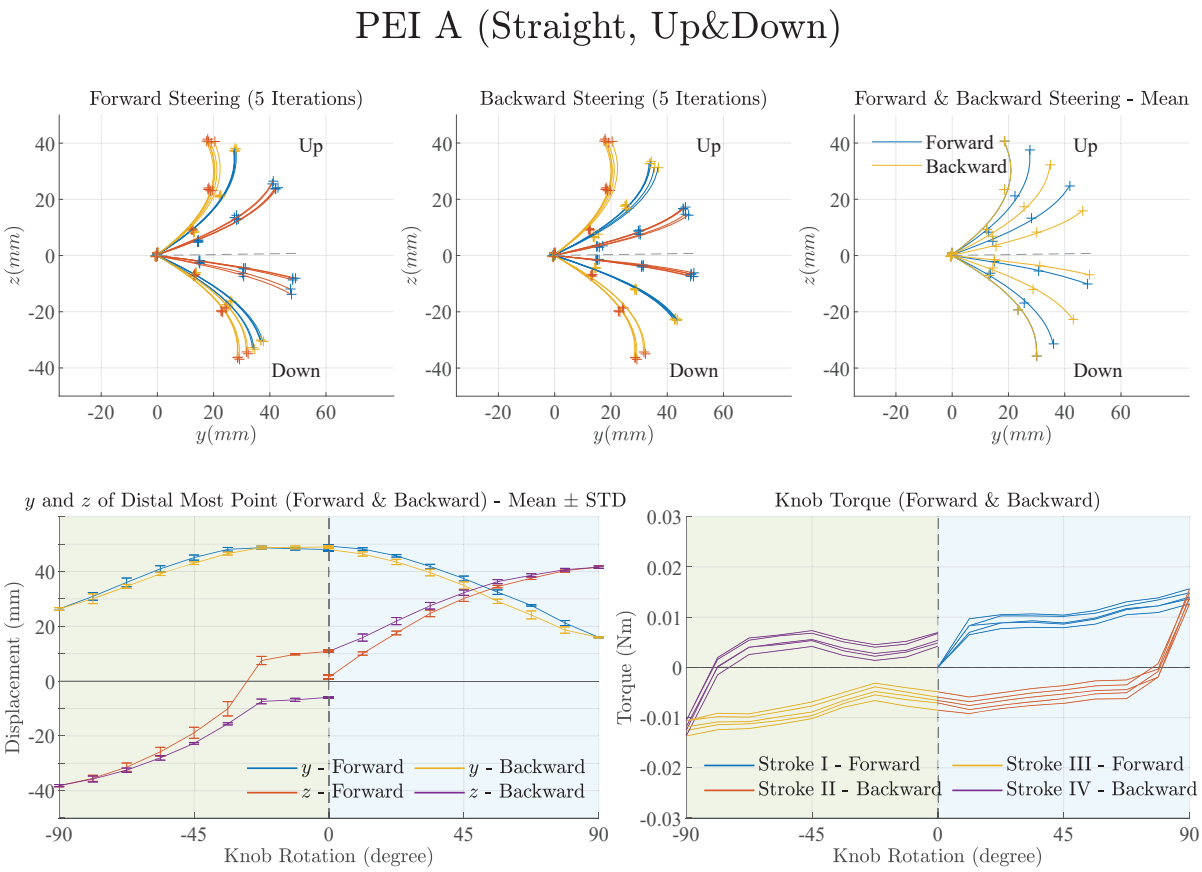



**Figure D.10:** Steerability results of the up and down steering of PEI A catheter in a straight configuration: Top left & middle plots indicate the geometry of the catheter tip for each trial when the catheter is subjected to forward steering (Stroke I and Stroke III) and backward steering (Stroke II and Stroke IV) respectively. Top right plot is the average catheter tip positions over five trials. The difference between the catheter tip positions corresponding to the same knob angle position during the forward and backward steering indicate backlash. For better visualisation, only the catheter tip shapes for knob rotation angles $\pm 22.5°$, $\pm 56.25°$ and $\pm 90°$, are represented. Bottom left plot is the average $x$ and $y$ coordinates (with standard deviation) of the distal most point of the catheter over the course of the experiment. Bottom right plot is the torque applied to the knob during the experiments.

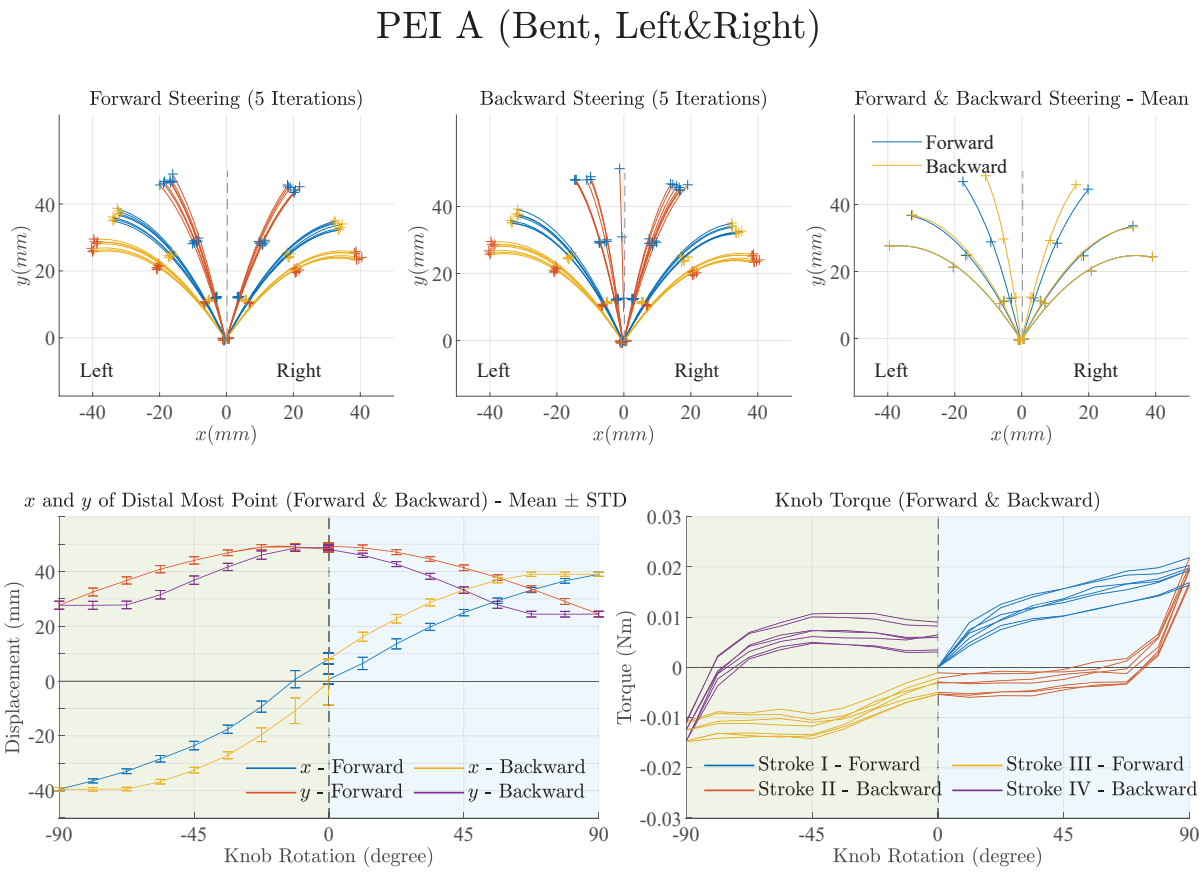



**Figure D.11:** Steerability results of the left and right steering of PEI A catheter in a bent configuration: Top left & middle plots indicate the geometry of the catheter tip for each trial when the catheter is subjected to forward steering (Stroke I and Stroke III) and backward steering (Stroke II and Stroke IV) respectively. Top right plot is the average catheter tip positions over five trials. The difference between the catheter tip positions corresponding to the same knob angle position during the forward and backward steering indicate backlash. For better visualisation, only the catheter tip shapes for knob rotation angles $\pm 22.5°$, $\pm 56.25°$ and $\pm 90°$, are represented. Bottom left plot is the average $x$ and $y$ coordinates (with standard deviation) of the distal most point of the catheter over the course of the experiment. Bottom right plot is the torque applied to the knob during the experiments.

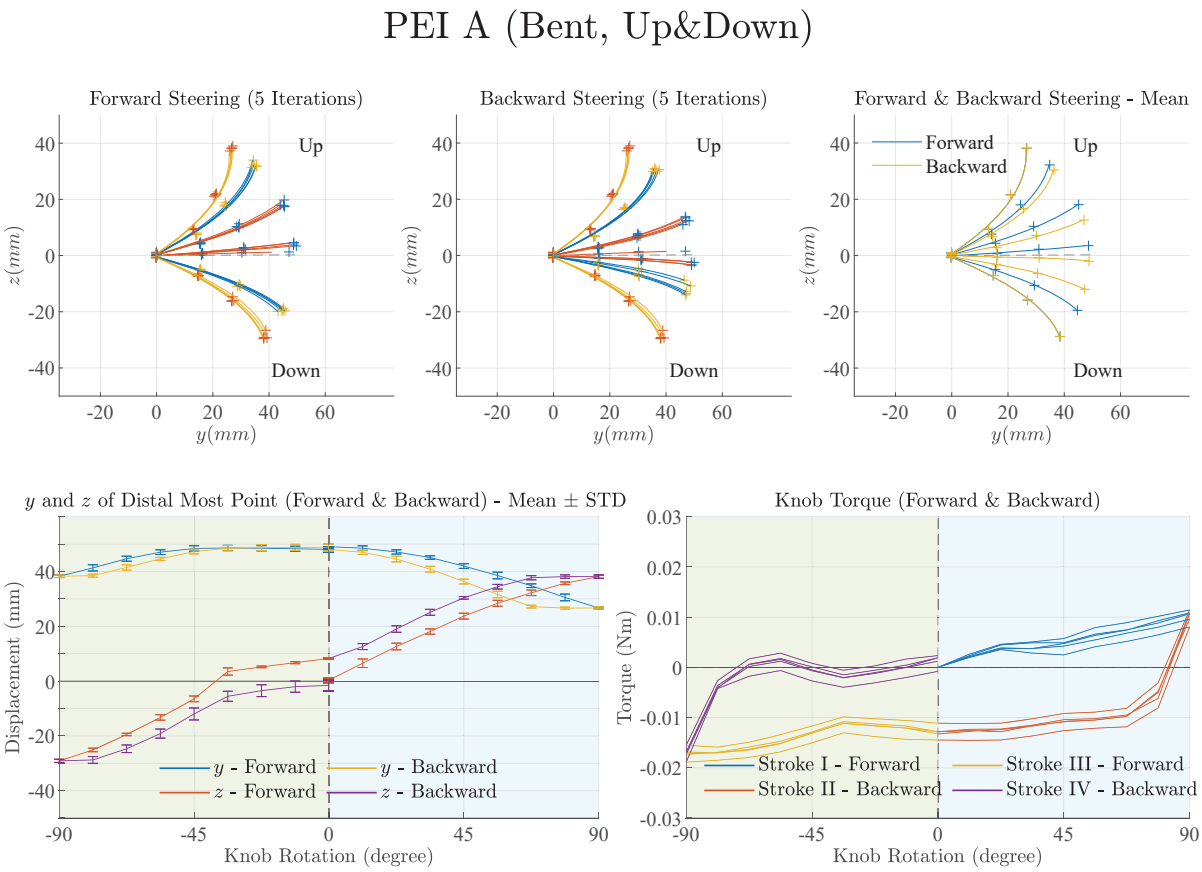



**Figure D.12:** Steerability results of the up and down steering of PEI A catheter in a bent configuration: Top left & middle plots indicate the geometry of the catheter tip for each trial when the catheter is subjected to forward steering (Stroke I and Stroke III) and backward steering (Stroke II and Stroke IV) respectively. Top right plot is the average catheter tip positions over five trials. The difference between the catheter tip positions corresponding to the same knob angle position during the forward and backward steering indicate backlash. For better visualisation, only the catheter tip shapes for knob rotation angles $\pm 22.5°$, $\pm 56.25°$ and $\pm 90°$, are represented. Bottom left plot is the average $x$ and $y$ coordinates (with standard deviation) of the distal most point of the catheter over the course of the experiment. Bottom right plot is the torque applied to the knob during the experiments.

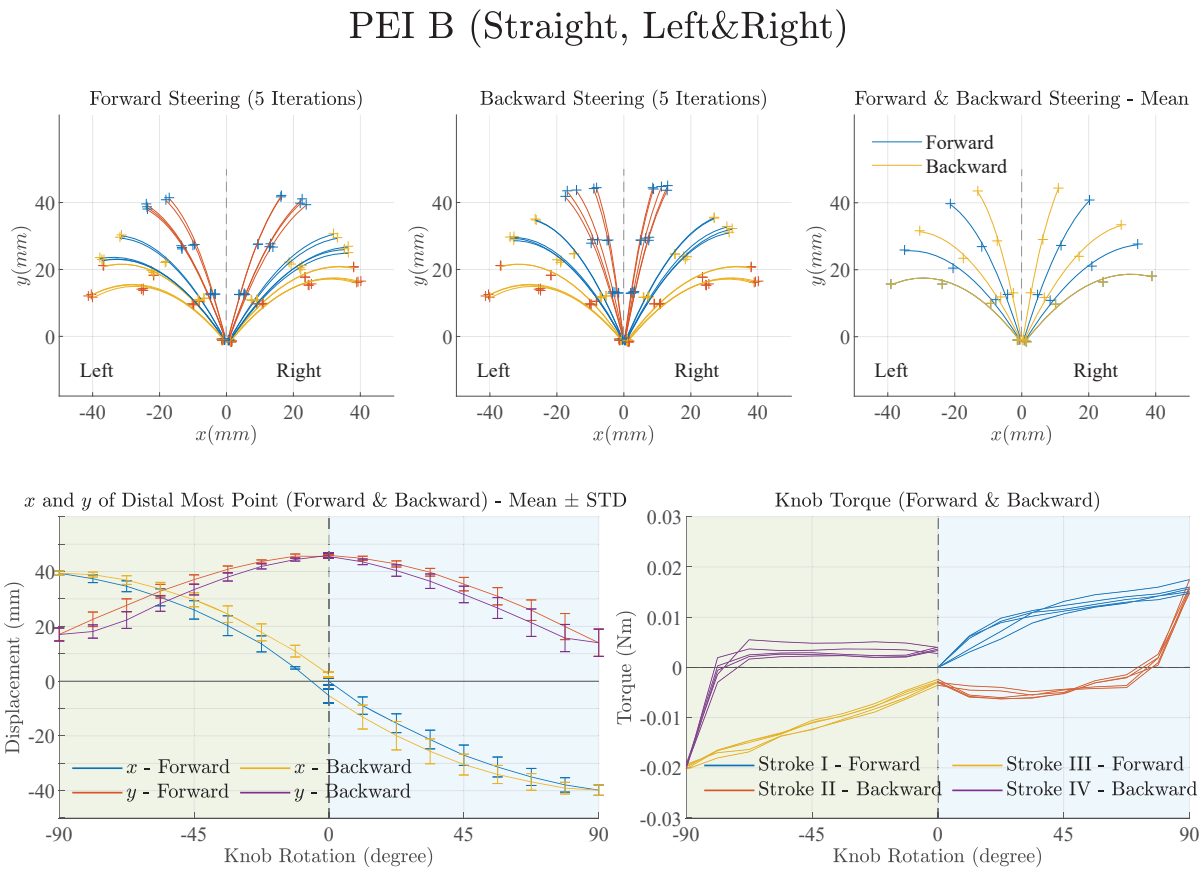



**Figure D.13:** Steerability results of the left and right steering of PEI B catheter in a straight configuration: Top left & middle plots indicate the geometry of the catheter tip for each trial when the catheter is subjected to forward steering (Stroke I and Stroke III) and backward steering (Stroke II and Stroke IV) respectively. Top right plot is the average catheter tip positions over five trials. The difference between the catheter tip positions corresponding to the same knob angle position during the forward and backward steering indicate backlash. For better visualisation, only the catheter tip shapes for knob rotation angles $\pm 22.5°$, $\pm 56.25°$ and $\pm 90°$, are represented. Bottom left plot is the average $x$ and $y$ coordinates (with standard deviation) of the distal most point of the catheter over the course of the experiment. Bottom right plot is the torque applied to the knob during the experiments.

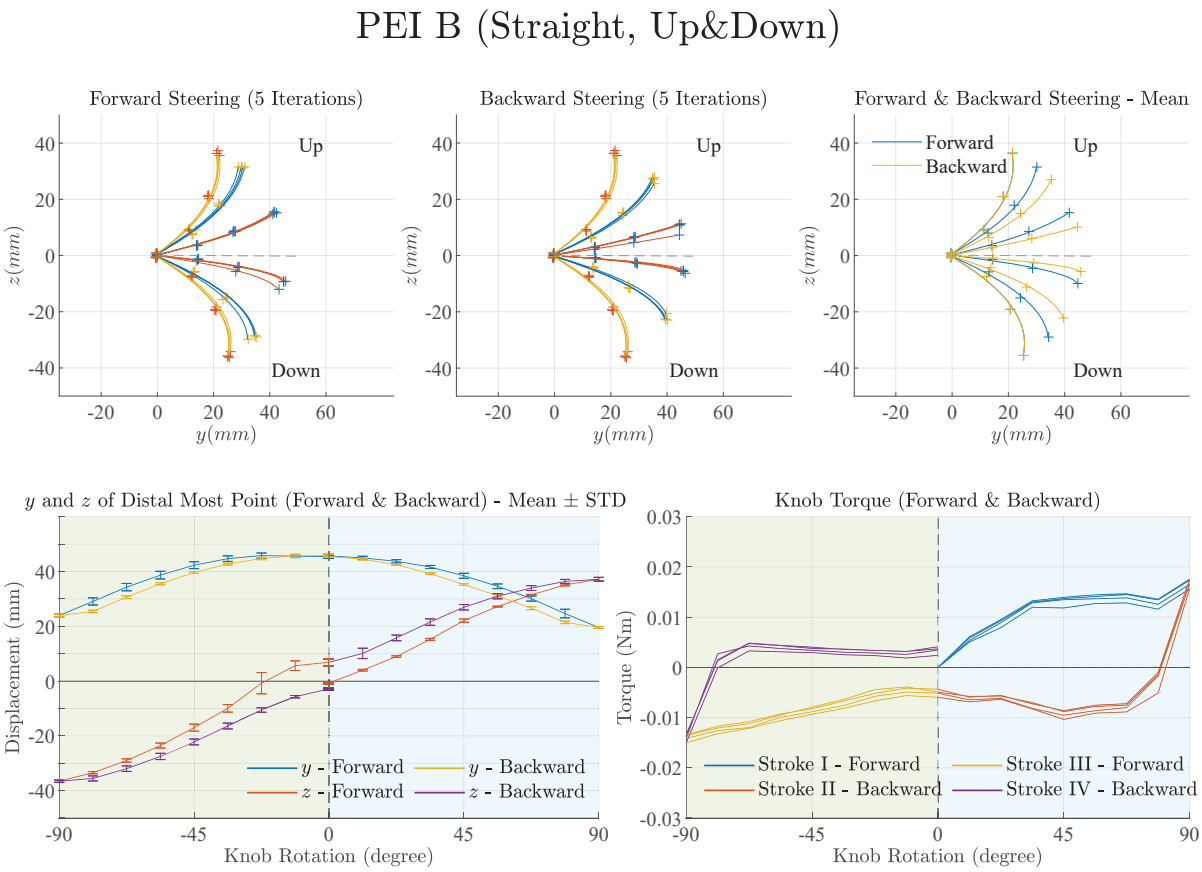



**Figure D.14:** Steerability results of the up and down steering of PEI B catheter in a straight configuration: Top left & middle plots indicate the geometry of the catheter tip for each trial when the catheter is subjected to forward steering (Stroke I and Stroke III) and backward steering (Stroke II and Stroke IV) respectively. Top right plot is the average catheter tip positions over five trials. The difference between the catheter tip positions corresponding to the same knob angle position during the forward and backward steering indicate backlash. For better visualisation, only the catheter tip shapes for knob rotation angles $\pm 22.5°$, $\pm 56.25°$ and $\pm 90°$, are represented. Bottom left plot is the average $x$ and $y$ coordinates (with standard deviation) of the distal most point of the catheter over the course of the experiment. Bottom right plot is the torque applied to the knob during the experiments.

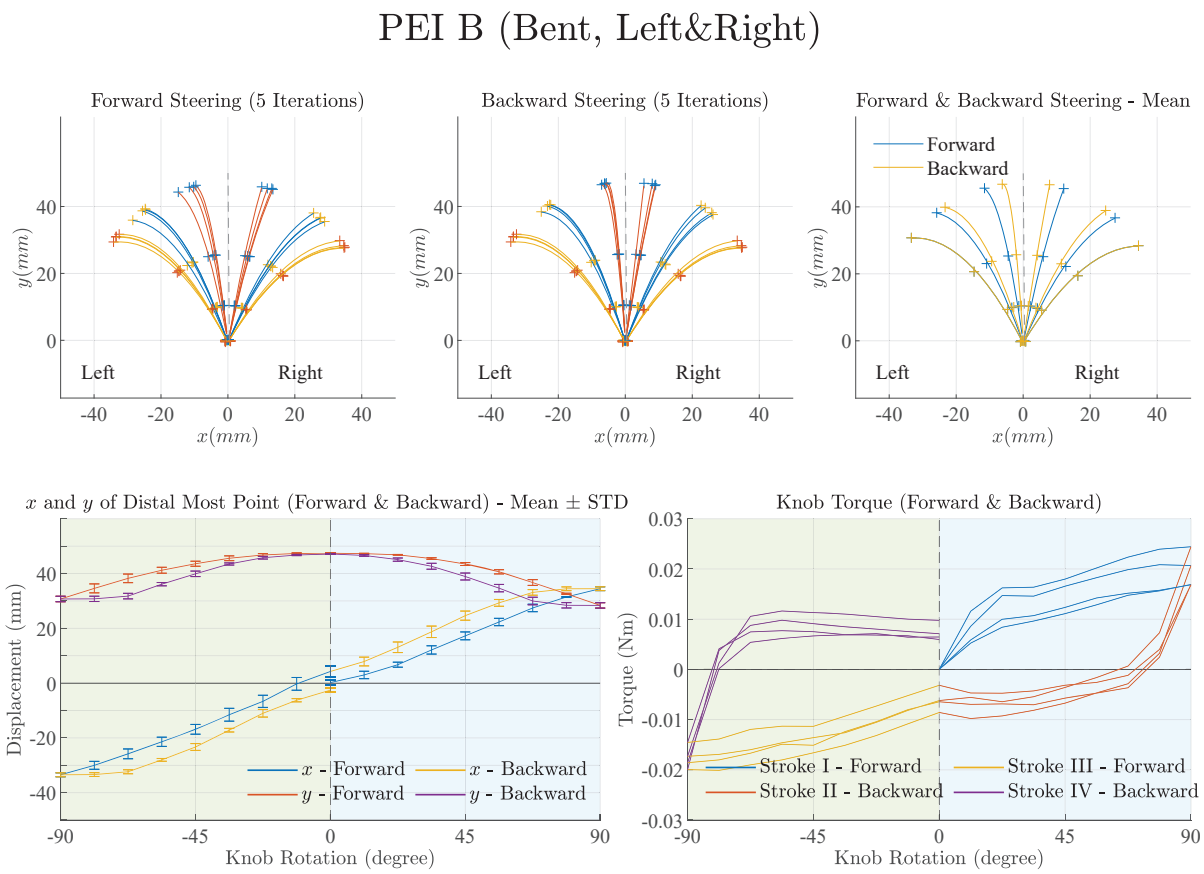



**Figure D.15:** Steerability results of the left and right steering of PEI B catheter in a bent configuration: Top left & middle plots indicate the geometry of the catheter tip for each trial when the catheter is subjected to forward steering (Stroke I and Stroke III) and backward steering (Stroke II and Stroke IV) respectively. Top right plot is the average catheter tip positions over five trials. The difference between the catheter tip positions corresponding to the same knob angle position during the forward and backward steering indicate backlash. For better visualisation, only the catheter tip shapes for knob rotation angles $\pm 22.5°$, $\pm 56.25°$ and $\pm 90°$, are represented. Bottom left plot is the average $x$ and $y$ coordinates (with standard deviation) of the distal most point of the catheter over the course of the experiment. Bottom right plot is the torque applied to the knob during the experiments.

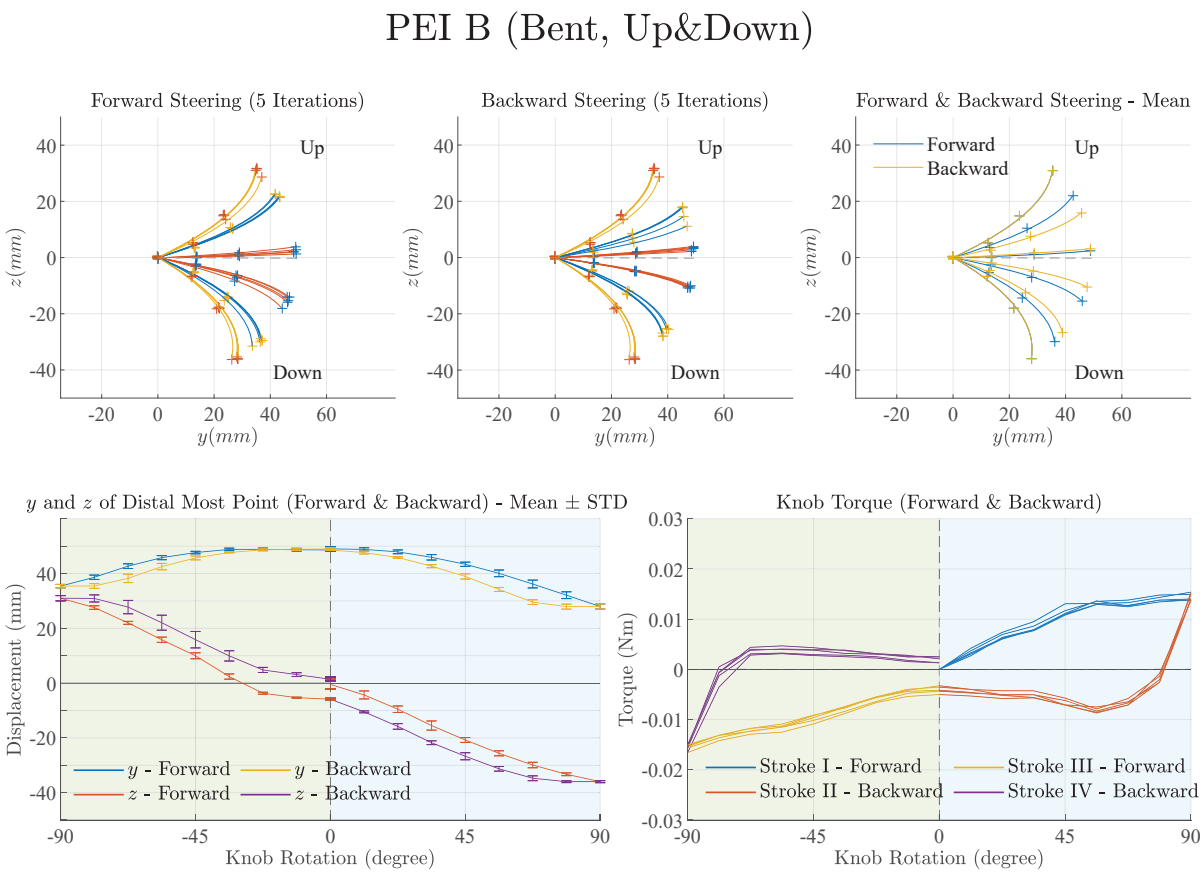



**Figure D.16:** Steerability results of the up and down steering of PEI B catheter in a bent configuration: Top left & middle plots indicate the geometry of the catheter tip for each trial when the catheter is subjected to forward steering (Stroke I and Stroke III) and backward steering (Stroke II and Stroke IV) respectively. Top right plot is the average catheter tip positions over five trials. The difference between the catheter tip positions corresponding to the same knob angle position during the forward and backward steering indicate backlash. For better visualisation, only the catheter tip shapes for knob rotation angles $\pm 22.5°$, $\pm 56.25°$ and $\pm 90°$, are represented. Bottom left plot is the average $x$ and $y$ coordinates (with standard deviation) of the distal most point of the catheter over the course of the experiment. Bottom right plot is the torque applied to the knob during the experiments.

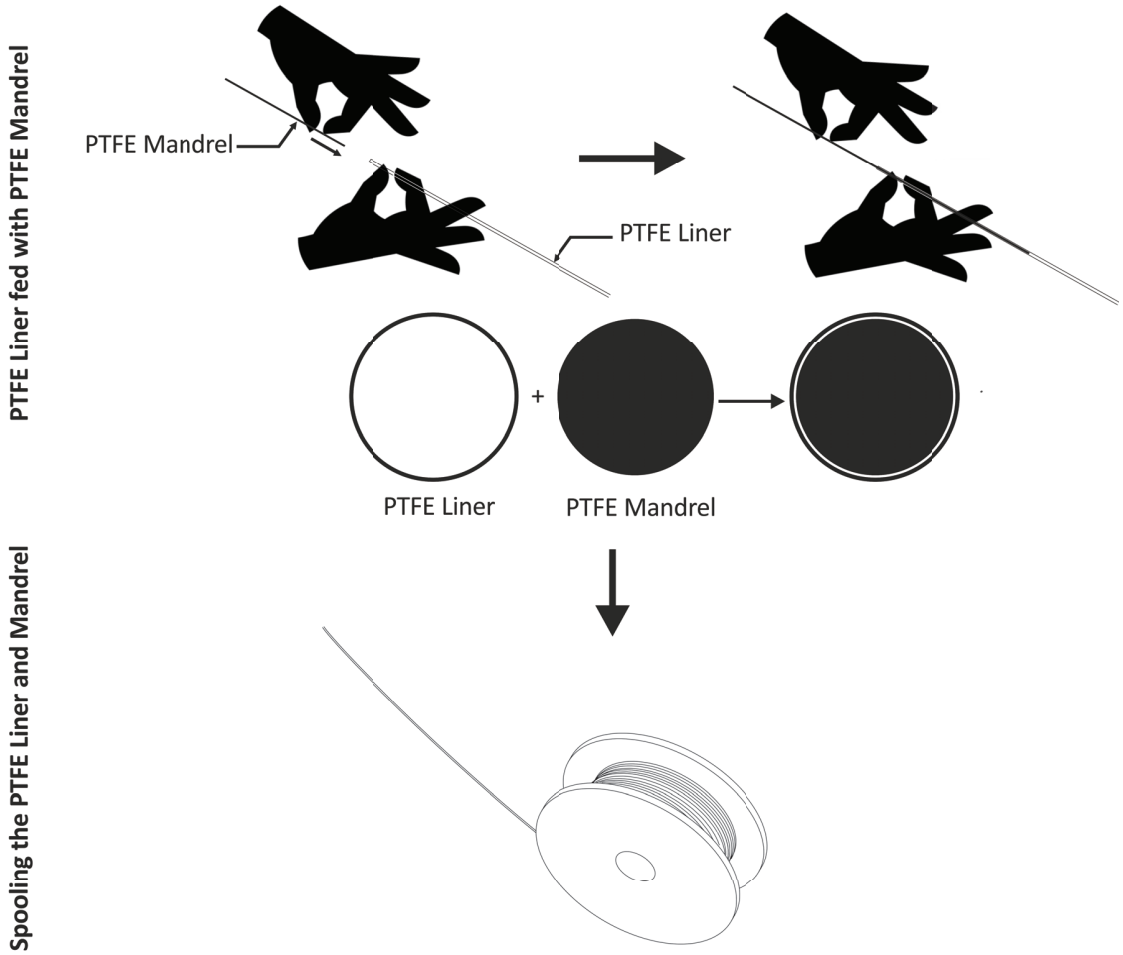
Chapter E

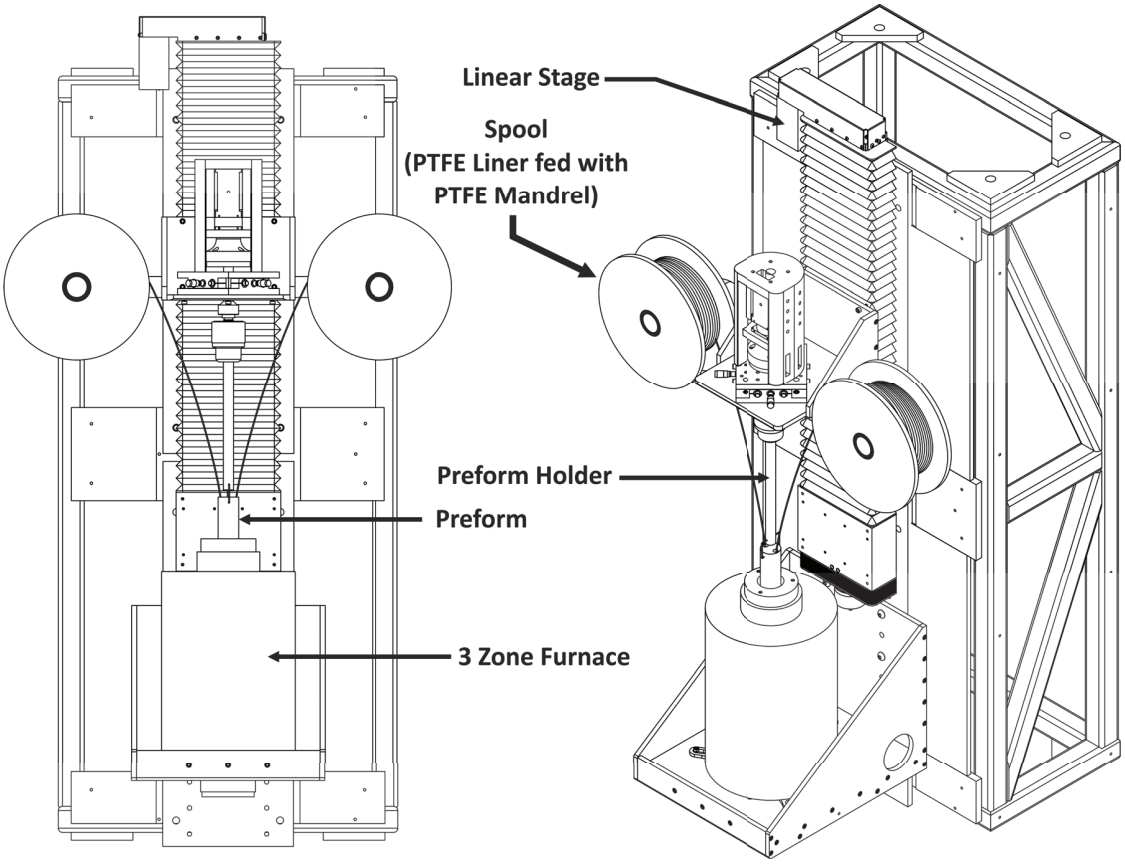
# Liner Feeding (Patent)

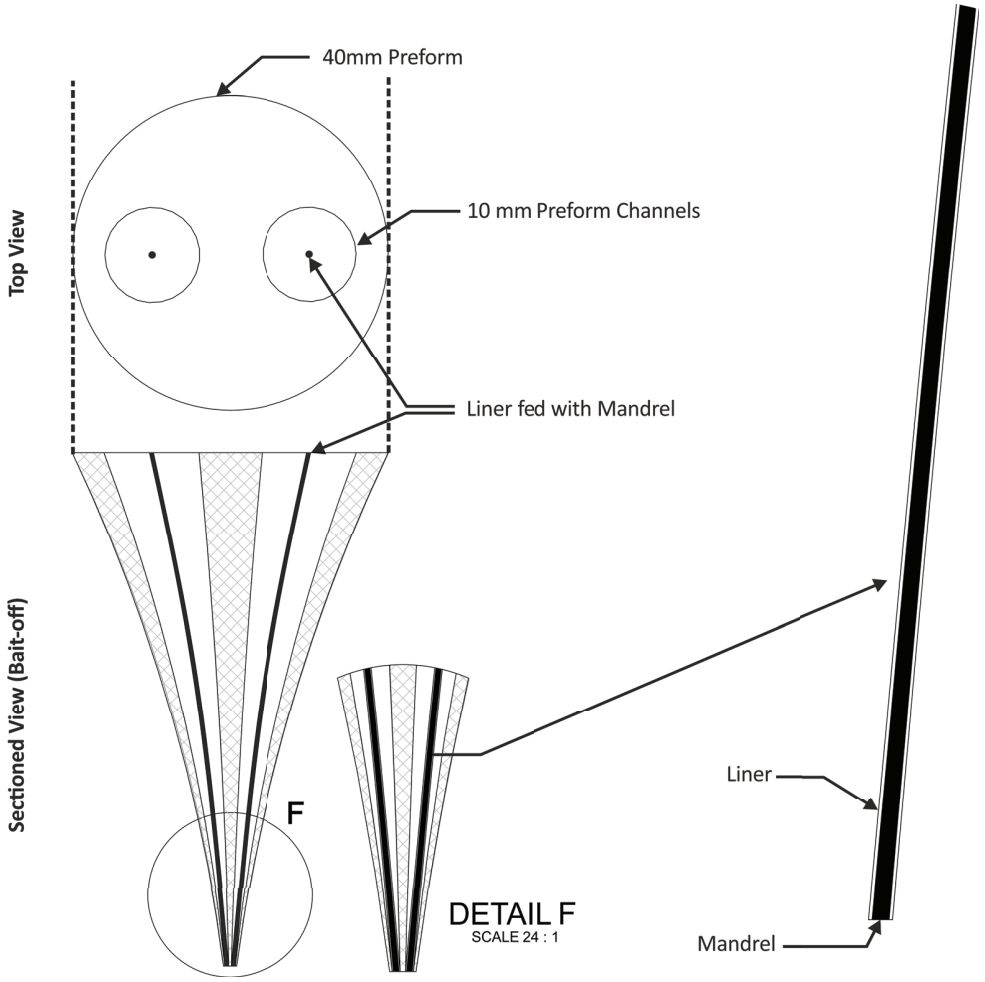
In the patent application we proposed a method of fabricating medical devices ideal for Minimally Invasive Surgeries (MIS) using the thermal drawing process. The idea here is not to replace the state-of-the-art manufacturing methods, but to expand the capabilities of the thermal drawing process by incorporating liners with desired features (lubricity, strength, etc) to any existing fibre draw tower. The figures below describe one of the ways of incorporating such liners into the thermal drawing process.

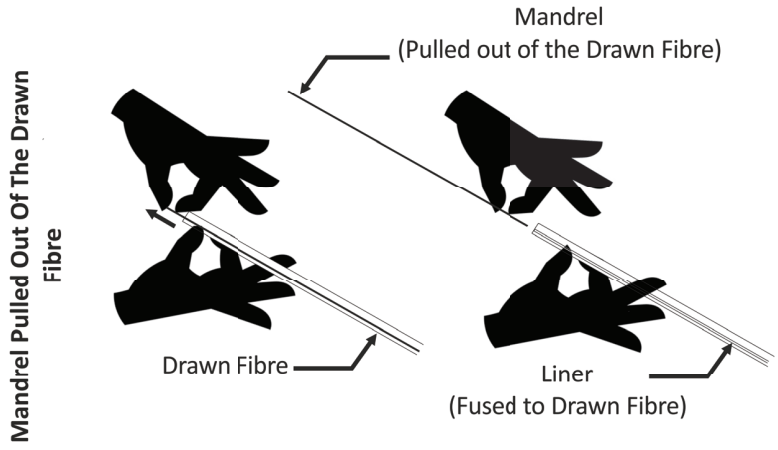
The etched liner fed with mandrel assembly is fed into the open preform channels as the preform is fed into the fibre draw tower, as shown in the figure below. Note: the drawing temperature shouldn't exceed the melting point of the liner/mandrel thermoplastic assembly. One or more spools can be employed (e.g.: 2 spools) into the thermal drawing process and the preform can be fabricated/arranged to accommodate "n" number of liner/mandrel assemblies. For example, a round etched PTFE liner (Outer Diameter 0.5mm) fed with a PTFE mandrel is fed into a 10mm channel through the entire length of the preform (with an outer diameter of 40mm). In this example, the preform channels are positioned eccentrically from the centre of the preform. During the draw, the channel draws down to the desired diameter of (0.5mm diameter) and the PTFE liner fed with PTFE mandrel fills the drawn down channel. Since the outer surface of the PTFE liner is etched, it bonds to the polymer it's in contact with. Once the draw is done, the drawn fibres are collected and the mandrels are pulled out for the next draw (re-usable).

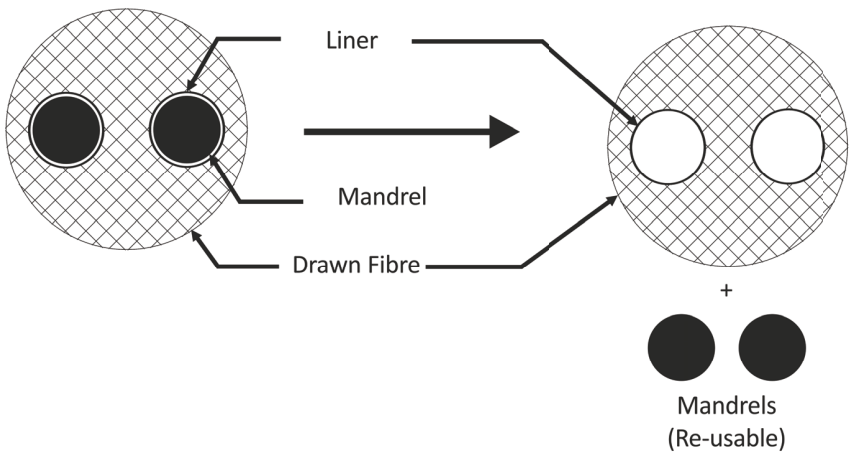
It's also important to note that with this approach it would also be possible to co-feed not only thermoplastics (e.g. fluoropolymers), but also thermosets with unique characteristics such as strength-per-unit-size (e.g. polyimide). This could also be advantageous not only for device (guidewire, balloon catheters, and stent catheters) insertion into these lined lumens/channels but also reduce the friction experienced whilst pulling tendons to manipulate (cable-driven) steerable catheters (especially during the cannulation of tortuous anatomies). Another possible application is fibre microfluidics where the hydrophilicity/hydrophobicity of channels is of great importance (or) even the steering of (hydraulically-driven) steerable catheters. Not to mention, feeding the liner/mandrel assembly or just even the mandrel could also play a role in preventing the reflow deformation of channels driven by surface tension (Laplace pressure) during the draw especially with polymers drawn at relatively low viscosities. Thereby achieving the desired shape and dimensions of empty channels. Different geometries of liners and mandrels could also be used (it's not limited only to circular profiles). Helical lined channels should also be achievable with the draw tower by connecting the spools to a rotating platform (feeding and rotating simultaneously). The helical path of the channel can compensate for length changes of the tendon when the surgical device is bent, particularly when there are pairs of channels with pairs of antagonistic tendons. The helical paths can facilitate accurate control of the bending of the surgical device. Helical channels could be of use in fibre microfluidics.


PTFE Liner fed with PTFE Mandrel
PTFE Mandrel
PTFE Liner
+
PTFE Liner
PTFE Mandrel
Spooling the PTFE Liner and Mandrel


Linear Stage
Spool
(PTFE Liner fed with
PTFE Mandrel)
Preform Holder
Preform
3 Zone Furnace


40mm Preform
10 mm Preform Channels
Liner fed with Mandrel
Top View
Sectioned View (Bait-off)
F
DETAIL F
SCALE 24 : 1
Liner
Mandrel


Mandrel
(Pulled out of the Drawn Fibre)
Mandrel Pulled Out Of The Drawn Fibre
Drawn Fibre
Liner
(Fused to Drawn Fibre)


Liner
Mandrel
Drawn Fibre
+
Mandrels
(Re-usable)